



Astronomical Society of India

The award for the Best Thesis presentation at the XXI meeting of the Astronomical

Society of India is given to

Pavan Chakraborty

for the Thesis talk entitled

Investigations of Dust from

Selected Comets

Pune, 8th February 2002

A. Srinivasa
President

Investigations of Dust from Selected Comets

*A Thesis
Submitted for the Degree of
Doctor of Philosophy*

*In
Faculty of Science
Bangalore University*

Pavan Chakraborty



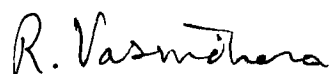
**Indian Institute of Astrophysics
Bangalore 560 034, India**

February 2001

*To my Late Father
Sweet Mother, Keya
and my Little Daughter*

Declaration

I hereby declare that this thesis, submitted to Bangalore University, Bangalore, for the award of a Ph.D. degree, is a result of the investigations carried out by me at Indian Institute of Astrophysics, Bangalore, under the supervision of Dr. R. Vasundhara. The results presented herein have not been subject to scrutiny, by any university or institute, for the award of a degree, diploma, associateship or fellowship whatsoever.



Dr. R. Vasundhara,
(Thesis Supervisor),



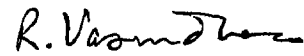
Pavan Chakraborty
(Ph.D. Candidate)

Indian Institute of Astrophysics
Bangalore 560 034, India

February 21, 2001

Certificate

This is to certify that the thesis entitled 'Investigations of Dust from Selected Comets' submitted to the Bangalore University by Pavan Chakraborty for the award of the degree of Doctor of Philosophy in the faculty of Science, is based on the results of the investigations carried out by him under my supervision and guidance, at the Indian Institute of Astrophysics. This thesis has not been submitted for the award of any degree, diploma, associateship, fellowship, etc. of any university or institute.



Dr R. Vasundhara
(Thesis Supervisor)

Bangalore 560034
February 21, 2001

Acknowledgements

It has taken many a long night and day to complete this little piece of work - a work built on the work of others and a study on a miniscule fraction undertaken in a vast field. I consider myself lucky to have got the opportunity of working in Astronomy in general and in the area of my work in particular. For this I am greatly indebted to Dr. R. Vasundhara for her guidance and encouragements throughout the work. I am extremely grateful to her for for obtaining the funds to build the spectropolarimeter. All along, the help I got from her and the discussion I had with her were motivations to do better each time. I thank her for the lessons learnt in the process.

I am grateful to Prof. Ramanath Cowsik, Director, Indian Institute of Astrophysics, for all the facilities provided to me. I am extremely indebted to him for having approved my two trips to the Vatican Observatory, Castel Gandolfo, Italy, in 1997 and 1998. My interactions with the experts, the ideas, suggestions and advise obtained from them during these two trips have helped me in developing some of the techniques, without which this thesis would have been incomplete. I thank the Chairman and members of the Board of Graduate studies for all their help during my stay at IIA.

I thank the Bangalore University for making the official processing smooth and I remain indebted to Prof. Anandaram, Chairman, Physics Dept., Bangalore University for his help in official matters. The officials at the PhD section, Bangalore University at Central College have always been helpful on all issues of official matters.

I profusely thank Prof. N. Kameswara Rao, Dean (Academic) for his helpful suggestions during the initial planning of the spectropolarimeter. I thank him for his strong support, encouragement and for launching me in the right direction so that I could contact the right person, Dr. Robert W. Goodrich for technical know-how of the spectropolarimeter. I thank Prof. R. Srinivasan, Dean (Engineering) for his keen interest and providing me with the facilities for fabrication of the Optical, Dual-Beam, Automated, Medium Resolution SpectroPolarimeter (O-DB.AMRSP). I am indebted to Prof. J. C. Bhattacharyya, former director of IIA for various discussions during the inception of building the O-DB.AMRSP. M/s. B. R. Madhava

Rao, P. U. Kamath, V. K. Subramanian, F. Gabriel, K. Sagayanathan, A. Mani and others from the Mechanical Division, were involved in the designing, testing and fabrication of the mechanical components of the spectropolarimeter. The electronics of the automation and instrument controls were implemented with the help of M/s K. Ravi, P. Anbazhagan, S. V. Rao and A. Ramachandran from the electronic division at VBO. Mr. Nagraj Naidu was always extremely helpful and would clear my doubts regarding different aspects of CCDs, electronics and instrument controls. I thank them all, for without their help and technical efficiency, building the O-DB.AMRSP would have remained a dream. I also thank the Photonics Division of IIA for helping me with the cutting of the order separating filters, attaching the Path Length Compensator (PLC) with the Modified Glan-Taylor Prism (MGTP). I thank profusely Mr P. K. Mahesh, in-charge of Mechanical Design Section and Mechanical Workshop, VBO, Kavalur, for all the discussions related to instrumentation and for helping me at all stages from acquiring the original Boller & Chivens (B&C) Spectrograph drawings to the technical proof reading of my thesis.

Greg Smith, Mech. & Opt. Design Group, AAO is profusely thanked for sending the original drawing of the B&C spectrograph which was converted to the spectropolarimeter. I am indebted to Dr Robert W. Goodrich for valuable discussions during the initial phase of building the spectropolarimeter. Hank Bensas, and Vino Vats, Sr. Engineer at Karl Lambrecht Corporation, Chicago, U.S.A., are thanked for their correspondence, suggestions and help in fabrication of the polarimetric optics. I thank Prof. (Fr.) George V. Coyne S. J., Director of the Vatican Observatory and Dr. Susan Trammell for their suggestions regarding the calibrations of the Spectropolarimeter. George, I also would like to thank you for going through the manuscript of my instrumentation work which now appears as Chapter 3 in this thesis.

Several colleagues at IIA stationed at VBO helped me during the observations of the comet close to the horizon, at the telescope limits. F. Gabriel, P. Anbazhagan and others kept a vigil on the telescope as the limits were bypassed so that the telescope could point at Hale-Bopp. I also acknowledge M/s. M. Appakutty M. Ganesan, K. Jayakumar, M. Muniraj, V. Murthy, E. Ramachandran, V. Ramesh, A.

for personally providing me with their phase dependent polarization data of Comet Hale-Bopp and Wild 2.

This research has made use of NASA's Astrophysics Data System Abstract Service. I thank profusely Prof. D.C.V.Mallik for reviewing the final draft of my thesis. His suggestions and meticulous corrections were the dominant factors that helped me improve my thesis to its present state. I also acknowledge Prof. Jayant Murthy for going through some of the chapters of my thesis. I thank Ms. Sandra Rajiva and Dr. R. Srikanth for proof reading some sections of my thesis.

I am grateful to the Librarian Ms. A. Vagiswari and the IIA library staff Ms. Christina Louis, M/s. Venkatesh, Yarrappa, and others for all the facilities and help they provided. The library with the wealth of knowledge in the form of books and journals has helped me immensely.

The computer center at IIA has been a second home to me. I taxed the computers with a lot of image processing and number crunching. I thank Mr. A. V. Ananth, in-charge of the computer center for all help provided. My heart felt regards to Mr. J. S. Nathan, system administrator who has always tried to help me with all my computational requirements and needs. I thank Prof. B. P. Das and Mr. Sonjoy Majumder, for allowing me to run some of my codes on their 4 CPU Sparc SUNW, Ultra-4 Computer. I also thank Dr. Baba Anthony Varghese for rescuing me from many crisis situations with computers. The Faculties and the scientific staff of IIA are thanked for their support.

I thank Mr. P. N. Prabhakara for Xeroxing the thesis, and M/s D. Kanakaraj and Thyagaraja for binding it. The help rendered by the administrative staff of IIA in making many of the official matters smooth going will always be remembered. I thank M/s. Narasimhan Raju and S. Dhananjaya for handling the Bangalore University official affairs, and for taking care of my accommodation. Mr. Mohan Kumar is thanked for taking care of the transportations to the observatory and other official trips. I also thank M/s. Raghupati, Iyengar, Prabhakara and Selvakumar of Stores for their help in procuring right from spoons to stationery when needed. I also thank Mr. K. T. Rajan, Mrs. Pramila Mohan, Mr. S. B. Ramesh, Mr. S. Nagaraj, Mrs Promila Jain and Mr. Md. Khan for their help right from my first

K. V. Ramana, G. Selvakumar and R. Sivakumar who helped me during the several nights of observations at VBT. M/s. N. Dinakaran, M. Gopal, K. Kuppuswami, A. Munirandi, J. Manoharan, C. Sundaravadivelu, N. Subramani, M. Vadivelu and C. Velu are acknowledged for helping me at the 1.02 m telescope. I would also like to thank Prof. T. P. Prabhu for his kind help during the first test observations of the O-DB.AMRSP. His suggestions were extremely valuable and enabled me to align the polarimetric optics more efficiently. Drs. A. C. Gupta, R. Swara and T. Sivarani are acknowledged for providing me with some of their observational time for comet observations.

I express again my gratitude to George for arranging the funds for my travel to Italy in 1997 and again in 1998. I thank you for the local hospitality and making my stay at Castel Gandolfo, an extremely memorable one. My thanks to the faculties of the 1997 Vatican Observatory Summer School; Mike (Prof. M. F. A'Hearn), Humberto (Prof. Humberto Campins), Faith (Prof. Faith Vilas) and Guy (Prof. Guy Consolmagno, S.J.), you all made the ground work for my understanding of comets and the solar system in general. My interactions with other faculties at the Vatican Observatory Prof. Christopher J. Corbally, S.J. and Prof. Richard P. Boyle, S.J. has also helped me a lot. Thank you again, Mike, for encouraging me and making me aware of different image enhancement techniques and providing the important and interesting tips during extra afternoon classes and during our travel to Florence. The secretary to the school, Elizabeth Maggio whom we fondly called Mother Superior, is also acknowledged. I have to specially mention Aigen Li whom I met as a fellow student at the Vatican Observatory. I thank him for providing us with the optical constants of the silicates and the strong tie we still cherish through e-mail.

Andreas Hänel, Erwin Heiser and Frederik Voss from the observatory of the Naturwissenschaftlicher Verein Osnabrück are thanked for collaboration. Their observations of Comet Hale-Bopp have been used in the present work.

For this thesis I have used a lot of published and unpublished data. I thank Dr. Harold A. Weaver for allowing me to use one of the early images of comet Hale-Bopp obtained from HST. Drs. E. Hadamcik, N. N. Kiselev and N. Manset are thanked

days at IIA. Thank you Mr. K. Sankaranarayanan, for your helpful nature, and for helping me in my needs.

It was a pleasure having the company of Drs. Eshwar Reddy, Sujan Sengupta, Dipankar Bannerjee, Uma Gorti, Annapurni, Pandey, Arun, Ramesh, Srikanth, Rajguru, Dilip, Krishnakumar, Swara, Sivarani and Mrs Bhargavi as my seniors. I thank all my batch-mates, Sankar, Rajesh, Sonjoy, Atish and Mangala for their wonderful company from those days we had shared during course work and many a help you rendered afterwards.

I take this opportunity to appreciate and express my gratitude to my other friends Sridharan, Dharam, Suresh, Geetha, Rajalakshmi, Ramachandra, Manoj, Ravindra, Preeti, Geetanjali, Rabbi, Kathiravan, Maheswar, Manas and others for the good times we have shared together. Without you all, the life here would have been dreary. I am lucky to have found a perfect house-mate in the guise of R. Srikanth, and a perfect friend and brother, Sonjoy Majumder.

Childhood is the ideal time to instigate someone's interest in a particular field. I thank my School SAICE, where I had my primary education. I thank Dilip Bhai, Deshpande ji and Sraddhalu at Pondicherry for instigating my interest in astronomy. You have taught me how to fall in love with the night sky.

No matter where I am, Father, I will keep in my mind your words "Direct your attention towards your goal, strengthen your willpower, will, will and will; be unperturbed and work hard". It is these words of yours which has kept me going through my difficult days. I so much wish that you were here physically to see my thesis. If not for the solace you have offered me, Mother, in times of despair, I would not have come out from patches of dark days. Keya, my wife, I appreciate your patience to bear my first love to Astronomy. Your support has held me upright. Thank you Srijita, my one year old daughter. Your pranks have brought my childhood back. Your keen interest to tap the computer key-board showed your intentions to help me type my thesis. I have finally done it, but I still acknowledge you for your interest showed towards my work.

ABSTRACT

Comets are the frozen reservoirs of primitive materials from the early solar nebula. They are some of the farthest objects in our solar system that permit a closer inspection during their perihelion passage. Dust in comets comprises a major part of the non-volatile material. Our present knowledge of cometary dust comes primarily from remote observations of IR spectral features and from *in situ* sampling of the impacting dust particles during the Halley flybys. It is now widely accepted that the cometary dust grains are porous structures of carbonaceous and silicatic material in amorphous and crystalline forms. At present it is not clear where the cometary silicates, especially in crystalline form, originated.

Extensive research on comet Hale-Bopp (C/1995-O1) since its discovery in 1995, has provided new insights into these cold and distant residual material of the solar nebula. A wealth of new information in a number of research areas of cometary dust, including a huge amount of data on the coma and jet/shell morphology, thermal properties and composition of grains and the process of dust ejection at large heliocentric distances were gathered. In this thesis, dust specific to comet Hale-Bopp is investigated. Limited data on Comet Wild 2 has also been utilized.

Chapter 1 contains the introduction to the field. Basic definitions of comets, cometary dust and the dynamical properties of dust grains are presented. The physics of dust scattering is discussed. A survey of the available observation and results by other groups on the comets observed for this thesis (comet Hale-Bopp and comet Wild 2) is made.

In *Chapter 2*, the telescopes and the instruments used for this study are discussed before going into the observations and the observational techniques. After touching upon the basic reduction and calibration methodology, the image enhancement

techniques are discussed.

Fabrication of an optical spectropolarimeter as an add-on facility to an existing astronomical spectrograph at the Vainu Bappu Telescope is described in *Chapter 3*. The polarimetric optics consists of a Pancharatnam design half-wave plate and a modified Glan-Taylor polarizing beam splitter. Instrumental response, calibration and characterization of the system are presented. Performance of the spectropolarimeter has been assessed based on the results of observations of polarized and unpolarized standard stars. The attainable accuracy of the instrument is found to be dependent on the S/N of the data. The present data set yields accuracies of $\sim \pm 0.5\%$ at 4000\AA and $\sim \pm 0.3\%$ at 7500\AA , at a spectral resolution of $\sim 7.2\text{\AA}$.

A Spectropolarimetric Reduction Software (SPRS) package developed for reducing spectropolarimetric data, is described. Tasks like eliminating instrumental polarization, telescope polarization and response corrections are implemented in the software. SPRS is designed to be versatile, user friendly and compatible with the IRAF image processing package. It is also general enough to be used for reduction of spectropolarimetric data from other instruments.

In *Chapter 4*, jet and shell structures from comet Hale-Bopp during the period September 1996 to October 1997, are modeled using data from the Vainu Bappu Observatory and from the observatory of the Naturwissenschaftlicher Verein Osnabrück. Evolution of jet and shell structures during the period of observations could be attributed to activity from sources near $+65^\circ$, $+35^\circ$, $+5^\circ$, -5° , -35° , -65° in latitude. Although no deliberate attempt was made to place the sources at symmetric latitudes, the best fit shows a remarkable symmetry. Due to changing solar illumination geometry, while only the southern sources were apparently active during 1996, most of the sources appeared active in February 1997 and October 1997. In the 10 April, 1997 image, under a near pole-on solar illumination, curiously, only the sources at $+65^\circ$, $+5^\circ$ and -5° appear to be active and not the source at $+35^\circ$. Pole positions which gave a reasonably good fit to the observed sets of shells varied from 260° to 290° in right ascension and -50° to -65° in declination.

Around April 10, 1997, while the gas production from the equatorial sources is expected to have been low because of the near grazing incidence of sunlight, the

fractional area of the high latitude source is limited for a spherically symmetric nucleus. To explain the well defined shells due to rotation of the jets, we assume that the source at $+65^\circ$ occupies 10% of the longitude belt and 10° in latitude. Assuming a radius of 35 km for the comet corresponding to the upper limit of Weaver and Lamy (1997) and Sekanina (1997a), an area of 56 km^2 for this source could account for 29% of the total production rate of 4.0×10^{30} molecules/sec observed by Schleicher *et al.* (1997). The intricate shell patterns during February - May, 1997 could not be exactly replicated using the model of a single nucleus. Complexity of the shell structures can be better explained using the binary model of comet Hale-Bopp as suggested by Sekanina (1997b, 1998b) with sizes of 70 km and 30 km across. Approximate estimates of the longitude of the sources active between February and May, 1997 are presented. The lower limits on the dust to gas mass production ratio are estimated to be, 4.8 ± 1.1 , 3.4 ± 1.0 and 6.2 ± 1.3 for 18 February, 10 April and 2 May, 1997, respectively.

Polarimetric observations of comets contain important information about cometary dust. Proper modeling of polarimetric data can reveal information on the complex refractive index of the material and the size distribution of the grains. Comets Hale-Bopp and Wild 2 were observed on April 23 and 24, 1997, using the newly built Optical, Dual-beam, Automated Medium Resolution Spectropolarimeter (O-DB.AMRSP) at the Vainu Bappu Telescope (*Chapter 3*). In *Chapter 5*, these observations and modeling of the data are presented. We first analyze the phase dependent polarization of comet Hale-Bopp and comet Wild 2 from published data and data obtained through private communication. The grain types that best fit the phase polarization curves at three wavelengths are then used for modeling the continuum polarization of the spectropolarimetric observations of comet Hale-Bopp. A similar procedure has been followed using single color and limited phase data for comet Wild 2. The coma is assumed to be a collection of porous crystalline and glassy silicates, with an organic component. Effect of porosity and a grain size distribution are investigated. The light scattering computations were made, using the Mie scattering and the Effective Medium Theory (EMT) has been used to compute the effective refractive index of the grains. Using these codes, the model polarization

is computed for the comets for comparison with the observation. From this comparison, we attempted to investigate the size distribution, silicate to organic ratio, and the porosity of the cometary dust grains. We also look into the fluorescence polarization from cometary molecules that emerge as a residual between the observed and modeled polarization.

In *Chapter 6*, the results from *Chapter 4* and *Chapter 5* are used. Trajectories of dust grains ejected during jet activity are computed to create the theoretical brightness and color maps of the shells of Comet Hale-Bopp. The dust grain types selected from spectropolarimetry of the cometary shell were used. The color of the observed dust shells with respect to the coma in the post-perihelion CCD images of comet Hale-Bopp are compared with the color derived from the simulated images. This is an independent method to test the dust compositions in the shell derived through polarimetry in *Chapter 5*.

The conclusions and future plans are presented in *Chapter 7*. Plans to facilitate better guiding of the telescope for the solar system objects and computations using a superior light scattering code are discussed. Designs of an imaging and spectroscopic polarimeter (I&S-P) and a four beam imaging polarimeter (FBIImP) are proposed.

Contents

List of Figures	xix
List of Tables	xxii
1 INTRODUCTION	1
1.1 Comets	1
1.2 Cometary Dust	3
1.3 Dynamical Properties of Cometary Dust	5
1.4 Dust Emission from Discrete Sources as Jets	7
1.5 Physics of Dust Scattering	11
1.6 Comet C/1995 O1 (Hale-Bopp)	16
1.7 Comet 81P/Wild 2	20
1.8 The Objective of the Thesis	21
2 INSTRUMENTS, OBSERVATIONS & DATA REDUCTIONS	27
2.1 Telescopes, Back-end Instruments and Detectors	27
2.1.1 Imaging camera	28
2.1.2 Spectropolarimeter	29
2.1.3 Detectors	29
2.2 Observations	30
2.3 Guiding on the Comet	33
2.4 Error Theory and Data Reduction	35
2.4.1 Signal to Noise (S/N)	35
2.4.2 Basics Calibration and Removal of Systematic Errors	36

2.4.2.1	Bias Correction	37
2.4.2.2	Dark Counts	37
2.4.2.3	Flat-field Correction	38
2.4.3	Extraction and Wavelength Calibration	41
2.4.4	Correcting for Rectangular Pixel CCD	41
2.4.5	Software Packages for Data Reduction	41
2.5	Image Enhancements	42
2.5.1	The Radial and Rotational Shift Algorithm	43
2.5.2	Normalization by a Synthesized Coma	45

3 AN OPTICAL, DUAL-BEAM, AUTOMATED MEDIUM RESOLUTION SPECTROPOLARIMETER FOR THE VAINU BAPPU TELESCOPE

		48
3.1	Introduction	49
3.2	Basic Experiment	50
3.3	Instrumentation	52
3.3.1	Section-1 – Mount for the Wavefront Rotator	54
3.3.2	Section-2 – Mount for the Polarimetric Analyzer	55
3.4	Instrument Control	56
3.5	Depolarization of the Dome/Sky Flats	57
3.6	Calibrations with a 100 % Linearly Polarized Source	58
3.7	Analysis and Methodology	60
3.7.1	Estimation and Elimination of Telescope and Instrumental Polarization	61
3.7.1.1	Correction for Instrumental Polarization $\vec{M}_i(\lambda)$	62
3.7.1.2	Correction for Telescope Polarization $\vec{M}_t(\lambda)$	63
3.7.2	Correction for Instrumental Response	64
3.8	Spectropolarimetric Reduction Software	65
3.9	Performance	67
3.10	Further Improvements	71
3.10.1	Instrumentation	71
3.10.2	Reduction Software	71

4	DUST MODELING OF COMETARY JETS	74
4.1	Introduction	75
4.2	Observations and Data Processing	76
4.3	Computation of the Track of the Dust Grains in the Jets	77
4.3.1	Velocity and Acceleration of the Grains	77
4.3.2	The Geometry	78
4.3.2.1	Comet-o-Centric Spherical Coordinates Referred to the Comet's Equator	80
4.3.2.2	Comet-o-Centric Spherical Coordinates Referred to the Earth's Equator	81
4.3.2.3	Transformation to Geocentric Spherical Coordinates	82
4.4	Fit of the Observations to the Model	83
4.4.1	Pole Position of the Comet and Latitude of the Active Sources	83
4.4.2	The Coefficients a and b	85
4.4.3	Longitude of the Active Sources	87
4.5	Results and Discussions	88
4.5.1	The Fitted Images	88
4.5.2	Gas and Dust Production Rates	93
4.5.3	Activity of the Various Sources	94
4.5.4	Size of the Sources	95
4.6	Conclusions	96
5	SPECTROPOLARIMETRY OF COMET HALE-BOPP AND COMET WILD-2	100
5.1	Introduction	101
5.2	Phase Dependent Polarization of Comet Hale-Bopp	102
5.3	Observations	105
5.3.1	Spectropolarimetry of comet 1995 O1, Hale-Bopp	105
5.3.2	Spectropolarimetry of comet 81P/Wild 2	107
5.4	Analyzing the Polarization results	108
5.5	Modeling Polarization from Scattering Properties of Dust Grains . . .	111
5.5.1	Size Distribution Law	115

5.5.2	Polarization Dependence on Silicate to Carbon Ratio and Porosity	118
5.5.3	Behavior of Highly Porous Grains	120
5.6	Fitting the Phase Dependent Polarization	121
5.6.1	Hale-Bopp Data	121
5.6.2	Wild 2 Data	127
5.7	Determining the Spectropolarimetric Continuum for Comet Hale-Bopp	128
5.8	Determining the Spectropolarimetric Continuum for Comet Wild 2	135
5.9	Summary and Conclusions	138
6	INVESTIGATIONS OF COLOR OF DUST SHELLS IN THE POST-PERHELION CCD IMAGES OF COMET HALE-BOPP (C/1995 O1)	144
6.1	Introduction	144
6.2	Observation and Data Processing	145
6.2.1	Computation of Color from Observed Images	147
6.3	The Model	148
6.4	Comparison of Observations with the Model	150
6.5	Results	153
7	CONCLUSIONS AND FUTURE WORKS	156
7.1	Conclusions	156
7.2	Future Works and Further Improvements	160
7.2.1	Guiding a Comet with a nearby Field Star	160
7.2.2	Estimation of the Coma Profile by Linear Fit to the Image	161
7.2.3	Measurements of Circular Polarization	162
7.2.4	Improvement in the Reduction Software SPRS	163
7.2.5	An Imaging and Spectroscopic Polarimeter (I&S-P)	163
7.2.6	A Four Beam Imaging Polarimeter (FBIImP)	165
7.2.7	Dust scattering Code	166

7.2.8	Polarization and Dust Modeling	167
Appendix:A		169
A.1	Half-Wave Plates	170
A.1.1	The Superachromatic HWP.	171
A.1.2	Response Curve of the Superachromatic HWP.	171
A.2	Modified Glan Taylor Prism and the Path Length Compensator . . .	173
A.2.1	Lab Test with the MGTP + PLC for the <i>e</i> and <i>o</i> beam response.	174
Appendix:B		177
B.1	Gratings and Diffraction Theory	177
B.2	Resolution and Resolving power	177
B.3	Dispersion	178
B.4	Throughput	178
B.5	Blazing Ruling	178
B.6	The Boller & Chivens long slit cassegrain spectrograph	179
Appendix:C		181
C.1	Engineering Drawings to The Section-1	181
C.2	Engineering Drawings to The Section-2	188
C.3	Shutter	191
Appendix:D		192
D.1	Real Time Instrument Control	192
D.1.1	Switching of the Comparison Source	193
D.1.2	Operation of the Protective Shutter for the I-CCD	193
D.1.3	Rotation of the HWP	193
D.1.4	Software	194
D.2	Execution of SPRS	196
Appendix:E		199
E.1	Phase Dependent Polarization of Comet Hale-Bopp	199
E.2	Phase Dependent Polarization of Comet Wild 2	205

Appendix:F	206
F.1 Acronyms Used In this Thesis	207

List of Figures

1.1 A Suspected cometary interplanetary dust particle.	4
1.2 Nucleus of Halley's comet from Giotto spacecraft.	8
1.3 Simulation of a simplified special case of dust ejecta (Sekanina and Larson 1984)	9
1.4 The early phase of evolution of dust ejecta (Sekanina and Larson 1984)	10
1.5 HST image comet Hale-Bopp on 26 September 1995	11
1.6 Cometary polarization with phase angle (Jockers, K., 1997)	14
2.1 Schematic Diagram of the VBT Prime Camera	29
2.2 Mosaic of the images of Comet Hale-Bopp obtained from 1995 to 1998 at VBO.	31
2.3 (x, y) to (ρ, θ) transformation of Comet Hale-Bopp image	45
3.1 Sampling the Stokes vector	51
3.2 The optical layout of the Boller & Chivens spectrograph.	53
3.3 Sketch of the two Sections mounted onto the spectrograph to convert it to a spectropolarimeter	54
3.4 The Experimental setup for the calibration with a 100 % polarized source.	59
3.5 Polarization response and the zero point offset.	60
3.6 The telescope polarization $Q_{n0}(\lambda)$ and $U_{n0}(\lambda)$	69
3.7 Polarization of standards stars (HD 43384 & HD 147084).	70
4.1 The Comet-o-Centric Geometry.	79
4.2 Fitted latitudes of the active regions.	85
4.3 Longitude of the sources.	88

4.4	Fit of the model to the pre-perihelion images.	89
4.5	Fit of the model to the post-perihelion images.	90
4.6	Fit of the model to the data from Osnabrück.	91
4.7	Fit of the model to the data from Osnabrück.	92
5.1	Phase dependent polarization of Comet Hale-Bopp	103
5.2	Position of the spectropolarimeter slit on comet Hale-Bopp	106
5.3	Spatial cut of the longslit Spectra at 5230Å	107
5.4	Phase dependent polarization of Comet Wild-2.	108
5.5	Trigonometric fits for $\alpha = 0^\circ$ to 180°	110
5.6	The refracted and reflected beams from a spherical particle	112
5.7	Complex Indices of Refraction $n(\lambda)$ and $k(\lambda)$ of Some Silicates.	113
5.8	Complex Indices of Refraction $n(\lambda)$ and $k(\lambda)$ of Amorphous Carbon and Interstellar Organic Refractory.	114
5.9	Variation of the dust grain Size distribution.	116
5.10	Variation of Polarization with R_m and p	119
5.11	A fractal representation of a porous dust gain.	120
5.12	Variation of Polarization with R_m , p and silicate content.	122
5.13	A model fit of the phase dependent polarization and wavelength de- pendent polarization of Comet Hale-Bopp	126
5.14	Size distribution laws for Wild 2	128
5.15	Relative scattered intensity at different grain sizes.	130
5.16	Wavelength dependent polarization of Comet Hale-Bopp	132
5.17	Wavelength dependent polarization on a jet of Comet Hale-Bopp	134
5.18	Wavelength dependent polarization of Comet Wild 2	136
6.1	Normalization by a synthetic coma.	146
6.2	The radial cuts.	147
6.3	The model dust shells for the 11 types of dust grains.	151
6.4	The radial cuts.	153
6.5	Composite color images of the dust shells of Comet Hale-Bopp.	154
7.1	Guiding the Telescope with a field star	160

7.2	A conceptual optical design for the I&S-P	164
7.3	A conceptual optical design for the FBImP	166
A.1	Polarimetric optics used in the spectropolarimeter	169
A.2	Input and output wavefronts from a HWP.	170
A.3	Schematic layout of the superachromatic HWP design.	171
A.4	Response curve of the superachromatic HWP	172
A.5	Drawing of the Modified Glan-Taylor Prism (MGTP)	173
A.6	The laboratory experiment setup with the MGTP + PLC.	174
A.7	An output image at the center of the MGTP input aperture.	175
A.8	The scan across the MGTP + PLC.	176
B.1	Un-blazed and Blazed Grating	179
B.2	The B & C spectrograph converted into a spectropolarimeter.	180
C.1	An assembly drawing of the <i>Section-1</i> of the spectropolarimeter.	182
C.2	The HWP holding cell and the drum	183
C.3	1:4 Spur Gear Unit	184
C.4	The stepper motor mount and the base plate for the <i>Section-1</i>	185
C.5	The outer surface of the mechanical absolute encoder cylinder.	186
C.6	The online calibration and the second order cutoff filter unit.	187
C.7	The analyzer unit: The MGTP + PLC assembly.	189
C.8	The “Inner Filter Wheel” that holds the analyzer unit.	190
C.9	Shutter for the spectropolarimeter.	191

List of Tables

2.1	32
2.2	Log of the Observation from the Observatory of the Naturwissenschaftlicher Verein Osnabrück	33
3.1	Features of <i>SPRS</i> (SpectroPolarimetric Reduction Software)	66
3.2	Output file of <i>SPRS</i> ; 5 Apertures, 2 Bands.	67
3.3	Observed polarized and unpolarized standards	68
4.1	Journal of Observations from VBO	76
4.2	The pole positions and the geometry (from VBO data)	84
4.3	The pole positions and the geometry (from Osnabrück data)	84
4.4	Longitude and latitude of the active regions.	84
4.5	Lower limits on gas and dust production rates (from VBO data)	86
4.6	Lower limits on gas and dust production rates (from Osnabrück data)	86
5.1	The parameters of the trigonometric fit.	109
5.2	The limits derived from the trigonometric fit.	110
5.3	The Combination of 11 grain types fitting the phase polarization curve for Comet Hale-Bopp.	124
5.4	The normalized percentile weights $\omega_i \cdot n_d(s_{p_d})$ for the fits to the wavelength dependent polarization.	129
5.5	The Combination of 6 grain types fitting the phase polarization curve for Comet Wild 2	135
D.1	The “imfort” subroutines used in <i>SPRS</i>	196
D.2	The eparm spolari parameter table used for <i>SPRS</i>	197

E.1	Phase dependent polarization data for Comet 1995 O1 Hale-Bopp . .	199
E.1	Phase dependent polarization: Comet Hale-Bopp (<i>continued</i>) . . .	200
E.1	Phase dependent polarization: Comet Hale-Bopp (<i>continued</i>) . . .	201
E.1	Phase dependent polarization: Comet Hale-Bopp (<i>continued</i>) . . .	202
E.1	Phase dependent polarization: Comet Hale-Bopp (<i>continued</i>) . . .	203
E.1	Phase dependent polarization: Comet Hale-Bopp (<i>continued</i>) . . .	204
E.1	Phase dependent polarization: Comet Hale-Bopp (<i>continued</i>) . . .	205
E.2	Phase dependent polarization data for Comet Wild-2	205

Chapter 1

INTRODUCTION

In this Chapter, the field is introduced through the basic definition of comets, leading to cometary dust and the dynamical properties of cometary dust. The physics of dust scattering and dust polarization are then discussed. A survey of the available results on the comets observed for this thesis (comet Hale-Bopp and comet Wild 2) is made. Finally the objective and the layout of the thesis is presented.

1.1 Comets

Comets are some of the farthest objects in our solar system that permit a close inspection as they travel close to us on their way to perihelion and while receding from perihelion. The name “comet” comes from the descriptive Latin phrase *Stellae comatae* which means hairy stars. Comets have a solid nucleus, usually around 1-10 km across, consisting of ices, dust and rock. They are hence often referred to as “dirty snowball”. This icy-conglomerate model was provided by Whipple (1950). According to the widely accepted current theories, comets are debris left over from the building of the outermost planets. The cometary material must be of interstellar origin from which the Sun and the planetary system evolved. Due to the cold environment of the cometary habitat, material in a comet did not evolve as the material in the Sun and the planetary system did. Comets thus offer us an opportunity to study primitive matter involved in the origin of our solar system that

has been stored in deep freeze for at least 4.6×10^9 years. Cometary objects are found in the Kuiper belt extending up to the Oort Cloud. They are scattered into the inner solar system by gravitational perturbation. As a comet travels into the solar system, its orbit is further perturbed due to gravitational interactions with the major planets.

When they are far from the Sun ($\geq 7AU$), in the outer reaches of the solar system, there is very little activity on the cometary nucleus (Prialnik and Dina 1997). A comet shows essentially the reflected solar spectrum like an asteroid. At large distances, the solar phase angle coverage is small and one can determine only the change of albedo with wavelength. As a comet approaches the Sun, the Sun's radiation warms the nucleus, causing the ices to sublimate outwards from various vents on the nucleus. The outflow of gas drags with it grains of different ices, dust and rock. Observations show that the volatile fraction is a mixture of molecule from H , C , N , O and S atoms, while the dust consists mainly of fine grains of silicates and organic refractory. However a small amount of larger grains is sometimes detectable (Sekanina 1974) and the existence of boulders cannot be excluded either from the present evidence (for a review see Delsemme 1982). The venting outwards of these materials creates the coma or, in other words, the atmosphere surrounding the nucleus. This coma extends to a very large distance compared to the nucleus. The true nucleus at the center of the coma, is almost invariably invisible from the Earth, due to masking by the inner coma. Attempts have however been made to determine the size of the nucleus (*e.g.* Fernández *et al.* 1999; Weaver and Lamy 1997; Sekanina 1997a; Kruchinenko and Churyumov 1997). Ionized gas and dust from the coma are pushed away by the solar wind and solar radiation pressure respectively to form the cometary tails. As a comet approaches the Sun, the gases in the coma begin to dissociate, excite and ionize; giving rise to an emission spectrum. One of the first species to show up is CN at $\lambda 3883\text{\AA}$ which appears in the spectrum of the comet at a heliocentric distance of about 3 A.U. Then, one sees triatomic species like C_3 and NH_2 , between 2 and 3 A.U., diatomic species like C_2 , OH , NH , CS , CH and S_2 at $r < 1.5A.U.$ and finally atomic lines at $r < 0.1A.U.$ In the tail of the comet we see ionic species like CO^+ , OH^+ , CH^+ and CN^+ at $r < 2 A.U.$.

1.2 Cometary Dust

Dust in comets comprises a major part of the non-volatile material. Historically, work on cometary dust began with the pioneering work by Bessel (1836) on the morphology of the coma of Halley's comet at its 1835 apparition. In this work, he introduced the concept of a repulsive force from the Sun, which later was identified as the solar radiation pressure (Arrhenius 1900; Schwarzschild 1901). The progress of work on cometary dust continued with Bredikhin's studies of tail formation (for a review see Jaegermann 1903). He introduced the terms "*Syndyname*" (or "*Syndyne*") as the locus of particles that are subjected to a constant acceleration due to the solar radiation pressure force and a "*Synchrone*" (or "*Ischrone*"), the locus of particles that are ejected by the comet at the same time.

At present our knowledge of cometary dust comes primarily from remote observations of IR spectral features and from *in situ* sampling of the impacting dust particles during the Halley flybys. There is however, another very important means to learn about cometary dust. The dust particles released by comets, form part of the interplanetary dust particles (IDPs) swept up by the Earth and retrieved for laboratory analysis. If the retrieved IDPs could be traced to a cometary origin, then it would be a powerful means to study the structure, mineralogy, and history of the cometary silicates. Comets are estimated to contribute about two-thirds of the IDPs, with the remainder coming from asteroid collisions and cratering events (Boice and Huebner 1999). Fig. 1.1 illustrates a sample of a suspected cometary IDP, recovered in the Earth's atmosphere by high-flying research aircraft. This dust particle is apparently a random collection of sub-micron silicate grains embedded in a carbonaceous matrix and is highly porous. As cometary grains are generally characterized by porous structures of carbonaceous and silicatic aggregate, it is therefore inferred that this IDP originated from a comet.

Mineralogy of the cometary dust can be conducted through remote observations using the IR spectral features. Silicates produce a weak continuum emission and resonance spectral features near $10\ \mu\text{m}$ and $20\ \mu\text{m}$ because of vibration and bending modes in Si-O bonds. Additional bending mode vibrations occur between $16\ \mu\text{m}$ and $35\ \mu\text{m}$. The wavelengths and shapes of these features provide means of identification

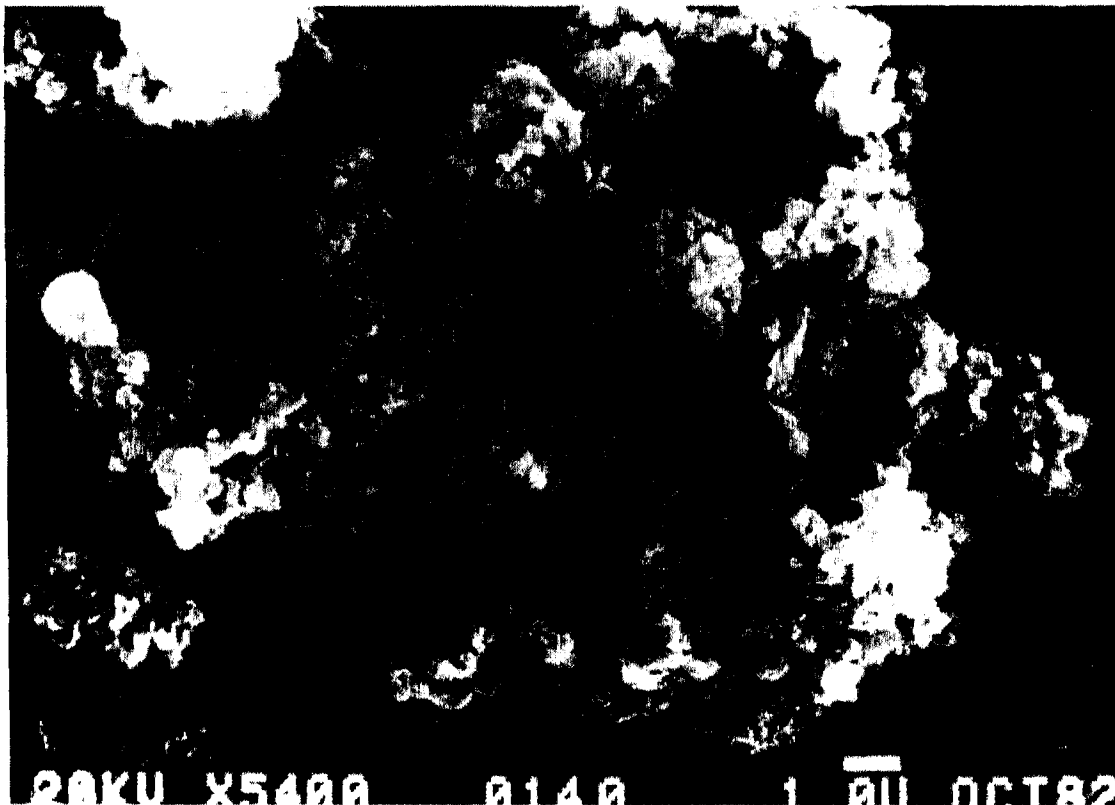


Figure 1.1: A Suspected cometary interplanetary dust particle. This dust particle is highly porous. It is apparently a random collection of sub-micron silicate grains embedded in a carbonaceous matrix. Samples of these grains have been recovered in the Earth's atmosphere by high-flying research aircraft. (Courtesy of D. Brownlee, University of Washington.)

of the mineral composition (Hanner 1999; Hayward, Hanner, and Sekanina, 2000; Wooden *et al.* 1997; Wooden *et al.* 1999). The analysis of the IR spectra of comet Hale-Bopp indicates that the cometary silicates are *Mg*-rich. This finding is consistent with *in situ* results from comet Halley (Hanner 1999). Carbonaceous grains contribute featureless emissions like a pseudo-continuum and rarely a $3.4 \mu\text{m}$ feature emission. Carbonaceous grains are referred to as organic material while silicates as inorganic. Since comets are the frozen reservoirs of primitive material from the early solar nebula, determination of the organic and inorganic material in cometary dust provides insight into both the early solar nebula environment and the process of planetary system formation.

Silicates are found in both amorphous and crystalline forms, that do not necessarily share a common origin. At present, the origin of crystalline cometary silicates is not

clear. Crystalline grains can form by direct condensation from vapor at $T = 1200$ - 1400 K with very slow cooling, or by annealing (heating) of amorphous silicate particles. Direct condensation provides a natural explanation for *Mg*-rich silicates, because Forsterite and Enstatite are first to condense in a hot gas and only react with *Fe* at lower temperatures (Hanner 1999). Comets were formed in the outer regions of the solar nebula where the temperatures were too low for crystalline grains to form. Hence these grains must have been present in the solar nebula from where the comets accreted them. It is possible that all cometary silicates are interstellar dust grains of pre-solar origin. These grains would have been incorporated in the comet without thermal alteration. The high $CO:H_2O$ ratio in comets implies that even interstellar ices may have survived (Hanner 1999). However, the past history of cometary dust in the solar nebula is not known. We do not know unequivocally if the grains were shock heated during in-fall to the circumsolar disk, altered by collisions, or if there was mixing between the warm and cold regions in the solar nebula.

1.3 Dynamical Properties of Cometary Dust

As mentioned in *Sec. 1.2*, dust ejections in comets are caused by sublimating ices. The gases emitted during sublimation, exert a drag force causing the cometary grains to accelerate. The dust grains reach a terminal velocity by the time these become dynamically decoupled from the expanding gas, *i.e.* when particle-molecule collision becomes dynamically insignificant (Sekanina *et al.* 1998). Now, as the gas drag drops, the solar radiation pressure and the Sun's gravity begin to play an important role. The cometary dust velocities are much higher than the comet's escape velocity and the gravitational attraction by the cometary nucleus is extremely insignificant. Thus gravitational attraction of the comet's nucleus on the dust particle is not considered.

A simple formula for dust dynamics in comets was derived by Whipple (1951). This formula was more recently generalized to non-spherical particles by Gustafson (1989). The first elaborate treatment of dust-gas dynamics in comets was presented by Probst (1969). This work was incorporated in the analysis of the dust

tail of comets by Finson and Probst (1968a). Probst's results were applied on comet 109P/Swift-Tuttle (Sekanina 1981a) and comet 1P/Halley (Sekanina and Larson 1984, 1986), showing an excellent correspondence with the theory. Fitting Probst's theoretical curves led Sekanina (1981a) to suggest an empirical formula connecting the terminal velocity v_{gr} with the ratio β of the forces due to solar radiation pressure on the dust grain to the gravitational force of the Sun

$$\frac{1}{v_{gr}} = a + \frac{b}{\sqrt{\beta}}. \quad (1.1)$$

Here a and b are coefficients expressible in terms of the physical parameters of Probst's theory. This empirical formula will be used in Chapter 4 and Eq.1.1 will be revisited in Sec. 4.3.1. Probst's theory assumes a single characteristic grain size, oversimplified energy conservation equation, neglects molecule-molecule collisions near the nucleus and other simplifying assumption. Numerous refinements and innovations to Probst's original approach have been made (e.g. Hellmich 1981; Hellmich and Keller 1981; Marconi and Mendis 1983, 1984; Gombosi et al. 1983, 1985; Gombosi 1986; see also a review by Crifo 1991). However, according to Sekanina, Jessberger and Fomenkova (1998), these refinements and innovations have led to no dramatic changes in the determination of the terminal velocity v_{gr} of the dust particles.

The ratio β in Eq. 1.1, varies proportionally to the particle's projected cross sectional area A and inversely to its mass m and is expressed as

$$\beta = \left(\frac{L_{\odot}}{4\pi c G M_{\odot}} \right) \frac{Q_{pr} A}{m}. \quad (1.2)$$

Here c is the speed of light, G is the gravitation constant, M_{\odot} and L_{\odot} are the Sun's mass and luminosity, and Q_{pr} the radiation pressure efficiency of the dust grain which depends on its size, shape and optical property. Assuming a spherical dust particle of radius s (in μm) of uniform density ρ (in g/cm^3), the mass m and the projected cross sectional area A , Eq. 1.2 can be expressed as a function of s and ρ . After substituting for the other constants, Eq. 1.2 reduces to

$$\beta = \frac{0.574 Q_{pr}}{\rho s}. \quad (1.3)$$

1.4 Dust Emission from Discrete Sources as Jets

Dust features observed in cometary head led to the belief that there is dust emission from discrete sources. One of the first observations of a distinct coma feature, documented in the literature, is that of Halley's comet by Hevelius (1682).

The presence of discrete emission sources on the nucleus, was one of the factors that contributed to the broad acceptance of the icy conglomerate model in the 1970's. From time evolution of these discrete emission features in the inner coma, evidence of a rotating nucleus was found. A review of the early morphological studies of cometary dust by Sekanina (1981b), showed that outgassing from many comets, especially the short-period ones are largely confined to discrete areas on the sunlit side of their rotating nuclei. He also showed that the appearance of the observed features is determined by the surface distribution of the sources, local day-night on the nucleus and on the continuous or erratic emission modes. These ideas were fully confirmed by the closeup image of the nucleus of the Halley's comet – particularly those taken by Giotto's Halley Multi color Camera (Keller *et al.* 1987)(Fig. 1.2). Since 1986 visit of comet Halley, significant progress has been achieved in the understanding of the outflow mechanism and the thermophysical properties of the anisotropic gas and dust emissions from cometary nucleus.

Cometary nuclear rotation has a dramatic effect on the distribution of dust in the coma and thereby on the coma morphology. Let us assume a simplified special case of a point like emission region located at the comet's equator and assume that the rotational axis of the comet is perpendicular to its orbital plane. A dust particle with initial velocity v_{gr} , is subjected to a constant acceleration a_r due to the solar radiation pressure. The cometocentric motion of these dust particles is described by Cartesian coordinates (x, y) , oriented respectively, toward the Sun and 90° ahead of it in the direction of rotation (Sekanina and Larson 1984):

$$\begin{aligned} x(t, \Theta) &= f(t, \Theta) \left[v_{gr} \cos \Theta - \frac{1}{2} a_r f(t, \Theta) \right] \\ y(t, \Theta) &= f(t, \Theta) v_{gr} \sin \Theta, \end{aligned} \quad (1.4)$$

Where t is time and Θ is the angle of dust ejection measured from the sunward direction in the direction of the comet's rotation (measured in radians). $f(t, \Theta)$ is

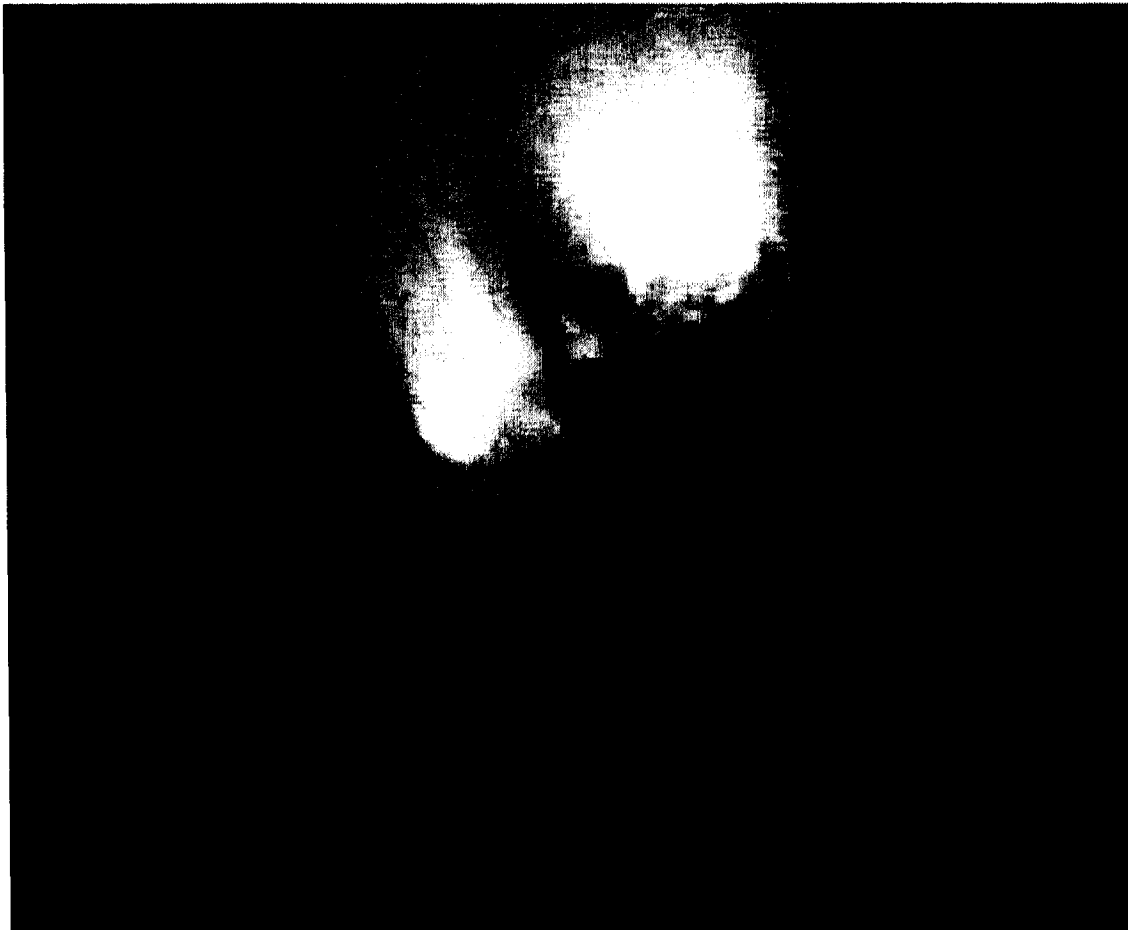


Figure 1.2: A composite image of the nucleus of Comet P/Halley as photographed by the multi color camera on board the Giotto spacecraft on March 14, 1986. The Sun is located toward the top of the picture, 29° clockwise from the vertical. The image shows that the dust ejections are confined to relatively small, isolated active areas on the sunlit side of the irregular shaped nucleus. (Keller *et al.* 1987).

given by

$$f(t, \Theta) = (t - t_b) - \frac{P}{2\pi}(\Theta - \Theta_b), \quad (1.5)$$

Where P is the period of rotation, while t_b and Θ_b are the time and ejection angle at the onset of emission at the local sunrise. Eq. 1.4 holds for any time $t \geq t_b$, but the function $f(t, \Theta)$ is defined only for one rotation, that is for $\Theta_b \leq \Theta_e$, where Θ_e is the ejection angle at the end of emission, at local sunset (Sekanina and Larson 1984).

Fig. 1.3 as illustrated by Sekanina and Larson (1984), shows the simulation of this simplified special case described by Eq. 1.4 and 1.5 for a fast and a slow rotating nucleus. The effect of cometary rotation on the coma morphology is exemplified. A

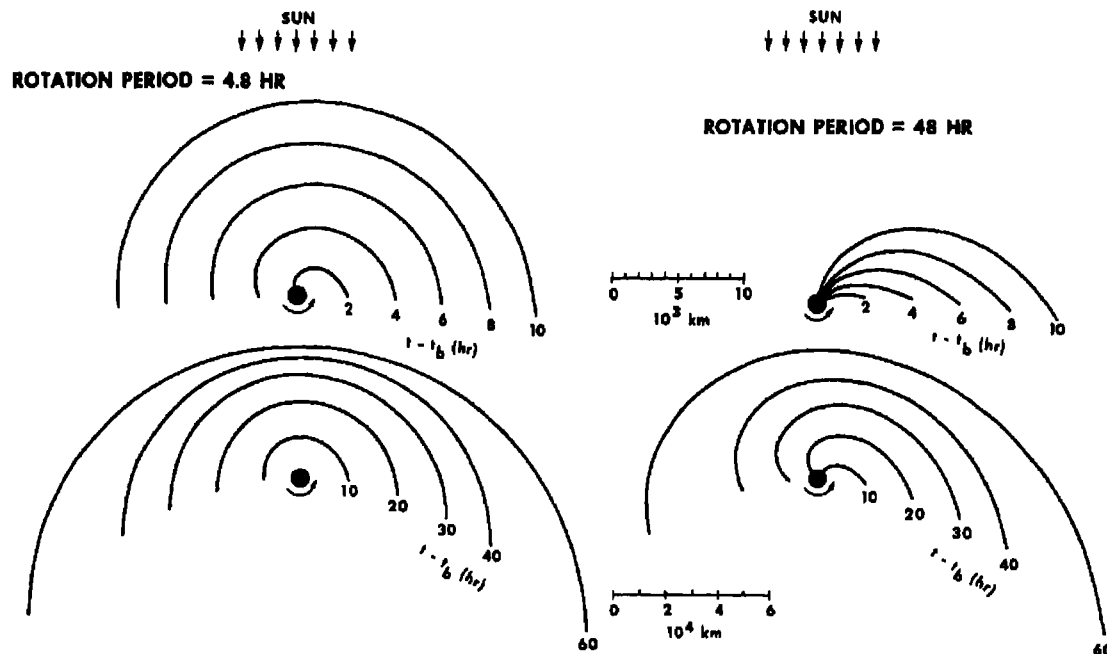


Figure 1.3: *Effect of spin rate on the evolution of dust ejecta from a point-like source on the equator of a rotating nucleus. The spin axis is normal to the comet's orbit plane (the plane of the figure). The source is active from sunrise ($\Theta_b = -90^\circ$) to sunset ($\Theta_e = +90^\circ$) and all particles are ejected with the same velocity of 500m/sec and subjected to the same solar radiation-pressure of 0.25cm/sec^2 . The circles show the position of the nucleus and the curves describe the loci of particles ejected at various times after the onset of emission, $t - t_b$. The sense of rotation and the direction to the Sun are also indicated. The left-hand side of the figure depicts the case of rapidly rotating nucleus; the right-hand side, of a slowly rotating nucleus. Note the scale differences for the early (top) and late (bottom) phase of evolution (From Sekanina and Larson 1984)*

schematic outline of the early phase of evolution of dust ejecta (Fig. 1.4) has also been illustrated by Sekanina and Larson (1984).

A comprehensive modeling and analysis of the coma morphology and dust ejecta is presented in *Chapter 4*.

At large heliocentric distances, when the coma is tenuous, observations of freshly ejected dust from a comet are at first detected as sharp central condensation or as a "false" nucleus. Fig. 1.5 shows one of the first images of comet 1995 O1 (Hale-Bopp) from Hubble Space Telescope. It was observed on 26th September 1995 with the WF3 CCD chip of the Wide-Field Planetary Camera 2 (WFPC2). The image is a composite created from two images with exposures of 60sec and 300sec, about

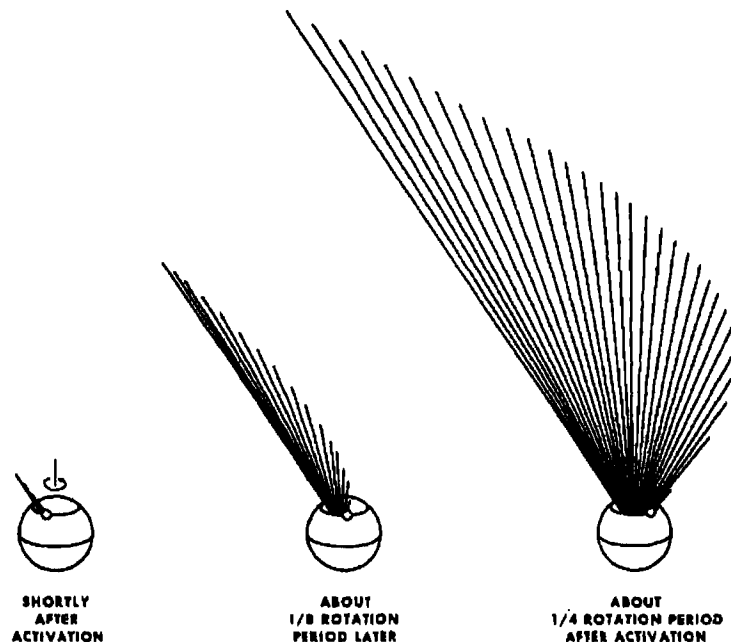


Figure 1.4: A Schematic outline of the early phase of evolution of dust ejecta continuously released from a discrete point-like active region (depicted by a small circle) on the sunlit hemisphere of a spherical nucleus of a rotating comet . Indicated are the sense of rotation, the equator, and the parallel of the latitude of the active region. As the effect of solar radiation pressure are minor in the early phase, the ejecta populate essentially a conical surface and their extent at any given time is determined by the duration of emission and by the range of the ejection velocities (assumed to vary between zero and a maximum) and flight times of the dust particles. The Sun is assumed to be above the plane of the figure. The dimensions of the nucleus and the emission are not drawn to scale. (From Sekanina and Larson 1984)

60hours after an outburst. The image shows a jet and a spiral pattern emanating from the nucleus and has been intensity stretched to emphasize the “clump” of dust located 1.35 arcsec directly above the nucleus.

The “clumpy” outburst on the comet later developed into a spiral jet that appear to “unwind” on the sunward side of the coma. The features, subsequently evolved into a slowly expanding envelop with decreasing surface brightness until it vanished completely. Sometimes the features were seen long enough and were noticed being swept into the tail from either side of the nucleus.

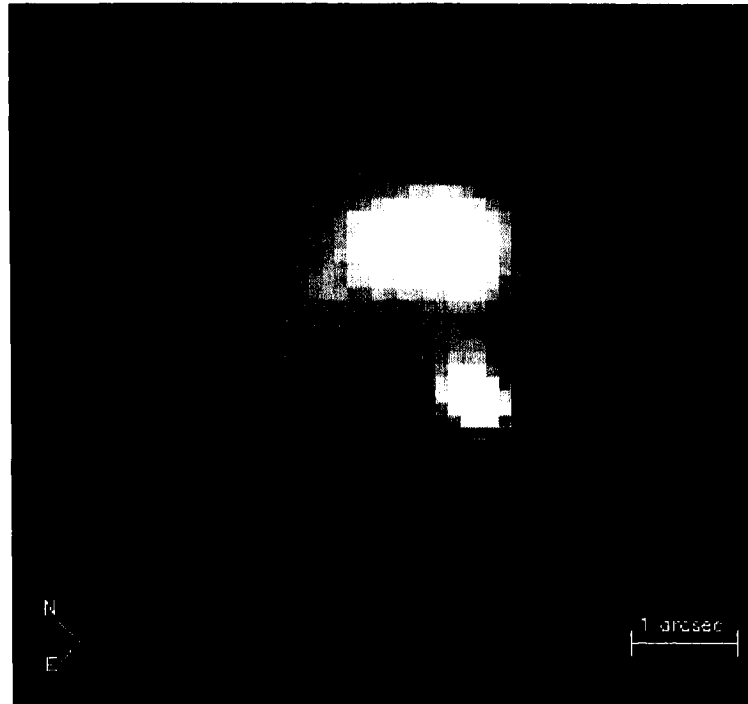


Figure 1.5: *HST image comet Hale-Bopp on 26 September 1995, just after an outburst. Credit: Dr. Harold A. Weaver and NASA.*

1.5 Physics of Dust Scattering

Dust particles present in comets scatter and absorb the incident solar radiation. The information on the refractory components of cometary dust can be obtained through light scattering by these small particles. The dust particles have their own characteristic spectra. The emission features of the dust grains are located in the infrared region of the spectra. Their strength depends on their temperature which is related to the amount of incident radiation absorbed by the dust particles. The spectra in the visible are dominated by molecular emissions. Narrow continuum wavelength regions representing scattered solar light are selected (*e.g.* 6840Å, 4845Å, 3650Å) for investigations of dust scattering. Light scattered by an aggregate of grains depends not only on their chemical composition but also on their size distribution and shapes. The chemical composition of the grains are usually specified by the complex refractive index, $m = n - ik$, where n and k are the wavelength dependent refractive and absorptive indices respectively (see *Chapter 5*). As radiation interacts with these grains, part of the radiation passes through, part is scattered, and the rest is absorbed. The amount of extinction of radiation in the incident beam (scattered

and absorbed) is generally expressed in term of a dimensionless efficiency factor Q_{ext} which is

$$Q_{ext} = Q_{sca} + Q_{abs}. \quad (1.6)$$

Q_{sca} is the scattering efficiency factor and Q_{abs} the absorptive efficiency factor. As the incident light interacts with the dust, it imparts momentum to it as radiation pressure. With the assumption that all the photons absorbed by the dust grain transfer all their momentum to the grains, the efficiency of the radiation pressure and since the scattered light also imparts momentum due to anisotropy of scattering, Q_{pr} can be calculated by

$$Q_{pr} = Q_{ext} - gQ_{sca}. \quad (1.7)$$

The parameter g in Eq. 1.7 is the average cosine of the scattering angle, or the asymmetry parameter;

$$g = \langle \cos \theta \rangle = \int_{4\pi} p \cos \theta d\Omega. \quad (1.8)$$

Here Ω is the solid angle and p is the normalized phase function;

$$\int_{4\pi} p d\Omega = 1. \quad (1.9)$$

For an isotropically scattering particle $g = 0$. For preferential scattering in the forward direction $g > 0$, for complete forward scattering $g = 1$ and for preferential back scattering, $g < 0$.

A cometary dust environment in general will consist of a distribution of particle of various sizes. If $n(s)$ represents the number density of particles in the size range s and $s + ds$ then the total extinction is given by the expression

$$Q_{total}(\lambda) = \int \pi s^2 Q_{ext}(s, \lambda) n(s) ds. \quad (1.10)$$

Light scattering theories have been developed for well defined particle shapes such as spheres, concentric coated spheres, spheroids, cylinders and so on. However, cometary dust grains, in general are likely to be irregular in shape, inhomogeneous and fluffy in nature. The theory of scattering for such grains are highly complex. Henning et al. (1999) have created a data base and an Internet site:

<http://www.astro.uni-jena.de/Users/database/entry.html>

This site contains references to the papers, data files and links to the Internet resources related to measurements and calculations of the optical constants of the materials of astronomical interest. Many different light scattering codes are freely available through this site. There is also a library of light scattering codes “*SCATTERLIB*” maintained by Piotr Flatau. The Internet site could be reached at:

<http://www.astro.uni-jena.de/Users/database/1-dbase.html#db>

In the scattering calculations the inhomogeneity is approximated by an average refractive index or the dielectric functions. The Effective Medium Theory (EMT) presents an approximation to the optical properties of an inhomogeneous particle by its substitution with a homogeneous particle having an effective refractive index. It is not easy, however to determine the average refractive index or the dielectric function of an inhomogeneous medium given the properties of its constituents. There are varied EMTs in literature, all of which are at least superficially different, with different types of approximations. For calculation of the average refractive index through EMT, Bruggeman’s rule will be used in the present work. The following expression for an average dielectric function ϵ_{av} was first obtained by Bruggeman (1935):

$$f \frac{\epsilon - \epsilon_{av}}{\epsilon + 2\epsilon_{av}} + (1 - f) \frac{\epsilon_m - \epsilon_{av}}{\epsilon_m + 2\epsilon_{av}} = 0. \quad (1.11)$$

The expression in Eq. 1.11 is for an inhomogeneous medium of two component mixture, where ϵ and ϵ_m are the respective dielectric functions for the two component homogeneous medium. The parameter f is the volume fraction of the first component. The Bruggeman’s rule or the Bruggeman dielectric function applies to a completely random homogeneous medium; a mixture in which there are no distinguishable inclusions embedded in a definite matrix: both the components are treated symmetrically (Bohren and Huffman 1983).

The Mie scattering code, published in the appendix of Bohren and Huffman (1983), is probably one of the most widely used and highly recommended Mie code. This code is used with EMT in *Chapter 5* and *Chapter 6*.

It is observed, that the mass ratio of silicate to organic M_{Sil}/M_{org} , and the porosity (the fluffiness) of the dust grains p , play an important role on the dynamical behavior

of the dust. Higher percentage of carbonaceous material will increase Q_{abs} (the absorption efficiency) and hence Q_{pr} (the radiation pressure efficiency) of the dust grains. Porosity is found to affect the ratio β of Eq. 1.3 in addition to Q_{pr} (Mukai et al, 1992). Thus the dynamics of the dust grains in the cometary jets can be utilized to investigate their nature and porosity. With this motivation, a study of the dynamical behavior of these grains, is taken up by modeling the cometary dust jet morphology in *Chapter 4* and color of jets and shells in *Chapter 6*.

Scattering introduces polarization, which depends on the direction of the scattered light. Hence polarization shows a strong phase dependence. Fig. 1.6 shows the variation of cometary polarizations with phase angle (Jockers, K., 1997) The existence

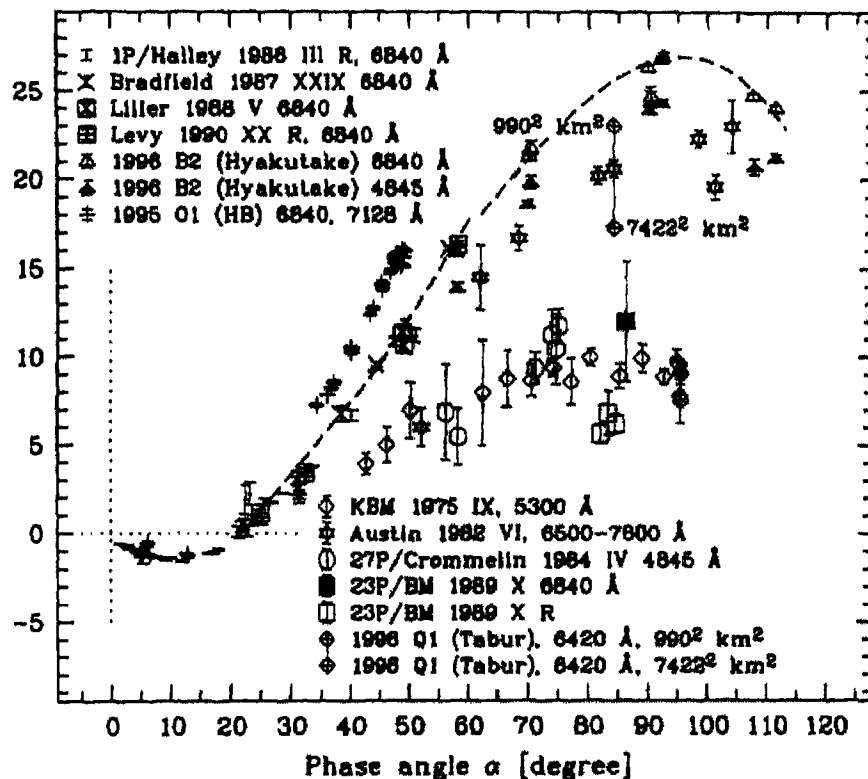


Figure 1.6: Cometary polarization with phase angle (Jockers, K., 1997) The polarization points are the measurements of the Kiselev group. The comets listed in the upper left corner are considered dusty, and in the lower right corner glassy. HB = Hale-Bopp, KHB = Kobayashi-Berger-Milon, BM = Brorsen-Metcalf. The dashed line marks the "common" phase curve of the dusty comets.

of a negative branch of polarization at small phase angle α in comets, asteroids and other solar system bodies was first demonstrated convincingly by the Dushanbe

group (see Kiselev and Chernova, 1997; Dobrovolski et al., 1986). It was believed that only solid surfaces could display negative polarization, but negative polarization in comets came as a surprise. Even today, the nature of negative polarization is not completely understood. The negative polarization is generally explained by the roughness of the grains or by multiple scattering in the agglomerate grains at back scattering angles or in other words at low phase angles.

At a given phase angle, the polarization of scattered light shows a wavelength dependence due to changes in the effective complex refractive index of the composite grains with wavelength and also due to the mean size parameter. The polarization of the resultant scattered light is the superposition of the reflected beam from the front surface which is polarized perpendicular to the scattering plane (Positively polarized) and the refracted beam which is polarized parallel to the scattering plane (negatively polarized). The resultant light will exhibit polarization depending on the absorption of the refracted beam along the path length (*i.e.* grain size) and the absorptivity of the grains (Kolokolova *et al.* 2001). The organic grain material has increased absorptivity in blue. Low *Mg* (or high *Fe*) content introduces broad absorption in the blue. From the color dependence of polarization, one can therefore attempt to constrain the organic and *Mg* content in the grains. For reliable results however the size distribution of the grains should be correctly modeled because the path-length within the grain is critical in determining the resultant polarization.

To study wavelength dependence of cometary polarization, a spectropolarimeter was built as part of the Ph.D. dissertation. The instrumentation and calibration of this spectropolarimeter is presented in *Chapter 3*. For comet Hale-Bopp, the published phase dependence of polarization at three colors was used to get a preliminary list of possible grain candidates. The spectropolarimetric data obtained as part of the present work has been used to check the wavelength dependence of scattering at the phase angle on the date of observations (April 24, 1997). The use of long slit has enabled us to investigate the spatial dependence of polarization and particularly the polarization on a jet. The dynamics of the candidate grains have been investigated in *Chapter 6*. The three color observed images (4450Å, 5260Å and R) obtained on April 10, 1997 have been compared with these simulations to further check the size

distributions and relative fraction of the grain in the collection in the jets. A similar spectropolarimetric study has been carried out for comet Wild 2 using the limited published phase *vs* polarization data in single wavelength and spectropolarimetric data obtained in the present study.

1.6 Comet C/1995 O1 (Hale-Bopp)

On July 23 1995, Comet C/1995 O1 (Hale-Bopp) was independently discovered by Alan Hale in New Mexico, using a 0.41 m reflector, and Thomas Bopp in Arizona, using a 0.44 m reflector. (Hale, Bopp, and Stevens, 1995).

The designation "C/1995 O1" means that this was the first comet found in the second half-month of July (letter O plus number 1) in the year 1995. In cometary designation, every half-month is designated by a letter of the alphabet. Letter "A" covers January 1-15, "B" covers January 16-31, "C" covers February 1-15, etc. The letter "I" is omitted and "Z" not needed. The notation "C/" indicates that this is a long-period comet (that is, one with a solar-orbiting period of more than 200 years). This system of designating a comet is similar to the one used for designating asteroids, and it was brought into use on January 1, 1995. This resolution on the designations and names of comets was adopted by the International Astronomical Union at its General Assembly in The Hague on Aug. 24. 1994 (MPC 23803-4).

Thanks to the early discovery of this comet, it was possible for scientists to obtain a substantial amount of observing time at the world's major observational facilities and to prepare their runs well. Moreover, the comet was visible in the sky for an extremely long period. As it was very bright, a large number of telescopes and instruments were used at all wavelengths from X-rays to radio. At discovery, the comet was 7.16 AU from the Sun and 6.20 AU from the Earth. A single, apparent pre-discovery image of the comet was found by McNaught (1995) of the Anglo-Australian Observatory from UK Schmidt plates taken on April 27, 1993, when the comet was about 13 AU from both the Sun and the Earth. The photographic plates showed that the comet was already active. This observation strengthened the early orbital calculations by greatly extending the arc of observation. The orbit of this comet is almost perpendicular to the ecliptic plane. During this apparition of the

comet, the perihelion on April 1, 1997, was at a distance of 0.91 AU from the Sun. The comet's aphelion distance is around 372 AU. Computing the orbit of the comet using more than 2600 astrometric observations from 1993-98, Marsden, (1997) predicted that the original period of the comet was 4211 years and that the future period will be 2392 years. The change in the orbital period is due to gravitational perturbations from major planets and its cometary activity (non gravitational perturbations). The closest approach of this comet to the Earth was about 1.315 AU, around March 22, 1997.

The images of Hale-Bopp during discovery, and its pre-discovery images, show considerable activity. This comet had considerably more emission than is usually seen in comets at such large distances from the Sun. Most bright comets are thought to be fueled mainly by H_2O -ice sublimation. Theory suggests that in space, significant H_2O -ice sublimation does not begin until the comet is within 3 AU of the Sun. Emission from such molecules as the hydroxyl radical (OH), diatomic carbon, and cyanogen (CN) were detected in this comet well over 4 AU from the Sun. At far distances, the activity on a comet is driven by the release of highly volatile gaseous species, mainly CO , from the surface of its nucleus. Hence detection of OH came as a surprise. Investigations of the pre-perihelion dust environment of the comet by Fulle, Cremonese, and Böhm (1998), showed that the comet was active throughout its approach to the Sun from 13 to 4 AU. The comet was most probably already active, much before it reached a distance of 13AU from the Sun. The molecular species C_3N , SO , and NH_2CHO were detected for the first time in a comet (Lis *et al.* 1997) from millimeter-wave observations of Hale-Bopp, . $HNCO$, first detected in comet C/1996 B2 (Hyakutake), was confirmed from comet Hale-Bopp observations. A number of other molecular species were detected, including HNC , OCS , HCO^+ , CO^+ , and CN (the last two were first detections in a comet at radio wavelengths).

Extensive work has been carried out by several groups on cometary dust, coma morphology and dust jet modeling. Jockers (1997), reported a review on extensive observations of the dust in Comet Hale-Bopp. These concern direct imaging, the distribution of colors within the coma and the tail and also the polarization. This

comet had a somewhat higher degree of polarization when observed at large phase angles than other comets, indicating differences in the dust component. To explain the high polarization, smaller dust grain sizes are proposed. Polarizational observations of this comet is more extensively discussed in *Chapter 5* and the data sets of polarization of the central coma, from literature, is tabulated in Table E.1 of *Appendix E.1*.

The morphology of the comet's porcupine-like appearance in 1996 and the expanding, nearly concentric dust halos, in 1997, were modeled by several groups, including the present work (see *Chapter 4*). Sekanina (1997c, 1998b) modeled the shells and jets by employing a Monte-Carlo computer-simulation technique. From jet simulations and morphological modeling Sekanina (1997b) pointed out the existence of an active satellite of the nucleus.

Most valuable information on the nature of silicates came through infrared observations of the comet (Hayward, Hanner, and Sekanina, 2000, Wooden *et al.* 1997, Wooden *et al.* 1999, Hanner *et al.* 1983). Ground-based and space-based observations of the detailed infrared spectrum of Comet Hale-Bopp have revealed for the first time many new spectral features which can be assigned to particular minerals with a great degree of certainty.

The spectral energy distribution from $\lambda = 3$ to 13μ was dominated by a 10μ silicate feature with a strong underlying continuum. The 10.0μ peak was sharper in Hale-Bopp near perihelion than in any previously observed comet except comet Mueller (C/1993 A1) at $2AU$. The 10μ silicate feature contains a 9.3μ shoulder attributable to amorphous pyroxene, broad emission from amorphous olivine at 9.7μ , and the 11.2μ peak associated with crystalline olivine. When close to perihelion, a newly discovered 9.3μ peak was identified as *Mg*-rich crystalline pyroxene. The Infrared Space Observatory (ISO) Short Wavelength Spectrometer (SWS) spectrum also shows the strong far-IR peaks of crystalline olivine at 18μ , 23μ , and 33μ . The color temperature of the 3 to 5μ continuum was ~ 1.8 times the equilibrium blackbody temperature at the relevant heliocentric distance. Both quantities are larger than in any previous comet and indicate a high abundance of submicron dust particles. The high *Mg* content of the pyroxenes in comet Hale-Bopp implies that they

are either pristine solar nebula condensates or pre-solar grains such as the Mg -rich crystals recently discovered by ISO around asymptotic giant branch stars.

It is interesting to compare the infrared spectra of Comet Hale-Bopp obtained from the ISO, with the spectra of stars which are surrounded by circumstellar dust. As Waelkens (1997), pointed out, there are great similarities, but also some differences. For instance, the spectrum of the star *HD* 100546 also displays the minerals mentioned above, as well as crystalline water, but contrary to the Comet, it also has strong spectral features of organic components in the 3.5μ band.

There may thus be a close relationship between comets like Hale-Bopp and the material observed in circumstellar disks, *e.g.* around the southern star Beta Pictoris. All of this may provide valuable new information about the formation of the cometary reservoirs in the solar system (Kuiper Belt and Oort Cloud). It has been suggested (Wooden *et al.* 1999) from the analogy with the young-star spectra that the crystalline nature of the silicates in comet Hale-Bopp dates from the early evolution of the solar system, and also that an Oort Cloud or a Kuiper Belt is presently forming around young stars observed by ISO.

Compared to other comets, the dust production of Comet Hale-Bopp was enormous, for instance it was 100 times more than in Comet Halley at comparable heliocentric distances. Similarly, the dust-to-gas ratio was very high, which ranged between 2 and 5 (*i.e.* Fulle, Cremonese, and Böhm 1998). The dust production at the maximum reached about 4×10^5 kg/sec, but since the nucleus is so large, the entire mass loss during this passage is probably still less than 0.1 % of its total mass (West 1998).

Comet Hale-Bopp has shown high activity and has been intrinsically very bright at relatively large distances from the Sun; in fact, it is intrinsically the brightest comet to date, whose orbit passes inside the Earth's orbit since the great comet of 1577. Its high rate of activity is the reason why it has created much excitement in the astronomical community.

1.7 Comet 81P/Wild 2

Apart from comet Hale-Bopp, another comet, 81P/Wild 2 had reached its perihelion in 1997. Comet 81P/Wild 2 is a short period comet. It is a relatively new comet to the inner solar system and therefore represents a comet which has not been overly heated and degassed by the Sun. Originally it was in an orbit between Jupiter and Uranus. Its orbit was altered due to close approach to Jupiter on 10 September 1974. It now orbits between Mars and Jupiter. It is a Jupiter family comet, discovered in 1978 (Wild and Marsden 1978). This comet has attained importance because of the STARDUST mission.

The STARDUST is a NASA spacecraft launched on February 7, 1999. If everything goes on as planned, the spacecraft will flyby comet 81P/Wild-2 on January 2, 2004, at a distance of 150 km from its nucleus and collect samples of dust and volatiles in the coma of the comet. It will then return these samples to Earth for detailed study. It will also image the comet nucleus. Sample collection will be achieved with the use of aerogel, a low-density (0.002 gm/cm^3) inert microporous (99.8% air) silica-based substance which will allow capture of high-relative-speed particles with minimal physical and chemical alteration. Each particle is expected to be less than a micron in size. After all collections are complete, the aerogel will be sealed in the sample vault of the sample re-entry capsule, and the samples will be recovered on Earth in January 2006, for study. The spacecraft is equipped with other sensors including a dust flux monitor. The dust flux monitor is a combination of low and high rate systems, a large area momentum sensor (LAMS) and PVDF sensors¹ respectively, sensitive to different momentum ranges (McDonnell *et al.* 1999).

Comet 81P/Wild 2 was selected as the target for study by the STARDUST space mission because of its being a new member of the Jupiter family of comet and because of the promise of a trajectory offering a low encounter velocity of 6.1 km/s (Meech and Newburn 1998).

Sarmecanic *et al.* (1997) from their mid-infrared imaging of comet Wild 2 reported that there was no evidence for excess silicate emission. Due to the absence of

¹ PVDF sensors are piezoelectric sensors uniquely suited for the measurement of induced stresses ranging from bars to hundreds of kilo-bars.

silicate emission and low maximum polarization of comet Wild 2 compared to other comets, Hadamcik and Levasseur-Regourd (2000) suggest from their polarimetric observations, that this comet could be less dust rich. However, a comparison between the dust to OH and CN ratios for this comet by A'Hearn *et al.* (1995), indicate that this comet is rich in dust.

Spectroscopic data of comet Wild 2 was collected and analyzed by Fink, Hicks, and Fevig (1999). Their imaging data indicate noticeable coma activity around February 01 1997, followed by relatively constant outgassing. The comet's visual magnitude shows a steep $25\log r_H$ dependence on the heliocentric distance r_H , indicating a mature crust common with Jupiter family comets.

1.8 The Objective of the Thesis

The objective of this thesis is to investigate the dust from selected comets, *viz.* comet C/1995 O1 Hale-Bopp and comet 81P/Wild 2. Instrumentation, observations, data reductions, and modeling of cometary jets, form the ground work of this thesis. In *Chapter 2* and *Chapter 3*, instrumentation, observations, and data reductions are covered. *Chapter 4* deals with modeling of dust jets from comet Hale-Bopp. In *Chapter 5*, investigation of polarization of comet Hale-Bopp and Wild 2 are taken up and the spectropolarimetric data is modeled. Using the results of *Chapter 4* and *Chapter 5*, the color of the dust shells in the post-perihelion images of comet Hale-Bopp is investigated in *Chapter 6*. In *Chapter 7*, the conclusions and plans for extended work are presented.

References

- A'Hearn, M. F., Millis, R. L., Schleicher, D. G., Osip, D. J., Birch, P. V., 1995. *Icarus* **118** 223.
- Arrhenius, S. A. 1900. Ueber die Ursache der Nordlichter. *Phys. Zeitschr.* **2**, 81.
- Bessel, F. W., 1836. Beobachtungen ueber die physische Beschaffenheit des Hal-

- ley'schen Kometen und dadurch veranlasste Bemerkungen. *Astron. Nachr.*, **13**, 185.
- Bohren C. F., and Huffman, D. R., 1983. *Absorption and scattering of light by small Particles*, A Wiley-Interscience Publication, John Wiley & Sons Inc., 1983.
- Boice D., and Huebner W., 1999. in *Encyclopedia of the Solar System*, Academic Press., 1999.
- Bruggeman, D. A. G., 1935. *Ann. Phys. (Leipzig)*, **24**, 636.
- Crifo, J. F. 1991. In *Comets in Post-Halley Era*, eds. R. L. Newburn, Jr., M. Neugebauer and J. Rahe (Dordrecht: Kluwer), p. 937.
- Delsemme, A. H., 1982 in *Comets* Ed. L. L. Wilkening, *Space Science Series* (University of Arizona Press, Tucson, Arizona) pp. 85.
- Dobrovol'ski, O. V., Kiselev, N. N., and Chernova, G. P., 1986. *EM&P* **34**, 189.
- Fernández, Y. R., Wellnitz, D. D., Buie, M. W., Dunham, E. W., Millis, R. L., Nye, R. A., Stansberry, J. A., Wasserman, L. H., A'Hearn, M. F., Lisse, C. M., Golden, M. E., Person, M. J., Howell, R. R., Marcialis, R. L., Spitale, J. N., 1999. *Icarus* **140**, 205.
- Fink, U., Hicks, M. P., and Fevig, R. A., 1999. *Icarus* **141**, 331.
- Finson, M. L., and Probst, R. F. 1968a. *ApJ* **154**, 327.
- Finson, M. L., and Probst, R. F. 1968b. *ApJ* **154**, 353.
- Fulle, M., Cremonese, G. and Böhm, C., 1998. *AJ* **116**, 1470.
- Gombosi, T. I., Cravens, T. E., and Nagy, A. F. 1985. *ApJ* **293**, 328.
- Gombosi, T. I. 1986. In *Exploration of Halley's Comet*, ESA SP-250, eds. B. Battick, E. J. Rolfe, and R. Reinhard (Noordwijk: ESTEC), Vol. 2, PP. 167.
- Gombosi, T. I., Szegő, K., Girbov, B. E., Sagdeev, R. Z., Shapiro, V. D., Shevchenko, V. I., and Cravens, T. E. 1983. In *Cometary Exploration*, ed. T. Gombosi (Budapest:Hungarian Academy of Sciences), Vol. 2, p. 99.

- Gustafson, B. Å. S., 1989. *ApJ* **337**, 945.
- Hadamcik, E., and Levasseur-Regourd, A. C., 2000. *C. R. Acad. Sci. Paris*, t. 1, *Série IV*, p. 127.
- Hale, A., Bopp, T., and Stevens, J. 1995. *IAUC 6187*, 1995 July 23. Edited by Green, D. W. E.
- Hanner, M. S., Gehrz, R. D., Harker, D. E., Hayward, T. L., Lynch, D. K., Mason, C. C., Russell, R. W., Williams, D. M., Wooden, D. H., Woodward, C. E., 1997. *EM&P* **79**, 247.
- Hanner, M. S., 1999. *Sp. Sci. Rev.* **90**, 99.
- Hayward, T. L., Hanner, M. S., and Sekanina, Z., 2000. *ApJ* **538**, 428.
- Henning, Th., Il'In, V. B., Krivova, N. A., Michel, B., and Voshchinnikov, N., V., 1999. *A&A Suppl.* **136**, 405.
- Hellmich, R. 1981. *A&A* **93**, 341.
- Hellmich, R., and Keller, H. U. 1981. *Icarus* **47**, 325.
- Hevelius, J. 1682. Excerpta ex epistola. II De cometa anno 1682 mense Augusto & Septimbri viso. *Acta Erudit.* Dec. 1682, p. 389.
- Jaegermann, R., 1903. *Prof. Dr. Th. Bredichin's Mechanisch Untersuchungen über Cometenformen.* (St. Petersburg: Voss.)
- Jockers, K., 1997. *EM&P* **79**, 221.
- Keller, H. U., Delamere, W. A., Huebner, W. F., Reitsema, H. J., Schmidt, H. U., Whipple, F. L., Wilhelm, K., Curdt, W., Kramm, R., Thomas, N., Arpigny, C., Barbieri, C., Bonnet, R. M., Cazes, S., Coradini, M., Cosmovici, C. B., Hughes, D. W., Jamar, C., Malaise, D Schmidt, K., Schmidt, W. K. H. and Seige, P. 1987. *A&A* **187**, 807.
- Kiselev, N. N., and Chernova, G. P., 1981. *Icarus* **48**, 473.

- Kolokolova, L., Jockers, K., Gustafson, B. Å. S., and Lichtenberg, G., 2001. *J. Geophys. Res. in Press*.
- Kruchinenko, V. G., and Churyumov, K. I., 1997. *EM&P* 77, 141.
- Lis, D. C., Mehringer, D. M., Benford, D., Gardner, M., Phillips, T. G., Bockele-Morvan, D., Biver, N., Colom, P., Crovisier, J., Despois, D., Rauer, H., 1997. *EM&P* 78, 13.
- Marconi, M. L., and Mendis, D. A. 1983. *ApJ* 273, 381.
- Marconi, M. L., and Mendis, D. A. 1984. *ApJ* 287, 445.
- Marsden, B. G., 1997. *EM&P* 79, 3.
- McDonnell, J. A. M., Burchell, M. J., Green, S. F., McBride, N., Vaughan, B. A. M., Zarnecki, J. C., Tsou, P., Hanner, M. S., Tuzzolino, A. J., Didonna, F., Brownlee, D. E., and Clark, B., 1999. *Advances in Space Research, Volume 25, Issue 2*, p. 335.
- McNaught, R. H., 1995. *IAUC 6240*, 1995 September 29. Edited by Green, D. W. E.
- Meech, K. J., and Newburn, R. L., 1998. *American Astronomical Society, DPS meeting* No.30, No.42.03.
- Mukai, T., Ishimoto, H., Kozasa, T., Blum, J., Greenberg, J. M., 1992. *A & A* 262, 315.
- Prialnik, and Dina, 1997. *ApJ* 478, L.107.
- Probstein, R. F. 1969. In *Problems of Hydrodynamics and Continuum Mechanics*, eds. F. Bisshopp et al. (Philadelphia: Soc. Ind. Appl. Math.), p.568.
- Sarmecanic, J., Osip, D. J., Fomenkova, M., and Jones, B., 1997 *IAUC 66601*, 1997 March 24. Edited by Marsden B. G.
- Schwarzschild, K. 1901. Der Druck des Lichtes auf kleine Kugeln und die Arrhenius'sche Theorie des Cometenschweife. *Akad. Wiss. München 1901*, p.293-327.

- Sekanina, Z., 1974. *Icarus* **23**, 502.
- Sekanina, Z., 1981a. *AJ* **86**, 1741.
- Sekanina, Z., 1981b. *Ann. Rev. Earth Planet Sci.* **9**, 113.
- Sekanina, Z., Hanner, M. S., Jessberger, E. K. and Fomenkova, M. N. 1998. In *Interplanetary Dust*, eds. S. F. Dermott, H. Fechtig, E. Grün, and B. Å. S. Gustafson (University of Arizona Space Sciences series) (*JPL Preprint series* No. 178)
- Sekanina, Z. and Larson, 1984. *AJ* **89**, 1408.
- Sekanina, Z. and Larson, 1986. *AJ* **92**, 462.
- Sekanina, Z., 1997. *EM&P*, **77**, 147.
- Sekanina, Z., 1997. *EM&P*, **77**, 155.
- Sekanina, Z., 1997. *EM&P*, **78**, 313.
- Sekanina, Z., 1998. *ApJ*, **494**, L121.
- Sekanina, Z., 1998. *ApJ*, **509**, L133.
- Waelkens, C., Malfait, K., and Waters, L. B. F. M., 1997. *EM&P* **78**, 285.
- Weaver, H. A., and Lamy, P. L., 1997. *EM&P* **79**, 17.
- West, R. M., 1998. in *Impressions from the Hale-Bopp Meeting on Tenerife (February 1998)*, <http://www.eso.org/outreach/info-events/hale-bopp/report-rw-hbitp98.html>.
- Whipple, F. L. 1950. *ApJ* **111**, 375.
- Whipple, F. L. 1951. *ApJ* **113**, 464.
- Wild P. and Marsden, B. G., January 1978. *IAUC* No. 3167. *IAUC 3167*, 1978 January 30. Edited by Marsden, B. G.
- Wooden, D. H., Harker, D. E., Woodward, C. E., Koike, C., and Butner, H. M., 1997. *EM&P* **78**, 285.

Wooden D. H., Harker, D. E., Woodward, C. E., Butner, H. M., Koike, C., Witteborn, F. C., and McMurtry, C. W. , 1999. *ApJ*, **517**, 1034.

Chapter 2

INSTRUMENTS, OBSERVATIONS & DATA REDUCTIONS

In this chapter, the telescopes and some of the instruments used for this study are discussed before going into the observations and the observational techniques. After touching upon the basic reduction and calibration methodology, the image enhancement techniques are discussed.

2.1 Telescopes, Back-end Instruments and Detectors

A telescope with a back-end instrument and a detector form the back-bone of observational astronomy. Celestial information is brought to us by photons of light. A telescope collects these photons, the back-end instrument analyses them and the detector registers and stores the information for further analysis.

The observational data used in this work were mainly obtained from the telescopes at the Vainu Bappu Observatory (VBO), Kavalur (78°E, 12°5 N, and 730m, above mean sea level), which is operated by the Indian Institute of Astrophysics (IIA). The time zone for the observatory is 5hours 30min.

Additional data observed by Andreas Hänel and Erwin Heiser, at the Observatory of Naturwissenschaftlicher Verein Osnabrück, Germany, form part of this work.

The telescopes used at VBO are the 2.34 m Vainu Bappu Telescope (VBT) and the 1.02 m Carl Zeiss reflector. VBT has a prime focus of $f/3.237$ with an image scale of 27.1 arcsec/mm and a cassegrain focus of $f/13$ with an image scale of 6.8 arcsec/mm. The prime focus was used for imaging the comet, while spectropolarimetry was done at the cassegrain focus with the newly built spectropolarimeter. VBT has an English (equatorial) mount, which is commonly known as a horseshoe mount. The 1.02 m Carl Zeiss reflector also operates at two foci: an $f/13$ cassegrain focus with an image scale of 15.6 arcsec/mm and an $f/30$ coudé focus with an image scale of 6.7 arcsec/mm. For our investigations, this telescope was used only at cassegrain focus for imaging the comet. The 1.02 m Carl Zeiss reflector is a Modified English (equatorial) mount. The telescope tube and the counter weight are on either side of the polar axis.

At the observatory of the Naturwissenschaftlicher Verein Osnabrück, the observations were made with a 60 cm ($f/12.43$) telescope.

The back-end instruments used in data acquisition, were an imaging camera with filters and the newly built spectropolarimeter for the VBT ($f/13$) at the cassegrain focus.

2.1.1 Imaging camera

An imaging camera (Fig. 2.1) consists of a filter wheel and a detector, mounted at the telescope focus, where the objects of study can be imaged onto the detector through different filters. A field-flattener, like the Wynne corrector at the VBT prime, provides a good distortion free image over an extended area on the flat image plane. At the 1.02 m Carl Zeiss telescope, no field flattener is provided at cassegrain $f/13$ focus, since the depth of the field is larger and the field distortion over the detector area is negligible. The exposure of the image is controlled by a shutter in front of the detector. In Fig. 2.1, the gray lines touching the edges of the CCD detector are the beam limits seen by the detector. To avoid vignetting, care must be taken that any optical element (i.e. the field flattener, the filters, the

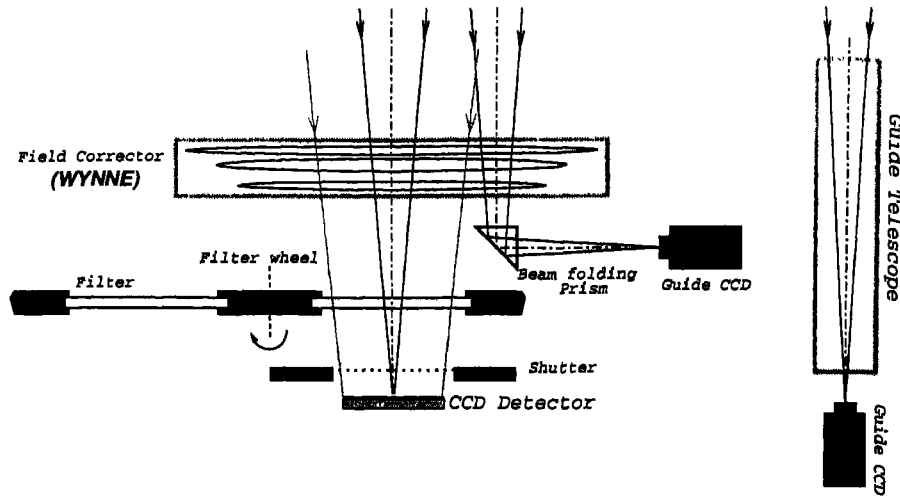


Figure 2.1: Schematic Diagram of the VBT Prime Camera

shutter and the detector window) should be sufficiently larger than the beam limits. A field magnification or reduction is also possible by changing the effective focal length of the telescope using additional lenses. A Barlow lens will increase the effective focal length and magnify the image on the image plane. A Shapley lens, on the other hand, will reduce the effective focal length so that a larger field is imaged on to the detector.

2.1.2 Spectropolarimeter

An optical, dual beam, automated, medium resolution spectropolarimeter (O-DB-AMRSP) for the $f/13$ cassegrain focus of the VBT, has been fabricated as a part of this work. The details on the instrumentation, data-acquisition and reduction for the spectropolarimeter are discussed in *Chapter 3*.

2.1.3 Detectors

For all observations, Charge Coupled Devices (CCD) were used as detectors. A CCD consists of an array of two dimensional (2-D) detectors made of a semiconductor device. An incident photon on the CCD creates a hole-electron pair through photo-electric effect. This electron is then trapped in a potential well at the point of incidence of the photon. The potential wells are in a (2-D) array and are maintained by applying a suitable electrostatic voltage. The electrons trapped in this 2-D array

of potential wells are proportional to the incident photons. Each of these 2-D array element of potential wells is referred to as a "pixel".

When an exposure is completed, charges from different pixels are read out one by one linearly. The electrostatic voltage maintaining the potential wells in each pixel is modified with a clock pulse in such a way that the charges stored as packets in each pixel, flow from one pixel to the other without mixing and are measured and digitized. The gain in the detector is set by biasing the semiconductor. We finally obtain a matrix of numbers representing a brightness map as the data.

CCD detectors have a high dynamic range, linearity and stability. The spectral response of these detectors are best in the red region of the spectrum. The blue and UV response of the detector is improved by a fluorescent coat like Meta-chrome II (MC II). Recently, the quantum efficiency of the CCD detectors has been further improved by making back illuminated CCD chips.

At the VBT prime and cassegrain foci, the CCD was a Photometrics system with a Tek1024 chip in a liquid nitrogen cooled dewar. This CCD has a pixel size of $24\mu \times 24\mu$. The acquired data from each pixel is digitized to an unsigned 16bit number. The average bias count for this system with $Gain = 1$ is ≈ 950 counts. The detector gain and readout noise are $9 \text{ photons/datanumber}$ and 10 photons respectively. At the 1.02 m Carl Zeiss telescope, we used a Photometrics CCD system with a 384×576 pixels Thomson chip in a liquid nitrogen cooled dewar. The pixel size for this detector is $22\mu \times 22\mu$. The acquired data from each pixel is digitized to a 14bit number. The average bias count for this system with $cgain = 0$ is ≈ 350 counts. The detector gain and readout noise are $27.26 \text{ photons/datanumber}$ and 17.90 photons respectively.

At the observatory of the Naturwissenschaftlicher Verein Osnabrück The detector was a SBIG ST-6 CCD camera that has 375×242 pixels with $23\mu \times 27\mu$ pixel size.

2.2 Observations

Observations of Comet 1995-O1, Hale-Bopp were carried out from VBO from November 1995 to March 1998. Beyond March 1998, the comet was extremely south for it to be observed from VBO. Approximately two nights per month of observation time

was obtained on either of the telescopes for the observations. Fig. 2.2 shows some of the images obtained during this 3 year period of comet observations from VBO.

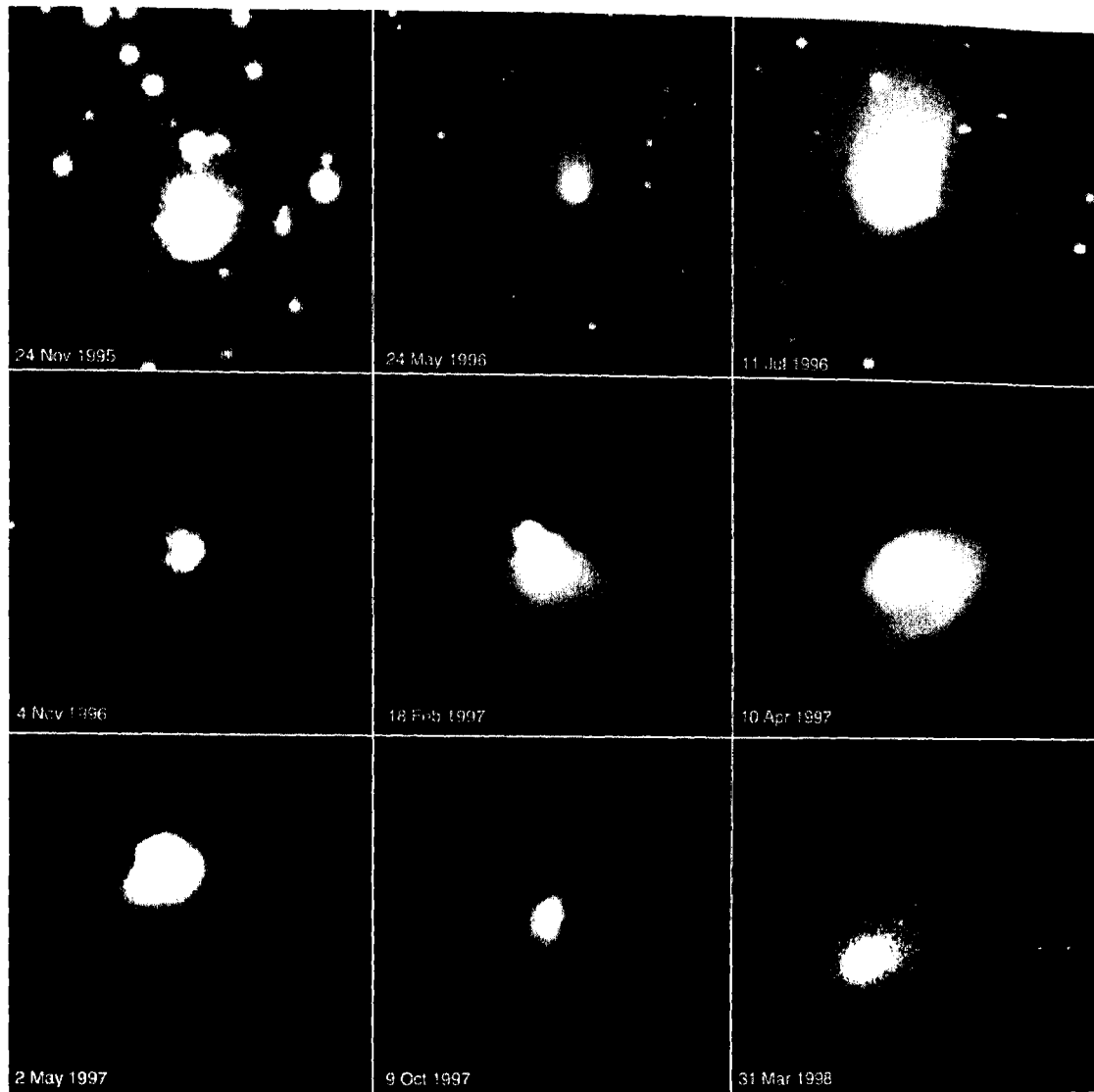


Figure 2.2: *Some of the best images of Comet 1995-O1 Hale-Bopp, obtained from 1995 to 1998 at VBO. The plate scales for each image in the mosaic are different.*

Spectropolarimetric observations of comet 81P/Wild 2 and comet 1995 O1, Hale-Bopp were successfully carried out on April 23 and 24, 1997. Further spectropolarimetric observations of these comets were not successful owing to bad sky conditions. A brief log of observations carried out from VBO is tabulated in Table 2.1. In addition, standard stars were observed on several other nights just for calibrating the newly built spectropolarimeter.

Observations from the Observatory of the Naturwissenschaftlicher Verein Osnabrück

Date of Observation	Telescope & Focus	Type of Observation
4 Nov 1995	VBT-Prim	R & I filter Imaging.
5 Nov 1995	VBT-Prim	R & I filter Imaging.
6 Nov 1995	VBT-Prim	R & I filter Imaging.
11 May 1996	1.02m-Cass	White light Imaging.
12 May 1996	1.02m-Cass	B, V, R & I filter Imaging.
24 May 1996	VBT-Prim	B & R filter Imaging.
11 Jul 1996	VBT-Prim	$\lambda 4861/50\text{\AA}$, $\lambda 5154/77\text{\AA}$, R & I filter Imaging.
6 Oct 1996	VBT-Prim	$\lambda 4861/50\text{\AA}$, $\lambda 5154/77\text{\AA}$, R & I filter Imaging.
4 Nov 1996	VBT-Prim	$\lambda 4861/50\text{\AA}$, $\lambda 5154/77\text{\AA}$, R & I filter Imaging.
18 Feb 1997	VBT-Prim	$\lambda 4861/50\text{\AA}$, $\lambda 5154/77\text{\AA}$, & R filter Imaging.
8 Apr 1997	1.02m-Cass	$\lambda 3870/62\text{\AA}$, $\lambda 5141/118\text{\AA}$, $\lambda 5260/57\text{\AA}$ & R filter Imaging.
9 Apr 1997	1.02m-Cass	$\lambda 3870/62\text{\AA}$, $\lambda 4062/62\text{\AA}$ & R filter Imaging.
10 Apr 1997	1.02m-Cass	$\lambda 3870/62\text{\AA}$, $\lambda 4062/62\text{\AA}$, $\lambda 4450/62\text{\AA}$, $\lambda 5141/118\text{\AA}$, $\lambda 5260/57\text{\AA}$ & R filter Imaging.
11 Apr 1997	1.02m-Cass	$\lambda 3870/62\text{\AA}$, $\lambda 4062/62\text{\AA}$, $\lambda 4450/62\text{\AA}$ & R filter Imaging.
12 Apr 1997	1.02m-Cass	$\lambda 5260/57\text{\AA}$ & R filter Imaging.
23 Apr 1997	VBT-Cass	Spectropolarimetry (4500 \AA to 7500 \AA)
24 Apr 1997	VBT-Cass	Spectropolarimetry (4500 \AA to 7500 \AA)
2 May 1997	1.02m-Cass	Cometary & R filter Imaging.
8 May 1997	1.02m-Cass	Cometary & R filter Imaging.
9 Oct 1997	VBT-Prim	B, V, R & I filter Imaging.
7 Jan 1998	1.02m-Cass	R filter Imaging.
31 Mar 1998	1.02m-Cass	R filter Imaging.

Table 2.1: Log of the Observation from VBO

Date of Observation	Exposure.	Type of Observation
8 Sep 1996	30s	White light Imaging.
15 Sep 1996	30s	White light Imaging.
6 Oct 1996	30s	White light Imaging.
2 Feb 1997	1s	White light Imaging.
4 Mar 1997	1s	White light Imaging, with Shapley lens
7 Mar 1997	1s	White light Imaging.
11 Mar 1997	1s	White light Imaging.
21 Mar 1997	1s	White light Imaging.
31 Mar 1997	6s	R filter Imaging.
2 Apr 1997	1s	White light Imaging.
3 Apr 1997	1s	White light Imaging.
6 Apr 1997	1s	White light Imaging.
9 Apr 1997	2 × 3s	White light Imaging.
15 Apr 1997	5s	R filter Imaging.
16 Apr 1997	2 × 6s	White light Imaging.
2 May 1997	2 × 10s	White light Imaging.

Table 2.2: *Log of the Observation of Comet 1995 O1 Hale-Bopp from the Observatory of the Naturwissenschaftlicher Verein Osnabrück provided by Andreas Hänel.*

is also tabulated in Table 2.2. The March 4, 1997 image was taken with a Shapley lens, with an effective focal length of 423 cm ($f/7.05$). All the images except those on March 31, 1997 and April 15, 1997 (which were obtained through a R filter) were obtained in white light (without a filter). These images had been presented at the AG meeting in Innsbruck 1997 and have been published by Heiser (1998).

2.3 Guiding on the Comet

Guiding the telescope is required during observations to compensate for the relative motion between Earth and the object and for compensation of the mechanical flexures of the telescope. In an equatorial mount telescope, as in case of our ob-

servations, the telescope is tracked East to West at a velocity of 15arcsec/sec to compensate for the rotation of the Earth. The slight errors in this velocity and telescope flexures, are corrected by an online guiding.

One of the ways of online guiding is performed by using a parallel guide-telescope looking at the object of observation, or a nearby field star. If the object of observation is extended, it is easier to guide on a field star, which is a point source. Another method of online guiding is by using the field from the main telescope itself. Light from a nearby field star, just out of the field of the main detector, is observed. In Fig. 2.1 both these methods of online guiding are schematically shown for VBT along with the schematic diagram of the VBT prime camera. The parallel guide-telescope was fixed with an eye-piece for manual guiding. During comet observations at low hour angles, it was difficult to physically reach the eye-piece for guiding. So an adapter was made and the eye-piece was replaced with an Intensified CCD (I-CCD). The video signal from this CCD was displayed on to a monitor in the console room for remote guiding using the parallel guide-telescope. Remote guiding using the nearby field from the main telescope with an I-CCD camera already existed. Here, the light from a nearby field star is bent with a beam folding prism into the I-CCD camera (Fig. 2.1).

Guiding is performed by restricting either the object or the guiding field star, from drifting. This is executed by occasional fine adjustment of the movement of the telescope in right ascension (*RA*) and declination (*Dec*).

The advantage of using a parallel guide-telescope is that guiding is possible on the object itself. However, the major disadvantages are: *a*) Relative mechanical flexures between the guide-telescope and the main telescope may exist and a drift between the telescopes when pointing at different locations on the sky cannot be ruled out. *b*) The guide-telescope aperture is generally much smaller than the main telescope, hence for faint objects or faint field stars, there might not be enough flux to guide on.

The advantages of guiding on a nearby field star observed through the main telescope are: *a*) Freedom from relative mechanical flexures. *b*) Flux level is certainly much higher and guiding on fainter objects, is possible. However, in this method it is

not possible to guide on the object. This becomes a major disadvantage for solar system objects, which have a relative velocity with respect to the field star. For comets especially near perihelion and closer to Earth, this velocity is much higher than when they are far away.

For guiding on a comet, we calculate its movement at regular intervals, $\dot{\alpha} = \Delta\alpha/dt$ in *RA* and $\dot{\delta} = \Delta\delta/dt$ in *Dec* and apply these as corrections to the telescope's track rate. However, online guiding as mentioned above will still be required for any residual drift. Guiding on a nearby field star observed through the main telescope is also possible if provisions are there to provide a velocity to the guiding unit in an opposite direction so that it can compensate for the relative motion between a field star and the comet (A'Hearn 1995). Such a guiding unit is ideal for observations of solar-system objects. However, due to non availability of such provision, at VBO, tracking had to be done using the 10 inch ($f/16$) parallel guide telescope. The track rates of the telescope was adjusted to follow the comet and for fine adjustments, we used the 10 inch ($f/16$) parallel guide telescope fitted with an I-CCD. A zero-point correction between the field of the main telescope and the guide telescope was performed close to the object of observation to minimize the relative flexure effects. At the 1.02 m Carl Zeiss telescope, the guiding was done manually using the 8 inch ($f/16$) guide telescope.

Guiding for the spectropolarimetric observations was done at the slit jaws of the spectropolarimeter. For more details see *Chapter 3*.

2.4 Error Theory and Data Reduction

For all observations presented here, data were obtained using a CCD detector. Thus in this section we will discuss the error theory and data reduction techniques pertaining to CCD data only.

2.4.1 Signal to Noise (S/N)

The data from a CCD is obtained as a matrix of numbers $S_{i,j}$ representing a brightness map. The Signal to Noise (S/N) is an index to describe the quality of this brightness map and provides a limit on how precisely we can distinguish differences

in brightness between the pixels. So what causes noise in a CCD data? Some of it arises from the fundamental properties of light itself. Photons, even from a perfectly constant source, arrive at the detector in sporadic bursts and are governed by photon statistics. When a photon strikes a pixel of a CCD, there is no guarantee that it will actually produce an electron-hole pair. This randomness is also because of the quantum nature of light. The fraction of photons recorded defines the quantum efficiency of the detector. Apart from the quantum efficiency of the detector, there is the readout noise. When the signal generated by light falling on a CCD is collected, amplified and converted to a digital value, noise is introduced at each step of the process. Since this noise is added by reading the signal, it is called the readout noise.

No matter how good the CCD or how careful we are in our work, the number of photons recorded in a given amount of time is uncertain by at least the square root of the number that has been collected ($S/N = \sqrt{S}$). This particular relationship between the signal and the noise arises whenever some randomly occurring events are counted within a fixed interval, and is called the Poisson statistics.

2.4.2 Basics Calibration and Removal of Systematic Errors

A CCD data set has some systematic errors. The basic reduction procedure for a CCD data consists of removal of these systematic errors. An element $S_{i,j}$ of an unprocessed CCD data can be represented as

$$S_{i,j} = G_{i,j} (F_{i,j}(t) + B_{i,j}(t)) + d_{i,j}(T, t) + b_{i,j}. \quad (2.1)$$

Where $G_{i,j}$ is the pixel gain factor, $F_{i,j}$, the flux from the object, $B_{i,j}(t)$, the background sky, $d_{i,j}(T, t)$, the dark counts, and $b_{i,j}$, the bias value for the duration t of this exposure and the temperature T of the detector. The systematic errors, $b_{i,j}$, $d_{i,j}(T, t)$, and $G_{i,j}$ have to be estimated and removed from the observed CCD data. Let us investigate each of these systematic errors in more depth, so that it may be estimated for calibration, keeping the resultant S/N as low as possible.

2.4.2.1 Bias Correction

The bias is an intrinsic property of a CCD detector. The CCD is biased to a value $b_{i,j}$ to set the gain of the detector. So at the beginning of an exposure, the CCD detector already has this residual count. A straight readout with a zero time exposure provides us with the Bias $b_{i,j}$ values. Bias correction is performed by subtracting the bias frame from the observed data.

When one image is subtracted from another like the bias correction, the S/N of the resultant image will be.

$$S/N = \frac{S_1 - S_2}{\sqrt{N_1^2 + N_2^2}}. \quad (2.2)$$

Although the two signals are subtracted, the noise still adds quadratically. This reduces the S/N of the resultant image. We can cut down on this degradation by reducing the noise in the bias frame. This implies that we need bias frame with a very high S/N . We achieve this by averaging or median combining many bias frames to obtain a “master” bias frame. This master bias frame is then subtracted from the observed frame so that least degradation in S/N is achieved.

2.4.2.2 Dark Counts

Even in the absence of light, electrons accumulate in a CCD. These are responsible for the dark counts. The term $d_{i,j}(T, t)$ in Eq. 2.1 represents this quantity. It increases with temperature T of the detector and the duration of the exposure t . To minimize $d_{i,j}(T, t)$, the temperature T of the detector is reduced by placing the CCD chip on a cold finger. The cold finger is cooled through variety of techniques like oil, water, Peltier or liquid nitrogen cooling.

For removal of the dark counts $d_{i,j}(T, t)$, an exposure is taken with the shutter closed. The duration of this exposure and the temperature of the detector, should be identical to that of the data observed. It is thus advisable to take a dark observations just before or after the actual observation. In a dark observation, we obtain

$$S_{i,j}^d = d_{i,j}(T, t) + b_{i,j}. \quad (2.3)$$

$d_{i,j}(T, t)$ is obtained by bias subtraction from the dark observation $S_{i,j}^d$. When $d_{i,j}(T, t)$ is subtracted from the bias corrected observed data, further deterioration

in the S/N will occur as shown in Eq. 2.2. It is thus always advantageous and advisable, to maintain the dark $d_{i,j}(T, t)$ to a negligible level; so that the dark counts could be entirely neglected from the reduction process. This will not only save the precious observation time but also reduce deterioration of the S/N due to an extra subtraction.

At the VBO, the CCDs used at both the telescopes are liquid nitrogen cooled to 173 K (-100°C). At this low temperature, $d_{i,j}(T, t)$ is negligible (less than one count) for an exposure time $t < 60$ min. The exposure time t is therefore always restricted to less than 60 min. If required, multiple short exposures are taken and co-added. For our observations, we did not require long exposures. The longest exposure was for the spectropolarimetric observations of comet 81P/Wild 2, which was of 30 min each (see *Chapter 5*). In our analysis and data reduction, therefore, dark counts were completely neglected.

2.4.2.3 Flat-field Correction

In Eq. 2.1, $G_{i,j}$ represents the variations in pixel to pixel response of the CCD combined with the non-uniformity of the chip illumination caused by the shadows cast on the CCD. The shadowing on the CCD could be caused by obstruction of light by dust particles on lenses, filters, or the optical windows in front of the CCD. The vignetting of the optical system will also cause a ring like shadow on the CCD. To obtain $G_{i,j}$, an evenly illuminated surface is observed. This data after bias and dark corrections, will be of the form

$$S_{i,j}^f = G_{i,j}C(t), \quad (2.4)$$

where $C(t)$ is a constant value representing the evenly illuminated surface. This frame could then be normalized by the median value of $S_{i,j}^f$, to remove $C(t)$ and obtain $G_{i,j}$.

The flat-field corrected data is obtained by dividing the bias and dark corrected observed data, by the flat frame $S_{i,j}^f$. We eventually obtain $F_{i,j}(t) + B_{i,j}(t)$ in Eq. 2.1 from the data, which is proportional to the actual intensity of the object and the background sky. The normalization of the flat frame by the median value of $S_{i,j}^f$, to eliminate $C(t)$ is redundant because only the proportionality constant to the actual

intensity is modified by $1/C(t)$. If the data of the flux calibrator (*i.e.* photometric standard star), and object data are flat-fielded by the same flat, it is not required to eliminate $C(t)$.

Flat-field Correction of an image will again alter the S/N of the result due to division, and the resultant S/N will be

$$S/N = \frac{1}{\sqrt{(S/N)_o^{-2} + (S/N)_f^{-2}}}. \quad (2.5)$$

In equation (Eq. 2.5), the subscripts o and f refer to the observed and flat-field frames respectively. The degradation of S/N of the observed frame by flat-fielding is minimized when the flat-field frame has a much higher S/N than the observed data being processed. Thus multiple flat-field images with high S/N are combined to form a master flat-field frame with an even higher S/N . This master flat is used for calibration of the observed frame. An averaging or a median is used for combining the flat images. Since noise follows Poisson statistics, it tends to distribute evenly on both sides of the real value. Thus a median combine will be closest to the real value.

The requirement for obtaining a flat-field frame is to observe an evenly illuminated surface. A flat white board is fixed on the dome of the telescope and illuminated with tungsten or halogen lamps. This well illuminated white board is some times used as a flat-field source and is generally called a "dome-flat". However, for flat fielding an imaging data, flats obtained by imaging an evenly illuminated twilight sky, known as "sky-flat", is preferred to a dome-flat. Over the small section of the sky observed by the telescope, the twilight sky is more evenly illuminated than a dome-flat.

In spectroscopy and spectropolarimetry, light is dispersed in wave-length on the CCD. Hence in the spectroscopic and spectropolarimetric sky-flats, all the telluric and sky lines appear on the CCD. This intensity variation makes the flat unusable. Hence for obtaining flats during spectroscopy or spectropolarimetry, sky-flats fail and dome-flats have to be used. Techniques of obtaining flats for spectropolarimetry is discussed in *Chapter 3*.

Flat field calibration for spectropolarimetric and spectroscopic data are identical and more complex than flat fielding an image data. In a spectropolarimetric and

spectroscopic flats, along with intensity response there is a wave length dependent response of the CCD along the spectral dispersion axis ($G_{i,j} \implies G_{i,j}g(\lambda)$). The dome-flat has it's own spectral variation depending on the spectral energy distribution of the illuminating source and on the reflection properties of the white board. $C(t)$ can no more be considered a constant, but a wavelength dependent $C(\lambda, t)$. A bias corrected spectropolarimetric or spectroscopic flat will be of the form

$$S_{i,j}^f = G_{i,j}g(\lambda)C(\lambda, t). \quad (2.6)$$

It is not possible to separate $g(\lambda)C(\lambda, t)$, hence both the quantities are normalized to obtain $G_{i,j}$. The $g(\lambda)$ calibration of the data is performed later using a spectrophotometric standard star, by normalizing the continuum, or using a differential technique as used in spectropolarimetry (*Chapter 3*).

Normalization of $g(\lambda)C(\lambda, t)$ is performed by first averaging the spectroscopic flat over an aperture along the spatial axis, perpendicular to the dispersion axis to obtain a one dimensional spectrum. This spectrum, is further smoothed by fitting a cubic spline or a polynomial function along the dispersion axis. This fitted spectrum corresponds to $g(\lambda)C(\lambda, t)$ term. The spectroscopic flat $S_{i,j}^f$ is then normalized by this fitted spectrum, to obtain $G_{i,j}$, which is the normalized flat independent of $g(\lambda)C(\lambda, t)$ (Eq. 2.6).

In a spectropolarimetric or spectroscopic flat, the S/N is dependent on λ through $g(\lambda)C(\lambda, t)$. When the red region of the spectra is well exposed, with a good S/N , the blue region is under exposed and as a consequence, has a poor S/N . If the S/N of the blue region has to be improved through a longer exposure, the red region of the flat will saturate. The S/N can to some extent, be improved by co-adding multiple flats. Sometimes the red region and the blue regions are separately flat-fielded. Due to these complexities, it is sometimes advisable not to flat-field spectroscopic or spectropolarimetric data. The error introduced in the data by flat-fielding using a poor flat frame, may be larger compared to the systematic response $G_{i,j}$ of the detector. During spectropolarimetric data reduction, the systematic response $G_{i,j}$ is automatically eliminated if the complementary observations at 0° and 90° or at 45° and 135° of the *HWP* are taken at the same region of the detector (see *Chapter 3*).

2.4.3 Extraction and Wavelength Calibration

Spectroscopic and spectropolarimetric data requires extraction of a one dimensional spectrum (counts *vs* pixels) from the spectral image. Apertures are defined on the spatial axis of the 2-D spectropolarimetric or spectroscopic data. For spectropolarimetric data, dual apertures are defined corresponding to the ordinary and the extraordinary spectra (see *Chapter 3*). The one dimensional (1-D) spectrum is extracted from each aperture by adding the flux from the pixels of the spatial axis within the defined aperture.

The dispersion axis may be tilted and may not exactly match with the row or the column of the CCD data array owing to misalignment between the CCD and the grating. The spectrum may also be slightly curved. These problems are taken care of by tracing the aperture center of a stellar spectrum by searching for the peak flux along the dispersion axis. The one dimensional spectrum is extracted along the traced path.

This spectrum has to be wavelength calibrated so that the count *vs* pixel data is converted to counts *vs* wavelength spectra. Calibrators, such as *Fe – Ne* and *Fe – Ar* sources, are used and their spectra are obtained between the observations of the program object. These spectra are used for finding the pixel to wavelength relation, which is then applied for wavelength calibration. Sometimes, the telluric lines on the spectra can also be used as calibrator lines.

2.4.4 Correcting for Rectangular Pixel CCD

The CCD detector used at the Observatory of the Naturwissenschaftlicher Verein Osnabrück has a rectangular pixel ($23\mu \times 27\mu$). An interpolation on the images were performed, using a quadratic polynomial and the pixels were scaled to a square pixel of $27\mu \times 27\mu$ to yield an image size of 319×242 *pixels*. Such a transformation is essential for further processing, *e.g.* image enhancement or photometry.

2.4.5 Software Packages for Data Reduction

The data reduction was carried out using the IRAF (Image Reduction and Analysis Facility) software. IRAF is distributed by the National Optical Astronomy Obser-

vatories which is operated by the Association of Universities Inc. (AURA) under cooperative agreement with the National Science Foundation.

Bias and flat field calibration can be performed using tasks in the *ccdred* package of IRAF. Master bias is created using the *zerocombine* task. Master flat is made by combining the bias corrected flats using *flatcombine*. The task *ccdproc* does multiple processing and can be used for bias as well as flat field corrections. The task *apnormalize* in *specred* package of IRAF is used for normalization of the flats for spectroscopic data. The extraction of the spectra, including the tracing of the aperture and background sky subtraction can be performed using the *apall* task. The tasks *identify*, *reidentify*, *refspectra* and *dispcor* are used for wavelength calibration. Corrections for rectangular pixel CCD could be made using the *magnify* command in IRAF that interpolate two dimensional images.

2.5 Image Enhancements

After pre-calibration of the data, further processing is required depending on the scientific aim for which the data is going to be utilized. Image Enhancement techniques are required when one wants to look at faint features in the images. Images obtained from ground based observations are affected by the atmospheric scintillation and hence are seeing limited. There are methods of modeling the atmospheric seeing so that the images could be deconvolved to account for the atmospheric effects. Here, such deconvolution techniques will not be dealt with, since it is beyond the scope of the present work.

From the bias and flat-field corrected images of comet Hale-Bopp (Fig. 2.2), faint jet and shell features embedded in the comet's coma are noticed. In order to model the shapes of these jets and the shells, it is first required to separate out the overwhelming contribution of the coma in which the jets are embedded. Several image enhancement techniques have been applied to comets by various authors to bring out the fine structures such as the jets and the shells (e.g., Klinglesmith 1981; Matuska *et al.* 1978; Sekanina and Farrell 1978; Wood and Albrecht 1981). The most common techniques utilize spatial filtering or derive intensity derivatives in some directions. These methods reduce the effect of the steep intensity gradation and allow

one to stretch the contrast. In all these approaches, great care must be exercised to identify the processing artifacts.

One of the most prevalent of such techniques was, until recently, the unsharp masking technique, which is essentially a photographic technique. In this technique, an unfocused image is made on a photographic plate. It is then kept in front of the original observed plate as a mask and the unsharp masked image is obtained. This technique essentially filters out the lower Fourier frequencies to allow an image of the higher Fourier frequencies to be made. In a digital CCD data, the unsharp masking technique is mimicked by “median-filtering”, as it is based on the same concept. The “Gaussian-filtering” instead of median-filtering, is sometimes useful where a point-spread function of the image is definable. Median-filtering is performed by subtraction of the image by its median image. A median image is made by defining a box around each pixel. Counts in each pixel of the image is then replaced by the median value of the pixels in the box around it. In Gaussian-filtering, the image is subtracted by its Gaussian convolution. The choice of an optimum box in median filtering and an optimum value of the full width at half maximum (FWHM) in Gaussian filtering must be found depending on the image quality and size of the features to be delineated.

There are even better techniques for enhancement of cometary images, like the radial and rotational shift algorithm by Larson and Sekanina (1984). Due to a somewhat spherical symmetry in cometary coma, this technique works extremely well with comet images. This technique suppresses the strong radial intensity gradient in the coma to enhance smaller fluctuations like the jets and the shells.

2.5.1 The Radial and Rotational Shift Algorithm

The brightest comet pixel on the CCD image is used as the initial point for interpolating the center (x_0, y_0) using a marginal distribution in x and y around it.

The image $I_0(i, j)$ is rotated around this center (x_0, y_0) by an angle $-\Delta\theta$ and $+\Delta\theta$ to create the two rotationally shifted images $I_{-\Delta\theta}(i, j)$ and $I_{+\Delta\theta}(i, j)$. A residual image $I_{s_\theta}(i, j)$ is then calculated by

$$I_{s_\theta}(i, j) = 2I_0(i, j) - (I_{-\Delta\theta}(i, j) + I_{+\Delta\theta}(i, j)). \quad (2.7)$$

Similarly, the radial shift images $I_{-\Delta\rho}(i, j)$ and $I_{+\Delta\rho}(i, j)$ are made by shifting the image radially by $-\Delta\rho$ and $+\Delta\rho$ from the center (x_0, y_0) and the residual image $I_{s\rho}(i, j)$ is calculated by

$$I_{s\rho}(i, j) = 2I_0(i, j) - (I_{-\Delta\rho}(i, j) + I_{+\Delta\rho}(i, j)). \quad (2.8)$$

The best way to apply the rotational shift algorithm to an image is, to perform an image transformation from Cartesian (x, y) coordinate to Polar (ρ, θ) coordinate. In the new coordinate system, ρ is the radial distance from the comet center (x_0, y_0) , while θ is the angle between a reference axis and the radial vector ρ .

$$I(i_x, j_y) \implies I^t(i_\rho, j_\theta), \quad (2.9)$$

$$i_\rho = \sqrt{(i_x - x_0)^2 + (j_y - y_0)^2} \quad j_\theta = \text{Arctan} \left(\frac{j_y - y_0}{i_x - x_0} \right).$$

Here the integer (i_x, j_y) coordinates are equivalent to the Cartesian (x, y) coordinates, while (i_ρ, j_θ) are equivalent to Polar (ρ, θ) coordinates.

As an example, Fig. 2.3 illustrates this transformation. The image on the right, is the (ρ, θ) transform of the image on the left, of comet Hale-Bopp observed on 10th April 1997 from VBO. The left edge of the right image is the center (x_0, y_0) of the comet. The spiraling jets and shells on the left image transform as near vertical strips on the right image.

The radial and rotational shift is now extremely easy on this transformed image,

$$\begin{aligned} I^t_{\pm\Delta\theta}(i_\rho, j_\theta) &= I^t(i_\rho, j_\theta \pm \Delta\theta), \\ I^t_{\pm\Delta\rho}(i_\rho, j_\theta) &= I^t(i_\rho \pm \Delta\rho, j_\theta), \\ I^t_{\pm\Delta\rho, \pm\Delta\theta}(i_\rho, j_\theta) &= I^t(i_\rho \pm \Delta\rho, j_\theta \pm \Delta\theta). \end{aligned} \quad (2.10)$$

The residual image can also be calculated directly as a transformed image $I^t_{s\rho}(i_\rho, j_\theta)$, $I^t_{s\theta}(i_\rho, j_\theta)$ or $I^t_{s\rho\theta}(i_\rho, j_\theta)$ applying the concepts of Eq. 2.7 and Eq. 2.8. The residual image can then be inverse transformed to obtain the jets and shells enhanced image of the comet in the (x, y) system. The choice of $\Delta\rho$ and $\Delta\theta$ depends on the jet and shell features in the image. Again, the optimum $\Delta\rho$ and $\Delta\theta$ are chosen, depending on the gradient of the faint features, so that in the final image, the jets or shells are best enhanced with least processing artifacts.

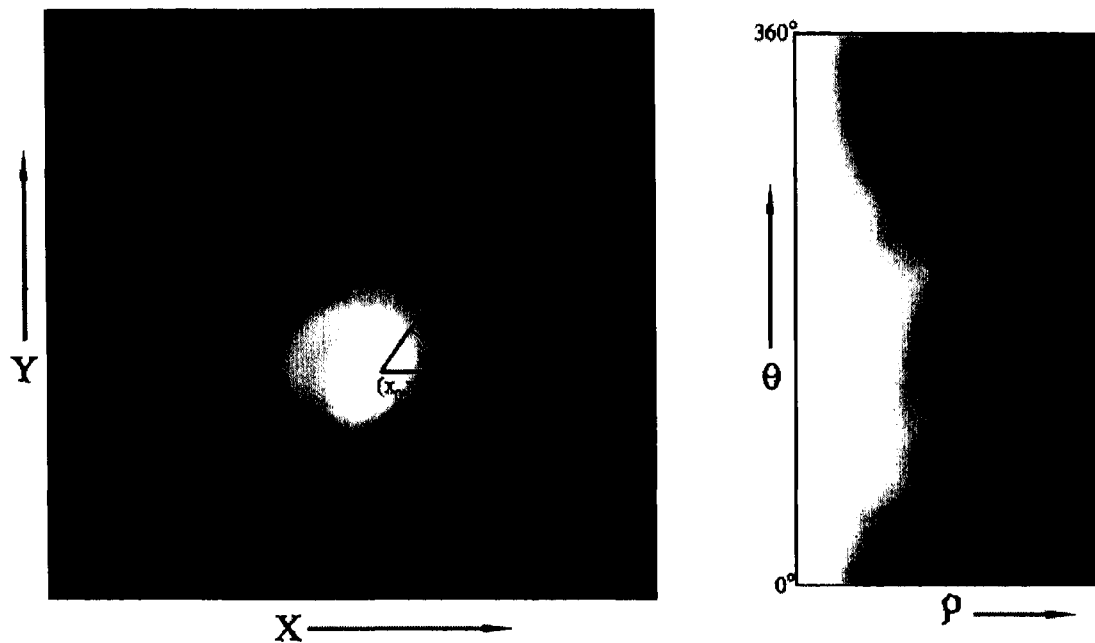


Figure 2.3: (x, y) to (ρ, θ) transformation of Comet Hale-Bopp image observed on 10th April 1997. The image on the right is the (ρ, θ) transform of the image on the left.

The residual image I_s constructed by the radial shift algorithm maps the rate of change of intensity at a given ρ , while the residual image I_s made by the rotational shift algorithm maps the rate of change of intensity at a given θ . Thus the residual image I_s is therefore effectively a derivative of the image I_0 in ρ and θ .

The images of comet Hale-Bopp were enhanced using this radial and rotational shift algorithm. A rotation shift of $\Delta\theta = \pm 10^\circ$ seemed suitable for these images. The enhanced images thus obtained are used for morphological modeling of the dust ejecta from the comet in *Chapter 4*.

In spite of the effectiveness of the above mentioned techniques to enhance the fine structures in images, the photometric information of the images are lost and the enhanced images cannot be used for photometric studies. For such studies, we normalize the image with a synthetic coma as explained below.

2.5.2 Normalization by a Synthesized Coma

It is assumed that in a comet, the coma is formed from a constant, spherically symmetric outflow of gas and dust. The number density of dust grains falls as $1/\rho^2$.

In an image, integration of all such grains along the line of sight for such an outflow, will produce a $1/\rho$ surface brightness gradient. So by dividing an image of a comet by a $1/\rho$ profile, the irregularities in the outflow will be emphasized. The intensities in the observed image $I_o(i, j)$, can be represented by $I_{o_C}(i, j)$ and $I_{o_J}(i, j)$. The former represents the constant and spherically symmetric outflow of the coma and the latter the spatial irregularities in the outflow.

$$I_o(i, j) = I_{o_C}(i, j) + I_{o_J}(i, j). \quad (2.11)$$

A synthesized image with a $1/\rho$ profile is created centered at the coma center (x_0, y_0) . This image is then convolved either with a well defined point spread function (PSF) of a star in the image or by a Gaussian profile, as it very well approximates the PSF due to seeing. This convolved synthesized image $I_{s_C}(i, j)$ is equivalent to $I_{o_C}(i, j)$ by a scaling factor k .

$$I_{o_C}(i, j) = k I_{s_C}(i, j) \quad (2.12)$$

The observed image is divided by this convolved synthesized image of the coma, which results in

$$I_{o_N}(i, j) = \frac{I_o(i, j)}{I_{s_C}(i, j)} = k \left(1 + \frac{I_{o_J}(i, j)}{I_{o_C}(i, j)} \right). \quad (2.13)$$

The scaling factor k is determined from the region of the image where there are no strong jets or shells and surface brightness declines nearly as $1/\rho$.

In the April 1997 images of comet Hale-Bopp, the region for determining k is selected from the North-East of the nucleus. We take the median value of this region in the image $I_{o_N}(i, j)$ as the value of k . From Eq. 2.13

$$\frac{I_{o_J}(i, j)}{I_{o_C}(i, j)} = \frac{1}{k} \frac{I_o(i, j)}{I_{s_C}(i, j)} - 1. \quad (2.14)$$

The normalized image created using Eq. 2.14 is free from the strong radial intensity gradient, while at the same time the relative flux distribution is conserved. Such an image can be used for photometric modeling. For morphological studies the radial and rotational shift algorithm is preferred as it produces sharper features. This technique of normalization by a synthesized coma has been used by Hayward *et. al.* (2000) on their Infrared images. This technique is made use of to study the color of the dust jets in *Chapter 6*.

References

- A'Hearn, M. F., 1997 *personal communication*.
- Hayward, T. L., Hanner, M. S., and Sekanina, Z., 2000. *ApJ* **538**, 428.
- Heiser, E., 1998. *Osnabrücker Naturwiss. Mitt.* **24**, 19 - 30.
- Klinglesmith, D. A., 1981. In *Modern Observational Techniques for Comets*, JPL Publ. 81-68 edited by J. C. Brandt, B. Donn, J. M. Greenberg, and J. Rahe (U.S. GPO, Washington, D.C.), p. 223.
- Larson, S. M., and Sekanina, Z., 1984. *ApJ*, **89**, 571.
- Matuska, W., Jr., Janney, D. H., Farrell, J. A., and Keller, C. F., Jr., 1978, *Opt. Eng.*, **17**, 661.
- Sekanina, Z., and Farrell, J. A., 1978. *AJ*, **83**, 1675.
- Wood, H. J., and Albrecht, R., 1981. In *Modern Observational Techniques for Comets*, JPL Publ. 81-68 edited by J. C. Brandt, B. Donn, J. M. Greenberg, and J. Rahe (U.S. GPO, Washington, D.C.), p. 216.

Chapter 3

AN OPTICAL, DUAL-BEAM, AUTOMATED MEDIUM RESOLUTION SPECTROPOLARIMETER FOR THE VAINU BAPPU TELESCOPE

Fabrication of an optical spectropolarimeter as an add-on facility to an existing astronomical spectrograph at the Vainu Bappu Telescope is described. The polarimetric optics consists of a Pancharatnam design half-wave plate and a modified Glan-Taylor polarizing beam splitter. Instrumental response, calibration and characterization of the system are presented. Performance of the spectropolarimeter has been assessed based on the results of observations of polarized and unpolarized standard stars. The attainable accuracy of the instrument is found to be dependent on the S/N of the data. The present data set yields an accuracy of $\sim \pm 0.5\%$ at 4000\AA and $\sim \pm 0.3\%$ at 7500\AA , at a spectral resolution of $\sim 7.2\text{\AA}$.

The Spectropolarimetric Reduction software (SPRS) developed for reducing spectropolarimetric data, is described. Tasks like eliminating instrumental polarization,

telescope polarization and response corrections are implemented in the software. The SPRS is designed to be versatile, user friendly and compatible with the IRAF image processing package. It is also general enough to be used for reduction of spectropolarimetric data from other instruments.

The preliminary version of the work presented in this Chapter has been published (Chakraborty 1999).

3.1 Introduction

Spectropolarimetry is a very powerful technique which has not been fully exploited in observational astronomy. Measurement of the polarization properties of astronomical sources can provide important diagnostic information not available by direct imaging or spectroscopy. In particular, data on the scattering properties of dust or electrons, and magnetic field strengths, can be collected. The overall geometrical shape and the interior structure of extended scattering objects can also be studied. During the last few decades, the technique has been applied to a number of research fields including quasar emission mechanism (Antonucci et al. 1996), active galaxies (e.g., Miller & Goodrich 1990; Brindle et al. 1990), dust in the SMC (Rodrigues et al. 1997), magnetic white dwarfs (Schmidt et al. 1986), Herbig-Haro objects (Schmidt & Miller 1979), post-AGB reflection nebulae (Schmidt & Cohen 1981; Trammell et al. 1991), cool red variable stars (Boyle et al. 1986), symbiotic stars (Schmid & Schild 1990), Wolf-Rayet stars (McLean et al. 1979), and comets (Perrin & Lamy 1987; Myers & Nordsieck 1984; Chakraborty and Vasundhara *in preparation*).

Despite considerable efforts, astronomical polarimetry remains relatively difficult, partly because of the complexities in data reduction as well as analysis. Estimation and elimination of systematic errors such as instrumental and telescope polarization pose a great difficulty.

The spectropolarimeter described by Miller et al. (1988) using an achromatic half-wave plate and a thin-film polarizing beam-splitter, has a very high efficiency over a somewhat limited wavelength range. The need for dual-beam spectropolarimetry was discussed in their paper. Single-beam polarimetric instruments, which completely throw away one of the cross polarizations, can operate only if the polarization

is modulated at a frequency higher than that at which system parameters change. A modulation frequency of about 10 Hz or higher is normally used to ensure that astronomical seeing changes and guiding errors do not significantly affect the data. The advantage with the dual-beam spectropolarimeter or imaging polarimeter, is that one can apply a differential technique between the two cross polarized beams, to eliminate the sky and instrumental transmissivity. One can also, in an efficient manner, estimate and remove the instrumental polarization during the reduction of spectropolarimetric data (Walsh 1992; di Serego Alighieri 1997).

Most often, the polarimetric optics are fitted onto existing or previously designed spectrographs. This is convenient and cost effective, since the instrument can also serve as a normal astronomical spectrograph. Among the recent spectropolarimeters are those built for the 3m telescope at the Lick Observatory (Miller et al. 1988), the 2.7m telescope at Mount Locke, the 5m telescope at Mount Palomar and the Keck telescope (Goodrich 1991; Goodrich et al. 1995). A multi-mode instrument, namely, FORS with spectropolarimetric capability is now being built for the VLT (Mitsch et al. 1994).

This Chapter, describes a dual-beam, medium resolution, long-slit spectropolarimeter which has been built for the 2.34 m Vainu Bappu Telescope (VBT) of the Indian Institute of Astrophysics (IIA), India, as part of the Ph.D. dissertation. The spectropolarimetric reduction software (SPRS) and its compatibility with IRAF reduction packages are discussed.

3.2 Basic Experiment

Light can be fully described by four parameters known as the Stokes parameters: $I(\lambda)$, the total intensity, $Q(\lambda)$ and $U(\lambda)$ describing linear polarization, and $V(\lambda)$, describing circular polarization.

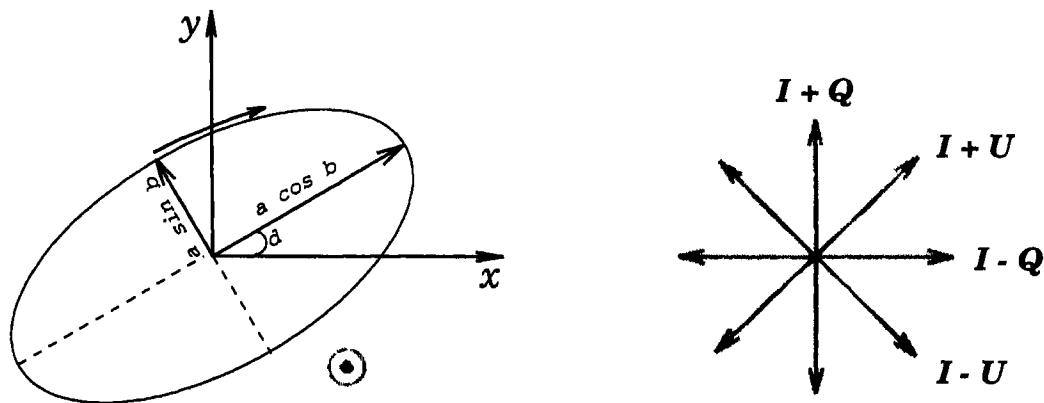


Figure 3.1: Sampling the Stokes vectors. The symbol \odot shows the direction of propagation of the electromagnetic wave and a is the amplitude.

$$I = a^2,$$

$$Q = a^2 \cos(2b) \cos(2d)$$

$$U = a^2 \cos(2b) \sin(2d)$$

$$V = a^2 \sin(2b)$$

To obtain maximum information from light, the task of observational astronomy is to study these Stoke's parameters as a function of wavelength λ , their time variability, and the scattering direction, which are important for studies of solar system objects. The magnitude of linear polarization is given by

$$P = \sqrt{(Q^2 + U^2)/I^2}, \quad (3.1)$$

and the position angle of the electric vector is along

$$\Theta = 0.5 \times \arctan(U/Q). \quad (3.2)$$

To measure Q and U , the wavefront needs to be sampled at different angles through an analyzer. To achieve this, one could either (a) rotate the analyzer or (b) rotate the incoming wavefront relative to the analyzer. Due to physical constraints, especially in dual beam polarimeters, the latter is generally adopted in modern polarimeters. Rotation of the incoming wavefront relative to the analyzer is possible with a wave retarder like a half-wave plate (HWP). A simple HWP is wavelength dependent.

Pancharatnam (1955) demonstrated construction of an achromatic wave plate by stacking three normal HWPs together. In the design by Goodrich (1991), a stack of such achromatic HWPs, made from quartz and magnesium fluoride (MgF_2) were used in the Pancharatnam configuration to obtain a superachromatic performance. In the present design, we use a superachromatic HWP and a polarizing modified Glan-Taylor prism (MGTP) as a dual-beam analyzer to measure Q and U to determine the linear polarization.

3.3 Instrumentation

The long slit Cassegrain spectrograph built by the Boller & Chivens Division of the Perkin-Elmer Corporation, USA for the Anglo-Australian Observatory (AAO), was acquired by IIA in 1985. After acquisition, the spectrograph camera was replaced with a Carl Zeiss camera of 110 mm aperture and 150 mm focal distance. The camera is a semi-solid Schmidt-Cassegrain system so that a CCD could be used as a detector. The field is flattened and corrected for an angular field of $\pm 5^\circ$; A TK1024 Photometrics liquid N_2 cooled CCD is now used as detector. An intensified CCD in video-mode is used for remote slit guiding.

The spectropolarimeter, was designed as an add-on equipment to this spectrograph. Fig. 3.2 shows the optical layout of the spectrograph. To allow the dual polarized beams, the spectrograph shutter was replaced by a larger shutter of 63.5 mm aperture. The spectropolarimeter is now remotely operated from a 66 MHz Intel-486 Personal Computer in the console room.

The polarimetric optics consisting of the HWP and the MGTP, follow closely the design by Goodrich (1991). Three plates of single MgF_2 and three plates of crystal quartz, cemented with UV transmitting Sylgard elastomer constitutes the superachromatic HWP, optimized for 3500 to 10000Å (see *Appendix A.1*). It has a diameter of 28.6 mm and has no anti-reflection coating.

The MGTP, with a 10 mm clear aperture, is made of A-grade calcite, without anti-reflection coating. The MGTP separates the cross polarization into two beams (*ordinary* and *extraordinary*), parallel to each other and separated by 11.86 mm. The ray diagram through the MGTP in Fig. 3.3 shows schematically how the par-

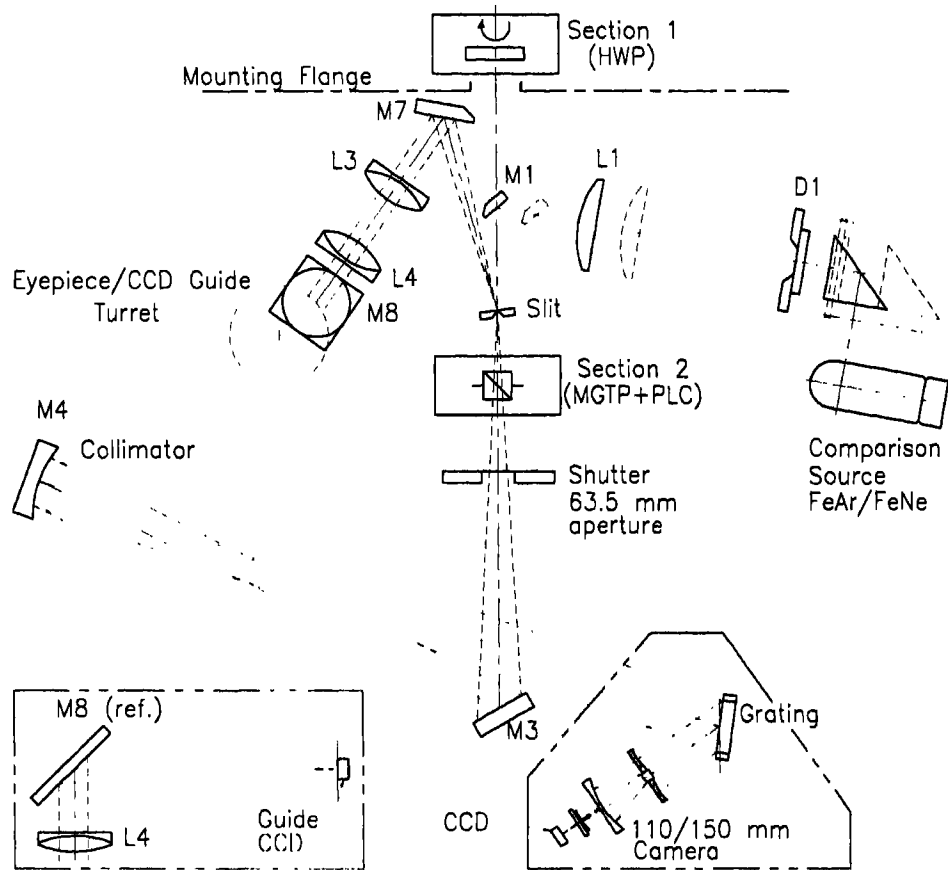


Figure 3.2: The optical layout of the Boller & Chivens spectrograph. M_3 is a flat folding mirror. Original drawing Courtesy, Dr. Greg Smith, Mech. & Opt. Design Group, AAO. The drawing has been modified to the present spectropolarimetric set up.

allel output beams are achieved. A path length compensator (PLC) is required on the *extraordinary* beam, so that both beams could be collimated by the same collimator. Extinction of the dual output beam is specified to be $\approx 10^{-4}$.

The PLC is a right rectangular prism of fused quartz with a 10 mm clear aperture and with a thickness of 19.845 mm. The entrance and exit surfaces have been polished to a high accuracy.

Sizes and position of the three optical components (HWP, MGTP, PLC) are optimized to accept the $f/13$ beam of the telescope. The optical elements were custom built to our specifications by Karl Lambrecht Corporation, Chicago, U.S.A. The lab test of these optics are provided in *Appendix A*.

The polarimetric optics is mounted on to the spectrograph in two separate sections. *Section-1* is attached at the top of the spectrograph flange, protruding through the

central hole of the telescope's instrument mounting flange, while *Section-2* replaces the existing filter wheel of the spectrograph (Fig. 3.2). Fig. 3.3 gives a sketch of these attachments (not to scale) with reference to the spectrograph slit.

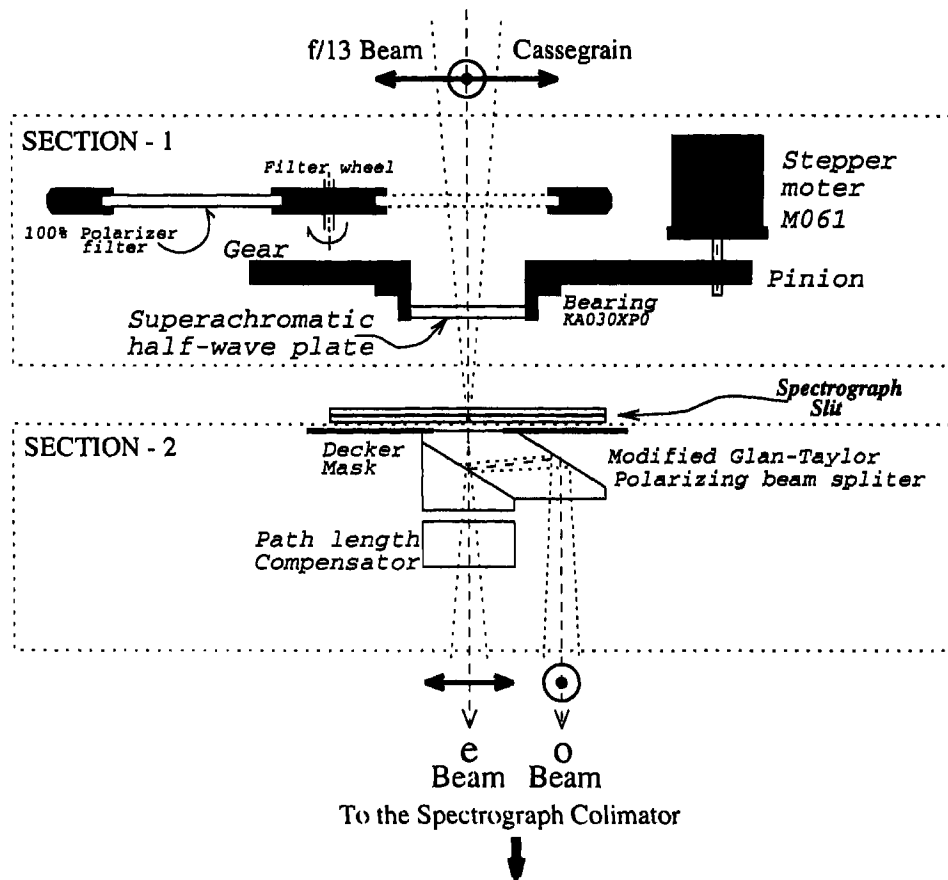


Figure 3.3: Sketch of the two Sections mounted on to the spectrograph to convert it to a spectropolarimeter (Figure not to Scale). Section-1 contains the HWP and Section-2 houses the MGTP + PLC assembly.

3.3.1 Section-1 – Mount for the Wavefront Rotator

The HWP is mounted centered on the optical axis. The mount is designed to keep it very close to the slit of the spectrograph to avoid vignetting. The HWP mount is attached to a 1:4 spur gear unit with anti-backlash tension spring mountings. The gear is fixed on a *KA030XP0* slim bearing supplied by Kaydon Corp., USA. This provides practically no axial deflection to the HWP during its rotation around the optical axis. The pinion is coupled to a stepper motor *M061FD08*, “Slo-syn” Warner electric, USA. The stepper motor torque is overrated by 10 times.

For moving the HWP by an angle¹ $\alpha/2$, the exact number of pulses provided to the stepper motor is

$$n_{\alpha} = \text{Integer of } \left(4 \times \frac{\alpha/2}{1.8} \right), \quad (3.3)$$

where 4 is the gear ratio and 1.8 is the step angle of the stepper motor. The rotational accuracy of the HWP, in the worst case when α is not a multiple of 0.9, is 0.45, which is the rounding-off error ($(\sigma_{\alpha})_r \leq 0.45$). Driving the stepper motor by providing exact number of pulses, has been found to be extremely reliable. However, as a further check, the position angle of the HWP, is read by a 4-bit absolute encoder with 4 binary coded limit switches at 16 positions of the HWP. This encoder signals back the position angle of the HWP at intervals of 22.5 to the instrument control computer. An extra limit switch is provided on the encoder to reset the HWP to zero position by resetting the gear. Though higher precision (10bit) absolute encoders are available off the shelf, we chose to tailor make our encoder for the following reasons. The encoder is used only for cross-checking the angle moved and does not play any role in the actual movement of the HWP. Secondly, due to constraints in available space, the encoder has to be compact and a compact 10 bit encoder is extremely expensive.

During an exposure, the HWP is held fixed by keeping the stepper motor energized. A filter wheel with a free-hole for normal observations and a stack of linear polarizing filters for on-line calibration (Section 3.6), is provided in front of the HWP.

3.3.2 Section-2 – Mount for the Polarimetric Analyzer

The order separating filter wheel of the spectrograph has been modified for mounting the polarimetric analyzing unit, consisting of the MGTP coupled with the PLC. A horizontal movement of this unit, along the length of the slit, has been provided for fine adjustments across the optical axis of the spectrograph. Precise leveling of the moving optics was ensured by accurate surfacing. The wheel is locked into position through a notch and a spring loaded ball. The 10 mm aperture at the entrance of the MGTP, along the slit, has been masked on either side by about 1 mm, with

¹As per the convention, the rotation of the HWP is expressed as $\alpha/2$ because the incoming wavefront through the HWP is rotated by twice this angle.

a decenter mask. This restricts the slit length to 8 mm or 48 *arcsec*. The masking is necessary to ensure that the diverging $f/13$ beam does not hit the sides of the MGTP or the PLC.

The PLC is held pressed to the on-axis exit of the MGTP. To avoid fringing, an optical oil drop with a refractive index of 1.5150 ± 0.0002 at 5875.618\AA was used between the MGTP and PLC. Normal spectroscopic observations can also be conducted by rotating the wheel to permit an order separating filter or an empty slot across the optical axis instead of the polarimetric unit.

A *He - Ne* Laser was used for alignment of these optical elements on to the spectrograph and tests with the telescope were performed. The final mechanical components were surface treated with electro-blackening to minimize internal scattering in the instrument. Detailed engineering drawings of these Mechanical components are provided in *Appendix C*.

3.4 Instrument Control

The existing instrument controls at the VBT have been used with minimal modifications for driving the spectropolarimeter. The spectropolarimeter is remotely commanded by a 66 MHz *PC*, and runs on *PASCAL* codes, specifically developed by Ravi et al. (1999) (see *Appendix D.1*).

The instrument control programs and the data acquisition software are installed on separate computers. This permits simultaneous operation of the instrument and data acquisition. Cross-communication between the two computers is achieved by sensing the spectropolarimeter shutter by the instrument control computer, while the shutter itself is operated by the data acquisition computer during exposures. Each time the shutter closes after an exposure is over, it is sensed and the HWP is rotated to the next instrument setting. This instrument movement is completed by the time the data is being transferred from the CCD to the data acquisition computer for display and storage. The macro routine which controls the data acquisition sequence, ensures that the next set of data acquisition with the new instrument setting is automatically initiated as soon as the previous data is saved. Thus for example, the required four observations with HWP position 0° , $22^\circ 5'$, 45° and $67^\circ 5'$ ($\alpha = 0^\circ, 45^\circ,$

90°, and 135°) are initiated through a single macro command. The advantage with such an automation is that time between the exposures is not wasted in typing the same sets of commands and ensures quick succession of data acquisition.

3.5 Depolarization of the Dome/Sky Flats

The spectropolarimetric data set must be flat fielded like conventional spectroscopic data, in order to correct for the pixel to pixel response variations on the CCD. Both sky and dome flats are intrinsically polarized, although in the latter case lower polarization levels can be achieved by illuminating the dome-flat surface from all sides as isotropically as possible. Hence, it is necessary to depolarize the incoming light. However, a perfect depolarizer does not exist, and can only be approximated by pseudo-depolarizers, for which the outgoing radiation is unpolarized only if it is averaged over some wavelength range λ , a period of time t , an area A or position angle Θ . The Mueller matrix definition of such a depolarizer is (Billings 1951):

$$[D] = \int \int \int \int [M(\lambda, t, A, \Theta)] .d\lambda .dt .dA .d\Theta = \begin{bmatrix} d_{11} & 0 & 0 & 0 \\ 0 & 0 & 0 & 0 \\ 0 & 0 & 0 & 0 \\ 0 & 0 & 0 & 0 \end{bmatrix} \quad (3.4)$$

where $[D]$ is the average Mueller matrix for depolarizer and $[M(\lambda, t, A, \Theta)]$ is the Mueller matrix of the component to be used for depolarization. In spectropolarimetry, an integration over wavelength λ is ruled out. To preserve the spatial information of the flat, an integration over A is also ruled out. Hence we adopt an averaging over t and Θ .

The HWP is made to rotate at a rate of 9.375 half-revolution/min continuously during the exposure. Using a 300l/mm grating, an exposure time of ≈ 1.5 min is required to obtain a dome-flat with good S/N . An average of 14.063 half-revolution is thus possible per exposure. To improve this number, a macro for continuous acquisition of about 30 exposures while the HWP is kept in rotation, has been written and tested. This effectively increases the average to 421.82 half-revolutions. A similar technique of depolarizing dome-flat has also been described by di Serego Alighieri (1997).

Thus, delinking the instrument control computer from the data acquisition computer permits automation during data acquisition as well as depolarization during dome flat acquisition.

3.6 Calibrations with a 100 % Linearly Polarized Source

The spectropolarimeter was calibrated with 100 % linearly polarized light. Variation of the polarization response and the zero point offset of the position angle of polarization with wavelength were obtained.

White light from a 12V 50W halogen lamp was first dispersed through a ground glass and then collimated with a Zenith $f=58$ mm camera lens. This collimated beam was passed through a polarizing prism to obtain the 100 % linearly polarized light. This polarized light was then passed through a pinhole aperture, which acted as a point source object. The pinhole is then imaged on the slit using another Zenith camera lens ($f=80$ mm) with the required aperture of $f/4.66$ to simulate the telescope's $f/13$ beam. Since the distance from the lens to the slit was constrained at 169.3 mm, the pinhole aperture was placed at a distance of 151.7 mm from the lens so that it could be in focused on to the slit (Fig. 3.4).

Spectropolarimetric data of this 100% polarized source were acquired at $\alpha = (0^\circ, 45^\circ, 90^\circ, 135^\circ)$. The spectrograph slit-width was kept at $800\mu m$ corresponding to a resolution of approximately 15\AA . Using this data, $P_c(\lambda)$, the linear polarization response of the spectropolarimeter (Fig. 3.5a) and $\Theta_c(\lambda)$, the zero point offset of the position angle of polarization (Fig. 3.5b), were estimated using Eqs. 3.8 to 3.18. Though the spectropolarimeter with the superachromatic HWP has a uniform polarization response over 4500 to 7500 \AA , the trade off is in the angle $\Theta_c(\lambda)$, which has a variation of approximately $\pm 2^\circ$. The curve in Fig. 3.5b has been zero offsetted by $\Theta_0 = \Theta_c(6000\text{\AA})$. The scatter in $P_c(\lambda)$ and $\Theta_c(\lambda)$ at $\lambda < 4500\text{\AA}$ is due to photon noise error. These two curves are used for correcting the instrumental response of the spectropolarimeter as discussed in the next section.

An on-line calibration check can be obtained, by observing a bright star through the

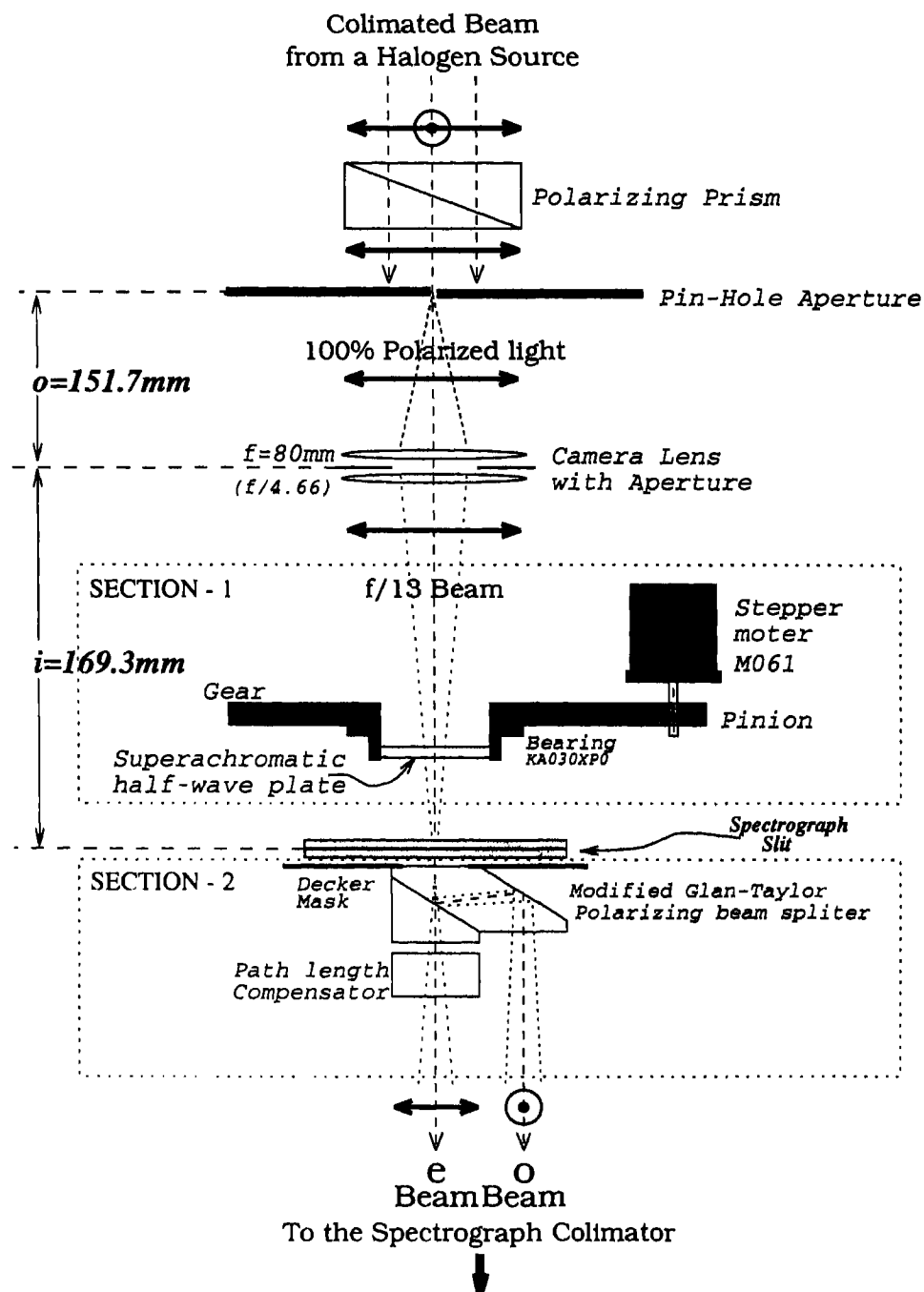


Figure 3.4: The Experimental setup for the calibration with a 100 % polarized source. The polarimetric attachments to the spectrograph, is integrated with Section-1 and Section-2 (Fig. 3.3) (Figure not to Scale).

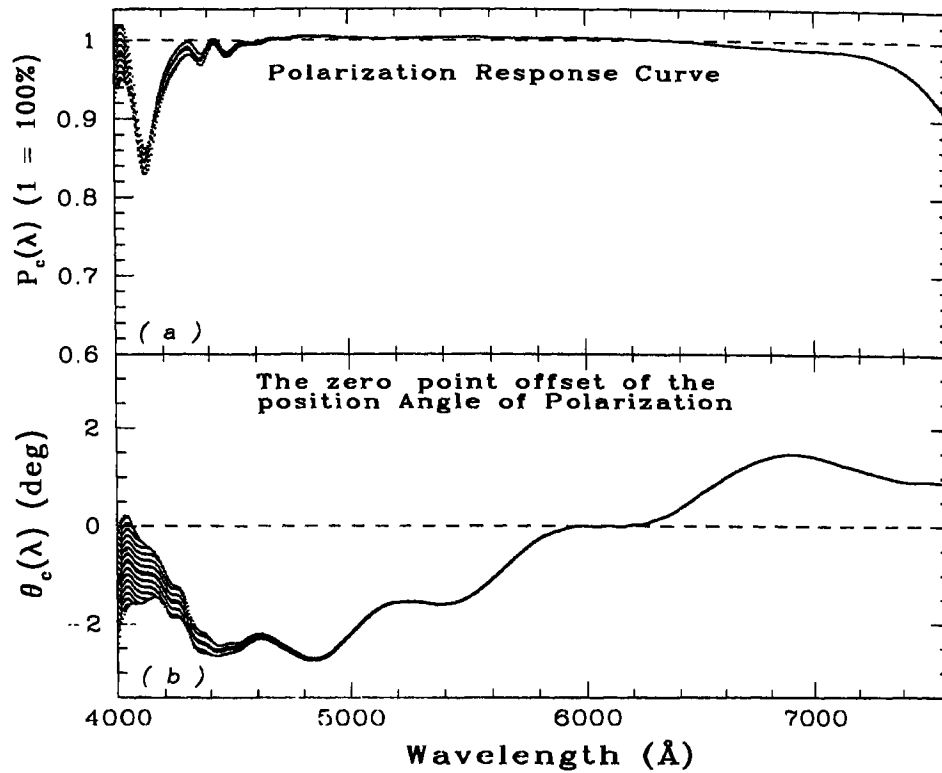


Figure 3.5: Variation of the polarization response and the zero point offset of the position angle of polarization with wavelength of the spectropolarimeter.

linear polarizing filters placed above the HWP as described in *Section 3.3*. However, characterizing the instrument is recommended at least once before an observing season, using white light and the polarizing prism, which has a much higher efficiency than the stack of polarizing filters.

3.7 Analysis and Methodology

Analysis of the spectropolarimetric data demands extreme care mainly because the data is contaminated by large instrumental polarization introduced by the telescope and the asymmetric reflections in the spectrograph. The polarization introduced by these sources are however systematic, and can therefore be estimated as described in the following sections.

3.7.1 Estimation and Elimination of Telescope and Instrumental Polarization

State of polarization of the incoming light received by the detector can be represented as the Stokes vector $\vec{S}_{\text{obs}}(\lambda)$, and can be written as

$$\vec{S}_{\text{obs}}(\lambda) = s_0 + \vec{M}_i(\lambda) \cdot [\vec{S}_{\text{dome}}(\lambda) + \vec{M}_t(\lambda) \cdot (\vec{S}(\lambda) + \vec{S}_b(\lambda))], \quad (3.5)$$

where s_0 is the electronic zero-point error. $\vec{S}_{\text{dome}}(\lambda)$ is the Stokes vector representing the stray radiations that bypass the telescope. $\vec{M}_i(\lambda)$ is the Mueller matrix for the instrumental polarization. $\vec{S}(\lambda)$ and $\vec{S}_b(\lambda)$ are the Stokes vectors for the source and background respectively. $\vec{M}_t(\lambda)$ is the Mueller matrix for telescope polarization. The instrumental polarization due to the telescope should ideally cancel out as it is in Cassegrain mode and has symmetrical optics. The matrix $\vec{M}_t(\lambda)$ should in principle be unitary. However, in practice, a finite telescope polarization is observed due to asymmetric defects, non-uniform aluminization and dust on the primary and secondary mirrors.

Eq. 3.5 looks complicated as such, but fortunately many elements of the matrices vanish or can be parameterized. Proper bias correction will remove s_0 . For estimating $\vec{M}_i(\lambda) \cdot \vec{S}_{\text{dome}}(\lambda)$, we pointed the telescope to the bright moonlit sky close to the moon with the primary mirror flaps of the telescope closed. Moonlight scattered from the telescope dome and the telescope body, that bypassed the telescope's primary mirror, were recorded. The observations of the same region of the sky was then repeated with the primary mirror flaps open to get $\vec{S}_b(\lambda)$. We found $\vec{S}_{\text{dome}}(\lambda)$ to be below the photon noise level of the sky, and therefore, in the present case this can be neglected in comparison with $\vec{S}_b(\lambda)$. Hence after bias subtraction *Eq. 3.5* reduces to

$$\vec{S}'_{\text{obs}}(\lambda) = \vec{M}_i(\lambda) \cdot \vec{M}_t(\lambda) \cdot [\vec{S}(\lambda) + \vec{S}_b(\lambda)] \quad (3.6)$$

Proper sky subtraction from each of these Stokes spectra will eliminate $\vec{M}_i(\lambda) \cdot \vec{M}_t(\lambda) \cdot \vec{S}_b(\lambda)$, after which the equation finally reduces to:

$$\vec{S}''_{\text{obs}}(\lambda) = \vec{M}_i(\lambda) \cdot \vec{S}_1(\lambda), \quad (3.7)$$

where $\vec{S}_1(\lambda) \equiv \vec{M}_t(\lambda) \cdot \vec{S}(\lambda)$. The Mueller matrices $\vec{M}_i(\lambda)$ and $\vec{M}_t(\lambda)$ can be parameterized and estimated as shown below.

3.7.1.1 Correction for Instrumental Polarization $\vec{M}_i(\lambda)$

The light from the object is separated into *ordinary* and *extraordinary* rays by the MGTP. As the two rays travel through the spectrograph, (folding Mirror, Collimator and Grating) their intensities are affected differently due to dependence of the response of the spectrograph optics on the state of polarization of the light. However, since the *ordinary* and the *extraordinary* beams are already separated, polarization cross-talk is eliminated. The Mueller matrix $\vec{M}_i(\lambda)$ reduces to a simple gain factor $G(\lambda)$ and transmission factor $T(\lambda)$. Elegant methods have been devised by various authors to cancel out these factors. We adopt the method described by Walsh (1992), and di Serego Alighieri (1997), as explained below.

With the HWP at $\alpha = 0^\circ$ the *ordinary* $L_0^o(\lambda)$ and the *extraordinary* $L_0^e(\lambda)$ spectra of a given source are:

$$\begin{aligned} L_0^o(\lambda) &= \frac{1}{2}(I(\lambda) + Q(\lambda)) \cdot G_o(\lambda) \cdot T_0(\lambda), \\ L_0^e(\lambda) &= \frac{1}{2}(I(\lambda) - Q(\lambda)) \cdot G_e(\lambda) \cdot T_0(\lambda), \end{aligned} \quad (3.8)$$

where $G_o(\lambda)$ and $G_e(\lambda)$ are the gains of the instrument after the MGTP for the *ordinary* and the *extraordinary* beam respectively and T_0 is the transmission of the sky and the instrument before the MGTP during the exposure at $\alpha = 0^\circ$. Similarly, with the HWP at $\alpha = 90^\circ$ we get, the $L_{90}^o(\lambda)$ and $L_{90}^e(\lambda)$ spectra:

$$\begin{aligned} L_{90}^o(\lambda) &= \frac{1}{2}(I(\lambda) - Q(\lambda)) \cdot G_o(\lambda) \cdot T_{90}(\lambda), \\ L_{90}^e(\lambda) &= \frac{1}{2}(I(\lambda) + Q(\lambda)) \cdot G_e(\lambda) \cdot T_{90}(\lambda), \end{aligned} \quad (3.9)$$

where T_{90} is the transmission of the sky and the instrument before the MGTP during the exposure for $\alpha = 90^\circ$.

Using these four spectra we compute the square root of the ratio:

$$R_Q(\lambda) = \left[\frac{L_0^o(\lambda)/L_0^e(\lambda)}{L_{90}^o(\lambda)/L_{90}^e(\lambda)} \right]^{\frac{1}{2}} = \left(\frac{I(\lambda) + Q(\lambda)}{I(\lambda) - Q(\lambda)} \right). \quad (3.10)$$

The normalized $Q_n(\lambda)$ Stokes parameter can be calculated from

$$Q_n(\lambda) = \frac{Q(\lambda)}{I(\lambda)} = \frac{R_Q(\lambda) - 1}{R_Q(\lambda) + 1}. \quad (3.11)$$

Similarly, from the exposure with the HWP at $\alpha = 45^\circ$ and $\alpha = 135^\circ$, we compute

$$R_U(\lambda) = \left[\frac{L_{45}^o(\lambda)/L_{45}^e(\lambda)}{L_{135}^o(\lambda)/L_{135}^e(\lambda)} \right]^{\frac{1}{2}}, \quad (3.12)$$

and the normalized Stokes parameter $U_n(\lambda)$,

$$U_n(\lambda) = \frac{U(\lambda)}{I(\lambda)} = \frac{R_U(\lambda) - 1}{R_U(\lambda) + 1}. \quad (3.13)$$

The ratios $R_Q(\lambda)$ and $R_U(\lambda)$ determined from the observed spectra using *Eqs.* 3.10 and 3.12 are free of the different grain factors $G_o(\lambda)$ and $G_e(\lambda)$ for the two beams and the changes in the sky transparency $T_\alpha(\lambda)$ during exposures at $\alpha = 0^\circ, 45^\circ, 90^\circ$ and 135° .

3.7.1.2 Correction for Telescope Polarization $\vec{M}_t(\lambda)$

The procedure, described above, permits estimation of $\vec{S}_1(\lambda)$ from the observed sky and bias subtracted data (*Eq.* 3.7). Theoretical determination of $\vec{M}_t(\lambda)$ for computing $\vec{S}(\lambda)$ from $\vec{S}_1(\lambda)$ is difficult. Hence the correction to the telescope polarization is normally obtained from observations of standard unpolarized stars.

When zero polarized standard polarimetric sources are observed, one generally obtains some significant output in $Q_{n0}(\lambda)$ and $U_{n0}(\lambda)$ due to telescope polarization. For large telescope polarizations, full Mueller matrix treatment is necessary. However, as long as this polarization is small, e.g. in the case of a cassegrain telescope, it can be vectorially added to the true polarization signal of an observed polarized source (Serkowski 1962), hence

$$\begin{aligned} \vec{Q}_n(\lambda) &= \vec{Q}_{n1}(\lambda) - \vec{Q}_{n0}(\lambda), \\ \vec{U}_n(\lambda) &= \vec{U}_{n1}(\lambda) - \vec{U}_{n0}(\lambda), \end{aligned} \quad (3.14)$$

where $\vec{Q}_{n1}(\lambda)$ and $\vec{U}_{n1}(\lambda)$ are the normalized Stokes vector obtained from observations of the polarized object and $\vec{Q}_{n0}(\lambda)$ and $\vec{U}_{n0}(\lambda)$ are the normalized Stokes vector obtained from observations of unpolarized stars.

The linear polarization $P(\lambda)$ and position angle $\Theta(\lambda)$ are given by,

$$P(\lambda) = \sqrt{Q_n^2(\lambda) + U_n^2(\lambda) - \sigma_P^2(\lambda)}, \quad (3.15)$$

$$\Theta = 0.5 \times \arctan(U(\lambda)/Q(\lambda)), \quad (3.16)$$

where,

$$\sigma_P(\lambda) = \begin{cases} \sqrt{2}\epsilon(\lambda) & \text{for } P \approx 0 \\ \epsilon(\lambda) & \text{for } P \gg \epsilon(\lambda), \end{cases} \quad (3.17)$$

$$\sigma_\Theta(\lambda) = \begin{cases} 51^\circ.96 & \text{for } P \approx 0 \\ 28^\circ.65 \times \sqrt{\frac{\epsilon^2}{Q_n^2 + U_n^2}} & \text{for } P \gg \epsilon(\lambda), \end{cases} \quad (3.18)$$

$$\epsilon(\lambda) = \sqrt{\frac{(Q_n(\lambda)\sigma_Q(\lambda))^2 + (U_n(\lambda)\sigma_U(\lambda))^2}{Q_n^2(\lambda) + U_n^2(\lambda)}}.$$

It is necessary to subtract σ_P from P in quadrature in Eq. 3.15, since P is a statistical quantity and the measured value is the most probable value (Serkowski 1962).

3.7.2 Correction for Instrumental Response

Finally, correction for the instrumental response was applied using the polarization efficiency $P_c(\lambda)$ of the spectropolarimeter and the zero-point offset $\Theta_c(\lambda)$ described in *Section 3.6*. The true polarization of the source and the position angle are

$$\begin{aligned} P(\lambda) &= P(\lambda)/P_c(\lambda) \\ \Theta(\lambda) &= \Theta(\lambda) - \Theta_c(\lambda) + \Theta_0 \end{aligned} \quad (3.19)$$

Θ_0 is a constant zero-point offset due to misalignment between the instrument's zero-point and the celestial North. Polarized standards with well determined position angles are observed to estimate Θ_0 .

After calibration of $P(\lambda)$ and $\Theta(\lambda)$ using Eq. 3.19, the stokes vectors $Q_n(\lambda)$ and $U_n(\lambda)$ can be recomputed.

$$\begin{aligned} Q_n(\lambda) &= P(\lambda) \cos[2\Theta(\lambda)] \\ U_n(\lambda) &= P(\lambda) \sin[2\Theta(\lambda)] \end{aligned} \quad (3.20)$$

3.8 Spectropolarimetric Reduction Software

A SpectroPolarimetric data Reduction Software (SPRS) was written to carry out the computations using Eqs.3.8 to 3.20. To make the software a general one, it has been designed as a task completely compatible with IRAF. The code has been written in Fortran-77 using “*IMFORT*” calls. This enables the code to access the data directly in IRAF data format. The code has been embedded into an IRAF *script*. The “*task*” command in IRAF has been used to define it as a new IRAF task “*spolari*”. The parameters in “*spolari*” can be changed using the standard “*epar spolari*” command in IRAF. “*Spolari*” accepts the four spectra (L_0 , L_{45} , L_{90} and L_{135}) in “*multispec*” format of IRAF. Each spectrum contains two apertures for *ordinary* and *extraordinary* beams.

With appropriate parameter selections using *epar*, the same package is also used for determining Instrumental response $P_c(\lambda)$ and $\Theta_c(\lambda)$ from a 100% polarized source, and the telescope polarization $Q_0(\lambda)$ and $U_0(\lambda)$ from an unpolarized star (Eqs.3.8 to 3.13).

The salient features of the package are given in Table 3.1. Most of these features can be individually controlled using appropriate boolean flags and constants using *epar*.

For basic pre-processing, like the bias and flat-field corrections, image reduction packages in IRAF can be used. During extraction of the spectra, the versatile spectroscopic reduction packages in IRAF are fully exploited. The “*apall*” task in the “*specred*” package of IRAF, provides functions for defining, modifying, tracing, and extracting apertures from two dimensional spectra. The task also performs background subtraction, and computes the Poisson noise statistical error on the spectra.

A “*multispec*” format is used for the extraction of *ordinary* and *extraordinary* spectra as a single two aperture data file with multiple bands for each aperture. The computed Poisson noise statistical error for each spectra is stored by the *apall* package, along with its respective aperture in a separate band in the file (See “*help apall*” in IRAF). Wavelength calibration of the extracted spectra are performed using the tasks in the “*specred*” packages of IRAF.

- a. Median smooth L_α
(The number of pixels for smoothing can be defined through *epar*).
- b. Compute Instrumental Response $P_c(\lambda)$ and $\Theta_c(\lambda)$ (Fig. 3.5)
(Eqs.3.8 to 3.13) and (Eqs.3.15 to 3.18).
- c. Compute Telescope Polarization $Q_0(\lambda)$ and $U_0(\lambda)$ from an unpolarized star
(Fig. 3.6). (Eqs.3.8 to 3.13).
- d. Compute $Q_{n1}(\lambda)$ and $U_{n1}(\lambda)$ of the program object (Eqs.3.8 to 3.13).
- e. Perform Telescope Polarization Correction (Eq.3.14).
- f. Compute the respective propagated errors from the photon noise errors in
the four input spectra L_α (Eqs.3.17 & 3.18).
- g. Calculate $P(\lambda)$ and $\Theta(\lambda)$ of the program object (Eqs.3.15 & 3.16) .
- h. Perform Instrumental Response Correction (Eq.3.19).
- i. Add a constant Offset angle to $\Theta(\lambda)$ for Zero Offset angle Correction
 $\Theta(\lambda) + \Theta_0$.
- j. Recompute $Q_n(\lambda)$ and $U_n(\lambda)$ after Instrumental Response Correction on
 $P(\lambda)$ and $\Theta(\lambda)$ are performed (Eq.3.20).

Table 3.1: Features of *SPRS* (SpectroPolarimetric Reduction Software)

To perform wavelength calibration, dual aperture comparison spectra are extracted using the object image as the reference image. Each aperture is individually identified on the comparison spectra to eliminate the small misalignment between the *ordinary* and *extraordinary* beams. However, during dispersion correction, same dispersion is applied to both apertures so that both apertures have the same number of data-points (pixels), starting wavelength and wavelength interval per pixel. This is extremely essential for precise wavelength alignment during computations using *SPRS*.

The output file of the *SPRS* is a 5 apertures 2 bands spectra. Table(3.2) shows the content of each apertures and its bands.

Ap	Band	
	1	2
1	Total Flux $F(\lambda)$	Error: $\sigma_F(\lambda)$
2	Stokes parameter $Q_n(\lambda)$	Error: $\sigma_Q(\lambda)$
3	Stokes parameter $U_n(\lambda)$	Error: $\sigma_U(\lambda)$
4	Polarization $P(\lambda)$	Error: $\sigma_P(\lambda)$
5	Angle $\Theta(\lambda)$	Error: $\sigma_\Theta(\lambda)$

Table 3.2: Output file of SPRS; 5 Apertures, 2 Bands.

The output spectra stores $P(\lambda)$ as $1 \equiv 100\%$ and $\Theta(\lambda)$, in degrees.

Since the instrumental response (Table 3.1,task b) and the telescope polarization file (Table 3.1,task c) are computed using “*spolari*”, they are precisely in the same format as the output-file. $Q_0(\lambda)$ and $U_0(\lambda)$ are automatically read from apertures 2 and 3 respectively, from the telescope polarization file. $P_c(\lambda)$ and $\Theta_c(\lambda)$ are read from apertures 4 and 5 respectively, from the instrumental response file.

The total flux

$$\begin{aligned}
 F(\lambda) = & L_0^o(\lambda) + L_0^e(\lambda) + L_{45}^o(\lambda) + L_{45}^e(\lambda) \\
 & + L_{90}^o(\lambda) + L_{90}^e(\lambda) + L_{135}^o(\lambda) + L_{135}^e(\lambda), \quad (3.21)
 \end{aligned}$$

can be used for spectrophotometric investigation, after correction for instrumental response and sky extinction, by using spectrophotometric standard stars, observed through the same instrument.

Spectropolarimetric Reduction Software has been successfully tested and used for reduction of the data obtained by the medium resolution spectropolarimeter.

3.9 Performance

Spectropolarimetric observations of Comet Hale-Bopp and comet Wild 2 and Polarimetric Standards, have been made using this instrument at the VBT. This work is presented in *Chapter 5* (Pavan Chakraborty & R. Vasundhara *in preparation*).

Here we present the results of only a few polarimetric standards observed on 6th and 7th March 1999 to evaluate the performance of the instrument. Multiple sets of observations were made of polarized stars selected from Hsu & Breger (1982) and

POLARIZED STANDARD

Star Name	Spectral Type	N	M_V mag	λ_{max} Å	P_{max} %	Θ_v ♣ (1985) (deg)
HD 147084 (<i>o Sco</i>)	A5 II	8	4.54	6950 ± 60 †	4.46 ± 0.03 †	32.2 ± 0.1
HD 43384 (9 Gem)	B3 Ia	3	6.27	5310 ± 110 † 5498 ± 17 ‡	3.01 ± 0.04 † 3.50 ± 0.06 ‡	169.8 ± 0.7

UNPOLARIZED STANDARD

Star Name	Spectral Type	N	M_V mag	Filter	P_B ♠ %
HD 47105 (<i>γ Gem</i>)	A0 V	5	1.9	B	0.076 ± 0.020
HD 127762 (<i>γ Boo</i>)	A7 III	8	3.0	B	0.002 ± 0.018

Table 3.3: Observed polarized and unpolarized standards on 6th and 7th March 1999.

N is the number of sets of Observations.

♣ Θ_v is the equatorial position angle in V filter (Hsu & Breger 1982).

♠ P_B is the percent polarization in the B filter Turnshek et al. 1990).

† (Hsu & Breger 1982). ‡ This work.

unpolarized stars from Turnshek et al. (1990). A 300l/mm grating (blazed at 5000Å) with a slit-width of 350μm was used to yield a spectral range from approximately 4000 to 7500Å with a resolution of approximately 7.2Å. Table(3.3) gives the log of the observations, and published polarimetric result of the stars by Hsu & Breger (1982) and Turnshek et al. (1990).

The basic pre-processing of the data was done with IRAF. The SPRS (*Section 3.8*) was used with 3 pixel smoothening. First, $Q_{n0}(\lambda)$ and $U_{n0}(\lambda)$ were computed for each set of unpolarized stars. From a total of 5 + 8 = 13 sets, 3 sets were rejected. The output files from the remaining 10 sets were averaged to obtain a master set of $Q_{n0}(\lambda)$ and $U_{n0}(\lambda)$ plotted as the crowded sets of points in Fig. 3.6. A continuum fit of $Q_{n0}(\lambda)$ and $U_{n0}(\lambda)$ was made using a 15-order spline 3 to remove the glitches due to larger photon noise at the stellar absorption lines. The thick central lines in Fig. 3.6 are the spline fit to the data. The two enveloping lines are at the 1σ

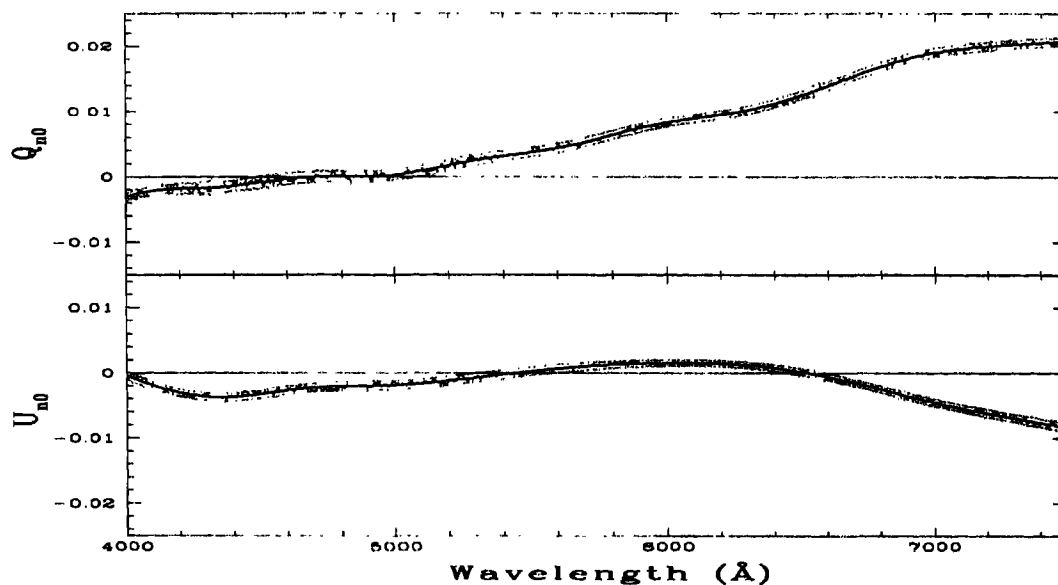


Figure 3.6: Effects of telescope polarization $Q_{n0}(\lambda)$ and $U_{n0}(\lambda)$ measured from the observations of unpolarized standards, on 6th and 7th March 1998. In each case the thick central line is the spline fit to the data. The two enveloping lines are the 1σ propagated errors derived from the photon noise errors in the four input spectra L_α (Eqs.3.17 & 3.18).

propagated errors derived from the photon noise errors in the four input spectra L_α (Eqs.3.17 & 3.18).

The instrumental response curves $P_c(\lambda)$ and $\Theta_c(\lambda)$ (Section 3.6), and the continuum fit for $Q_{n0}(\lambda)$ and $U_{n0}(\lambda)$ were used to obtain $Q_n(\lambda)$, $U_n(\lambda)$, $P(\lambda)$ and $\Theta(\lambda)$ for each set of polarized standard star observations. From 8 sets for the star HD 147084 and 5 sets for the star HD 43384, 1 set each were rejected after close examination of the output files. The remaining sets were averaged to obtain a master sets for each star. Values of $Q_n(\lambda)$, $U_n(\lambda)$, $P(\lambda)$ and $\Theta(\lambda)$ were recomputed using the corresponding master set. It may be noted that the initial S/N improves, by performing averaging on the input files rather than the output file. The percentage of polarization vs wavelength for the two polarized stars are shown in Fig. 3.7(a,b). Filter polarimetry of these stars by Hsu & Breger (1982), have been over-plotted. For HD 147084, our results fits extremely well. For HD 43384, present result show a polarization larger by 0.5%. We attribute this difference to the long term variation in $P(\lambda)$ of 0.25% during 1979-1981 for this star, as reported by Hsu & Breger (1982) and 0.7% during 1969-1971 reported by Coyne (1971). As further check, we fitted our results ($P(\lambda)$ vs λ) of this star using the Levenberg-Marquardt's method (Press et al. 1992)

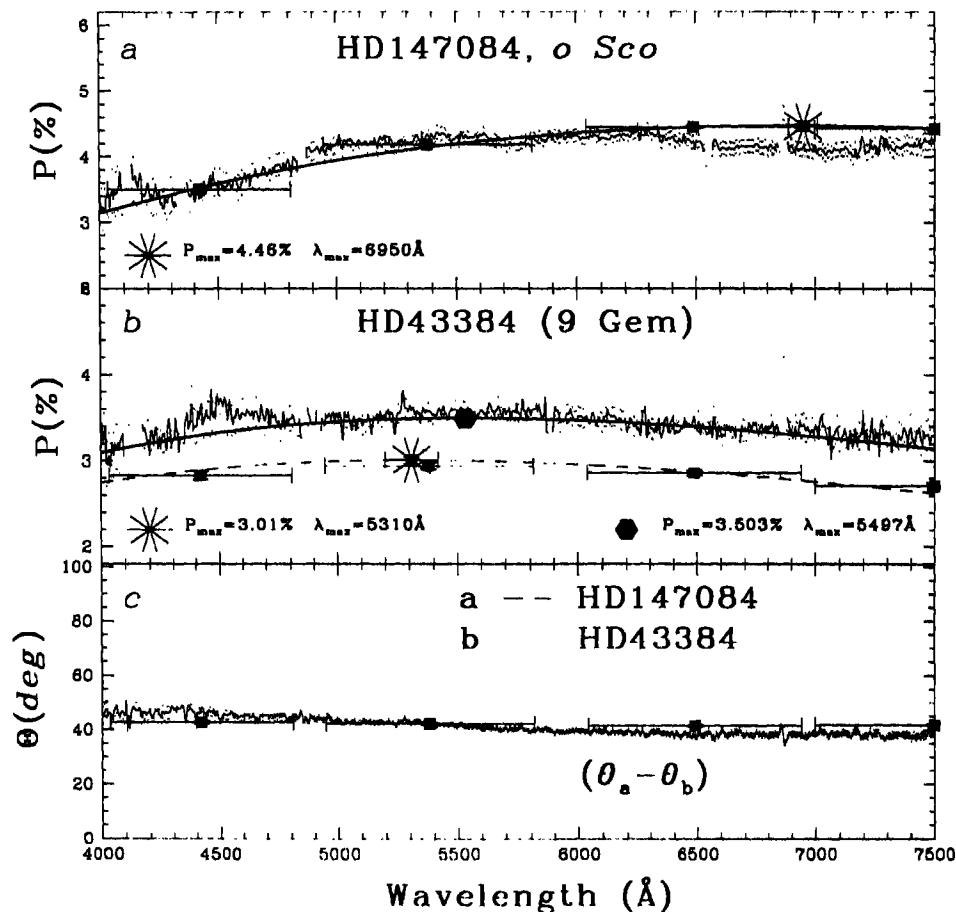


Figure 3.7: Polarization of standard stars. Here we present the result of Polarimetric standards from Hsu & Breger (1982), observed on 6th and 7th March 1998. Filter polarimetry of these stars by Hsu & Breger (1982), for stars (HD 43384 & HD 147084) have been over-plotted (filled squares). Location of the starred symbol and the corresponding curve indicate λ_{max} and the Serkowski (1973)'s relation. For 9 Gem the filled hexagon and the curve; corresponds to the best fitting value of λ_{max} and P_{max} in the present work.

to compute the parameters P_{max} and λ_{max} , in the empirical relation by Serkowski (1973) for the wavelength dependence of polarization due to the interstellar medium given by

$$P(\lambda) = P_{max} \exp[-K \ln^2(\lambda_{max}/\lambda)], \quad (3.22)$$

where $K = 1.15$. The fitted values of P_{max} and λ_{max} given in Table (3.3). The smooth thick curve in Fig. 3.7 shows the fitted curve. The dashed curve indicates the Serkowski's relation using the values of λ_{max} and P_{max} by Hsu & Breger (1982). Our fitted P_{max} is larger by 0.49% compared to the values quoted by Hsu and Breger. Our fitted value of λ_{max} however matches within 200Å. The study of variability of

this star is out of the scope of the present work.

The difference between the observed angles of polarization of both the stars (Fig. 3.7c), compare well with the difference of the values reported by Hsu and Breger (Overplotted in Fig. 3.7c).

3.10 Further Improvements

3.10.1 Instrumentation

The instrument can be used for measurements of circular polarization by replacing the HWP by a superachromatic Quarter wave plate (QWP). The present design of “Section-1” permits such an alteration even during the observations if required.

3.10.2 Reduction Software

The present version of SPRS cannot be directly applied to a long-slit spectropolarimetric observation. However, the software with a little modification can handle a long-slit data as series of $1d$ spectropolarimetric data.

Astronomical observations are often photon starved. Consequently many astronomical spectra have a poor S/N and are considerably corrupted by photon noise. Many sets of observations were averaged and were also subjected to a median smoothening to improve the S/N . Fourier smoothening could also be applied to the data before the application of the SPRS. Fligge & Solanki (1997) have developed a method of noise reduction in astronomical spectra using wavelet packets. The wavelet representation of a signal due to the additional wavelength resolution of the decomposed signal, offers great flexibility in de-noising astronomical spectra compared to the classical Fourier smoothening. Fligge and Solanki’s code when incorporated as a pre-SPRS module, would significantly improve the accuracy of polarization measurements.

References

- Antonucci, R. Geller, R., Goodrich, R. W. and Miller, J. S., 1996. *ApJ* **472**, 502.
- Billings, B. H., 1951. *J. Opt. Soc. Am.* **41**, 966.
- Boyle, R. P., Aspin, C., Coyne, G. V., and McLean, I. S., 1986. *A & A* **164**, 320.
- Brindle, C., Hough, J. H., Bailey, J. A., Axon, D. J., Ward. M. J., Sparcks, W. B. and McLean, I. S., 1990. *MNRAS* **244**, 604.
- Chakraborty, P., 1999. in *International Symposium on Astrophysics Research and Science Education* Ed. Chris Impey, *Sponsored and hosted by the Vatican Observatory*, p. 109.
- di Serego Alighieri, S., 1997. in *Instrumentation for Large Telescopes* Ed. by Rodríguez Espinosa, J. M., Herrero, A. and Sánchez, (Cambridge Contemporary Astrophysics), p.287.
- Fligge, M. and Solanki, S. K., 1997. *A & A Suppl. Ser.* **124**, 579.
- Coyne, G. V., 1971. in *Colloquium on Supergiant Stars*, ed. M. Hack (Trieste: Osservatorio Astronomico Trieste), p.93.
- Goodrich, R. W., 1991. *PASP* **103**, 1314.
- Goodrich, R. W., Cohen, M. H. and Putney, A., 1995. *PASP* **107**, 179.
- Hsu, Jin-Chung and Breger, M., 1982. *ApJ* **262**, 732.
- McLean, I. S., Coyne, G. V., Frecker, J. E. and Serkowski, K., 1979. *ApJ* **231**, L141.
- Miller, J. S. and Goodrich, R. W., 1990. *ApJ* **355**, 456.
- Miller, J. S., Robinson, L. B. and Goodrich, R. W., 1988. in *Instrumentation for Ground-Based Astronomy*. ed. by L.B. Robinson (NewYork, Springer), p.157.
- Mitsch, W., Rupprecht, G., Seifert, W., Nicklas, H. and Kieseewetter, S., 1994. in *SPIE Proceeding Series* **2198**, 213.

- Myers, R. V. and Nordsieck, K.H., 1984. *Icarus* 58 431.
- Pancharatnam, S., 1955. *Proc. Indian Acad. Sci.*, Vol. **XLI**, No. 4, Sec. A, 137.
- Perrin, J.-M. and Lamy, P. L., 1987. in *ESA SP-278, Proc. of the International Symp. on the Diversity and Similarity of Comets*, p.411.
- Press, W. H., Teukolsky, S. A., Vetterling W. T., Flannery, and Flannery, B. P., 1992. *Numerical Recipes in Fortran* (Cambridge University Press)
- Ravi, K., Anbazhagan, P. Rao, S. V., Ramchandran, A., Chakraborty, P., and Gabriel, F., 1999. *VBT Electronic Lab - Technical Report 1999/a*
- Rodrigues, C. V., Magalhães, A. M., Coyne, G. V. and Piirola, V., 1997. *ApJ* **485**, 618.
- Schmid, H. M. and Schild, H., 1990. *A & A* **236**, L13.
- Schmidt, G. D., and Cohen, M., 1981. *ApJ* **246**, 444.
- Schmidt, G. D., and Miller, J. S., 1979. *ApJ* **234**, L191
- Schmidt, G. D., Stockman, H. S. and Grandi, S. A., 1986. *ApJ* **300**, 804.
- Serkowski, K., 1962. *Polarization of Starlight*, in *Advances in Astronomy and Astrophysics*, **1**, 289
- Serkowski, K., 1973. in *IAU Symposium 52, Interstellar Dust and Related Topics*, ed. J. M. Greenberg and H. C. van de Hulst (Dordrecht: Reidel), p.145.
- Trammell, S. R., Dinerstein, H. and Goodrich, R. W., 1991. *BAAS* **23**, 915.
- Turnshek, D. A., Bohlin, R. C., Williamson II, R. L., Lupie, O. L., Koornneef, J. and Morgan, D. H., 1990. *AJ* **99** No.4, 1243.
- Walsh, J. R., 1992. in *4th ESO/ST-ECF Data Analysis Workshop* ed. by P. J. Grosbøl and R.C.E. de Ruijsscher, ESO Conf. and Workshop Proc. No.41, 53

Chapter 4

DUST MODELING OF COMETARY JETS

Jet and shell structures from comet Hale-Bopp during the period September 1996 to October 1997, are modeled using data from the Vainu Bappu Observatory and from the observatory of the Naturwissenschaftlicher Verein Osnabrück. Evolution of jet and shell structures during the period of observations could be attributed to activity from sources near $+65^\circ$, $+35^\circ$, $+5^\circ$, -5° , -35° , -65° in latitude. Although no deliberate attempt was made to place the sources at symmetric latitudes, the best fit shows a remarkable symmetry. Due to changing solar illumination geometry, while only the southern sources were apparently active during 1996, most of the sources appeared active in February 1997 and October 1997. In the 10 April image, under a near pole-on solar illumination, curiously, only the sources at $+65^\circ$, $+5^\circ$ and -5° appear to be active and not the source at $+35^\circ$. Pole positions which gave a reasonably good fit to the observed sets of shells varied from 260° to 290° in right ascension and -50° to -65° in declination.

Around April 10, while the gas production from the equatorial sources is expected to be low due to the near grazing incidence of sunlight, the fractional area of the high latitude source is limited for a spherically symmetric nucleus. To explain the well defined shells due to rotation of the jets, we assume that the source at $+65^\circ$ occupies 10% of the longitude belt and 10° in latitude. Assuming a radius of 35 km for the

comet corresponding to the upper limit of Weaver and Lamy (1997) and Sekanina (1997a), the area of 56 km^2 for this source could account for 29% of the observed total production rate of 4.0×10^{30} molecules/sec by Schleicher *et al.* (1997). The intricate shell patterns during February - May, 1997 could not be exactly replicated using the model of a single nucleus. Complexity of the shell structures can be better explained using the binary model of comet Hale-Bopp suggested by Sekanina (1997b, 1998b) with sizes of 70 km and 30 km across. Approximate estimates of the longitude of the sources active between February and May, 1997 are presented. The lower limits on the dust to gas mass production ratio are estimated to be, 4.8 ± 1.1 , 3.4 ± 1.0 and 6.2 ± 1.3 on 18 February, 10 April and 2 May, 1997 respectively.

The work presented in this Chapter has been published (Vasundhara *et al.* 1997, Chakraborty *et al.* 1998, and Vasundhara and Chakraborty 1998).

4.1 Introduction

Modeling of dust jets and shells from a comet provides information on the orientation of its pole. Inter-separation of the shells due to jets from a given latitude of the comet yields information on the terminal velocity of the ejected grains, which in turn depends on the size, nature and the mass loading of the gas by the dust. In the absence of the knowledge of the nature of the grains, limits on the production rates of the gas and dust can be set (Sekanina 1987, Sekanina and Larson 1984). Sekanina (1996) carried out detailed modeling of the three outburst events of comet Hale-Bopp, which occurred in 1995.

Starting May 1996, several observers reported multiple jets from comet Hale-Bopp. O'Meara *et al.* (1996) reported several secondary jets in August 1996 which gave the comet the "appearance of a porcupine". Sekanina and Boehnhardt (1997a, 1997b) interpreted jet pairs (one pair per source) as the boundaries of fan-shaped formations described by dust ejected from the sources continually between local sunrise and sunset. To explain the observations during May - November, 1996, they proposed two models, one with six sources and a spin axis undergoing a complex motion and another with a fixed spin axis and a large diurnal dust ejection fluctuations for one of the jets. Sekanina (1998a) used Monte Carlo computer simulation to show

that the dust source producing the south westerly halo in the time-resolved image sequences by Jorda *et al.* (1997) is located at $+55^\circ$ and derived the pole positions. Samarasinha *et al.* (1997) constrained the direction of the spin axis of the nucleus referred to the ecliptic. The cometary jets were also modeled using the images of the comet obtained from the Vainu Bappu Observatory (VBO) during October 1996 and October 1997 and 12 images of the comet obtained at the observatory of the Naturwissenschaftlicher Verein Osnabrück during September 1996 - May 1997 to determine the location of the active regions and the pole positions (Vasundhara *et al.* 1997, Chakraborty *et al.* 1998, and Vasundhara and Chakraborty 1998). This Chapter presents these results.

4.2 Observations and Data Processing

The observations (filter imaging) of comet Hale-Bopp were carried out at the prime focus ($f/3.237$) of the 2.34 m Vainu Bappu Telescope (VBT) and at the cassegrain focus ($f/13$) of the 1.02 m telescope at VBO. The detectors used were the TK1024 Photometrics liquid nitrogen cooled CCD at the 2.34 m telescope and the 384×576 Thompson chip Photometrics liquid nitrogen cooled CCD at the 1.02 m telescope (*Chapter 2*). Images taken through R-filter were selected for investigating the dust shells and jets from this comet. Table 4.1 gives the log of these selected observations.

Table 4.1: Journal of Observations from VBO

Date	Time (UT)	Exposure	Telescope	Image Scale arcsec/pixel	Phase Deg
1996 Oct. 06	13:55	20 sec	2.34 m	0.60	19.4
1996 Nov. 04	13:30	30 sec	2.34 m	0.60	16.9
1997 Feb. 18	00:03	2 sec	2.34 m	0.60	35.4
1997 Apr. 10	13:32	7 sec	1.02 m	0.36	43.3
1997 May 02	13:33	20 sec	1.02 m	0.36	29.2
1997 Oct. 09	22:12	10 sec	2.34 m	0.60	18.6

Observations from the observatory of the Naturwissenschaftlicher Verein Osnabrück were made by Dr. A. Hänel and Ervin Heiser with a 60 cm ($f/12.43$) telescope. The detector was a SBIG ST-6 CCD camera that has 375×242 *pixels* (8.6×6.5 mm \equiv

3.9×3.0 arcsec with $f = 7460$ mm) with $23 \times 27\mu$ pixel size. The images were then scaled to quadratic pixels to yield an image size of 319×242 pixels. The March 4, 1997 image was taken with a Shapley lens, with an effective focal length of 423 cm ($f/7.05$). All the images except those on March 31, 1997 and April 15, 1997 (which were through a R filter) were obtained without a filter.

The radial and rotational shift algorithm by Larson and Sekanina (1984) was applied on the Bias and Flat-field corrected images to suppress the strong radial intensity gradient in the coma to enhance smaller fluctuations like the jets and the shells. A rotation of $\pm 10^\circ$ around the comet centroid in the rotational shift algorithm seemed suitable for these images. The images were then scaled over the comet's intensity range saturating the brighter field stars to obtain the best gray scale. These operations were carried out using the IRAF packages and the XV 3.10.

The enhanced white light and R filter images from Osnabrück did not show significant differences in the structures. Further, while modeling the morphology in this chapter, we only model the shapes and separations and not the intensity. The white-light images were considered adequate for this investigation.

4.3 Computation of the Track of the Dust Grains in the Jets

Our computer simulations are based on the basic concepts introduced by Sekanina (1981a, 1981b, 1991) and Sekanina and Larson (1984). The model (Vasundhara 2001) predicts the loci of the dust grains as seen projected on the sky plane relative to the comet at any instant of time. The various stages of computation are explained in the following sections.

4.3.1 Velocity and Acceleration of the Grains

The sources are assumed to emit jets of gas and dust from local sunrise to sunset. Diurnal changes in production rates from the sources are neglected. A mean period of 11.34 hr reported by Licandro *et al.* (1998), which is close to the value of 11.35 ± 0.04 hr reported by Jorda *et al.* (1997) is used in the present analysis. On leaving the

nucleus radially, the dust grains move under the combined force of solar radiation pressure and solar gravity. We neglect the gravitational force of the nucleus. The velocity v_{gr} and acceleration α due to solar radiation pressure depend on the size and nature of the grains and the heliocentric distance. An attempt was made to investigate the composition of the grains using spectropolarimetric data in *Chapter 5* and continuum wavelength images in *Chapter 6*. For investigating the morphology, since the dynamics mainly depends on β , the ratio of the force due to solar radiation pressure on the grain to the gravitational force, we estimated α for a range of β values between 0.03 and 0.6, using the relation:

$$\alpha = \beta g_{sun(1)}/r^2, \quad (4.1)$$

where $g_{sun(1)}$ is the acceleration due to solar gravity at one AU (0.6×10^{-5} km/sec²). Note that r , the distance of the cometary dust grain from the Sun, should be in units of AU.

The velocity attained by the grains by the time the dust and gas get decoupled from each other within a few nuclear radii (Probstein, 1969) was calculated using the empirical relation by Sekanina (1981b):

$$\frac{1}{v_{gr}} = a + \frac{b}{\sqrt{\beta}}, \quad (4.2)$$

where a and b are coefficients which depend on the velocity of the gas driving the dust, dust and gas production rates, nature of the dust grain and the nuclear radius. Sekanina and Larson (1984) have used with success, this equation for dust emission from discrete sources and pointed out that the linear relation between $(1/v_{gr}, 1/\sqrt{\beta})$ in Eq. 4.2 is valid for grains of $\beta \leq 0.6$, for slightly absorbing grains.

4.3.2 The Geometry

In a simulation of the cometary dust jets, it is essential that the dynamics is treated vectorially. Acceleration due to radiation pressure α (Eq. 4.1) is in the Sun-comet direction, while the gravity on the dust particle due to the Sun is in the opposite direction. The initial velocity v_{gr} is radially outward from the comet. To compare the simulation of the cometary dust jets with actual observations on the skyplane, it

is essential that the simulation be represented in a geometry as seen by the observer. The 3-dimensional simulation needs to be mapped and projected on to the sky-plane. The basic steps are given in the following sections. The geometry is shown in Fig. 4.1. The ascending node of the comet's equator on the Earth's equator is N_{equ} and that on the ecliptic is N_{ecl} . The points S and E are the sub-Sun and sub-Earth points respectively and N_C is the comet's north pole. The vector v_{gr} is the ejection velocity of the grain and α the acceleration due to solar radiation pressure.

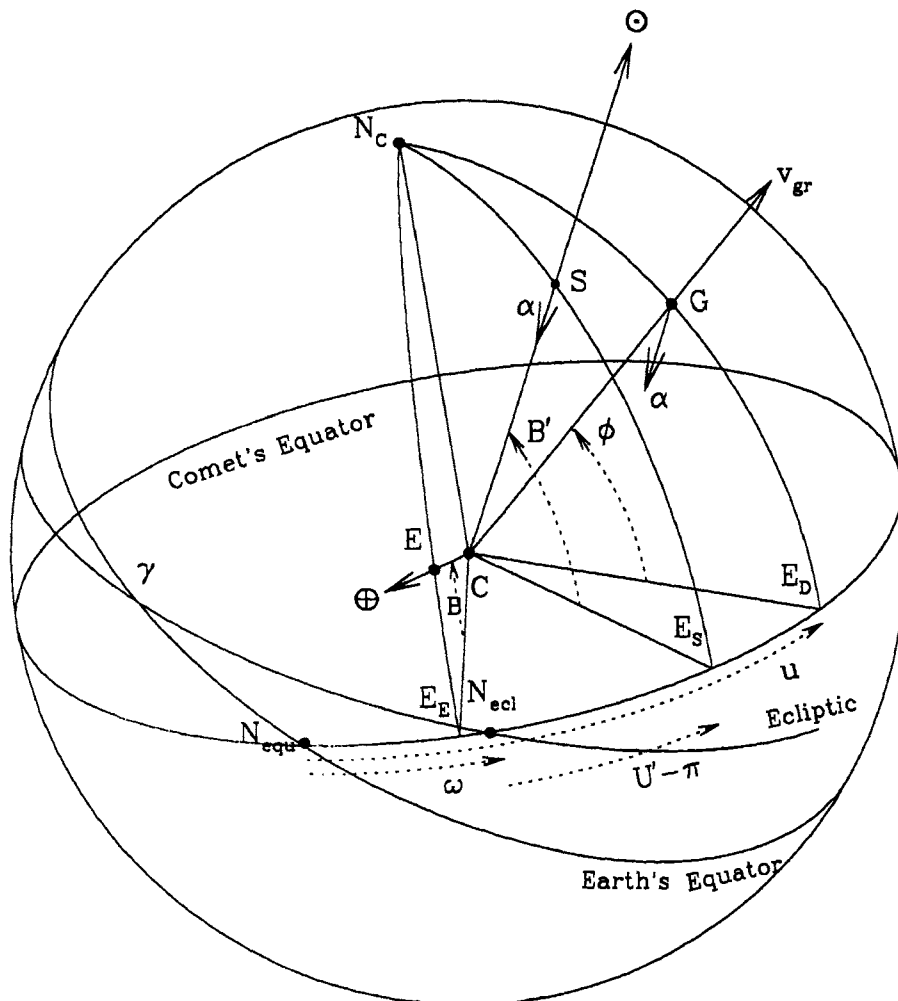


Figure 4.1: Geometry indicating the location of the source G and the directions of the initial velocity v_{gr} and acceleration α of the ejected grain. The sub-Sun point, sub-Earth point and the North pole of the comet are S , E , and N_C respectively.

4.3.2.1 Comet-o-Centric Spherical Coordinates Referred to the Comet's Equator

In the simulation, we follow the track of the dust grain ejected from an active region $G(u, \phi, R, t = 0)$ at longitude u and latitude ϕ on the surface of a spherical nucleus of radius R in the comet-o-centric frame referred to the comet's equator (Fig. 4.1). The longitude is measured along the direction of rotation of the comet from N_{equ} . Relative to the comet, during time t , the dust traverses a distance $v_{gr}t$ radially outwards from the comet and a distance $\frac{1}{2}\alpha t^2$ along the Sun - comet direction due to solar radiation pressure. Since the comet-o-centric distances of the shells are much larger than the size of the nucleus, the longitude u' , latitude ϕ' and radial distance r' ($u', \phi', r', t = t$) of the grain at time t reckoned after ejection are given by:

$$\begin{aligned} r' \cos \phi' \cos u' &= (v_{gr} \cos \phi \cos u)t - (1/2)(\alpha \cos B' \cos U'')t^2 \\ r' \cos \phi' \sin u' &= (v_{gr} \cos \phi \sin u)t - (1/2)(\alpha \cos B' \sin U'')t^2 \\ r' \sin \phi' &= (v_{gr} \sin \phi)t - (1/2)(\alpha \sin B')t^2 \end{aligned} \quad (4.3)$$

where U'' is the longitude of the sub-Sun point S measured from N_{equ} and B' , the comet-o-centric latitude of the Sun. From Fig. 4.1, it is easy to see that

$$U'' = \omega + U' - \pi,$$

where $U' - \pi$ is the comet-o-centric longitude of the Sun measured along the direction of rotation of the comet from N_{ecl} , and ω is the distance of N_{ecl} from N_{equ} , both points being on the equatorial plane of the comet. The angles ω can be calculated from the following relations:

$$\begin{aligned} \sin \omega \sin i &= \sin \epsilon \sin N \\ \cos \omega \sin i &= \cos \epsilon \sin J - \sin \epsilon \cos J \cos N \\ \cos i &= \cos J \cos \epsilon + \sin J \sin \epsilon \cos N, \end{aligned} \quad (4.4)$$

where i is the inclination of the comet's equator to the ecliptic. The angles $N = \widehat{\gamma C N_{equ}}$ and J , the inclination of the comet's equator to the Earth's equator are

related to the right ascension and declination of the comet's pole :

$$\begin{aligned} N &= \alpha_p + \pi/2 \\ J &= \pi/2 - \delta_p. \end{aligned} \tag{4.5}$$

The expressions in Eq. 4.3 are strictly valid only if α is constant in direction and magnitude. A constant value of α may be a reasonably good approximation in the present case, as we fit only a maximum of 8 shells ejected during a time span of about 90 hours.

4.3.2.2 Comet-o-Centric Spherical Coordinates Referred to the Earth's Equator

The comet-o-centric coordinates (u', ϕ', r', t) of the grains referred to the comet's equator were then transformed to the comet-o-centric spherical coordinates with respect to the Earth's equator (A, D, r', t) where A and D are the comet-o-centric right ascension and declination of the grain. This transformation depends on the right ascension α_p and declination δ_p of the north pole of the comet. The inclination of the comet's equatorial plane to the Earth's equator is given by $J = \pi/2 - \delta_p$ and position of the node N_{equ} is given by $N = \alpha_p + \pi/2$. The comet-o-centric latitude of the Earth B , the position angle of the projection of the north pole of the comet on the sky plane P and the angles B' and U' were calculated utilizing the equations used for calculating the planet-o-centric positions of the satellite with respect to the planets (Rhode and Sinclair 1992).

$$\begin{aligned} \cos B \sin U &= \cos J \cos \delta \sin(\alpha - N) + \sin J \sin \delta \\ \cos B \cos U &= \cos \delta \cos(\alpha - N) \\ \sin B &= \sin J \cos \delta \sin(\alpha - N) - \cos J \sin \delta \\ \cos B \sin P &= -\sin J \cos(\alpha - N) \\ \cos B \cos P &= \sin J \sin \delta \sin(\alpha - N) + \cos J \cos \delta \\ \cos B' \sin U' &= \cos i \cos b \sin(l - \Omega) + \sin i \sin b \\ \cos B' \cos U' &= \cos b \cos(l - \Omega) \\ \sin B' &= \sin i \cos b \sin(l - \Omega) - \cos i \sin b, \end{aligned} \tag{4.6}$$

Where α , δ , l and b are the geocentric right ascension, declination, heliocentric ecliptic longitude and latitude of the comet respectively. The angle $\Omega = \gamma N_{ecl}$ can be calculated using the following relations:

$$\begin{aligned}\cos \Omega \sin i &= -\cos J \sin \epsilon + \sin J \cos \epsilon \cos N \\ \sin \Omega \sin i &= \sin N \sin J\end{aligned}\quad (4.7)$$

The angles U , P and B are not directly needed for calculating the trajectory of the dust grain. These are nevertheless useful to visualize the effect of solar illumination on the comet, the orientation and aspect angle of the dust jet and shell patterns.

4.3.2.3 Transformation to Geocentric Spherical Coordinates

In the comet-o-centric Earth's equatorial frame, position of the Earth is specified by the distance Δ , right ascension $\alpha_c + \pi$ and declination $-\delta_c$ and that of the grain as (A, D, r') , where $(\alpha_c, \delta_c, \Delta)$ are the geocentric spherical coordinates of the comet. The geo-centric spherical coordinates of the grain (α_g, δ_g) were calculated from A , D , r' , α_c , and δ_c utilizing the rigorous expressions involving the comet-o-centric Earth's equatorial coordinates of the sub-Earth point and the grain (Gurnette and Woolley 1960):

$$\tan(\alpha_g - \alpha) = \frac{\xi}{(1 + \zeta) \cos \delta - \eta \sin \delta} \quad (4.8)$$

$$\tan(\delta_g - \delta) = \frac{\eta - \xi \tan \frac{1}{2}(\alpha_g - \alpha) \sin \delta}{(1 + \zeta) + \xi \tan \frac{1}{2}(\alpha_g - \alpha) \cos \delta} \quad (4.9)$$

where,

$$\xi = r' \cos D \sin(A - \alpha) / \Delta \quad (4.10)$$

$$\eta = r'(\sin D \cos \delta - \cos D \sin \delta \cos(A - \alpha)) / \Delta \quad (4.11)$$

$$\zeta = r'(\sin D \sin \delta + \cos D \cos \delta \cos(A - \alpha)) / \Delta, \quad (4.12)$$

where α_g and δ_g are the geocentric right ascension and declination of the grain and Δ its geocentric distance. These equations, meant for computing the differential coordinates of satellites (here the grain) with respect to the primary (comet), do not make any assumptions regarding the latitude of satellites and hence are directly applicable in the present case of the comet - dust geometry.

4.4 Fit of the Observations to the Model

The differential co-ordinates, $\Delta\alpha_g \cos \delta_g = (\alpha_g - \alpha_c) \cos \delta_g$ and $\Delta\delta_g = \delta_g - \delta_c$, of the dust grains with respect to the comet center on the simulated shell depend on the pole positions, location of the sources on the comet (Eq. 4.3), the parameter β of the grain and its velocity v_{gr} given by Eq. 4.2. The simulated jet and shell structures were fitted with the observed structures by iteratively adjusting these parameters. In order to limit the computer file size of the simulated plots, the longitude sampling was selected between 5° and 30° . Such a discrete sampling however produces radial streaks in the 1996 and October 1997 images instead of a more realistic continuous surface of the ejection cones.

4.4.1 Pole Position of the Comet and Latitude of the Active Sources

In the images of February - May 1997, sets of shells were fitted with computer synthesized patterns. At distances of about 3 AU and with seeing discs of about 2 arcsec, the helical structure due to the diurnal motion of the comet in the 1996 and October 1997 images are not discernible. For these images, pairs of jets were recognized as the projected boundaries of cones of jets generated by the rotating sources (Sekanina and Bochnhardt 1997a) and these were fitted. The fits were determined by visual matching between the images and the computed structures after superposing them. Separation between the shells depends on the orientation of the line of sight to the equatorial plane (i.e. the comet-o-centric latitude B), the latitude of the source, velocity and acceleration of the grains determined by the parameters a and b in Eq. 4.2. Orientation of shells depends on P and is modified by the direction of solar radiation pressure. The first step in comparison was carried out by varying (α_p, δ_p) as well as the latitude of sources in order to simultaneously match the orientation of various shells. Even though a variety of combinations of α_p and δ_p values yield the desired position angle P , the corresponding values of B differ. Again, the same shell pattern could be generated by different combinations of B and ϕ . It was attempted to resolve this ambiguity by assuming that the same sources were active (if sunlit) in images taken 1 to 2 months apart. After about two

Date	$\alpha_p(2000)$ (Deg)	$\delta_p(2000)$ (Deg)	P (Deg)	B (Deg)	B' (Deg)	I (Deg)	Φ (Deg)
1996 Oct. 6	270	-60	175	-34	-32	80	78
1996 Nov. 4	260	-65	183	-28	-21	77	84
1997 Feb. 18	290	-60	189	-03	22	90	78
1997 Apr. 10	283	-63	216	49	84	87	81
1997 May 2	285	-55	210	51	62	88	73
1997 Oct. 9	267	-50	158	-06	-01	77	68

Table 4.2: The pole positions and the geometry derived from the data observed from VBO.

Date	$\alpha_p(2000)$ (Deg)	$\delta_p(2000)$ (Deg)	P (Deg)	B (Deg)	B' (Deg)	I (Deg)	Φ (Deg)
1996 Sep. 15	265	-50	178	-46	-44	76	68
1996 Oct. 6	270	-60	175	-34	-32	80	78
1997 Feb. 2	275	-45	196	-26	-07	82	63
1997 Mar. 4	263	-57	209	15	31	76	76
1997 Mar. 7	260	-60	211	23	40	75	79
1997 Apr. 9	290	-60	221	46	88	90	78
1997 May 2	285	-55	210	51	62	88	73

Table 4.3: The pole positions and the geometry derived from the data observed from the observatory of the Naturwissenschaftlicher Verein Osnabrück (Chakraborty et al. 1998)

iterations the pole positions and the source latitudes could be constrained within $\pm 5^\circ$. An optimal solution was selected which reasonably fitted all the observed sets of shells. Fitted pole positions are given in Table 4.2 and Table 4.3.

The best fitting comet-o-centric latitude of the sources are given in Table 4.4. Although no deliberate attempt was made to place the sources at symmetric lati-

Latitude ($\pm 05^\circ$)	+65°	+35°	+5°	-5°	-35°	-65°
Date	Longitude (± 38)					
1997 Feb 18	111	174	151	359	252	75
1997 Apr 10	142		58	26		
1997 May 02	332		271	157		
Color code :	Magenta	Purple	Red	Green	Cyan	Yellow

Table 4.4: Longitude and latitude of the active regions.

tudes, the best fit shows a remarkable symmetry. The sources that appeared to be

active on the dates of our observations are shown in Fig. 4.2. Since the fits were car-

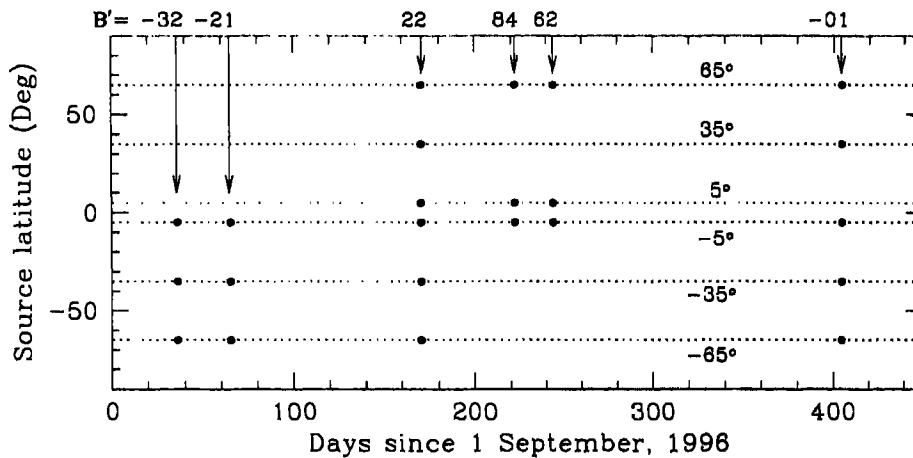


Figure 4.2: Fitted latitudes of the active regions on 6 October & 4 November, 1996, 17 February, 10 April & 2 May 1997. During late 1996, the solar illumination on the southern side ($B' < 0^\circ$) activated the southern sources, while the northern and near-equatorial sources were active during April-May 1997 ($B' > 0^\circ$).

ried out interactively by visual inspection, the uncertainties in the computed values of the pole positions and the latitudes indicate the range over which the fits appeared good and remained indistinguishable. The computed values of argument of the subsolar meridian at perihelion Φ and the obliquity I (Sekanina 1981a) corresponding to the fitted pole position of the date are given in Table 4.2 and Table 4.3.

4.4.2 The Coefficients a and b

After the orientation and shape of the shells were matched, the coefficients a and b in Eq. 4.2 were allowed to vary, to match the separation between the individual shells. The parameter a determines the mean grain velocity and b , the velocity dispersion and hence the width of the shells. Reliable estimates of the parameter b can only be made by including the entire range of grain sizes which can be detected in the visible region. In the present investigation, for fitting 4-6 shells, grains with β values of 0.03, 0.06, 0.1, 0.2, 0.3, 0.4, 0.5, 0.6 and 0.8 were found to be adequate. Heavier grains fall behind and the lighter ones are swept away by solar radiation pressure. A quantitative modeling by incorporating the scattering efficiency of the grains and a realistic size distribution of the grain population will be needed to reliably match the observations and has been attempted in *Chapter 5* and *Chapter 6*. Finite

size of the source will also contribute to the width of the shells. Assumption of a point source and forcing the fit by adjusting only ' b ' in Eq. 4.2 will overestimate this parameter. Further, sorting of grains of different compositions will lead to branching in the older shells (Sekarina 1981b). Spreading of finer dust grains due to surface breeze (Huebner et al., 1986) may cause smearing effects which will influence the estimates of b . Changes in the grain size with time due to possible splitting or

Date		a sec/km ± 0.1	b sec/km ± 0.05	Dust Loading Ψ	Production Rates		r AU	v_g km/sec
					Gas $\dot{\mu}$ $10^{-5} \text{g/cm}^2 \text{sec}$	Dust $\Psi \dot{\mu}$		
1997 Feb.	18	1.85	0.15	4.8 ± 1.1	2.2 ± 1.5	10.6 ± 2.4	1.175	0.535
1997 Apr.	10	1.50	0.13	3.4 ± 1.0	2.6 ± 2.0	9.0 ± 2.7	0.932	0.601
1997 May	2	1.90	0.15	6.2 ± 1.3	2.1 ± 1.4	13.1 ± 2.8	1.069	0.561

Table 4.5: Lower limits on gas and dust production rates derived from the data observed from VBO (Vasundhara and Chakraborty 1998).

Date		a sec/km ± 0.1	b sec/km ± 0.05	Dust Loading Ψ	Production Rates		r AU	v_g km/sec
					Gas $\dot{\mu}$ $10^{-5} \text{g/cm}^2 \text{sec}$	Dust $\Psi \dot{\mu}$		
1997 Feb.	2	2.20	0.25	7.8 ± 1.3	1.5 ± 0.6	11.7 ± 1.9	1.355	0.498
1997 Mar.	4	1.90	0.20	7.1 ± 1.4	2.1 ± 1.0	14.6 ± 2.9	1.050	0.566
1997 Mar.	7	1.90	0.20	7.5 ± 1.5	2.0 ± 1.0	15.1 ± 3.0	1.017	0.575
1997 Apr.	9	1.25	0.25	2.3 ± 0.9	1.2 ± 0.5	2.8 ± 1.1	0.927	0.602
1997 May	2	1.90	0.15	6.2 ± 1.3	3.7 ± 2.5	22.9 ± 2.5	1.068	0.561

Table 4.6: Lower limits on gas and dust production rates derived from the data observed from the observatory of the Naturwissenschaftlicher Verein Osnabrück (Chakraborty et al. 1998).

grain evaporation could lead to variation in the width of successive shells. All these effects are difficult to model and further, since the fits were carried out by visual inspection, the estimated values of the parameter b may have large uncertainties. For this reason, no attempt was made to fit a and b values separately for each source. For the 1996 images and the October 9, 1997 image, the individual shell structures are not resolved. The uncertainty in estimation of a and b is further degraded for these dates as these were derived by matching the observed curvature

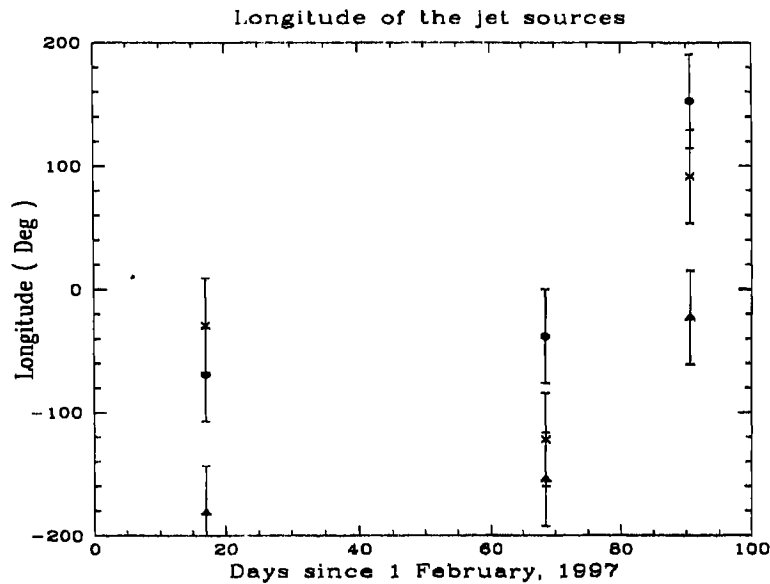


Figure 4.3: Longitude of the sources on 17 February, 10 April and 2 May 1997. Filled circles, crosses and filled triangles represent sources at latitudes $+65^\circ$, $+5^\circ$ and -5° respectively.

4.5 Results and Discussions

4.5.1 The Fitted Images

The observed structures are compared with the simulations in Figs. 4.4, 4.5, 4.6 and 4.7. In Figs. 4.4 and 4.5, the left and middle panels show the observed processed images from VBO, and the simulated structures respectively. These two are superposed in the right panels to enable critical comparison. In Figs. 4.6 and 4.7 the observed processed images from the observatory of the Naturwissenschaftlicher Verein Osnabrück, and the simulated structures are superposed. The observed images are in gray scale, while the simulations are in color. The color codes for jets from different latitudes are given in Table 4.4. The projected comet-Sun radius vector is indicated by the arrow. Identification of the source producing a given shell pattern at first appeared to be the major source of error as $B = B \pm 30^\circ$ may simulate similar structures for sources at $\phi = \phi \pm 30^\circ$. However, the overall pattern of the shells expanding in other directions matches better with the solution tabulated in Table 4.3. Further continuous data at frequent intervals over several months has helped to constrain the pole positions.

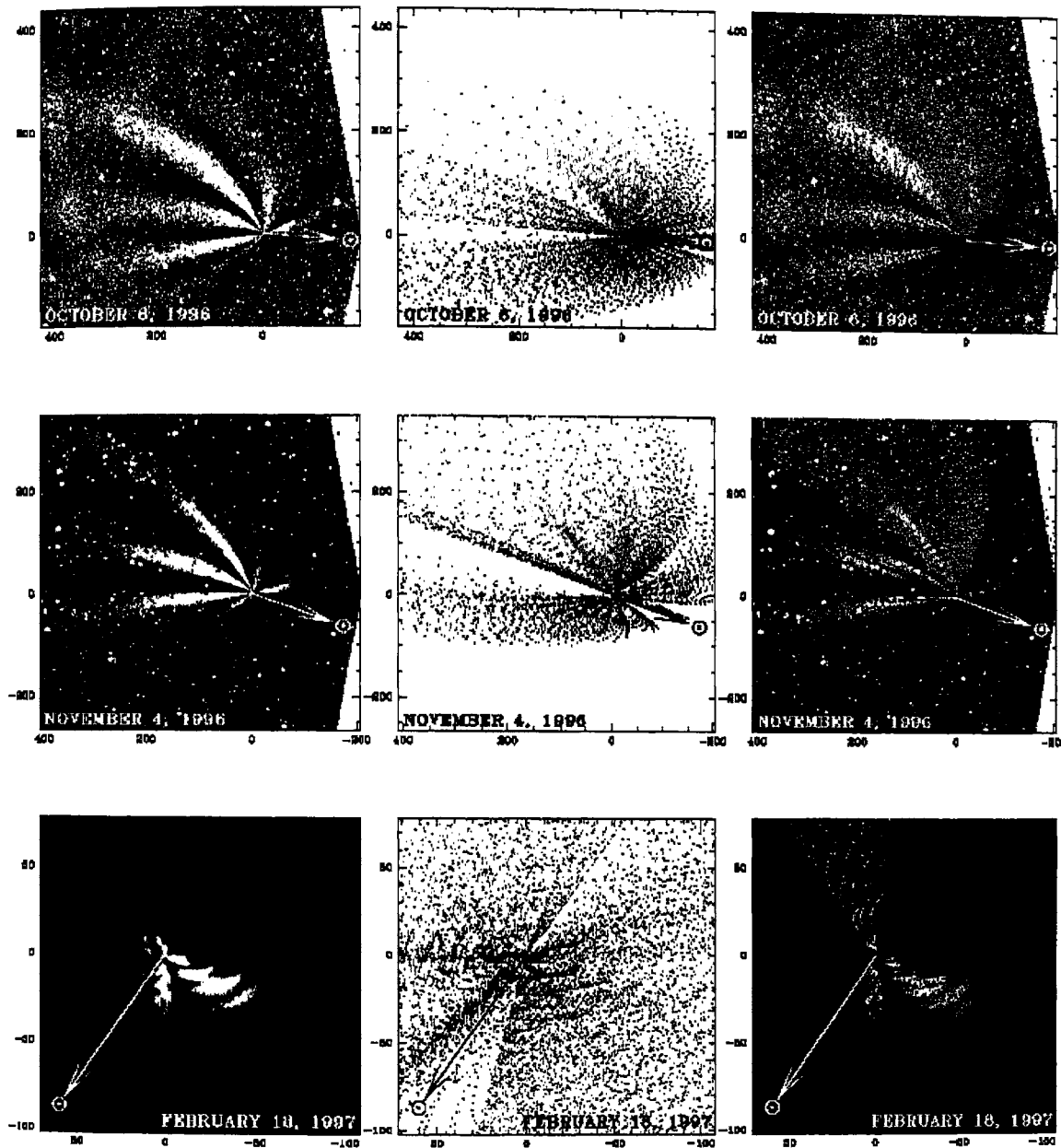


Figure 4.4: Fit of the model to the pre-perihelion images. In each row, the left panel shows the observed processed image and the middle panel the simulated structures. On the right panel, both observed and simulated structures are superposed. The β values of the grains range between 0.06 and 2.5. The projected direction of the Sun is indicated by the arrow. North is up and east is to the left. The scales are in arcsec centered on the comet. Color code for ϕ are : $-65^\circ = \text{Yellow}$, $-35^\circ = \text{Cyan}$, $-5^\circ = \text{Green}$, $+5^\circ = \text{red}$, $+35^\circ = \text{Purple}$ and $+65^\circ = \text{Magenta}$.

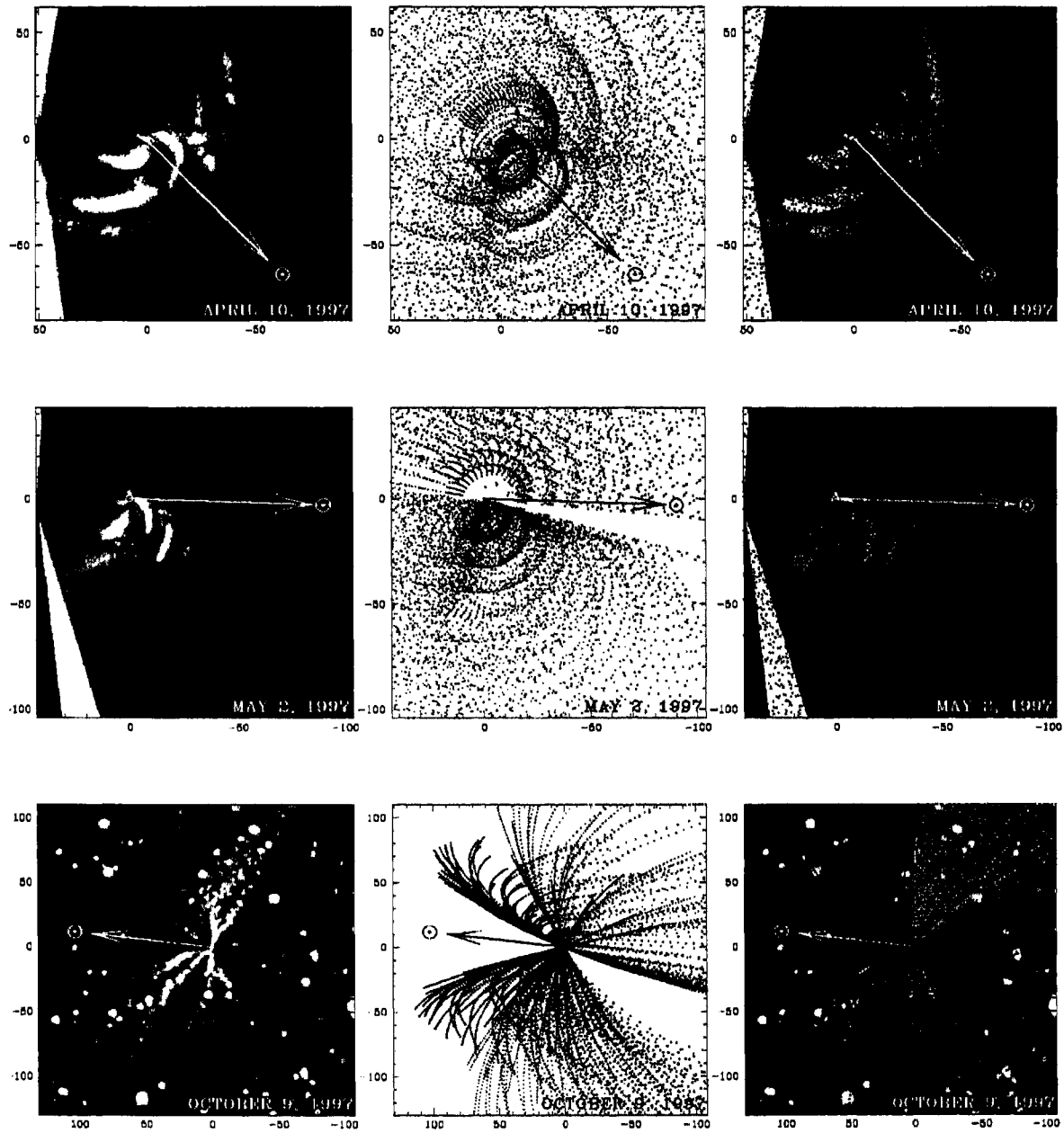


Figure 4.5: *Fit of the model to the post-perihelion images. Other details are same as those of Fig. 4.4.*

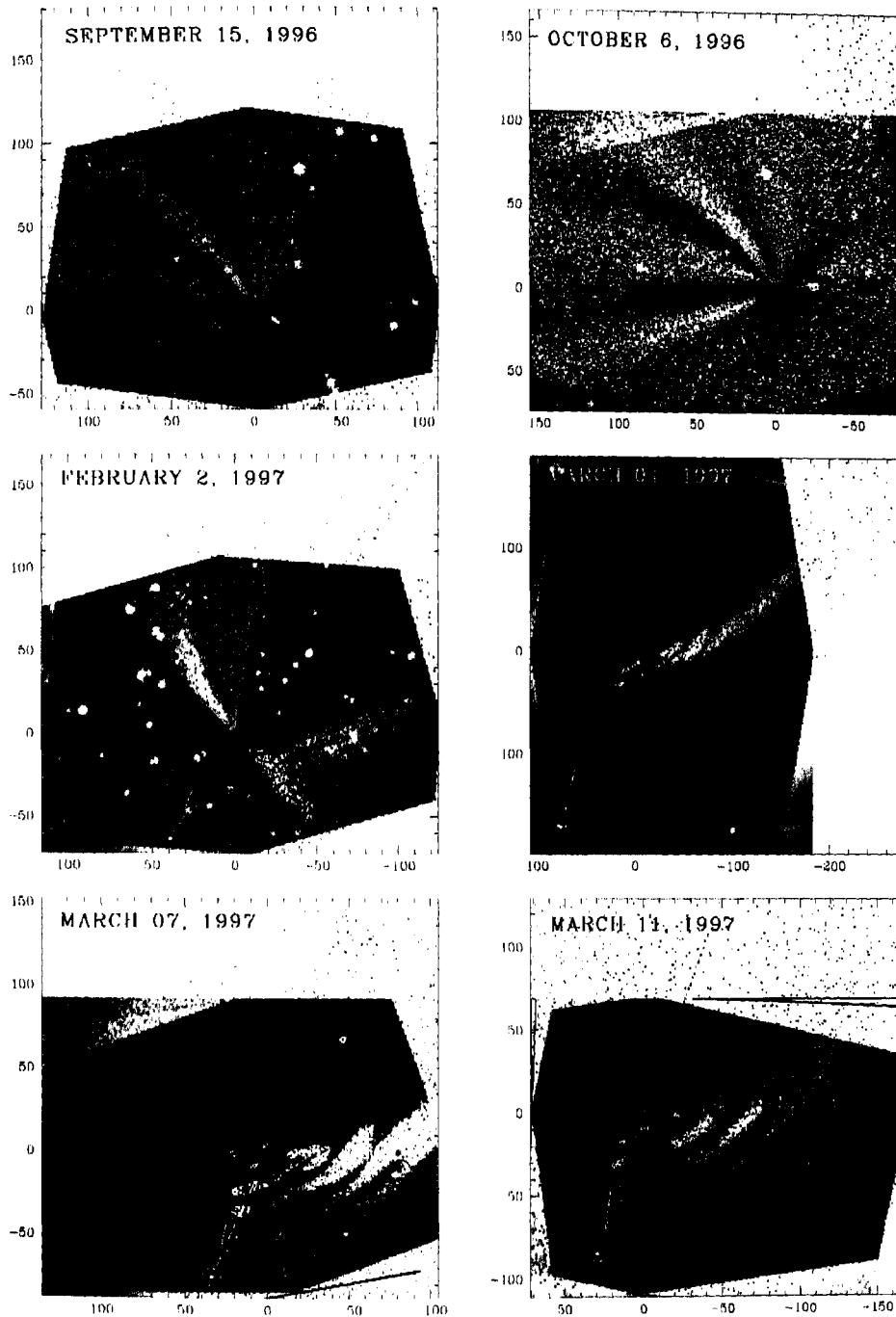


Figure 4.6: Trajectory of the dust grains from the active region over-plotted on the observed processed images of comet Hale-Bopp observed from the observatory of the Naturwissenschaftlicher Verein Osnabrück. Each simulated shell contains 7 points representing dust grains with β values of 0.06, 0.08, 0.12, 0.20, 0.30, 0.45 and 0.60 and three additional points for the March images at 1.2, 1.8 and 2.5 to demonstrate the trajectory of sub micron size grains. The direction of the Sun is indicated by the white arrow.

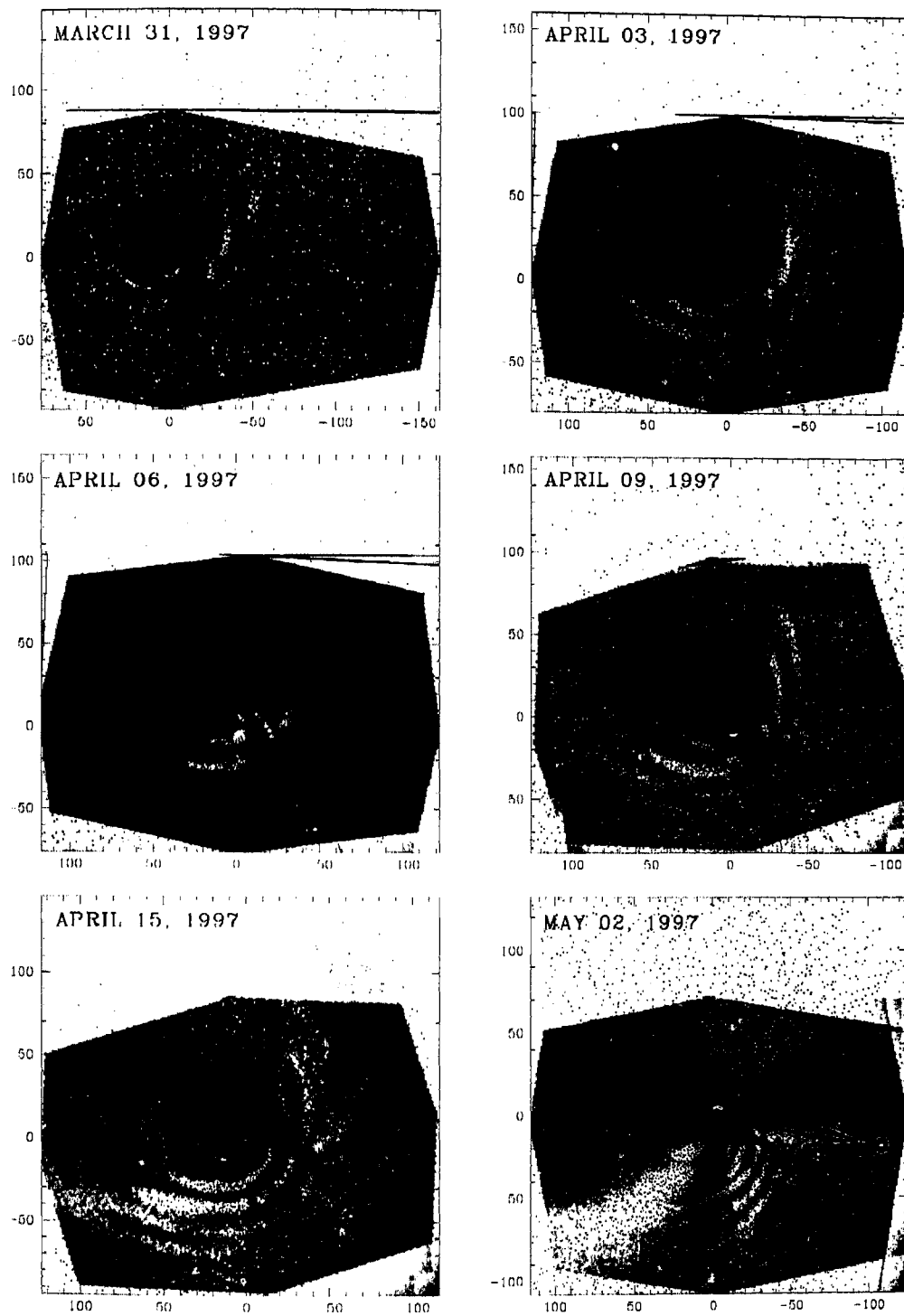


Figure 4.7: Trajectory of the dust grains from the active region over-plotted on the observed processed images of comet Hale-Bopp observed from the observatory of the Naturwissenschaftlicher Verein Osnabrück. (details are same as those of Fig. 4.6).

No attempt was made to match the intensity of the shells. In order to simulate the hazy features consisting of finer grains with $\beta > 0.8$ in the projected anti-Sun direction, the simulated plots contain in addition, points representing grains with β values of 1.2, 1.5, 1.8 and 2.5. Since very small grains with radii less than 1μ attain nearly constant velocities (Gombosi 1986, Delsemme 1982), with sufficient accuracy, the velocity of these smaller grains were assigned the value corresponding to $\beta = 0.8$. Each simulated shell thus contains 13 points. Ideally, the number of points of a given grain size should be governed by a power law distribution (Hanner 1983, Sekanina 1998a). In the present work, except for the end points, we have sampled β values of equal interval between 0.1 and 0.6. Since $\beta \propto 1/s$ (Finson and Probst 1968), where s is the radius of the grain, such a sampling of β results in over sampling of smaller grains mimicking a s^{-2} law. Further, in the simulated image, contributions of grains of all sizes are represented by dots of the same size. The number of grains a dot represents is therefore proportional to s^{-2} . Thus the simulated pattern with the sampling of β value discussed above represents approximately a power law distribution with an index of ≈ -4 .

4.5.2 Gas and Dust Production Rates

Sekanina and Larson (1984) have shown that for the outbursts of comet Halley in 1910, the linearity of Eq. 4.2 was satisfied for $\beta \leq 0.6$. We relaxed this restriction on β to 0.8 to simulate the extensions of the shells along the projected anti-Sun direction consisting of finer grains. We used the following equations used by these authors to calculate the lower limit on Ψ , the the mass loading by dust and $\dot{\mu}$, the gas production rate corresponding to an upper limit of 0.8 for β

$$\Psi > 5.0 \left[3av_g \left[1 - \frac{0.65}{1.65 + 8.5(bv_g)^{4/3}} \right] - 1 \right]^{5/3}$$

$$\dot{\mu} > 0.93 \times 10^{-5} / Rb^2v_g. \quad (4.13)$$

The nuclear radius R was taken to be 35 km, the upper limit by Weaver and Lamy (1997) and Sekanina (1997a). The thermal velocity of the gas v_g at heliocentric distance r was calculated using the relation by (Delsemme 1982):

$$v_g = 0.58r^{-0.5}. \quad (4.14)$$

The estimated lower limits on production rates of gas and that of the dust using the fitted values of a and b are given in Table 4.5 along with the heliocentric distance of the comet and the gas velocity v_g . If water constitutes 80 % of the total gas production, the lower limit on the gas production rate $\dot{\mu}$ in April 1997 estimated in the present work of 2.6×10^{-5} g/cm²sec (Table 4.5), yields a lower limit on the evaporation rate of water of 7×10^{17} molecules/cm²sec. This is 35% of the upper limit on the production rate of about 20×10^{17} molecules/cm²sec (Delsemme 1982) expected at the heliocentric distance of 0.93 AU for normal incidence of sunlight for a zero albedo surface. This estimate can be further improved if a quantitative fit is carried out for the estimation of the parameter b taking into account the finite size of the jet sources. As mentioned in Section 4.4.2, the finite size assumption may result in the over estimate of the parameter b and an under estimate of $\dot{\mu}$.

4.5.3 Activity of the Various Sources

Gradual changes in the appearances of the dust shells from the comet with time can be understood in terms of the varying Earth-comet geometry and changes in the comet-o-centric latitude of the Sun (B') which determines activation of sources at different latitudes and fractional period of their activity. Large value of the comet-o-centric latitude of the Earth B , in April permitted high latitude view of the sets of concentric rings and arcs elongated in the projected anti-Sun direction. It is interesting to note that the source at $+35^\circ$ which was apparently active during February 1997 to March 1997 (Fig. 4.4 & Fig. 4.6), ceased to be active in April (Fig. 4.5 & Fig. 4.7) in spite of the high northern (cometary) latitude of the Sun. Activity of a source near this latitude is again seen in the image of the comet taken in October 1997 when the comet-o-centric latitude of the Sun was near zero. If the pre and post perihelion features are from the same source, one of the reasons for its inactivity during April - May 1997 may be local shadowing, possibly by a overhanging mountain ridge north of this source. This explanation is supported by the fact that the activity from this source was noticed to resume again when the solar illumination became near equatorial, e.g., October 1997 image (Fig. 4.5).

4.5.4 Size of the Sources

During early April 1997, three sets of shell structures are inferred from the present analysis (Table 4.4). One from the high latitude active source at $+65^\circ$ and the two near equatorial sources at $+5^\circ$ and -5° . On April 10, the rotation averaged values of the cosine of the Sun's zenith distance $\langle \cos z_\odot \rangle$ as seen by these sources were .913, .092 and 0.003 respectively. Schleicher *et al.* (1997) report a total water production rate of 4×10^{30} molecules/sec from the comet, near perihelion. To assess the contribution from these sources to the observed water production rate during early April, it may be noted that the equatorial sources were illuminated by the Sun at near-grazing incidence and that the source at $+65^\circ$ must be small in size. The constraint on the size of the high latitude source is evident because the total area north of the latitude ϕ for a spherically symmetric comet is given by $0.5(1 - \sin \phi)$ of the total surface area of the comet (Sekanina 1987). If we assume that this source spans between 60° and 70° in latitude, the total area between the two latitude circles is 567 km^2 . The observed well defined shells from this source due to the diurnal variation cannot be explained if this source occupies a substantial fraction of this area. Assuming that the source occupies 36° in longitude, the total production of water from this source will be 11.4×10^{29} molecules/sec. This is 29% of the total observed production rate. In spite of the near-grazing incidence of sunlight, the shells from the equatorial sources appear comparable in intensity to the high latitude source at $+65^\circ$. Further, the shells from -5° and $+5^\circ$ are not resolved in any of the images between February and May. Hence it is likely that a single source or a source complex stretches from -5° to $+5^\circ$. It is difficult to comprehend the reason for the near equal brightness of the two sets of shells when the values of $\langle \cos z_\odot \rangle$ at the respective sources differed by a large factor. Further, the best fitting pole position for the shells from the source at $+65^\circ$ does not yield a very good fit for the equatorial shells during April (Fig. 4.5). The interwoven shells observed during February 1997 appear too complex to be explained using a single nucleus. The 10 April 1997 image shows two sets of shell structures. While the high latitude source at 65° explains the shells (magenta) expanding in the south-westerly direction, we found it impossible to fit the near equatorial shell with a single

source corresponding to the apparent anti-clockwise rotation of the nucleus during April. We have therefore invoked two sources, one at $+5^\circ$ latitude producing the shell structures (colored red) S-E of the nucleus and another at -5° to produce the shells (colored green) N-W of the nucleus. In spite of best efforts, even this bimodal matching is not perfect. The observed shells have smaller curvature compared to the simulated ones. Further, if the activity of the source at $+5^\circ$ had continued till sunset as per our assumptions, the longitudinal extent of the shells in the simulated image should have continued till the N-E across the N point. But the region N-E of the nucleus is devoid of any shell structure. The projected comet-o-centric separation of the observed shells in the N-W and S-E corresponding to a given diurnal cycle match better for a clockwise motion of the source and in such a case, a single source can explain the observed feature. The curvature of these equatorial shells could be adjusted with a separate pole solution. Thus there appears to be the need for two separate bodies with opposite sense of rotations, one hosting the high latitude source and the other the near equatorial source. This is in conformity with the binary model by Sekanina (1998b) with the two nuclei having their spin vectors subtending an angle $> 90^\circ$ with each other to explain the complex shell structures in the images of late February, 1997 and late March, 1997. In order to explain the constant phase difference between the two sets of shell patterns, the two components must have nearly the same synodic period. The binary scenario is also in conformity with the reported differences in color and polarization of the two sets of shells by Jockers et al. (1997).

4.6 Conclusions

Although the observations could be reasonably matched with the simulations, the present model assuming a single nucleus does not however replicate the exact shapes of the shells and the complex observed shell patterns. Detailed modeling taking into account the binary nature of the comet (Sekanina 1997b, 1998b) may be required to explain the observed intricate shell structures. The pole positions during the one year period of observations are found to vary between 260° and 290° in right ascension and -50° to -65° in declination indicating a complex state of rotation

of the comet. The present data set is insufficient to draw a meaningful conclusion on the possible precession or complexity of the rotation of the comet. The derived pole positions compare well with the reported values of $\alpha_p = 257^\circ$ and $\delta_p = -61^\circ$ by Sekanina (1998a) for late February, 1997 and $\alpha_p = 275^\circ$ & $\delta_p = -57^\circ$ by Jorda *et al.* (1997) for February-March 1997. Our average value of $\alpha_p = 276^\circ$ is close to the value of $\alpha_p = 270^\circ$ corresponding to the ecliptic longitude of 270° and latitude of -20° pertaining to a complex rotational state of the nucleus with a small precessional angle reported by Samarasinha *et al.* (1997). The latitude of the northern most source of 65° derived in the present study is in conformity with the value of $64 \pm 5^\circ$ reported by Jorda *et al.* (1997). The average value of dust to gas production ratio between February 1997 - May 1997 is found to be near 5. During April, the source at $+65^\circ$ appears to account for about 29% of the observed total water emission reported by Schleicher *et al.* (1997). In addition, several smaller jet sources not delineated in Figs. 4.4 and Figs. 4.5, distributed sources of water from evaporation of the grains in flight and outgassing from the inactive regions of the comet may contribute to the total observed water production rate.

References

- Chakraborty, P., Heiser, E.; Hänel, A., Vasundhara, R., 1998. *Astronomische Gesellschaft Meeting, Poster presented at the Annual Scientific Meeting of the Astronomische Gesellschaft at Heidelberg, September 14-19, 1998*, poster No. P3.
- Delsemme, A. H., 1982. In *Comets* (L.L.Wilkening Ed.), p-85. University of Arizona Press, Tucson.
- Finson, M. L. and R. F. Probstein, 1968. *ApJ*, **154**, 327.
- Gombosi, T. I., 1986. In *Proc. 20th ESLAB Symposium on the Exploration of Halley's Comet*, 167. *ESA SP-250*.
- Gurnette, B. L., Woolley, R. v. d. R. (Eds.), 1960. In *Explanatory Supplement to the Astronomical Ephemeris and The American Ephemeris & Nautical Almanac*, 342. Prepared by the Nautical Almanac Offices, UK & USA.

- Hanner, M. S., 1983. In *Cometary Exploration* (T.I. Gombosi Ed.), 2, 1. Central Research Institute for Physics Press, Budapest.
- Huebner, W. F., Keller, H. U., Wilhelm, K., Whipple, F. L., Delamere, W. A., Reitsema, H. J., and Schmidt, H. U., 1986. In *Proc. 20th ESLAB Symposium on the Exploration of Halley's Comet*, 363 ESA SP-250.
- Jockers, K., Rosenbush, V. K., Bonev, T. and Credner, T., 1997. *EM&P*, 78 373.
- Jorda, L., Rembor K., Lecacheux, J., Colom, P., Colas, F., Frappa E. and Lara, L. M., 1997. *EM&P*, 77 167.
- Larson, S. M. and Sekanina, Z., 1984. *AJ*, 89, 571.
- Licandro, J., Rubio, L. R. B., Bochnhardt, H., Casas, R., Göetz, B., Gómez, A., Jorda, L., Kidger, M. R., Osip, D., Sabalisk, N., Santos, P., Serra-Ricart, M., Tozi, G.P. and West, R., 1998. *ApJ*, 501, L221.
- O'Meara, S. J., Bortle, J. E., Birkle, K., Thommes, E., Hippelein, H. H., Manzini, F., Guaita, C., and Crippa, F., 1996. *IAUC 6463*, 1996 August 28. Edited by Marsden B. G.
- Probstein, R.F., 1969. In *Problems of Hydrodynamics and Continuum Mechanics*, *Soc. Industr. Appl. Math.* (F. Bisshopp et al. eds), 568.
- Rhode, J.R. and Sinclair, A., 1992. In *Explanatory Supplement to the Astronomical Almanac* (P.K.Seidelmann Ed.), 325. *Prepared by the Nautical Almanac Offices, UK & USA, Jet Propulsion Laboratory, Bureau des Longitudes and the Time Service & Astrometry departments, U.S.Naval Observatory.*
- Samarasinha, N. H., Mueller, B. E. A. and Belton M. J. S., 1997. *EM&P*, 77 189.
- Schleicher, D.G., Millis, R.L., Farnham, T. L., Lederer, S. M., 1997. *Bull. Am. Astron. Soc.* 29, p.1033.
- Sekanina, Z., 1981a. *Annu. Rev. Earth Planet. Sci* 9, 113.
- Sekanina, Z., 1981b. *AJ*, 86, 1741.

- Sekanina, Z., 1987. In *proc. Symposium on the Diversity and Similarity of Comets* (E. J. Rolfe and Battrick eds.), 323. *ESA SP-278*.
- Sekanina, Z., 1991. In *Comets in the Post-Halley Era* (R. L. Newburn, Jr., M Neugebauer & J. Rahe Eds.), 769. Kluwer Academic. Dordrecht/Norwell, MA.
- Sekanina, Z., 1996. *A & A*, **314**, 957.
- Sekanina, Z., 1997a. *EM&P*, **77** 147.
- Sekanina, Z., 1997b. *EM&P*, **77** 155.
- Sekanina, Z., 1998a. *ApJ*, **494**, L121.
- Sekanina, Z., 1998b. *ApJ*, **509** L133.
- Sekanina, Z. and Boehnhardt, H. 1997a *IAUC 6542*. 1997 January 21. Edited by Green D. W. E.
- Sekanina, Z. and Boehnhardt, H., 1997b. *EM&P*, **78** 313.
- Sekanina, Z. and Larson, S. M., 1984. *AJ*, **89**, 1408.
- Vasundhara, R. Pavan Chakraborty, Andreas Hänel, Erwin Heiser., 1997. *EM&P* **78**, 321.
- Vasundhara, R., and Chakraborty, P., 1999. *Icarus* **140**, 221.
- Vasundhara, R. 2001. *in preparation*.
- Weaver, H. A. and Lamy, P. L., 1997. *EM&P*, **79** 17.

Chapter 5

SPECTROPOLARIMETRY OF COMET HALE-BOPP AND COMET WILD-2

Polarimetric observations of comets contain important information about cometary dust. Proper modeling of polarimetric data can reveal information on the cometary grain type, its silicate to organic ratio, and the porosity. In this chapter, the phase dependent polarization of comet Hale-Bopp and comet Wild 2 from published data and unpublished data obtained elsewhere, is first analyzed. The grain types that best fit the phase polarization curves at three wavelengths, are then used for modeling the continuum polarization of the spectropolarimetric observations of comet Hale-Bopp. A similar procedure has been followed using single color and limited phase data for comet Wild 2. These comets were observed on April 23 and 24, 1997. The observations were made using the newly built Optical, Dual-beam, Automated Medium Resolution Spectropolarimeter (O-DB.AMRSP) for the Vainu Bappu Telescope (Chapter 3). The coma is assumed to be a collection of crystalline and glassy silicates, with an organic component. Effects of porosity and a grain size distribution are investigated. Computations of the scattered light are made using the Mie scattering code published by Bohren and Huffman (1983), and the Effective Medium Theory (EMT) has been used to compute the effective refractive index of the grains.

Using these codes, the model polarization is computed for the comets. Through the modeling of continuum polarization we try to determine the composition, the silicate to organic ratio, and the porosity of the cometary dust grains. We also look into the emission polarization from cometary molecules that emerges as a residual between the observed and modeled polarization.

5.1 Introduction

Except for rare in-situ observations of comets by space missions, our information on comets come mostly from remote observations of the scattered and emitted electromagnetic radiation from them. The scattered solar radiation contains a lot of information on the refractory characteristics, the size distribution and shapes of the cometary dust grains. The information on the chemical composition are best obtained from their IR signatures (Hayward, Hanner and Sekanina, 2000, Wooden *et al.*, 1999, Diane *et al.*, 1997 *etc.*). On the other hand the porosity and the organic content in a grain dictate its effective refractive index. As grain heating depends on the amount of light absorbed in the UV and visible band, knowledge of the composition and texture (porosity) are important. Polarization studies are one of the best ways to determine the properties of dust. Color of the cometary dust mainly depends mainly on the size distribution of the cometary particles whereas the polarization of the scattered light is mainly determined by the complex refractive index of the grain material (Kolokolova and Jockers, 1997 and Kolokolova *et al.*, 1997).

The comet 1995/O1 (Hale-Bopp) being intrinsically a very bright and dusty comet, was a potential candidate for polarimetric studies. Numerous polarimetric observations of this comet have been reported. Ganesh *et al.* (1998), Kiselev and Velichko (1997) from their aperture polarimetric observations of comet Hale-Bopp in the continuum regions, report that this comet belongs to the high polarization class of comets and that it exhibits stronger wavelength dependence of polarization compared to other comets. The positive branch of the polarization phase dependence of this comet is significantly higher than from that of the other dusty comets. Imaging Polarimetry of comet Hale Bopp has been reported by Tanga *et al.* (1997), Hadameik *et al.* (1997), Jockers *et al.* (1997) and Furusho *et al.* (1999). Results of

polarimetric imaging indicated that the polarization is larger in the dust shells than in the coma. Hasegawa *et al.* (1997) and Woodward *et al.* (1998) have reported the near-infrared and infrared polarimetric observations of this comet respectively. The former also classify the comet as a high polarization comet. Rosenbush, Shakhovskoj and Rosenbush (1997) and Manset and Bastien (2000) have measured the comet's linear as well as the circular polarization of the Comet. Manset and Bastien (2000) have measured the polarization through different aperture sizes which indicated a change of polarization with aperture size. They also find the polarization to be significantly lower in the CO^+ and C_3 emission filters at 4260 and 4060Å than in an adjacent 4840Å continuum filter and significantly higher in the red in the H_2O^+ emission filter (7000Å) than in the adjacent 6840Å continuum filter. The observation in C_3 and C_2 emission filters at 4060Å(70Å) and (5141Å(118Å) & 5140Å(90Å)) by Kiselev (2000) also show significantly lower polarization.

All these reported observations indicate that comet Hale-Bopp has a high linear polarization among the high polarization class of comets which suggests that the cometary grains must be of sub-micron size.

5.2 Phase Dependent Polarization of Comet Hale-Bopp

The polarizations of the central coma of comet Hale-Bopp with respect to the phase angle, has been plotted in Fig. 5.1. The datasets of the central coma, tabulated in Table E.1 of *Appendix E.1*, were obtained from Ganesh *et al.* (1998), Hadamcik *et al.* (1997), Hadamcik (1999), Kiselev *et al.* (1997), Kiselev and Velichko (1997), Kiselev (2000) and Manset and Bastien (2000). Manset and Bastien (2000) have observed the central coma through different aperture sizes. In Fig. 5.1 the largest aperture for each phase angle from their dataset, was selected for the plot. This was done, to have uniformity in aperture sizes in the data set. It is also assumed that the small scale variation on the central coma, resulting in the variation of polarization will be averaged out.

Comet Hale-Bopp exhibited a spatial as well as a wavelength dependence of polar-

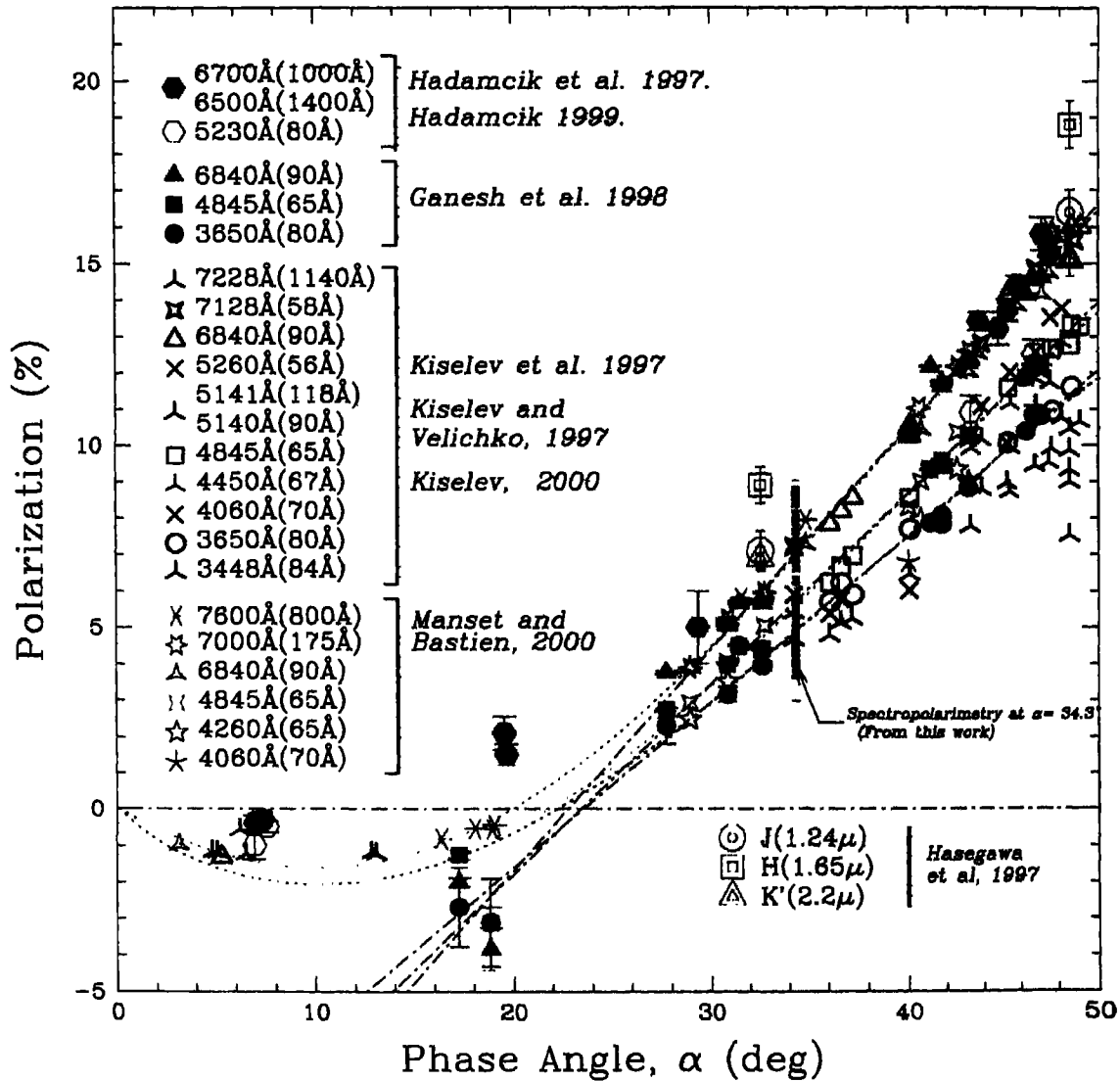


Figure 5.1: Phase dependent polarization of Comet Hale-Bopp. The spectropolarimetric data of comet Hale-Bopp at $\alpha = 34.3^\circ$ from this work is plotted in multiple colors corresponding to the wavelengths. The linear and trigonometric fits are also over-plotted.

ization. In Fig. 5.1 we see that the wavelength dependence increases with phase angle, as is evident from the divergence in the data points. We have grouped the data plotted in Fig. 5.1, into six groups (*Groups 1 - 4* in continuum and *Group 5 - 6* in emission). The observations in the wavelength range from 7600Å to 6500Å, shown in red color, forms the first group (*Group 1*). The observations with the filters 5230Å(80Å) and 5260Å(56Å) shown in green color is the second group (*Group 2*). Observation points through 4845Å(65Å) and 4450Å(67Å) (colored cyan) constitute the third group (*Group 3*). The fourth group (*Group 4*) shown in blue data points are observed through the 4260Å(65Å), 3650Å(80Å) and 3448Å(84Å). The fifth group (*Group 5*), shown in black are some of the cometary emission bands which are well separated from the normal trend of the polarization-phase curve. The 4060Å(70Å) filter corresponds to the C_3 emission and 5141Å(118Å) and 5140Å(90Å) filters are for the C_2 emission band. Though the filter at 7000Å(175Å) corresponds to the H_2O^+ emission and the filter 4260Å(65Å) to CO^+ emission, we have grouped them in the first and fourth group respectively, since they do not show drastic differences in polarization compared to nearby continuum filters. The sixth group (*Group 6*) shown in magenta are the infra-red *J*, *H* and *K* band observations. Of these six groups, the *Group 1* has the largest phase coverage.

The technique of spectropolarimetry allows an evaluation of the continuum polarization and polarization of molecular emission bands (Le Borgne and Crovisier, 1987) separately. Spectropolarimetry of Comets Austin and Churyumov-Gerasimenko has been reported by Myers and Nordsieck (1984). Spectropolarimetric observations of comet Hyakutake C/1996B2 has been reported by Harris, Wood and Fox (1996) and by Harris *et al.* (1996). The spectropolarimetric observations of the comet 1995 O1 (Hale-Bopp) and comet 81P/Wild 2 are reported here. The wavelength dependent continuum polarization are modeled to investigate the dust compositions, porosity and organic fraction.

5.3 Observations

5.3.1 Spectropolarimetry of comet 1995 O1, Hale-Bopp

Spectropolarimetric observations of the central coma of comet 1995/O1 (Hale-Bopp) was carried out on 24 April, 1997 using the newly built optical, dual-beam, automated medium resolution spectropolarimeter (O-DB-AMRSP) for the 2.34m Vainu Bappu Telescope. A 300 l/mm grating blazed at 5000\AA with a slit width of $800\mu\text{m}$ was used. A TK1024 Photometrics liquid N_2 cooled CCD was used as the detector. A detailed report on the Instrumentation and calibration of this instrument is presented in *Chapter 3*.

The spectropolarimeter slit was kept along North-South. The comet center was placed close to the northern edge of the slit to enable observations of the southern part of the coma where a prominent shell at 11.5 arcsec south of the nucleus was visible. Fig.5.2 shows the position of the spectropolarimeter slit on a simulated image of comet Hale-Bopp, for the geometry on this date.

An unpolarized standard star (HD 127762) (Turnshek *et al.*, 1990) was observed to determine the telescope polarization and a polarized standard star (HD 147084) (Hsu and Breger, 1982) was observed to obtain the instrumental zero-point of the position angle. The instrumental response curves $P_c(\lambda)$ and $\Theta_c(\lambda)$ were obtained from the calibrations of the spectropolarimeter (*Chapter 3*).

The basic pre-processing of the data was done with IRAF reduction packages. A dual aperture spectra for the *c* and *o* beam, with two aperture sizes, were extracted from the pre-processed data centered on the central coma. The first aperture size of 14.1 arcsec (*Ap1*), corresponded approximately to the full width at half maximum of the central coma, while the other aperture selected was 26.5 arcsec (*Ap2*), for comparison with the phase dependent observations of the comet by Ganesh *et al.* (1998), Hadamcik *et al.* (1997), Hadamcik (1999), Kiselev and Velichko (1997), Kiselev (2000) and Manset and Bastien (2000). Fig. 5.3 shows the spatial profile of comet Hale-Bopp as observed by the O-DB-AMRSP at 5230\AA . The size and location of apertures *Ap1* and *Ap2* are marked. A second peak seen prominently on the spatial cut due to the prominent shell at 11.5 arcsec south of the nucleus. We select an aperture *Ap_j* centered on the prominent shell with an aperture size of

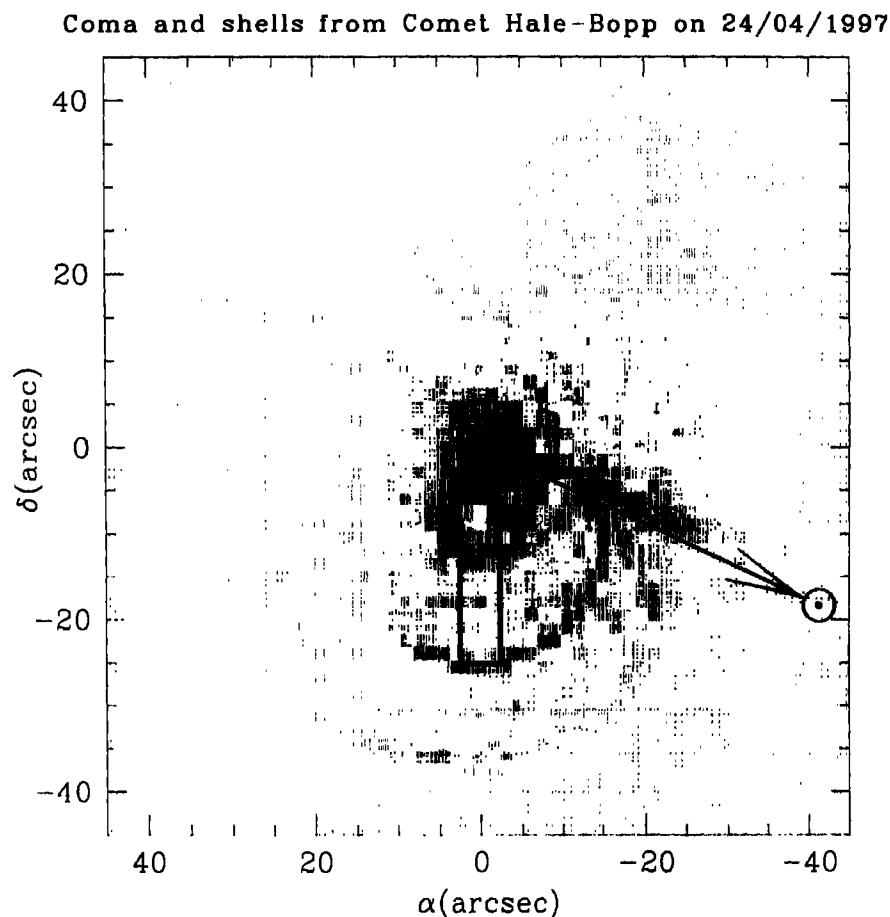


Figure 5.2: Position of the spectropolarimeter slit on comet Hale-Bopp is shown by the vertical rectangular box. The coma and the shells were simulated using the model for the geometry on 24th April 1997 (Chapter 4). North is up and East is to the left. Projected direction of the Sun is indicated by the arrow. The simulated shells expanding towards S-W of the comet center are from the source at 65°.

5.8 arcsec.

Spectropolarimetric data reduction software (SPRS) discussed in *Chapter 3* and *Appendix D*, was used for computing the normalized Stokes' vectors $[Q/I](\lambda)$ and $[U/I](\lambda)$, the percentage $P(\lambda)$ and the angle $\Theta(\lambda)$ of polarization. The wavelength coverage is from 4500Å to 7800Å with a 10Å resolution at $\approx 4.9\text{Å}/\text{pixel}$. Our spectropolarimetric observations of comet Hale-Bopp corresponds to a phase angle of $\alpha = 34^\circ.3$. We have over-plotted $P(\lambda)$ obtained from *Ap2* on the polarization-phase curve in Fig. 5.1. This appears as a spectral strip at $\alpha = 34^\circ.3$. Our results from *Ap2* fits well into the phase dependent observations.

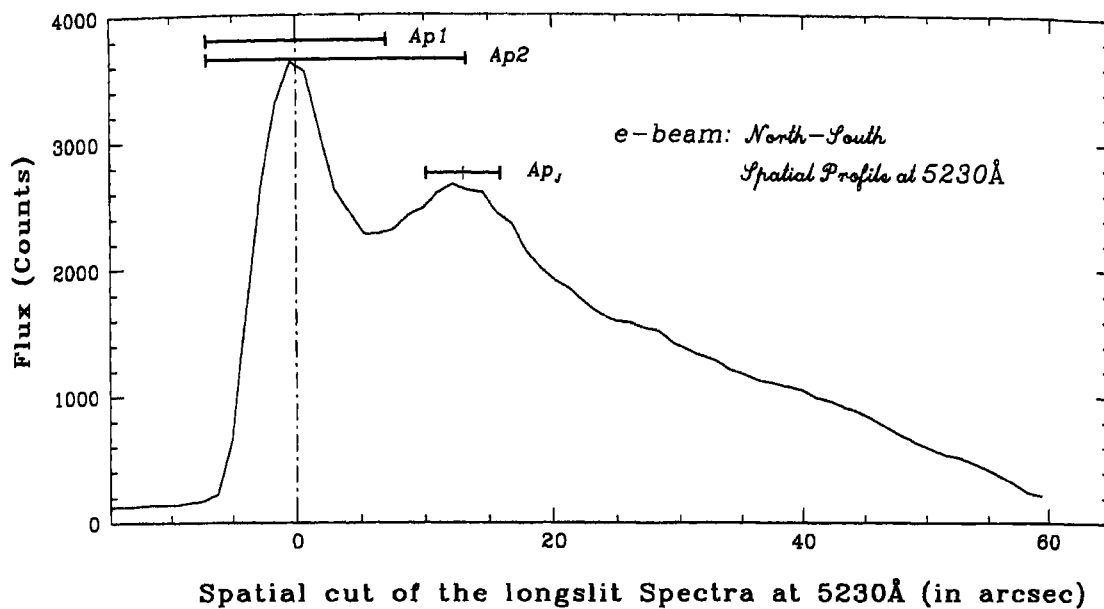


Figure 5.3: Spatial 1-d North-South profile of comet Hale-Bopp as observed by the O-DB-AMRSP at 5230Å. The x-axis is in arcsec, centered on the comet. Left is North and right is south. The y-axis is flux in counts. Note that the flux has not been calibrated for instrumental response. The positions of the apertures Ap1, Ap2 and Ap_J are marked.

5.3.2 Spectropolarimetry of comet 81P/Wild 2

Comet 81P/Wild 2 is the target of NASA's STARDUST mission which will flyby this comet in January 2004 and bring back for the first time, dust samples from the coma of a comet. Thus, any information related to the dust from this comet is extremely valuable before the spacecraft's encounter with the comet.

In spite of strong moon light, it was possible to detect and observe the comet with 30min exposure for each position of the *HWP*. We could obtain enough signal above the background of the moonlit sky. Special care was taken for sky subtraction to eliminate the sky polarization. The unpolarized and polarized standard stars HD 176425 and HD 147084 respectively (Turnshek *et al.*, 1990, and Hsu and Breger, 1982), were observed on April 23, 1997.

The basic preprocessing and data analysis of the April 23, 1997 data is similar to that described in *Section 5.3.1* for comet Hale-Bopp. However, in this case only the central coma was apparent above the bright sky level. An aperture of 8 arcsec, corresponding to the total central coma flux was extracted. *SPRS* was used for determining $[Q/I](\lambda)$, $[U/I](\lambda)$, $P(\lambda)$ and $\Theta(\lambda)$ for this comet.

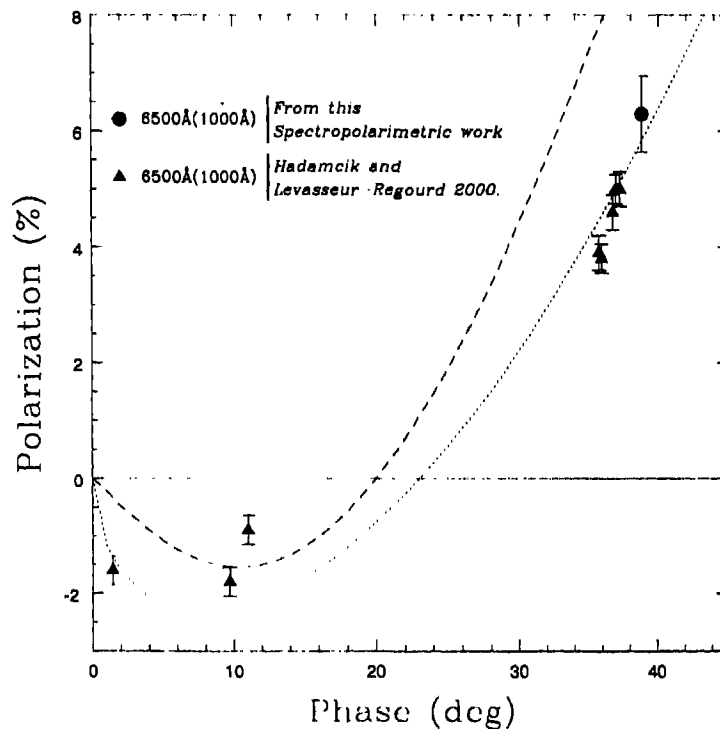


Figure 5.4: Phase dependent polarization of Comet Wild-2. The dotted line is the trigonometric fit to the Wild 2 data, while the dash line is the trigonometric fit to the Hale-Bopp data of (Group 1).

Apart from our observations, the only other polarimetric observations of this comet known to us has been by Hadamcik and Levasseur-Regourd (2000). Fig. 5.4 shows the phase dependent observations by Hadamcik and Levasseur-Regourd through a red filter (6500Å(1000Å)). From the spectropolarimetric data, average polarization from 6000 to 7000Å, corresponding to an ideal square band filter of 6500Å(1000Å) was calculated. This point is also plotted in Fig. 5.4. These data points are tabulated in Table E.2 of *Appendix E.2*.

5.4 Analyzing the Polarization results

Polarization of a comet is dependent on the phase angle α . Manset and Bastien (2000) and Kiselev and Velichko (1997) (Fig. 5.1) have made a linear fit to the positive branch of the phase curve in order to find the slope averaged over 10° beyond the inversion point α_0 (see Geake and Dollfus (1986). However in their paper, Manset and Bastien object to the empirical slope-albedo relation developed

Groups	P_0	a	b	α_0	χ^2
1	58.15 ± 0.64	1.03 ± 0.08	3.02 ± 0.24	19.90 ± 1.64	1643.51
3	53.47 ± 0.20	(0.98)	3.60 ± 0.10	(21.8)	333.11
4	44.04 ± 0.70	(0.85)	3.30 ± 0.39	(22.2)	46.82

Table 5.1: The parameters of the trigonometric fit.

by Dollfus (1989). For comet Hale-Bopp the slope found by Manset and Bastien (2000), is too high and the albedo of the cometary grains cannot be deduced using the slope-albedo relation by Dollfus (1989). A trigonometric fit was also made by these authors to their respective data. In the present work, a trigonometric fit to the collective data of *Groups 1, 3 and 4* has been carried out. Trigonometric fit is a technique developed to represent all data between phase angles 0° and 180° . This function empirical is of the form,

$$P(\alpha) = P_0 (\sin \alpha)^a \left(\cos \frac{\alpha}{2} \right)^b \sin(\alpha - \alpha_0), \quad (5.1)$$

where P_0 , a , b and α_0 are fitted parameters. α_0 is also phase angle of the inversion point, where polarization becomes positive from a negative polarization; typically at a phase angle close to 20° .

The data sets of *Group 1*, which cover a large range in phase angle, were fitted to Eq. 5.1, using the Levenberg-Marquardt's method (Press *et al.* 1992). All the four coefficients P_0 , a , b and α_0 were treated as free parameters. The two main parameters that determine the shape of the trigonometric fit at low phase angles are a , and α_0 , while P_0 , and b determine the shape at larger phase angles. So we fixed the values of a , and α_0 close to the fitted value for the *Group 1*, and varied the other two parameters P_0 , and b to fit the points of *Group 3* and *Group 4*, which hardly have any points at low phase angle. The fitted parameters are shown in Table 5.1. The values, P_{max} at α_{max} and P_{min} at α_{min} , computed from the fit are enumerated in Table 5.2.

A trigonometric fit was also attempted for the data sets of Comet Wild-2, however due to paucity of data, it is very difficult to make a decisive fit.

Groups	P_{max}	α_{max}	P_{min}	α_{min}
1	22.955	72°22	-1.625	9°99
3	18.276	69°87	-1.946	10°62
4	16.043	70°89	-2.075	10°06

Table 5.2: The limits derived from the trigonometric fit.

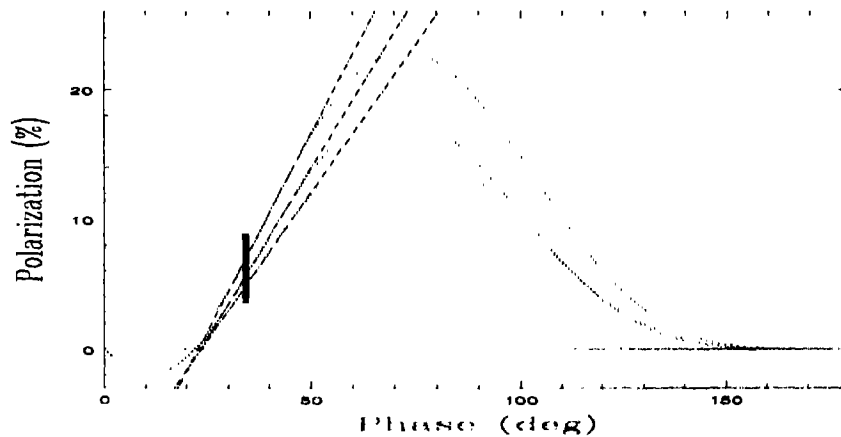


Figure 5.5: Trigonometric fits for $\alpha = 0^\circ$ to 180° . The fits are to the phase dependent polarization of Comet Hale-Bopp. The linear fits and our spectropolarimetric data are also over-plotted.

The methods described so far (linear and trigonometric fits), are just empirical fits with no known basis to any physical law or properties of dust grains. Linear fit was used by Geake and Dollfus (1986) for comparison with laboratory measurements of dusty surfaces. The trigonometric fit was developed to have a good phase dependent representation of polarization.

The best way to analyze polarization data, will be to determine the scattering properties that causes it. An attempt to determine the scattering properties of an ensemble or collection of different types of dust grains with respect to the phase angle and which also explains the wavelength dependent polarization, is made in the present work.

5.5 Modeling Polarization from Scattering Properties of Dust Grains

The dust particles present in a cometary coma scatter and absorb the unpolarized incident solar radiation. The scattered light reaching the earth is partially polarized. The scattering properties, namely the polarization, depend upon the shape, structure, and composition of the cometary grains. Theories of scattering have been developed for well defined particle shapes like spheres, concentric spheres, cylinders, spheroids and so on. These particle shapes only approximate the shape of the actual cometary grains, which are suspected to be rather irregular. In our study here, we make use of the code published in the appendix of the book “Absorption and Scattering of light by Small Particles” by Bohren and Huffman (1983) to compute the model polarization due to scattering of sunlight from the cometary grains.

Scattering properties of grain depend on the size parameter $2\pi s/\lambda$, where s is the size of the particle and λ the wavelength of incident radiation. In addition, it depends on the properties of the grain, usually specified by the complex refractive index $m(\lambda) = n(\lambda) - ik(\lambda)$, where $n(\lambda)$ and $k(\lambda)$ are the refractive and absorptive indices respectively. Since $n(\lambda)$ and $k(\lambda)$ are wavelength dependent, the scattering depends on the wavelength of incident radiation. Some researchers use the complex dielectric constant $\epsilon(\lambda) = \epsilon_1(\lambda) - i\epsilon_2(\lambda)$ instead of the complex refractive index $m(\lambda) = n(\lambda) - ik(\lambda)$. Knowing one set of quantities, the other set can be easily calculated. The relation for $\epsilon_1(\lambda)$ and $\epsilon_2(\lambda)$ are given by

$$\epsilon_1(\lambda) = n^2(\lambda) - k^2(\lambda) \quad \text{and} \quad \epsilon_2(\lambda) = 2n(\lambda)k(\lambda). \quad (5.2)$$

Similarly the relation for $n(\lambda)$ and $k(\lambda)$ are given by

$$\left. \begin{array}{l} n(\lambda) \\ k(\lambda) \end{array} \right\} = \sqrt{\frac{\sqrt{\epsilon_1^2(\lambda) + \epsilon_2^2(\lambda)} \pm \epsilon_1(\lambda)}{2}}, \quad (5.3)$$

where the “+” is to obtain $n(\lambda)$, while the “-” is to obtain $k(\lambda)$ (Krishna Swamy, 1997, Draine, 1994).

The spectral dependence of polarization follow the absorptive index $k(\lambda)$ more closely than the wavelength dependence of the refractivity $n(\lambda)$ (Kolokolova *et al.*,

1997). The polarization increases with $k(\lambda)$ (Bohren and Huffman, 1983). The increase in polarization with $k(\lambda)$ can easily be explained. The scattered light from a grain has a reflected and a refracted component (Fig 5.6). The reflected component

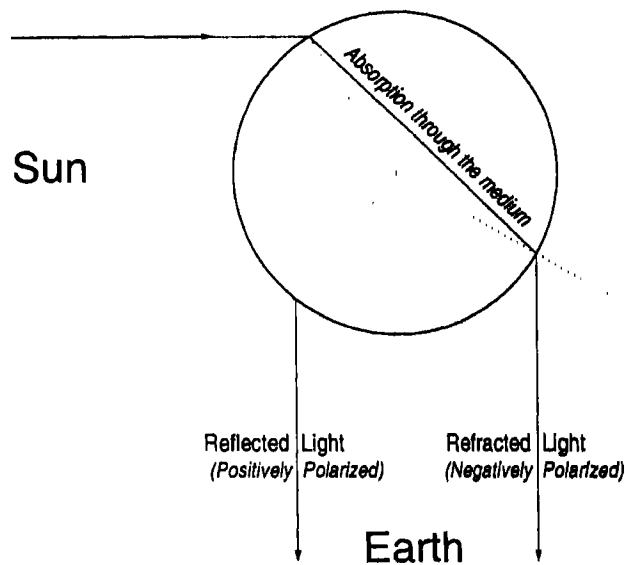


Figure 5.6: The refracted and reflected beams, emerging from a spherical particle at a phase angle $\alpha = \pi/2$. (Adapted from Bohren and Huffman, (1983) [Section 7.1]).

of light is positively polarized, while the refracted component is negatively polarized. The contribution of the refracted component will thus decrease the resulting polarization. The refracted component of light also undergoes an absorption through the medium. As a consequence, the resulting polarization increases with the absorption index $k(\lambda)$. In this chapter we will look at the absorptive index $k(\lambda)$ of several types of grains more closely.

Fig. 5.7 and Fig. 5.8 show the complex indices of refraction $n(\lambda)$ and $k(\lambda)$ of some silicates and carbonaceous matter respectively. The left-side plots are the refractivity $n(\lambda)$ and the right-side plots are the absorptive index $k(\lambda)$. The refractive indices in Fig. 5.7 have been plotted in four sets (*a*, *b*, *c* and *d*) so that the wide range in the absorptive index $k(\lambda)$ could be shown clearly.

In Fig. 5.7*a* the refractive indices of amorphous or glassy Olivine ($Mg_{2y}Fe_{2-2y}$ for $y = 0.4$ and $y = 0.5$) have been plotted (Dorschner, 1995). For $y =$

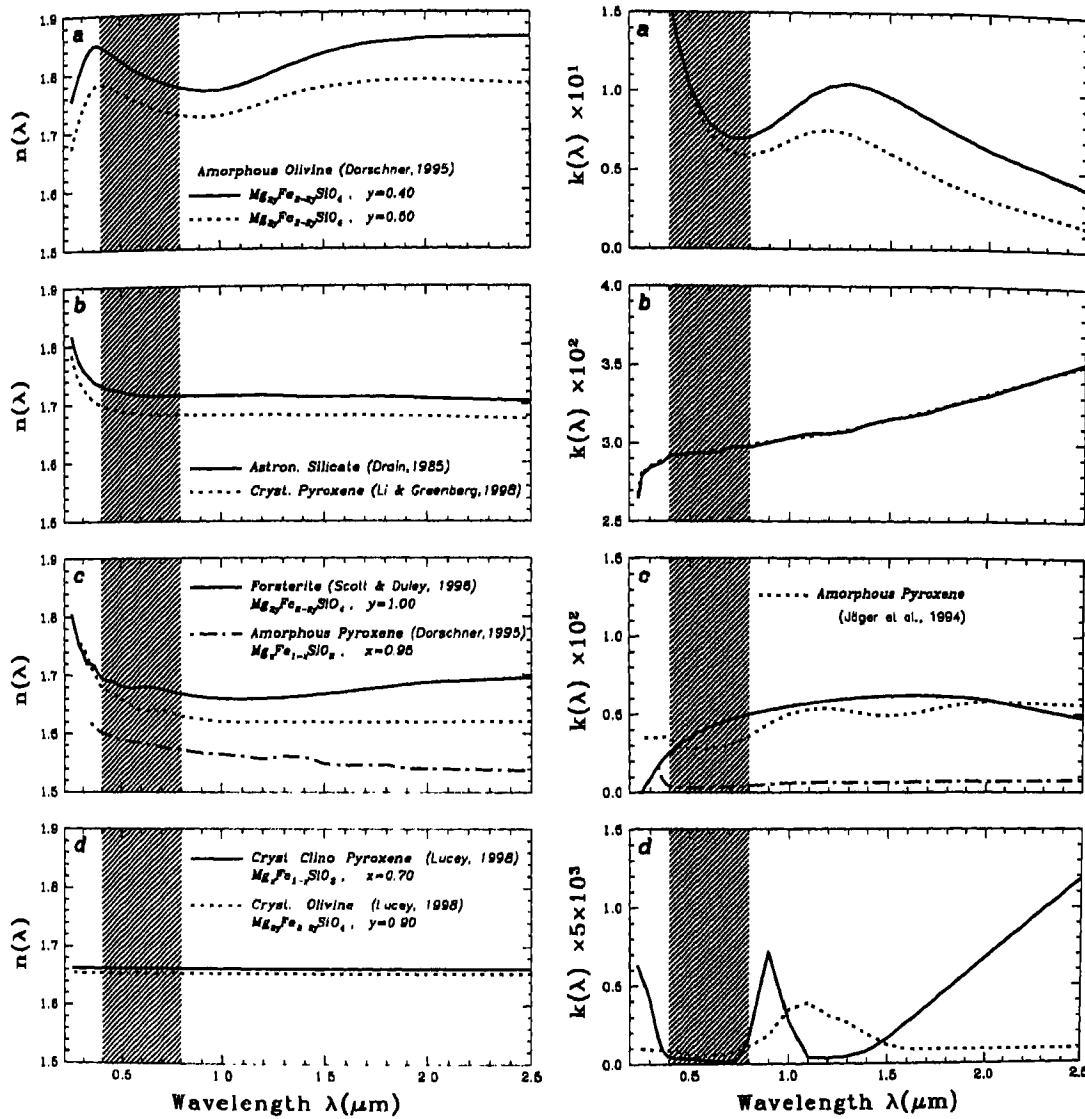


Figure 5.7: Complex Indices of Refraction $n(\lambda)$ and $k(\lambda)$ of Some Silicates. The shaded region in the figure is the optical region that we are interested in this work.

$n(\lambda)$ and $k(\lambda)$ are higher compared to $y = 0.5$. This indicates that the refractive index increases with the Fe content in the amorphous Olivine. In the optical region (The shaded regions in the figures), $k(\lambda)$ decreases very steeply with wavelength λ . In Fig. 5.7b the refractive indices of Astronomical Silicate from Draine (1994) and crystalline Olivine as constructed by Li and Greenberg (1997) are plotted. Note that the $k(\lambda)$ for crystalline Olivine chosen by Li and Greenberg is identical to that of Astronomical Silicate. In Fig. 5.7c, the refractive indices of Forsterite from Scott and Duley (1996), amorphous Pyroxene ($Mg_xFe_{1-x}SiO_3$) with $x = 0.95$ from Dorschner (1995), and amorphous Pyroxene from Jäger *et al.* (1994), are plotted.

Forsterite is part of the Olivine family ($Mg_{2y}Fe_{2-2y}SiO_4$) with $y = 1.0$. In Fig. 5.7d the refractive indices of crystalline Clino-pyroxene ($Mg_xFe_{1-x}SiO_3$ with $x = 0.7$) and crystalline olivine ($Mg_{2y}Fe_{2-2y}SiO_4$ with $y = 0.9$) obtained from Lucey (1998) are plotted.

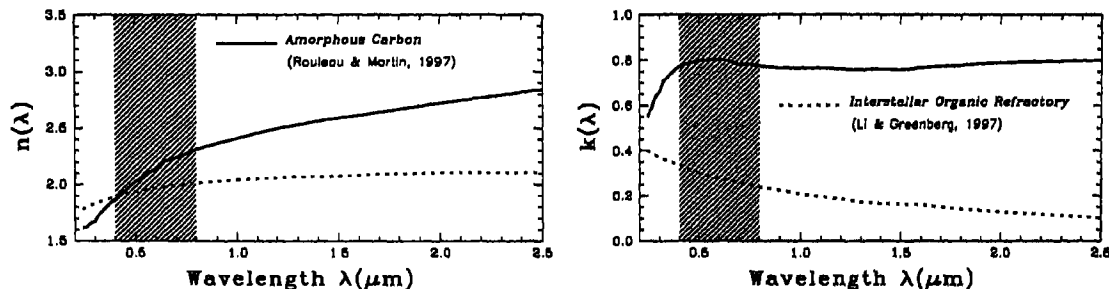


Figure 5.8: Complex Indices of Refraction $n(\lambda)$ and $k(\lambda)$ of Amorphous Carbon and Interstellar Organic Refractory. The shaded region in the figure is the optical region that we are interested in this work.

In Fig. 5.8 the refractive indices of amorphous Carbon (Rouleau and Martin, 1991) and Interstellar Organic Refractory (Li and Greenberg, 1997) are plotted. These two carbonaceous materials have been used by Li and Greenberg (1998) as the organic refractory component in cometary dust to explain the infrared emission from comet Hale-Bopp. In our analysis of cometary polarization, we adopt their assumption and represent the organic refractory in the cometary dust by equal-mass of amorphous Carbon and Interstellar Organic Refractory.

The composition of interstellar, interplanetary, and cometary grains is poorly known. Studies by Mathis, Rumpl, and Nordsieck (1977), Mathis (1979), Mathis and Wallenhorst (1981), Mezger, Mathis, and Panagia (1982), Mathis, Mezger, and Panagia (1983), and Draine and Lee (1988) suggest that the dust grains could be assumed as a mixture of silicate and organic grains. The ratio of silicate to organic mass ($R_m = M_{sil}/M_{org}$) has been measured *in situ* (Greenberg and Hage, 1990) for comet Halley. In absence of *in situ* observations, this ratio in comets, could be determined by considering different R_m values and comparing them with the observations. For simplicity, Li and Greenberg (1998) have considered only three values: $R_m = \infty$, 2 and 1. $R_m = \infty$ represents the case that the dust grain is entirely silicate.

Greenberg and Hage (1990), Hage and Greenberg (1990), Krishna Swamy *et al.* (1988) and Xing and Hanner (1997) have all concluded that cometary grains are

porous and contain an organic component. Investigation of polarization spectra of several possible grain materials by Kolokolova and Jockers (1997) suggest that astronomical silicate must be the most abundant constituent of cometary grains. In the present study, the dust grains are assumed to be formed of silicates and carbonaceous organic compounds. We considered Astronomical Silicate (Draine, 1994) as an example of medium $k(\lambda)$, amorphous pyroxene (Dorschner, 1995) and amorphous Forsterite (Scott and Duley, 1996) as examples of low $k(\lambda)$. Following Wooden *et al.* (1999), amorphous olivine with $y = 0.5$ has been included in the combination as grains of high $k(\lambda)$. As shown in the following section, presence of even a small fraction of organic will grossly alter the refractive index. Hence no attempt was made to identify the nature of the Mg poor silicate components. The effective complex indices of refraction, n and k is calculated adopting the Effective Medium Theory (EMT)¹, using the Bruggeman dielectric function (Bruggeman, 1935). The Mie scattering code by Bohren and Huffman (1983) (see *Chapter 1*) was used for computing the intensity of light scattered by a spherical grain of radius s . If i_{\perp} and i_{\parallel} represent the components of the scattered light intensity perpendicular and parallel to the scattering plane, the model polarization due to scattering from this dust grain is expressed by

$$P(s) = \frac{i_{\perp}(s) - i_{\parallel}(s)}{i_{\perp}(s) + i_{\parallel}(s)} \times 100 \quad (\text{in}\%). \quad (5.4)$$

Light scattered by the whole ensemble of dust grains of different sizes contribute to the overall polarization.

5.5.1 Size Distribution Law

It is extremely important that a proper size distribution of cometary dust grains is selected since it will influence the overall scattering intensity, color and polarization. A cometary grain distribution as derived by Hanner (1983) and Hanner *et al.* (1985)

¹The EMT presents an approximation to the estimate of the optical properties of an inhomogeneous particle by its substitution with a homogeneous particle having an effective refractive index (see *Chapter 1*).

has been used in the present work. This distribution law is of the form

$$n(s)ds = \left(1 - \frac{s_0}{s}\right)^M \left(\frac{s_0}{s}\right)^N, \quad (5.5)$$

where s_0 is the minimum grain radius or the lower cut-off size. M is related to the peak grain size (the size where $n(s)$ is maximum), and N defines the slope of the power-law size distribution at large s . The grain size s_p where $n(s)$ peaks is

$$s_p = s_0 \left(\frac{M + N}{N}\right) \quad (5.6)$$

Fig. 5.9, shows how the distribution varies with the three parameters, M , N and s_0 . In Fig. 5.9a, b and c, the parameters M , N and s_0 are varied respectively,

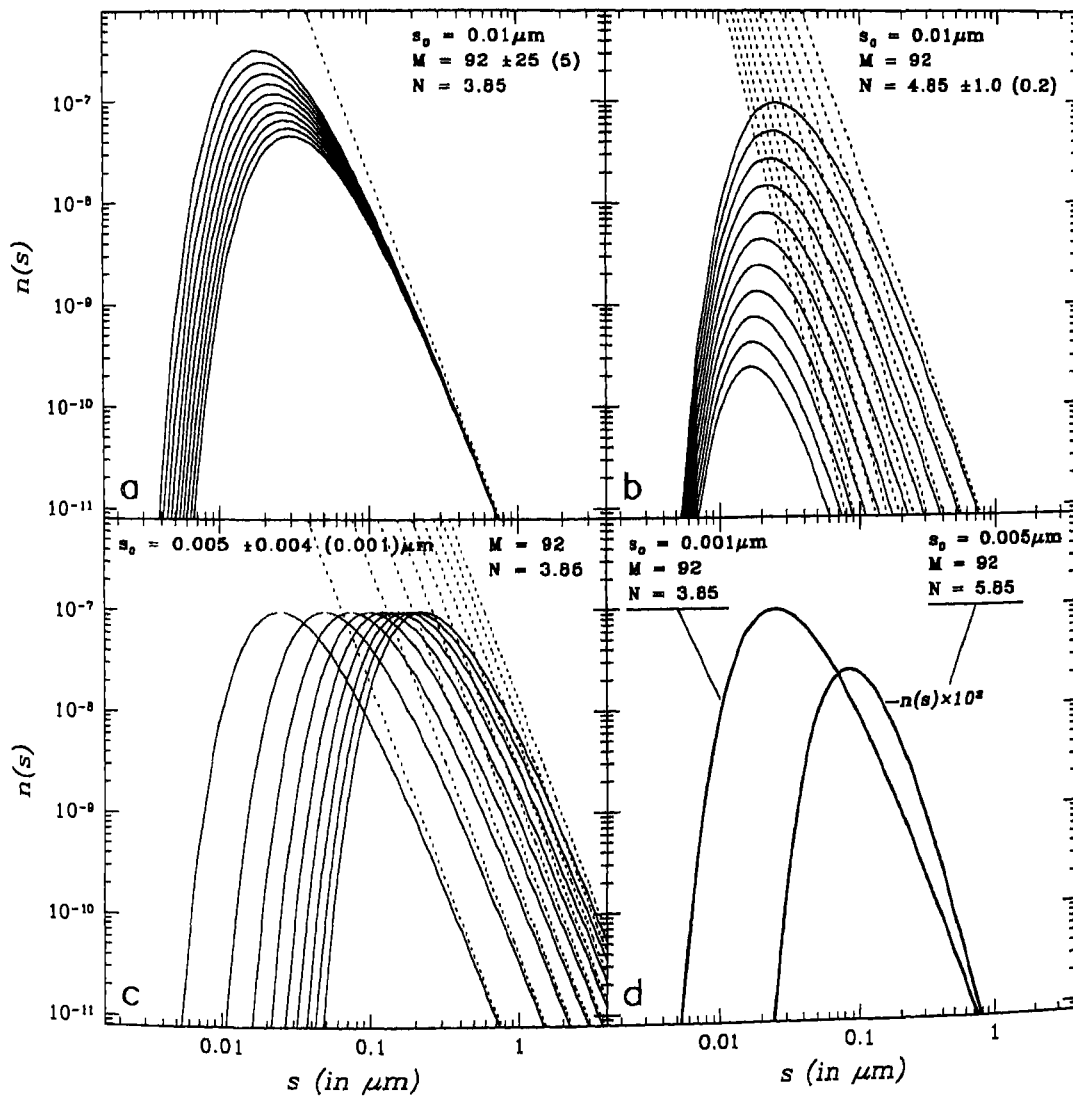


Figure 5.9: Variation of the dust grain size distribution with the three parameters M , N and s_0 . The dotted lines are the power law distributions $(s/s_0)^N$.

while the other two are held fixed. In Fig. 5.9a, M varies from 67 to 117 with steps of 5 (represented in the figure as 92 ± 25 (5)). In Fig. 5.9b, N varies from 3.85 to 5.85 with steps of 0.2. In Fig. 5.9c s_0 is varied from $0.001\mu m$ to $0.009\mu m$ with steps of $0.001\mu m$. After trying out the least square fits to observed phase dependent polarization, using different combinations of the parameters M , N and s_0 (Section 5.6), a combination of the following dust grain size distributions was selected:

$$\text{Distribution A : } s_0 = 0.001\mu m, \quad M = 92.0 \quad \text{and} \quad N = 3.85,$$

$$\text{Distribution B : } s_0 = 0.005\mu m, \quad M = 92.0 \quad \text{and} \quad N = 5.85.$$

From Eqs.5.5 and 5.6, the grain size s_p and its number density $n(s_p)$ for these distributions are,

$$s_{pA} = 0.02490\mu m, \quad n_A(s_{pA}) = 9.70285 \times 10^{-8},$$

$$s_{pB} = 0.08363\mu m, \quad n_B(s_{pB}) = 2.39863 \times 10^{-10}.$$

The distributions A and B , are plotted in Fig. 5.9d. The distribution B in the figure has been multiplied by 10^2 . These values for the size distribution gave us the best fit to the polarimetric data between the phase angles $\alpha = 20^\circ$ to 35° .

Polarization of the coma computed using the distribution A with different Silicate and organic compositions, can fairly well fit the phase dependent polarization curve for Comet Hale-Bopp. However an addition of dust grains with a size distribution B to the ensemble, improved the phase dependent polarization curve for Comet Hale-Bopp at three different wavelengths.

The total intensity of scattered radiation, parallel and perpendicular to the scattering plane, for such a distribution, is

$$I_{\perp} = \int_s i_{\perp}(s)n(s)ds = \sum_{A,B} \sum_s i_{\perp}(s) \left(1 - \frac{s_0}{s}\right)^M \left(\frac{s_0}{s}\right)^N,$$

$$I_{\parallel} = \int_s i_{\parallel}(s)n(s)ds = \sum_{A,B} \sum_s i_{\parallel}(s) \left(1 - \frac{s_0}{s}\right)^M \left(\frac{s_0}{s}\right)^N. \quad (5.7)$$

We take 70 different grain sizes from 0.05μ to 30.00μ ($0.05\mu \leq s \leq 30.00\mu$) in our computation. In Eqs. 5.7, I_{\perp} and I_{\parallel} are computed for a single grain type. For a

collection of different grain types with different distributions, the scattered radiation I_{\perp}^i and I_{\parallel}^i have to be summed for all the grain types. Assuming equal proportion of each grain type the total polarization due to this collection will be

$$P = \frac{\sum_i (I_{\perp}^i - I_{\parallel}^i)}{\sum_i (I_{\perp}^i + I_{\parallel}^i)} \times 100 \quad (\text{in}\%) \quad (5.8)$$

5.5.2 Polarization Dependence on Silicate to Carbon Ratio and Porosity

Cometary dust is assumed to be a porous conglomeration of silicates and organic elements. In our computations different silicate to organic ratios ($R_m = M_{sil}/M_{org} = 0, 2, 8, 12, \text{ and } \infty$) and porosities ($p = 0\%, 30\%, 35\%, 40\%, 45\%, 50\%, 60\%, 70\%, 80\%, \text{ and } 95\%$) have been considered. As the effective refractive indices depend on the grain composition and porosity, the scattering polarization from these grains will vary. As an illustration, Fig. 5.10 shows the variation in phase dependent polarization with different R_m and p .

The ratio R_m varies horizontally, while porosity is varied vertically in the figure. The left most column ($R_m = 0$) is pure organics (equal mass of amorphous Carbon and interstellar organic refractory) with no silicate. The rightmost column ($R_m = \infty$) is pure silicate. Astronomical Silicate (Draine, 1994) is the silicate compound used in these plots. The porosities for each row of figures are indicated on the right hand axis. The dust grain size distribution law used for these plots is the *Distribution A* (see Sec. 5.5.1). The phase dependent curves have been plotted for three wavelengths, 6840Å (continuous lines), 4845Å (dotted lines) and 3650Å (dashed lines). The phase dependent polarization data (Fig. 5.1) of comet Hale-Bopp for cometary continuum filters 6840Å(90Å), 4845Å(65Å) and 3650Å(80Å) are also over plotted. It is immediately clear that the phase dependent polarization curves vary to a large extent with R_m and p . In all grain types with porosity of 95% the phase dependent polarization curves are almost identical for all the three wavelengths plotted. This is obvious because, 95% of these grains are vacuum. The refractive index of these elements computed using the Bruggeman dielectric functions, is close to the vacuum refractive index. As explained in the next section, at high porosity levels these results

are unreliable and use of DDA techniques (*Chapter 1*) is recommended.

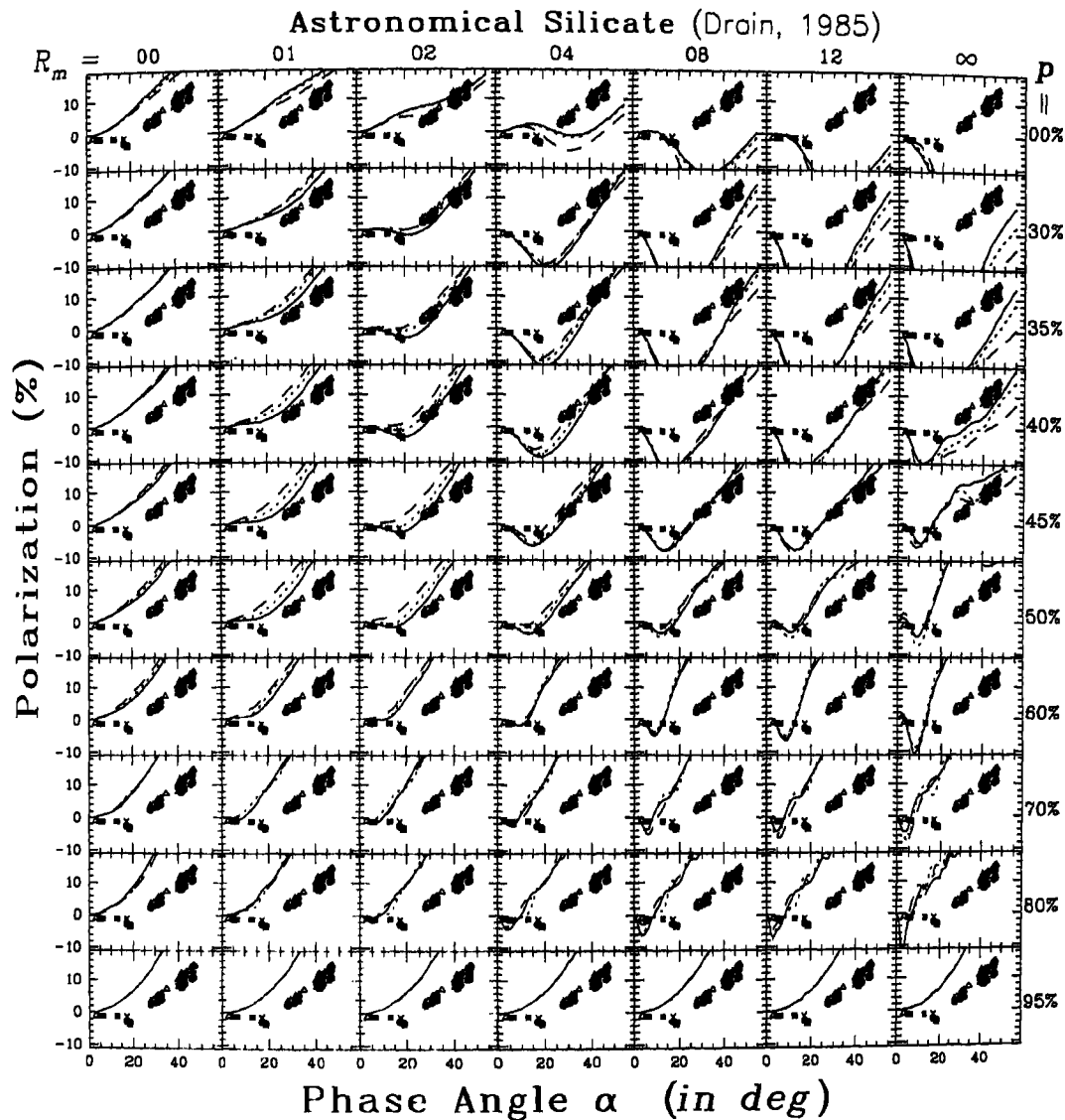


Figure 5.10: Phase dependent polarization for different R_m and p . Astronomical Silicate (Draine, 1994) is the silicate compound used in these plots. The phase dependent curves are for three wavelengths (Continuous lines for 6840\AA , dotted lines for 4845\AA and dashed lines for 3650\AA). The phase dependent polarization data of comet Hale-Bopp, at these wavelengths from Fig. 5.1 are also plotted.

5.5.3 Behavior of Highly Porous Grains

In Fig. 5.10 the polarization from the highly porous grains have been plotted using their effective refractive indices. It is however not very adequate to represent these dust grains of such high porosity by a homogeneous spherical grain with an effective refractive index. Mukai *et al.* (1992) in their work on radiation pressure force finds that the value of β (Eq. 1.2) becomes independent of the size of the aggregate porous grain and finally approaches a constant value deduced for the individual constituent particles. This implies that, the scattering properties of the porous aggregate will behave as a composite of many smaller, either individual or clumps of less porous grains. Fig 5.11 is a simulation of a porous grain with a fractal structure of fractal dimension $D = 1.93 \pm 0.07$ (Mukai *et al.*, 1992). The region in the box of Fig 5.11, is



Figure 5.11: A fractal representation of a porous dust grain. This porous aggregate is a ballistic cluster-cluster aggregation (BCCA), produced by three dimensional Monte-Carlo simulation (Mukai *et al.*, 1992).

one such sample of a region that could behave as one of the smaller and less porous grains. Therefore the presence of highly porous grains will effectively increase the number of smaller grains. We believe, that majority of the small grains in the selected distribution law (*Distribution A*) represent elements in these porous grains.

5.6 Fitting the Phase Dependent Polarization

5.6.1 Hale-Bopp Data

Predicted polarization of an ensemble of grains at the three continuum wavelengths 6840Å, 4845Å and 3650Å corresponding to observations of comet Hale-Bopp by Ganesh et al. (1998) and Manset & Bastien (2000) were computed. For a proper match with the observations over the entire range of phase angle and the three colors, combinations of grain types and proper choice of their size distribution are essential.

Cometary dust grains (Fig. 1.1) are assumed to be a collection of different silicate-organic elements. As a first guess, a four component combinations of silicates each with 30 different combinations of p and R_m of grain types with low, medium and large $k(\lambda)$ were considered. Polarization computed using Eq. 5.8 for a total of 810,000 combinations were compared with the observed phase curves in the least square sense. As mentioned in Sec. 5.5.1 the χ^2 s using distribution A ($s_0 = 0.001\mu m$, $M = 92.0$ and $N = 3.85$) was found to be better than other combinations of these parameters. Hence size distribution A was chosen to represent the combined grain population in the coma and shell in the aperture.

Almost all the good fitting combinations had Astronomical Silicate with medium porosity with $30\% < p < 45\%$ in common. Others were repetitions with different members of Mg rich olivine or pyroxene in amorphous or crystalline form with slightly differing values of R_m and p . This readily follows from Fig. 5.12 which shows the phase dependence of the polarization produced by grains of four different silicate content and for different values of R_m and p .

The four different silicate contents are,

Fig. 5.12a : Astronomical Silicate (Draine, 1994),

Fig. 5.12b : Amorphous Pyroxene with Mg number 0.95 (Dorschner, 1995),

Fig. 5.12c : Forsterite (Scott and Duley, 1996),

Fig. 5.12d : Mg poor amorphous Olivine with Mg number 0.5
(Dorschner, 1995).

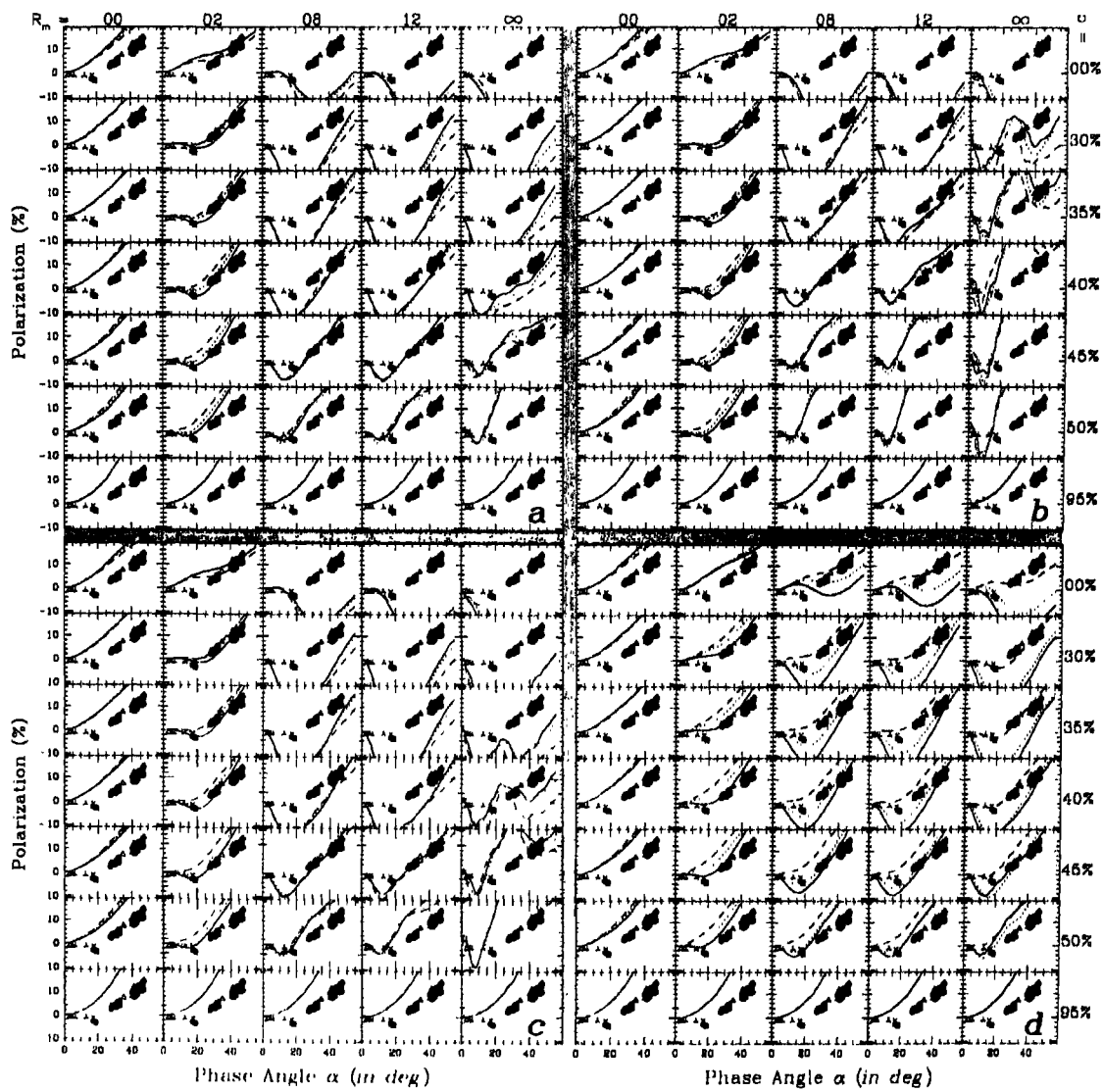


Figure 5.12: Phase dependent polarization for a varied R_m and p . The silicate contents are: a) Astronomical Silicate, b) Amorphous Pyroxene, c) Forsterite and d) Mg poor Amorphous Olivine. Other details are similar to that of Fig. 5.10.

Astronomical Silicate has been re-plotted in Fig. 5.12a for comparison with the other three silicates.

For $R_m \leq 12$, the polarization *vs* phase curves for Mg rich crystalline olivine, amorphous pyroxene and Forsterite are not only similar to each other but also resemble curves of Astronomical Silicate apart from a shift in porosity within $\pm 10\%$. The fluctuations in the curves occur because of interference of refracted and reflected components (Kolokolova *et al.*, 1997). These fluctuations disappear for Astronomical Silicate and Mg poor olivine because of the reduction of the refracted component (see Fig 5.6) due to a higher value of the absorptive constant k ($k \approx 0.03$ for As-

tronomical Silicate and $k \geq 0.1$ for *Mg* poor olivine, while k is less than 0.01 for other silicates). Thus even a small value of $R_m = 12$ is sufficient to significantly increase the absorptive part of refractive index which mainly controls the polarization (see Fig. 5.6). Similarly, the influence of porosity masks the differences in the intrinsic absorptivity of the different silicate types. *Mg* rich pure silicates (pyroxenes and olivines in crystalline or amorphous state) which have the absorptive part of the refractive index $0.0001 < k < 0.01$ could be differentiated as a group from Astronomical Silicate which has a larger absorptive index of $k \approx 0.03$. Amorphous olivine with *Mg* fraction of 0.5 displays a very different polarization curve. The large wavelength dependent gradient increasing towards blue, of the absorptive constant k , increases the positive polarization for all colors and more so in blue. The color dependence of polarization for grains of olivine with low *Mg* content are opposite to what is observed for comets. These grains may however constitute a minor fraction of the cometary grain ensemble.

From the preliminary fits to the phase dependent polarization, the necessity of adding elements to the collection with varied weights was felt. Eq. 5.8 with varied weights ω_i will modify to,

$$P = \frac{\sum_i \omega_i (I_{\perp}^i - I_{\parallel}^i)}{\sum_i \omega_i (I_{\perp}^i + I_{\parallel}^i)} \times 100 \quad (\text{in}\%). \quad (5.9)$$

In reality a range of porosity and organic fractions should be considered. However due to computational constraints the combinations had to be restricted. Eight grain types with *Distribution A* were selected based on the least-square fit. The weights were adjusted interactively. During this fit, An additional amount of Astronomical Silicate with the dust grain size distribution of *Distribution B* (see *Sec. 5.5.1*) improved the fits. This *Distribution B* peaks at $0.083\mu m$, with a short band width. The short bandwidth is due to the larger lower cut-off size of $s_0 = 0.005\mu$ and higher power-law gradient of $N = 5.85$ (Fig. 5.9).

The combination of the 11 grain types with 8 grain types of *Distribution A* and the remaining 3 with the *Distribution B*, with porosity ranging from 0% to 45% taken as the initial value in the next rigorous least-square fit in *Sec. 5.7*

types are enlisted in Table 5.3 with their corresponding R_m , p , size distribution and normalized weights $\omega_i \cdot n_d(s_{pd})$. The highly porous grains were not directly

i	Grain Type		R_m	Porosity	Dist.	Norm. Weights
			M_{sil}/M_{org}	%	d	$\omega_i \cdot n_d(s_{pd})$
1	Astronomical Silicate	SiA/SiX †	2	0%	A	33.8%
2	Astronomical Silicate	SiA/SiX	2	35%	A	24.2%
3	Astronomical Silicate	SiA/SiX	2	45%	A	9.7%
4	Astronomical Silicate	SiA ♠	∞	45%	A	4.8%
5	Forsterite	SiX ♣	8	35%	A	4.8%
6	Amorphous Pyroxene	SiX	12	35%	A	9.7%
7	Amorphous Pyroxene	SiX	∞	40%	A	1.2%
8	Amorphous Olivine	Mg poor	∞	45%	A	7.3%
9	Astronomical Silicate	SiA/SiX	2	35%	B	2.4%
10	Astronomical Silicate	SiA/SiX	2	0%	B	1.2%
11	Astronomical Silicate	SiA	∞	45%	B	1.0%

Table 5.3: The Combination of 11 grain types fitting the phase polarization curve for Comet Hale-Bopp. Note that “ ∞ ” represent that the particular element does not have any organic content.

♠ SiA : Astronomical Silicate as a sample of medium absorptive index $k(\lambda)$.

♣ SiX : Mg rich silicate, either crystalline or amorphous/pyroxene/olivine: Forsterite and Amorphous Pyroxene were taken as sample member of low absorptive index $k(\lambda)$.

† SiA/SiX : Due to high organic content ($R_m = 2$), it is difficult to distinguish between Astronomical Silicate, SiA and SiX with certainty (see Fig. 5.12). Astronomical Silicate was taken as the sample member.

considered. As explained in Sec. 5.5.3, at high porosities ($p > 95\%$), the scattering properties of the grains resemble those of individual subunits of sub-micron size (Xing and Hanner, 1997, Mukai *et al.*, 1992). Hence highly porous grains of larger size may be implicitly included in *Distribution B* which has the sub-micron size grains.

In Table 5.3, Mg rich silicate is represented as SiX . It could be crystalline or amorphous pyroxene, or olivine, or Forsterite. At high organic content ($R_m = 2$), it is difficult to distinguish between SiA and SiX with certainty (see Fig. 5.12). Therefore, the grain types with $R_m = 2$ are represented as SiA/SiX . The normalized weights $\omega_i \cdot n_d(s_{pd})$ in percentage of the total weight, have been tallied so that relative abundance of grains with *Distribution A* and

could be directly compared. It may be noted that the peak number density $n_A(s_{p_A})$ is 404.516 times larger than $n_B(s_{p_B})$ (see *Sec. 5.5.1* and Fig. 5.9d).

The negative polarization of comets at small phase angle is generally explained by the roughness of the grains or by coherent back-scatter and multiple scattering in the agglomerate grains at back scattering angles *i.e.* at low phase angles. The Mie theory does not consider these effects and thus may not explain the data at low phase angles. To explain the negative polarization of comets at small phase angles, Xing and Hanner (1997) proposed that there is a mixture of transparent and absorbing grains in comets such that at small phase angles, the absorbing particles are unpolarized and the negative polarization is produced by the transparent particles. For comet Hale-Bopp, high polarization at large phase angles is contrasted by a weak negative branch at low phase angles (Hadamcik, Levasseur-Regourd and Renard (1997), Kiselev and Velichko (1997), Manset and Bastien (2000)). It is seen from Fig. 5.12, that high silicate content in the grains produce large negative polarization at small phase angles ($\alpha < 20^\circ$). In our phase dependent fit, the dust grains with large organic content ($R_m = 2$) help to reduce the negative branch. Following Vasundhara (2001) the polarization at phase angles $\alpha > 38^\circ$ have been matched by increasing the *Mg* poor silicate content. Since at large phase angles during 1997, the northern region of the comet being sunlit, such an increase is suspected by Vasundhara, to be due to the dichotomy in the surface composition in the northern and southern region of the comet Hale-Bopp.

Our spectropolarimetric observations of comet Hale-Bopp at $\alpha = 34.3^\circ$ is at a lower phase angle hence no additional weights were assigned to *Mg* poor silicate component. In Fig. 5.13, the computed phase dependent polarization (*Top Panel*) and wavelength dependent polarization (*Lower Panel*) of Comet Hale-Bopp are plotted along with the phase dependent polarization data of Fig. 5.1, and the wavelength dependent polarization from *Ap1* and *Ap2* (see *Sec. 5.3.1*). The model polarizations are computed using the 11 grain types with their respective weights tabulated in Table 5.3.

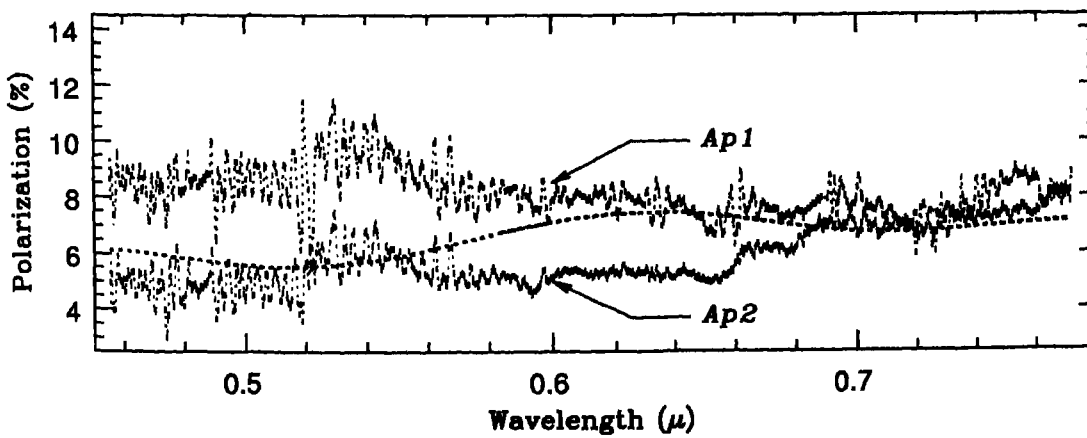
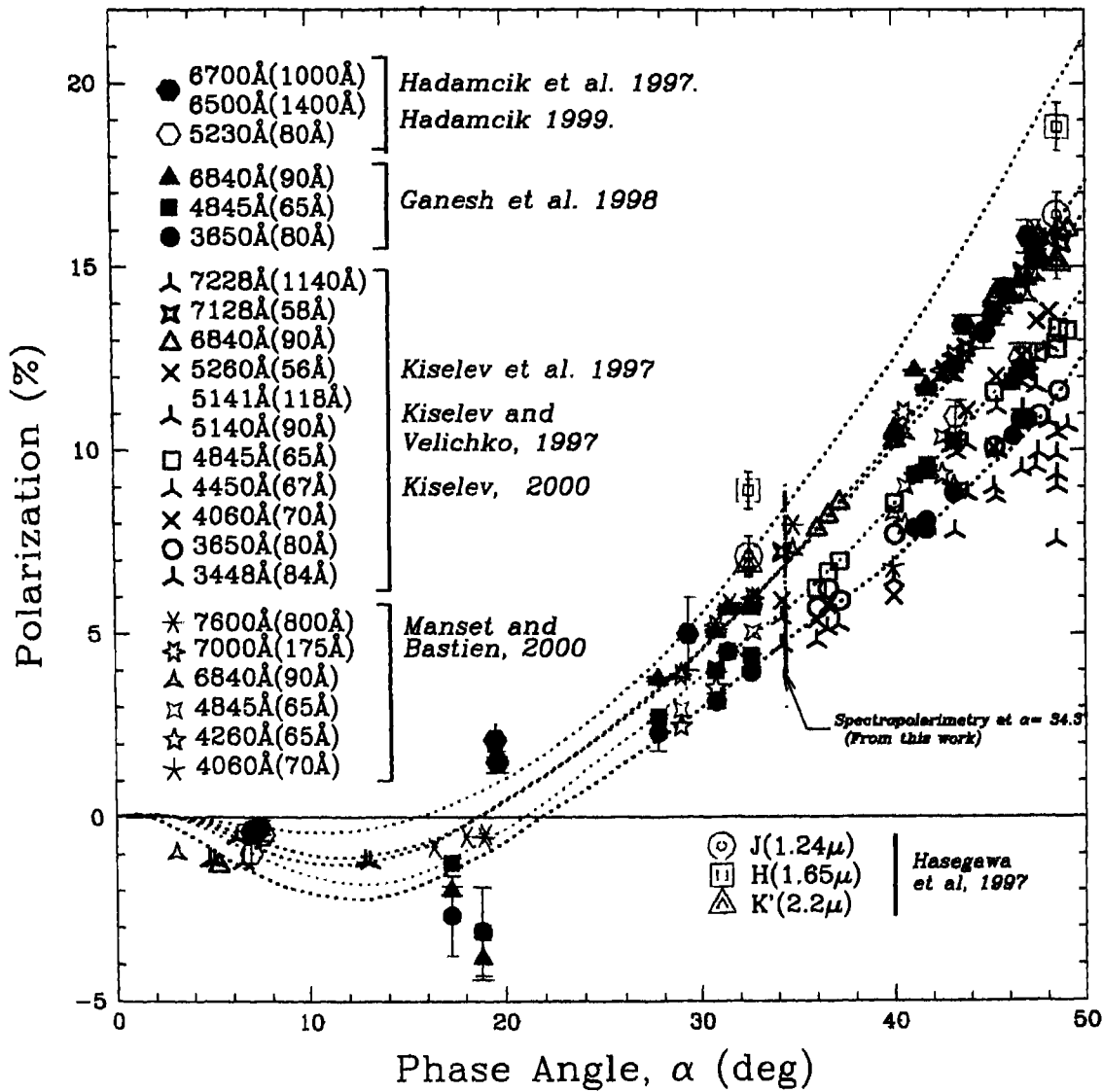


Figure 5.13: A model fit of the phase dependent polarization and wavelength dependent polarization of Comet Hale-Bopp. The wavelength dependent polarizations are through the aperture Ap1 and Ap2. Over-plotted is the wavelength dependent model polarization (dotted line), optimized through phase dependent polarization at three wavelengths.

The relative weights of the grain types optimized through phase dependent polarization at three wavelengths, matches reasonably well with Ap_2 while Ap_1 has a higher polarization in the blue. Equipped with this fit, a much more rigorous weight determination by fine tuning with wavelength dependent fit to our spectropolarimetric data through aperture Ap_1 , Ap_2 and Ap_J was carried out. This work is presented in *Section 5.7*.

5.6.2 Wild 2 Data

For comet Wild 2, due to the paucity of polarization measurements at different phase angles, and non availability of multi-color polarization data; it was not possible to carry out a rigorous three color phase dependent polarization fit, as was done for Comet Hale-Bopp. For fitting the Wild 2 phase polarization curve, the computer code that performs the χ^2 fit by computing the total polarization using Eq. 5.8, for different combinations of the collection; was improved and extended to have a maximum combination of 6 grain types of equal weight collection. A combination of 3 different distribution laws were tried.

$$A: \quad s_0 = 0.001\mu m, \quad M = 92.0 \quad \text{and} \quad N = 3.85$$

(Used for Hale-Bopp, present work)

$$C: \quad s_0 = 0.050\mu m, \quad M = 8.47 \quad \text{and} \quad N = 3.70$$

(Hayward, Hanner and Sekanina, 2000)

$$D: \quad s_0 = 0.100\mu m, \quad M = 12.89 \quad \text{and} \quad N = 3.60$$

(Jorda *et al.*, 1997)

Fig. 5.14 shows these three distributions. Note that the *Distribution A* has been used along with *Distribution B* for some grain types for modeling the polarization of comet Hale-Bopp (*Sec. 5.5.1*). The other two distributions, *Distribution C* and *Distribution D* have higher percentage of larger grains.

A model fit to the data was performed by using different permutations and combinations of 6 grain types with the 3 different distribution laws, with organic contents ($R_m = 0, 2, 8, 12$ and ∞) and with porosities $p = 0\%, 40\%$ and 60% . A finer grid of R_m and p is unwarranted because these cannot be tightly constrained in any case

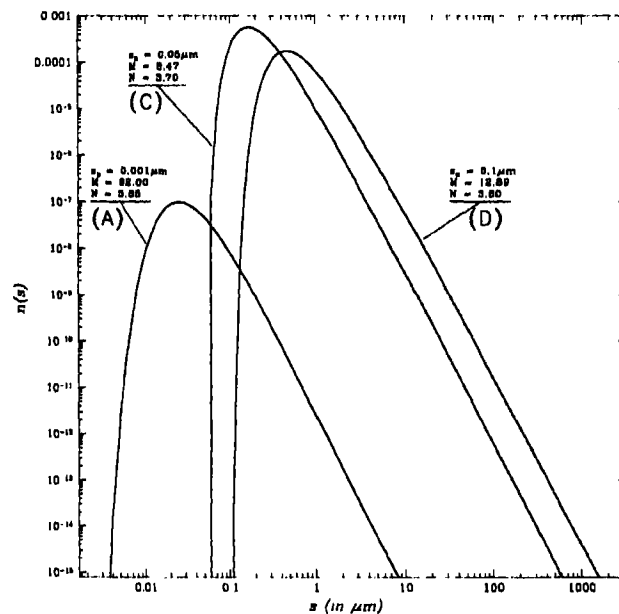


Figure 5.14: Size distribution laws for Wild 2. The Distribution A has been used for comet Hale-Bopp (Fig. 5.9d).

due to limited data points. From the first 2000 best χ^2 fits to the phase dependent polarization at 6500\AA , the best ones were selected visually by plotting them. It was however difficult to distinguish between some of the combinations because only a single wavelength constraint could be applied vis-a-vis the three wavelength phase dependent polarization fit for comet Hale-Bopp. From the first 2000 best χ^2 fits, 500 combinations were selected.

5.7 Determining the Spectropolarimetric Continuum for Comet Hale-Bopp

The dust composition of 11 grain types with their corresponding weights ω_i enlisted in Table 5.3, are assumed as the initial guess. Keeping the least significant weight of *Distribution A*, ($\omega_6 = 1.00$) constant, we iterate the rest of the 10 weights, to fit our spectropolarimetric data from Ap_1 , Ap_2 and Ap_J independently. The 10 weights were changed over grid values around the initial guess (Table 5.3). For each and every variation of the weights ω_i , the model polarization was compared with the observed polarization. By spline fitting the model polarization with the data point grids, χ^2 fits were made. After each iteration, the new weights ω_i , for the best χ^2 fit

were selected and a fresh iteration was performed around these new weights. After multiple iterations, good fits to Ap_1 , Ap_2 and Ap_J were obtained which converged reasonably well. Table 5.4 enlists the total percentile weights $\omega_i \cdot n_d(s_{pd})$ for the best

i	Grain Type		R_m	p %	Dist.	$\omega_i \cdot n_d(s_{pd})$ (in %)		
						(for Ap_1)	(for Ap_2)	(for Ap_J)
1	Ast. Silicate	SiA/SiX	2	0%	A	29.59%	39.54%	2.00%
2	Ast. Silicate	SiA/SiX	2	35%	A	23.80%	0.47%	0.20%
3	Ast. Silicate	SiA/SiX	2	45%	A	40.08%	2.04%	2.05%
4	Ast. Silicate	SiA	∞	45%	A	0.28%	0.08%	79.95%
5	Forsterite	SiX	8	35%	A	1.54%	25.49%	0.20%
6	Amor. Pyroxene	SiX	12	35%	A	2.52%	0.79%	0.22%
7	Amor. Pyroxene	SiX	∞	40%	A	0.54%	0.70%	1.33%
8	Amor. Olivine	Mg poor	∞	45%	A	1.40%	24.65%	0.38%
9	Ast. Silicate	SiA/SiX	2	35%	B	0.05%	0.08%	0.03%
10	Ast. Silicate	SiA/SiX	2	0%	B	0.05%	1.42%	0.04%
11	Ast. Silicate	SiA	∞	45%	B	0.15%	4.74%	13.61%

Table 5.4: The normalized percentile weights $\omega_i \cdot n_d(s_{pd})$ for the combination of 11 grain types, fitting the wavelength dependent polarization of Comet Hale-Bopp through Ap_1 , Ap_2 and Ap_J .

fits to the three apertures (Ap_1 , Ap_2 and Ap_J). From these weights the relative abundance of each species of grain types could be inferred.

In the innermost aperture on the central coma (Ap_1), we notice a substantial amount of Astronomical Silicate with large organic content ($R_m = 2$). The porosity of these dust grains as computed by the model, falls in the range of 0 to 45%.

A larger area of the comet around the coma is sampled by the aperture Ap_2 compared to aperture Ap_1 . A comparison of the weights $\omega_i \cdot n_d(s_{pd})$ from these apertures reveals the relative abundance between the inner and outer regions of the comet coma. In Ap_2 , the amount of Astronomical Silicate with the large organic content ($R_m = 2$) of *Distribution A*, decreases drastically, while number of lower organic content Forsterite with $R_m = 8$ with the same size distribution and Astronomical Silicate with *Distribution B* is increased. This difference in the relative abundance of grains with high and low organic content, between the inner and outer regi-

be due to evaporation of the volatile organic content as suggested b

al. (2001), who find evidence of organic material being destroyed due to heating by the Sun. It may be noted that *Distribution B* indicates high population of grains with a limited bandwidth. Although the number density peaks at 0.083μ , as the scattering efficiency peaks when the size parameter is near unity, the maximum contribution to intensity comes from grains in the range 0.1μ to 0.5μ with a flat maximum and steep fall on both sides (Fig. 5.15). Such a narrow size range could

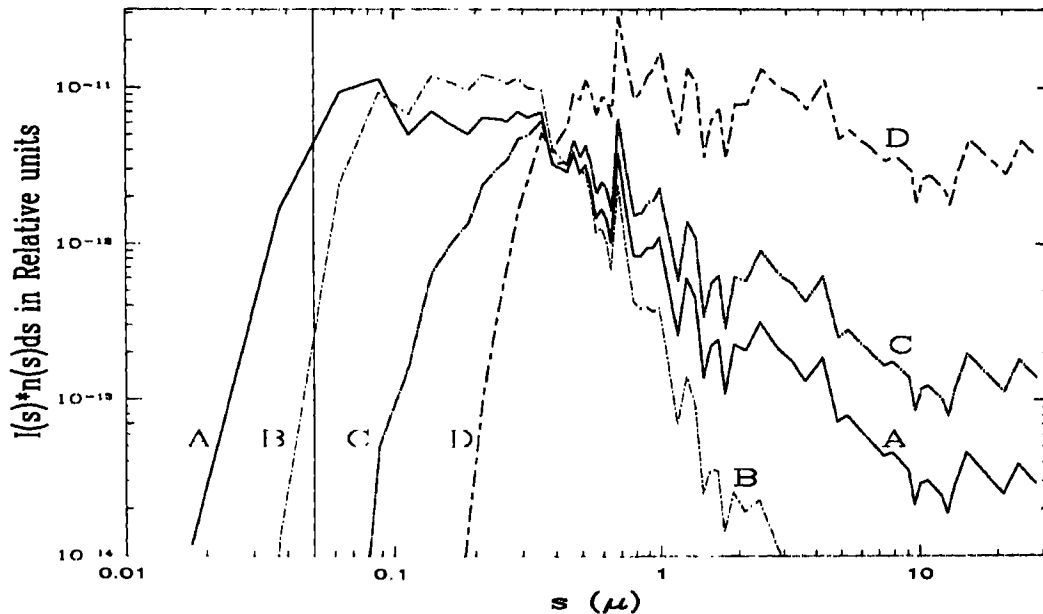


Figure 5.15: The relative scattered intensity at different grain sizes. with four distributions (*Distribution A*, *Distribution B*, *Distribution C*, and *Distribution D*) used in this work. The vertical line at $s = 0.05/\mu$ is the starting grain size used for the computation of the model polarization. (Adapted from: Vasundhara, 2001)

either result from breaking of the very fragile highly porous grain of porosity $\geq 95\%$; or as pointed out by Xing and Hanner, (1997), Kolokolova *et al.* (2001), these may represent the sub-units of large fluffy grains. Larger population of *Distribution B* at larger distances from the nucleus may therefore imply larger fraction of porous grains as a result of evaporation of the volatiles as suggested by Kolokolova.

Forsterite (*SiX*) with $R_m = 8$ and $p = 35\%$, increases approximately by about seventeen times from *Ap1* to *Ap2*. The reason of this difference is not well understood. As mentioned in *Sec. 5.6.1*, it is difficult to differentiate a *Mg* rich silicates from Astronomical Silicate. Hence this grain could also be Astronomical Silicate. In which case partial dispersal of organic refractory could leave behind grains of reducing organic content or increasing R_m value of 8. The same could be true for

the *Mg* poor Olivine which has increased weight in *Ap2*.

Fig. 5.16a, shows the wavelength dependent polarization of *Ap1* and *Ap2* obtained from the spectropolarimetric observations of comet Hale-Bopp and the fitted model continuum polarizations. In Fig. 5.16b and Fig. 5.16c, the residuals between the observed and model continuum polarization for *Ap1* and *Ap2* are plotted respectively. For an ideal fit of the model continuum polarization to the continuum cometary polarization, the residuals in Fig. 5.16b and Fig. 5.16c, would represent the polarization of molecular emission bands in the comet. (Borgne and Crovisier, 1987).

The present approach of computing the model polarization due to a collection of only 11 types of spherically shaped grains computed using the EMT Mie code, is over simplified. With our limited computing facility, the treatment of the problem with EMT is only adequate enough to give us an insight into the organic content and porosities of the grains. Therefore the residuals shown in Fig. 5.16b and Fig. 5.16c, may not be solely due to polarization of molecular emission bands, however the presence and signature of molecular polarization is clearly visible. The regions of the major cometary molecular bands are marked. The signature of solar H_α and H_β are not present on the polarization spectra, and they are not expected to have any polarization features. However, an absorption like feature is seen at *Na-D* lines. distinct C_2 and NH_2 features are seen. The region of C_2 -band sampled by the Hale-Bopp 5141Å(118Å) filter has a slight ^{negative dip} negligible dip compared to the continuum points on both sides. This is in conformity with Kiselev's (2000) data. Kiselev's data shows that this dip increases with the phase angle. A higher polarization at the H_2O^+ band observed with 7000Å(175Å) by Manset and Bastien (2000) shown in Fig. 5.1, is seen as a broad enhancement with spectral features in our data. The region has many H_2O^+ lines corresponding to the (0,6,0) H_2O^+ band. The H_2O^+ lines marked in the Fig. 5.16b and Fig. 5.16c, are laboratory lines for the (0,6,0) and (0,5,0) H_2O^+ band, (Wehinger *et al.*, 1974).

The mechanism of polarization of cometary emission bands is not very well understood. Generally fluorescence process is understood to be isotropic and unpolarized. The theory of the polarization of fluorescence cometary molecular bands is reviewed by Borgne and Crovisier (1987). According to them light emission from cometary

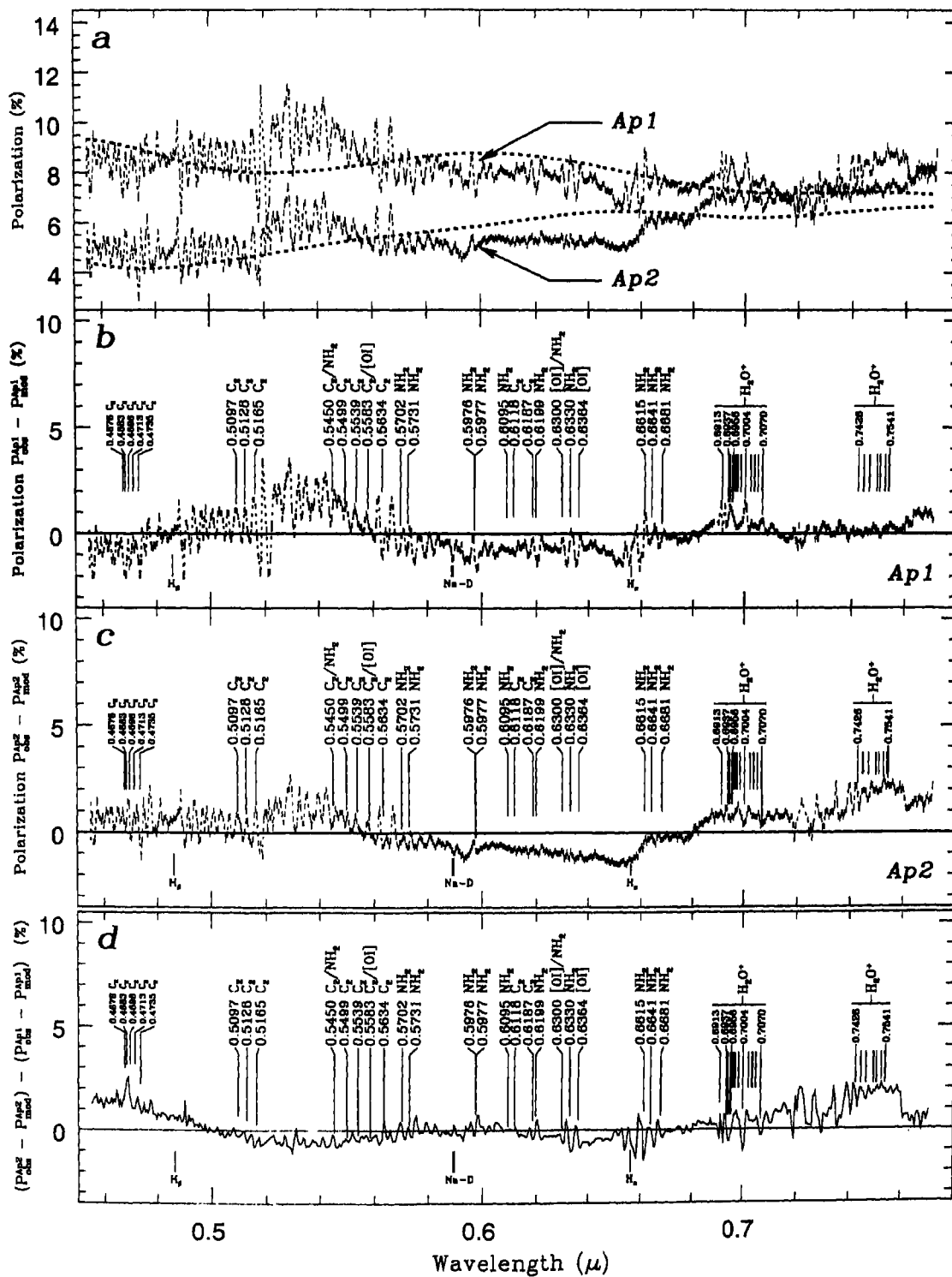


Figure 5.16: Wavelength dependent polarization of Comet Hale-Bopp. The smooth dotted lines in the top panel (a) are the model polarization fitted to Ap_1 and Ap_2 . In the next two panels (b & c) the residuals between the observed and model polarizations are plotted. The bottom most panel (d) is the difference between the residuals of Ap_2 to Ap_1 .

gases are governed by fluorescence process caused by the excitation by the unidirectional radiation of the sun. They argue that this process is thus not isotropic, hence the fluorescent emissions in comets are linearly polarized. Polarization due to unidirectional incident radiation is also shown in the text-books of Mitchell and Zemansky, 1934 and Feofilov, 1959.

Conventionally, linear polarization is positive for polarization perpendicular to the plane of scattering ($I_{\perp} > I_{\parallel}$). When we observe the line or band polarization as an absorption like features on the continuum polarization, the line or band polarization is more parallel than perpendicular to the plane of scattering ($I_{\perp}^f > I_{\parallel}^f$). This effect is seen for the $5141\text{\AA}C_2$ band and the $Na-D$ lines. When line or band polarization appears as emission like features on the continuum polarization, then $I_{\perp}^f < I_{\parallel}^f$. This is seen for the NH_2 and H_2O^+ features. NH_2 and H_2O^+ are isoelectronic and are very similar in their excitation. No theoretical prediction of the polarization of the cometary radiation of these molecules is known (Jockers, 1997).

In Fig. 5.16d the difference between the residuals of $Ap2$ to $Ap1$ has been plotted which can be attributed to the outer parts of the coma, which is encompassed by the aperture $Ap2$. Among the prominent signatures of molecular fluorescence band is the C_2 at $4705 \pm 30\text{\AA}$. This band is not clearly visible in Fig. 5.16b and c, but clearly shows up in the difference. The other prominent feature is the H_2O^+ bands. In Fig. 5.16d the (0,6,0) band at 6987\AA is negative indicating a higher polarization in this band at the inner parts of the coma, while the positive peak for (0,5,0) band at 7468\AA indicate a higher polarization in this band at the outer parts of the coma. This increase in polarization at different regions of the coma is most probably related to the amount of emission by the molecule at different region of the comet. The region between the (0,6,0) and (0,5,0) band of H_2O^+ shows spurious features. This is due to the extremely bad S/N at the telluric absorption band. These spurious features are seen to some extent in Fig. 5.16c which gets further enhanced in Fig. 5.16d.

Fig. 5.17a shows the wavelength dependent polarization on a jet (from aperture Ap_J) of Comet Hale-Bopp. The dotted line is the model fit to the observed polarization which yielded the best χ^2 . The model polarization for $Ap1$ and $Ap2$ are also plotted for comparison. The polarization on the jet is much higher than that on the coma

indicate that SiA with $R_m = \infty$ and $p = 45\%$ seem to be most predominant on the cometary jet while SiX is very much depleted. The predominance of $R_m = \infty$ also indicate that this jet has extremely low organic content.

5.8 Determining the Spectropolarimetric Continuum for Comet Wild 2

A rigorous weight determination for a collection of 6 grain types and fine tuning with wavelength dependent fit to our spectropolarimetric data of comet Wild 2 was undertaken with the selected 500 combinations described in *Sec. 5.6.2*.

To begin with, equal weights of $\omega_i = 1.0$ for $i = 1$ to 6. were applied as initial guess. Keeping the weight of the sixth element fixed ($\omega_6 = 1.0$), the rest of the five weights were iterated to fit our spectropolarimetric data of comet Wild 2. The method was similar to that used for the spectropolarimetric data of comet Hale-Bopp but in this case, all 500 different selected combinations were visually compared with the spectropolarimetric data. Using wavelength dependent polarization, it was possible to clearly select one combination from all the 500 combinations. The best fitting weights of the selected combination was then taken as the initial guess for the least square fit using a finer grid of weights.

Table 5.5 enlists the selected grain types, their organic fraction R_m , porosity p , size distributions and weights ω_i . The model fitting code rejected size distributions A

i	Grain Type	Organic Content $R_m = M_{sil}/M_{org}$	Porosity %	Dist. d	Weights ω_i
1	Forsterite SiX	∞	40 - 60%	C	1.02%
2	Crystalline Olivine SiX	12 - ∞	40 - 60%	C	1.02%
4	Astronomical Silicate SiA	12 - ∞	0 - 40%	C	1.15%
3	Amorphous Olivine Mg poor	12 - ∞	0 - 40%	C	22.19%
5	Amorphous Pyroxene SiX/SiA	2 - 4	0 - 40%	C	10.67%
6	Organic SiX/SiA	0 - 1.5	0 - 40%	C	63.94%

Table 5.5: The Combination of 11 grain types fitting the phase polarization curve for Comet Wild 2. Note that $R_m = 0$ represent that the particular element does not have any Silicate content.

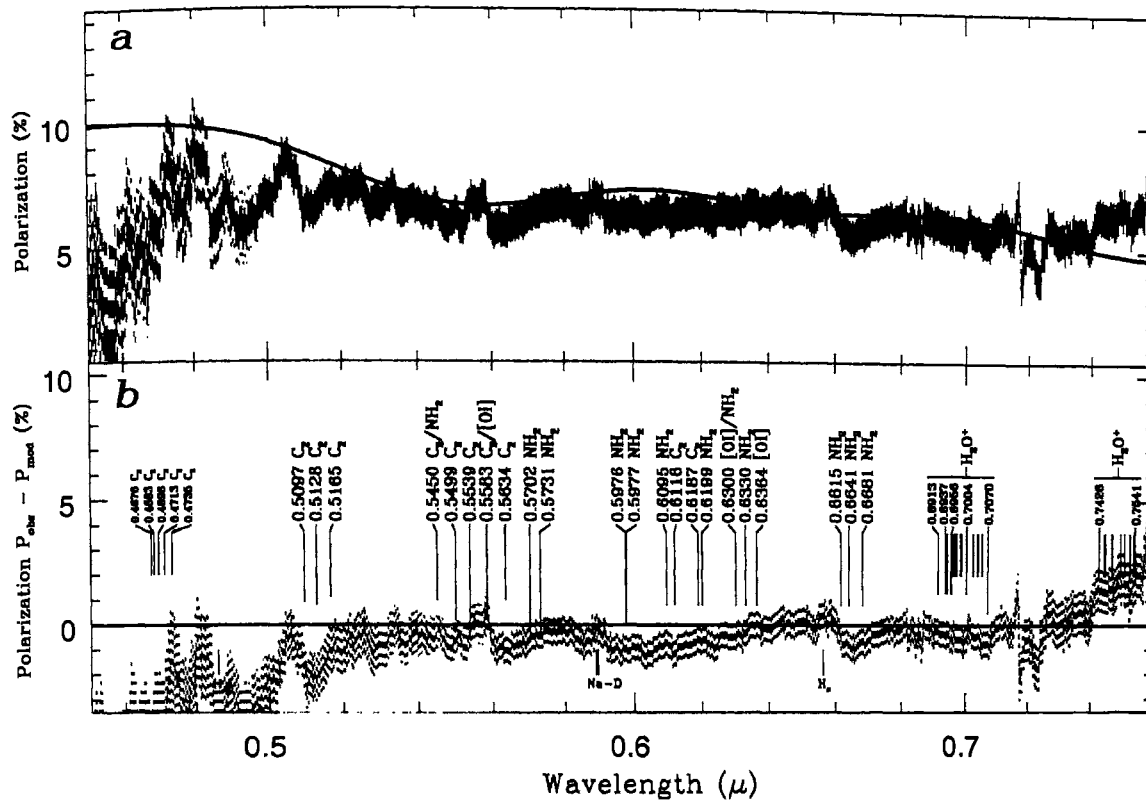


Figure 5.18: Wavelength dependent polarization of Comet Wild 2

and D for all the six grain types. *Distribution C* provided the best χ^2 solution. Therefore, normalization of the weights with $n_C(s_{pD})$ was not required.

The selected combination has high organic content. Among the combinations, the grain type with highest weight ($\omega_1 = 5.99$) is for $R_m = 0$, which is for pure organic. Other grain types with high abundance are, *Mg* poor Amorphous Olivine with low organic content ($R_m = 12$) and Amorphous Pyroxene (*SiX*), again with high organic content ($R_m = 2$). The best fitting distribution *C* indicates that the grains are considerably large.

In Fig. 5.18a, the wavelength dependent polarization obtained from the spectropolarimetric observations of comet Wild 2 is plotted. Over-plotted is its model continuum polarization. In Fig. 5.18b, as in Fig. 5.16b and c, the residual between the observed polarization and model continuum polarization is plotted. Though the comet Wild 2 data is extremely noisy compared to that of comet Hale-Bopp, we can still see the polarization signature of molecular fluorescence band on the residuals. Among the prominent features that could be identified are the absorption like

feature on the C_2 band at 5128\AA , and NH_2 band at 6615\AA . A clear emission like feature is also seen at the $Na-D$ lines.

Sarmecanic *et al.* (1997) from their mid-infrared imaging of comet Wild 2 reported that there was no evidence for excess silicate emission. Due to absence of Silicate emission and low maximum polarization of comet Wild 2 compared to other comets, Hadamcik and Levasseur-Regourd (2000) suggests that this comet could be less dust rich. However, a comparison between the dust to OH and CN ratios for this comet by A'Hearn *et al.* (1995), indicate that this comet is rich in dust.

From our spectropolarimetric data modeling of comet Wild 2, we find that the comet is depleted in silicates. It is therefor, most probably why Sarmecanic *et al.* (1997) do not find any evidence for excess silicate emission.

This comet with high organic content may still be rich in dust as indicated by A'Hearn *et al.* (1995) and be at the same time low in maximum polarization. This low polarization is maybe due to the Mg poor Amorphous Olivine with $R_m = 12 - \infty$, $p = 0\% - 40\%$ in the collection of dusts (See Fig. 5.12d).

The wavelength dependent polarization for comet Wild 2 (Fig. 5.18 is quite flat. For comet Hale-Bopp, the presence of a population of narrow size distribution (as sub-units of large porous clusters/individual grains) appear to produce the large color gradient. For Wild 2, the fits indicate the presence of larger grains and high absorptive grains either due to high organic content or poor Mg content. Both these components have high absorption in blue. Generally comets have larger polarization in the red region of the spectrum compared to that in the blue region (Levasseur-Regourd, Cabane, and Handeborg, 1999). Selective absorption in blue or a larger grain size will increase the polarization at shorter wavelengths and reduce the polarization gradient as it is noticed for comet Wild 2. Investigation of the nature of the grain of this comet is, exciting as it could be substantiated and verified *in situ* by the STARDUST mission.

If our prediction of the dust nature of this comet is correct, it may help to understand a priory the nature of the dust grain impact on the aerogel dust sample collector of the STARDUST spacecraft.

5.9 Summary and Conclusions

The polarization of the scattered light from a cometary grain is strongly dependent on the phase angle and the wavelength. Trigonometric fits on the phase dependent polarization data of comets Hale-Bopp and Wild 2 were performed to determine the minimum and maximum polarizations (P_{min} & P_{max}). The fitted values of P_{min} and P_{max} indicate that Hale-Bopp is an extremely high polarization comet, while Wild 2 is a low polarization comet.

To explain the continuum polarization, the scattering properties of the dust grains were investigated. Different grain types with a range of absorptivities, organic content R_m , porosity p and size distribution laws were considered. As first step, a combination of two grain size distributions (*Distribution A* and *Distribution B*) with a total of 11 grain types, was short-listed by fitting the phase dependent polarization data for comet Hale-Bopp at three wavelengths. The contributions from each of these grain types were weighted by a factor ω_i , while fitting the spectropolarimetric data. Spatial resolution in the N-S direction of the spectropolarimeter data of comet Hale Bopp enabled investigations of the different regions of the comet. Two apertures of different sizes were centered on the coma ($Ap1$ & $Ap2$) while a third aperture (Ap_J) was centered on one of the shell of the comet. The observed wavelength dependent polarization from the three apertures were fitted to the model polarization by varying ω_i . From the fits to $Ap1$ and $Ap2$, it was found that regions close to the center within ≈ 7 arcsec, contain a larger fraction of organics compared to the surrounding outer regions within ≈ 13 arcsec. This could be due to breaking up of the porous grains and evaporation of the volatile organic content. Such a mechanism has been suggested by Kolokolova, *et al.* (2001) from their imaging polarimetric data. Partial dispersal of organic refractory will leave behind grains of reducing organic content or increasing the number of grains with $R_m > 8$. The spectropolarimetric data on the shell (aperture Ap_J) indicate larger polarization and larger color of polarization. Fits to this data set between 4000Å to 6400Å indicate a large fraction of pure silicates with $k < 0.03$. A steep increase in polarization at longer wavelength in this aperture is puzzling. This could be due to aligned non spherical of grains in the shells. The present model assuming spherical grain is inad-

equate to model aligned non spherical grains. Hence our result of modeling of shell polarization may not be conclusive.

For comet Wild 2, the phase dependent observations by Hadamcik and Levasseur-Regourd (2000) at 8 phase angles, through (6500Å(1000Å)) is the only data set that is available to this date. In the absence of enough phase and wavelength dependent polarization data for Wild 2, a rigorous analysis was not possible. A combination of only 6 grain types was considered.

From the model fit to the spectropolarimetric data of this comet, indicate that the grains are rich in organics and less porous compared to Hale-Bopp.

The polarization *vs* wavelength curve for comet Wild 2 is quite flat. For comet Hale-Bopp, the presence of a population of narrow size distribution which could be subunits of large porous clusters or individual small grains, appear to produce the large polarization color gradient. For Wild 2, the fits indicate the presence of larger and high absorptive grains either due to high organic content or poor *Mg* content. Both these components have high absorption in blue. Selective absorption in blue or a larger grain size will increase the polarization at shorter wavelengths and reduce the polarization gradient as it is noticed for comet Wild 2.

The model polarization computed from scattering theory accounts for the continuum polarization of the comet. The residual between the observed and model polarizations, shows an indication of fluorescent polarization of cometary molecular bands. Investigations of fluorescent polarization of molecular bands in comets is challenging and not well explored. An in-depth study of the polarization of molecular bands seen in our data will be taken up in a future work.

References

- A'Hearn, M. F., Millis, R. L., Schleicher, D. G., Osip, D. J., Birch, P. V., 1995. *Icarus* **118** 223.
- Bohren, C. F., and Huffman, D. R., 1983. *Absorption and Scattering of light by Small Particles*, A Wiley-Interscience Publication, John Wiley & Sons Inc., 1983.

- Le Borgne, J. F., and Crovisier J., 1987. In *Symposium on the Diversity and Similarity of Comets ESA SP-278* p. 171.
- Bruggeman, D. A. G., 1935. *Ann. Phys. (Leipzig)*, **24**, 636.
- Diane H. Wooden, David E. Harker, Charles E. Woodward, Chiyo Koike, and Harold M. Butner, 1997. *EM&P*, **78**, 285.
- Dollfus, A., 1989. *A & A* **213**, 469.
- Dorschner, J., Begemann, B., Henning, Th, Jäger, C., and Mutschke. H., 1995. *A & A* **300**, 503.
- Draine, B. T., 1985. *ApJS* **57**, 587.
- Draine, B. T., and Lee, H. M., 1984. *ApJ* **285**, 89.
- Feofilov, P. P., 1959. *The physical basis of polarized emission*, State Physico-Mathematical Press, Moscow (English translation: Consultants Bureau, New York, 1961).
- Furusho, Reiko; Suzuki, Bunji; Yamamoto, Naotaka; Kawakita, Hideyo; Sasaki, Toshiyuki; Shimizu, Yasuhiro; and Kurakami, Tomio, 1999. *PASJ* **51**, 367.
- Ganesh, S., Joshi, U.C., Baliyan, K. S. and Deshpande, M. R., 1998. *A & A Suppl. Ser.* **129**, 489.
- Geake, J. E., and Dollfus, A., 1986. *MNRS*, **218**, 75.
- Greenberg, J. M., and Hage, J. I., 1990. *ApJ*, **361**, 260.
- Hadamcik, E., Levasseur-Regourd, A. C., and Renard, J. B., 1997. *EM&P*, **78**, 365.
- Hadamcik, E., 1999. Ph.D. Thesis, l'Université Paris 6.
- Hadamcik, E., and Levasseur-Regourd, A. C., 2000. *C. R. Acad. Sci. Paris, t. 1, Série IV*, p. 127.
- Hage, J.I. and Greenberg, J.M., 1990, *ApJ* **361**, 251.

- Hanner, M. S., 1983. in *Cometary Exploration*, ed. T. I. Gombosi (Debrecen: Hungarian Acad. Sci.), 1.
- Hanner, M. S., Tedesco, E., Tokunaga, A. T., Veeder, G. J., Lester, D. F., Witteborn, F. C., Bregman, J. D., Gradie, J., and Lebofsky, L., 1985. *Icarus* **64**, 11.
- Harris, W. M., Wood, K., and Fox, G. K., 1996. *AAS Meeting* **188**, No.62.10.
- Harris, W. M., Percival, J. W., Nordsieck, K. H., Mueller, B. E. A., Harmer, D., MacDonald, A., Honeycutt, K., and Scherb, F., 1996. *AAS Meeting* **188**, No.62.09.a
- Hasegawa, H., Ichikawa, T., Abe, S., Hamamura, S., Ohnishi, K., and Watanabe, J., 1997. *EM&P*, **78**, 353.
- Hayward, T. L., Hanner, M. S., and Sekanina, Z., 2000. *ApJ* **538**,, 428.
- Hsu, Jin-Chung and Breger, M., 1982. *ApJ* **262**, 732.
- Jäger, C., Mutschke, H., Begemann, B., Dorschner, J., and Henning, Th., 1994. *A & A*, **292**, 641.
- Jockers, K., Rosenbush, V.K., Bonev, T. and Credner, T., 1997. *EM&P*, **78**, 373.
- Jockers, K., 1997. *EM&P*, **79**, 221.
- Jorda, L., Rembor K., Lecacheux, J., Colom, P., Colas, F., Frappa E. and Lara, L. M., 1997. *EM&P* **77**, 167.
- Kiselev, N. N., Kiselev, K. N., Lupishko, D. F., and Krugly, Yu. N., 1997. *28th Annual Lunar and Planetary Science Conference*, p. 735.
- Kiselev, N. N., and Velichko, F. P., 1997. *EM&P*, **78**, 365.
- Kiselev, N. N., 2000. (*Privet Communication*).
- Kolokolova, L., and Jockers, K., 1997. *Planet. Space Sci.*, **45**, No. 12. 1543.
- Kolokolova, L., Jockers, K., Chetenova, G., and Kiselev, N., 1997. *Icarus* **126**, 351.

- Kolokolova, L., Jockers, K., Gustafson, B. Å. S., and Lichtenberg, G., 2001. *J. Geophys. Res. in Press*.
- KrishnaSwamy, K. S., Sandford, S. A., Allamandola, L. J., Witteborn, F. C., and Bregman, J. D., 1988, *Icarus*, **75**, 351.
- KrishnaSwamy, K.S., 1997. In *Physics of Comets 2ed.* (World Scientific series in astronomy and astrophysics; Vol. 2)
- KrishnaSwamy, K. S. and Shah, G. A., 1987. *EM&P*, **38**, 273.
- Levasseur-Regourd, A. C., Cabane, M., and Handeborg, V., 1999. *Journal of Quantitative Spectroscopy & Radiative Transfer*, **63**, 631.
- Li, A. and Greenberg, J. M., 1998. *ApJ*, **498**, L83.
- Li, A. and Greenberg, M., 1997. *A & A*, **323**, 566.
- Lucey, P. G., 1998. *J. Geophys. Res.*, **103**, 1703.
- Manset, N., and Bastien, P., 2000. *Icarus*, **145**, 203.
- Mathis J. S. ,1979. *ApJ*, **232**, 747.
- Mathis, J. S., Mezger, P. G., and Panagia, N., 1983. *A & A*, **128**, 212.
- Mathis, J. S., Rumpl, W., and Nordsieck, K. H., 1977. *ApJ*, **217**, 425.
- Mathis, J. S., and Wallenhorst, S. G., 1981. *ApJ*, **244**, 483.
- Mezger, P. G., Mathis, J. S., and Panagia, N., 1982. *A & A* **105**, 372.
- Mitchell, A. C. G. , and Zemansky, M. W., 1934. *Resonance radiation and excited atoms*, Cambridge University Press.
- Mukai, T., Ishimoto. H., Kozasa, T., Blum, J., and Greenberg, J. M., 1992. *A & A* **262**, 315.
- Myers. R. V. and Nordsieck, K.H., 1984. *Icarus* **58**, 431.

- Press, W. H., Teukolsky, S. A., Vetterling, W. T., Flannery, and Flannery, B. P., 1992. *Numerical Recipes in Fortran* (Cambridge University Press).
- Rosenbush, V. K., Shakhovskoj and Rosenbush, A. E., 1997. *EM&P*, **78**, 381.
- Rouleau, F. and Martin, P. G., 1991. *ApJ*, **377**, 526.
- Sarmecanic, J., Osip, D. J., Fomenkova, M., and Jones, B., 1997 *IAUC 66601*, 1997 March 24. Edited by Marsden B. G.
- Scott, A and Duley, W. W., 1996. *ApJS*, **105**, 401.
- Tanga, P., Cellino, A., and Martino, M. D., 1997. *EM&P*, **78**, 359.
- Turnshek, D. A., Bohlin, R. C., Williamson II, R. L., Lupie, O. L., Koornneef, J. and Morgan, D. H., 1990. *AJ* **99**, No.4, 1243.
- Vasundhara, R. 2001. submitted to *A & A*.
- Wehinger, P. A., Wyckoff, S., Herbig, G. H., Herzberg, G. and Lew, H., 1974. *ApJ*, **190**, L43.
- Wooden D. H., Harker, D. E., Woodward, C. E., Butner, H. M., Koike, C., Witteborn, F. C., McMurtry, C. W. , 1999. *ApJ*, **517**, 1034.
- Woodward, C. E., Gehrz, R. D., Mason, C. G., Jones, T. J., and Williams, D. M., 1998. *EM&P*, **81**, 217.
- Xing, Z. and Hanner, M.S., 1997, *A&A*, **324**, 805.

Chapter 6

INVESTIGATIONS OF COLOR OF DUST SHELLS IN THE POST-PERIELION CCD IMAGES OF COMET HALE-BOPP (C/1995 O1)

Trajectories of dust grains ejected during jet activity are computed to create the theoretical brightness and color maps of the shells of Comet Hale-Bopp. The dust grain types selected from spectropolarimetry of the cometary shell were used. The color of the observed dust shells with respect to the coma in the post-perihelion CCD images of comet Hale-Bopp are compared with the color derived from the simulated images. This is an independent method to test the dust compositions in the shell derived through polarimetry in Chapter 5.

6.1 Introduction

Images of Comet Hale-Bopp (1995 O1) show distinct dust jets and shells, indicating distributed sources of dust emission. The color variation across a newly formed dust shell depends on the nature of the grains and the initial size distribution. The color

profile across the older shells gets modified due to sorting of the grains by solar radiation pressure. Hence the color of the shells are best investigated by studying the dynamics of the grains in the shells.

Monte Carlo simulation of dust particle motions in the coma of comet Hale-Bopp by Hayward, Hanner, and Sekanina, (2000) indicated that the observed patterns of jets and halos were dominated by submicron-sized grains. They further find from their modeling of the thermal emission from small grains that the principal features of the 3 to 13 μ continuum and the 8 to 13 μ silicate feature can be synthesized from a mixture of amorphous carbon and amorphous and crystalline silicates.

The present work concentrates in the optical wavelengths. The dust composition in the shells is selected from the spectropolarimetric results of *Chapter 5*. A comparison of observed color variation across the shells with that predicted using our model is made.

6.2 Observation and Data Processing

For the investigation of color of the dust shells, post-perihelion observations of comet Hale-Bopp on April 10, 1997, were selected. On this date, the comet was at a heliocentric distance of 0.930 AU and a geocentric distance of 1.449 AU. The solar phase angle was 43°4. Observations of the comet were carried out from the cassegrain focus ($f/13$) of the 1.02m Carl-Zeiss telescope at VBO (*Chapter 2*). The comet was observed through the HB narrowband comet filters (Farnham, Schleicher, and A'Hearn, 2000) and a standard R filter on a liquid N_2 cooled CCD. Since standard stars for photometric calibrations were not observed, in the present investigation, an estimation of color of the dust shells relative to the coma is made. The cometary continuum filter 4450Å(62Å), 5260Å(57Å) and the R filter (6550Å(1300Å)) were used for the purpose. The filter 4450Å(62Å) will be referred to as "B" and 5260Å(57Å) as "G".

The basic reductions, like Bias and Flat-field corrections were performed on the images. The background sky and the scaling factor in each image were determined by radially fitting the intensity in the anti-sunward direction (North-East part of the image) where there are no strong shells, with a $k/\rho + SKY$ relation. These

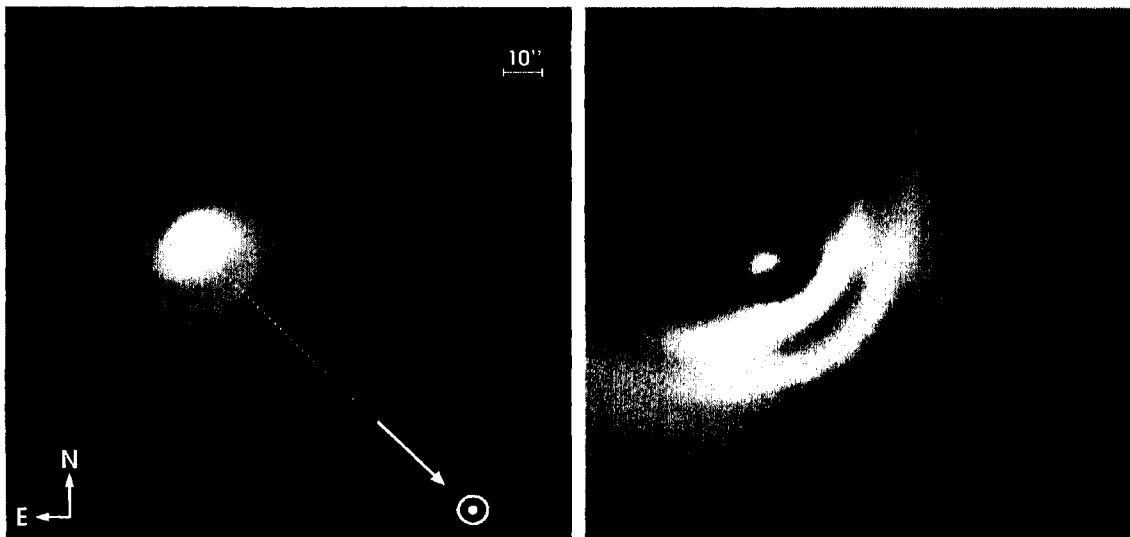


Figure 6.1: Normalization by a synthetic coma: R-filter image of comet Hale-Bopp before and after normalization by the synthetic coma (image to the left and right respectively). Both the images are of the same scale.

estimated sky values were subtracted from the respective images.

The observed image brightness map, $I_{O_{j+c}}(x, y)$ of the comet contains contribution from the coma as well as the jets. In order to remove the steeply varying contribution of the coma, a synthetic coma with a radial profile varying as $1/\rho$ was generated (Chapter 2). This generated profile was convolved with a Gaussian function of $2\sigma = 4$ pixels to account for a seeing of 1.42 arcsec. This synthetic image of the coma $I_{S_c}(x, y)$, after multiplication by the derived scaling factor k , was used to normalize the observed images (Chapter 2).

$$I_{O_{j+c}}^n(x, y) = \frac{I_{O_{j+c}}(x, y)}{k \cdot I_{S_c}(x, y)} \quad \text{for R, G \& B} \quad (6.1)$$

Fig. 6.1 shows the R-filter image of comet Hale-Bopp before and after normalization by the synthetic image of the coma. The dark spot at the center of the comet on the normalized image $I_{O_{j+c}}^n$ is an artifact of the normalization process using $1/\rho$ relation. This region will be excluded in our analysis. The normalization, enhances the shells to a large extent and many more shells become apparent. These normalized images can be used for estimation of color from these shells relative to the coma.

6.2.1 Computation of Color from Observed Images

The relative color from the normalized observed images were computed using the following expressions.

$$COLOR(R, B) = \frac{I_{O_{j+c}}^n(x, y)_R}{I_{O_{j+c}}^n(x, y)_B} \quad (6.2)$$

Fig. 6.2, shows radial cuts of $I_{O_{j+c}}$, $I_{O_{j+c}}^n$ and $COLOR$ along 8 directions. Fig. 6.2e shows the directions of the cuts superposed on the normalized R filter observed image

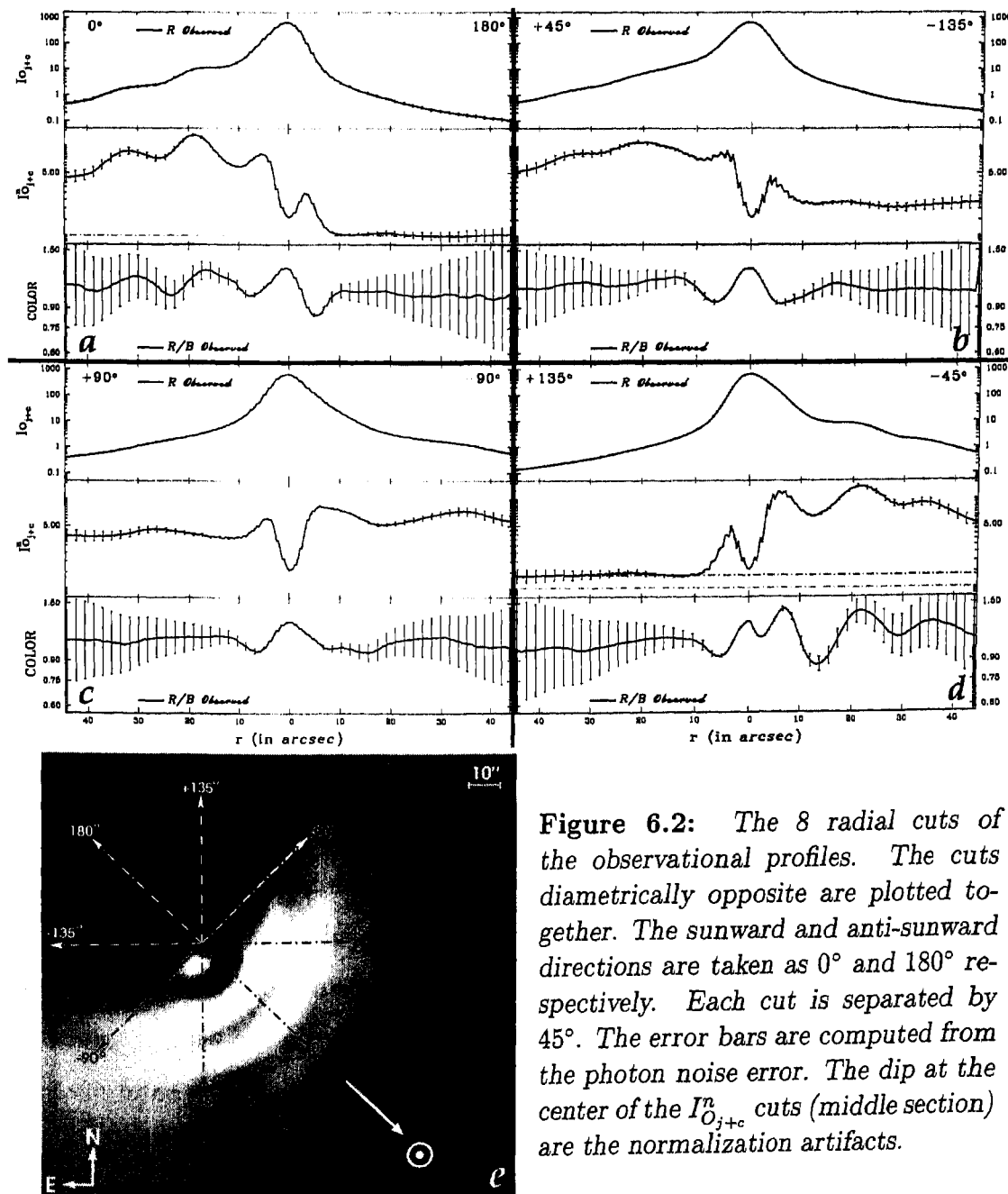


Figure 6.2: The 8 radial cuts of the observational profiles. The cuts diametrically opposite are plotted together. The sunward and anti-sunward directions are taken as 0° and 180° respectively. Each cut is separated by 45° . The error bars are computed from the photon noise error. The dip at the center of the $I_{O_{j+c}}^n$ cuts (middle section) are the normalization artifacts.

of the comet. Each cut is separated by 45° . The diametrically opposite cuts are plotted together. The sunward and anti-sunward directions are taken as $[0^\circ, 180^\circ]$ respectively and plotted in Fig. 6.2a. The other three diametrically opposite pairs of cuts ($[+45^\circ, -135^\circ]$, $[+90^\circ, -90^\circ]$ and $[+135^\circ, -45^\circ]$) are plotted in Fig. 6.2b, c, and d respectively. The error bars are computed from the photon noise error. The dip at the center of the $I_{O_{j+c}}^n$ cuts, are due to the normalization artifacts mentioned above. The cut of $I_{O_{j+c}}^n$ along the anti-sunward direction (cut along 180°) in Fig. 6.2a, shows a constant profile equal to 1 for $\rho \geq 10$ arcsec, indicating an exact $1/\rho$ relation for the coma in this direction.

The peaks on the COLOR profiles of the cometary shells show a shift from the intensity peaks. The dips in the COLOR profiles occur at the outer edges of the cometary shells, indicating that these regions are relatively bluer. This is in conformity with Furusho et al. 1999, who describe the color of the shell structures to be bluer compared to the coma regions. The dips in the color profile in the anti-sunward direction and along $\pm 135^\circ$ stand out clearly. The reason for the blue color close to the comet center away from the Sun, is not very clear.

6.3 The Model

On April 10, 1997, the comet was near pole-on solar illumination and only the sources with latitudes of $+65^\circ$, $+5^\circ$, and -5° appeared to be active (*Chapter 4*). It was assumed that the dust grains, were ejected continually from the sources, radially outwards, from local sunrise to sunset. The pole position which gave a reasonably good fit to the set of shells was $\alpha_p(2000) = 283^\circ$ and $\delta_p(2000) = -63^\circ$.

The observed cometary shells are close to the nucleus within a distance of $\approx 10^5$ km. For these distances it can be assumed that the dust grains follow the same Keplerian motion as that of the comet due to solar gravity. Thus, relative to the comet, the position of a dust grain can be calculated from its initial velocity v_{gr} , the radiation pressure force and the ejection geometry (see *Chapter 4*).

The acceleration α due to the solar radiation pressure depends on the nature of the grain and the heliocentric distance.

$$\alpha = (\beta g_{sun(1)})/r^2, \quad (6.3)$$

where β is the ratio of the force due to solar radiation pressure on the grain to the gravitational force, $g_{sun(1)}$ is the acceleration due to the gravity at 1AU ($0.6 \times 10^{-5} \text{ km/sec}^2$) and r is the heliocentric distance of the comet. In *Chapter 4*, a range of β values between 0.03 and 0.6 were considered without specifying the grain types. The value of β is now calculated for a grain of given size and composition using the relation by Finson and Probst (1968);

$$\beta = F_{rad}/F_{grav} = \frac{3Q_{pr}(s, \lambda)L_{\odot}}{4\pi cGM_{\odot}} \frac{1}{\rho_{gr}s}, \quad (6.4)$$

where $Q_{pr}(s, \lambda)$ is the scattering efficiency for radiation pressure of the grain, s its radius and ρ_{gr} its density. L_{\odot} is the total solar luminosity (radiation per second), c the velocity of light, M_{\odot} the mass of the Sun and G the universal gravitational constant. Since $Q_{pr}(s, \lambda)$ is dependent on the wavelength of radiation, the value of β for a grain of radius s can be calculated more precisely by the relation

$$\beta = \frac{3}{4\pi cGM_{\odot}} \frac{1}{\rho_{gr}s} \int_{\lambda_1}^{\lambda_2} Q_{pr}(s, \lambda)F_{\odot}(\lambda)d\lambda, \quad (6.5)$$

Where $F_{\odot}(\lambda)$ is the mean total solar radiation per second per Angstrom at wavelength λ . $Q_{pr}(s, \lambda)$ was estimated for the grain types used in *Chapter 5* (Table 5.4), using the Mie scattering code. The integration in Eq. 6.5, was carried out from $\lambda_1 = 0.1\mu$ to $\lambda_2 = 5.0\mu$.

The initial velocity v_{gr} of the dust at the time of decoupling of the dust and gas was calculated using Eq. 4.2 with the coefficients a and b from Table 4.5 on the date of observation.

In *Chapter 5*, the dust composition was derived using published three color polarization data at a range of phase angles and our spectropolarimetric data (Table 5.4). Hanner's law for size distribution (Hanner 1983, Hanner *et al.* 1985) was used. A combination of *Distribution A* and *Distribution B* (Sec. 5.5.1) were needed to fit the polarimetric data.

The estimated $Q_{pr}(s, \lambda)$ for each of the 11 grain types were used for calculating β , α and v_{gr} (Eqs. 6.5, 6.3 and 4.2). These terms were used for tracing the trajectories of the dust particles ejected from sources at cometary latitudes of $+65^\circ$, $+5^\circ$, and -5° . Taking the comet's rotation into account, the projected positions of the dust grains on the sky-plane from these trajectories were computed (see *Chapter 4*). A Gaussian randomness to the positions of the dust grains was introduced through a Monte-Carlo simulation to account for the broadened dust shells, seen in the observed images.

The intensity of light $I_s(\theta, \lambda)$ scattered by the grain towards the observer is computed by (Krishna Swamy & Shah, 1987) :

$$I_s(\theta, \lambda) = \frac{I_\odot(\lambda)\lambda^2}{8\pi r^2\Delta^2} (i_\perp(s, \lambda) + i_\parallel(s, \lambda)) \quad (6.6)$$

where θ is the scattering angle ($\theta = \pi - \alpha$, where α is the phase angle) and $I_\odot(\lambda)$ is the solar intensity at 1 AU. The terms $i_\perp(s, \lambda)$ and $i_\parallel(s, \lambda)$ are the intensity scattering functions perpendicular and parallel to the scattering plane.

6.4 Comparison of Observations with the Model

The scattered intensity $I_s(\theta, \lambda)$ is convolved with the filter response of the observed *R*, *G* and *B* passband, and the brightness maps were created for each grain size s . These maps for grain sizes from 0.05μ to 30.0μ in 70 steps were added using the *Distribution A* and *B* described in Sec. 5.5.1 of *Chapter 5*, to create images of the dust shells $I_{Mj}^s(x, y)$, in *R*, *G* and *B* filters, for each of the 11 dust grain types enlisted in Table 5.4. Figure 6.3 shows the model dust shells for these 11 types of dust grains created for the *R*-filter. The top left corner image is the observed normalized image in *R*-filter. The difference between the model images *No. 1* and *No. 10* is due to the size distribution factor. The former is with the dust size *Distribution A* while the latter is with the *Distribution B*. The *Distribution B* has only the smaller grain sizes while the *Distribution A* also covers the larger grain sizes (Fig. 5.15). As expected, the effect of the solar radiation pressure is more pronounced in image *No. 10* due to presence of smaller grains with larger β value. The other images show subtle changes in the profile due to changes in R_m (Images *No. 5* and *No. 6*) or changes

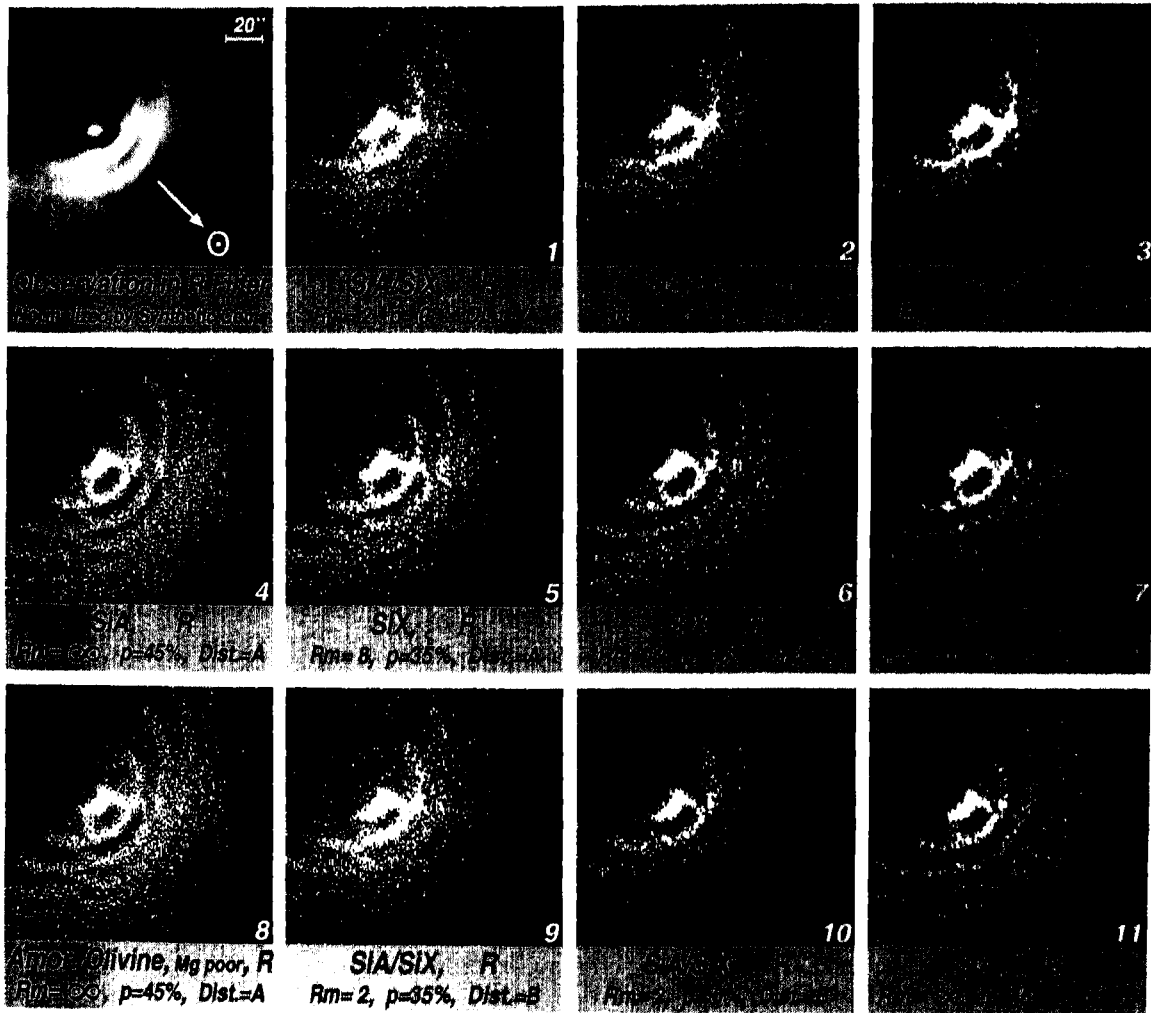


Figure 6.3: The model dust shells $I_{M_j}^i(x, y)$ for $i = 1$ to 11 types of dust grains enlisted in Table 5.4 with the observed normalized image of comet Hale-Bopp on the top left corner.

with porosity p (Image No. 9 and No. 10) or both (Images No. 1 to No. 7) for a given size distribution parameters. The 11 grain types basically help to cover a range in porosities between 0% and 45% for grain types of given R_m value.

The model coma $I_{M_c}(x, y)$ in R , G and B were made separately assuming dust ejection from the sunlit surface of the comet. The dust composition used in the coma was taken from Vasundhara (2001).

The model comet image was then created by

$$I_{M_j+c}(x, y) = \sum_{i=1}^{i=11} \omega_i \cdot I_{M_j}^i(x, y) + \omega_c \cdot I_{M_c}(x, y), \quad (6.7)$$

for R , G and B filters. The weights ω_i were adapted from the spectropolarimetric data fit to the jet (Aperture Ap_J), in Chapter 5. The weights ω_c for the model coma

for all the three filters (R , G and B), were determined by matching $I_{M_{j+c}}(x, y)$ to $I_{O_{j+c}}(x, y)$. This matching was done along the 8 radial cuts shown in Fig. 6.2c. Following the method adopted to normalize the observed image $I_{O_{j+c}}^n$ (Eq. 6.1), the model image was normalized by using the relation

$$I_{M_{j+c}}^n(x, y) = \frac{I_{M_{j+c}}(x, y)}{\omega_c I_{M_c}(x, y)} = \frac{\sum \omega_i I_{M_j^i}(x, y)}{\omega_c I_{M_c}(x, y)} + 1. \quad (6.8)$$

The normalization artifact seen in $I_{O_{j+c}}^n$, is absent in $I_{M_{j+c}}^n$ as it does not use the $1/\rho$ relation.

The model color was thus computed by

$$COLOR(R, B) = \frac{I_{M_{j+c}}^n(x, y)_R}{I_{M_{j+c}}^n(x, y)_B}. \quad (6.9)$$

In Fig. 6.4, the 8 radial cuts of $I_{M_{j+c}}$, $I_{M_{j+c}}^n$ and $COLOR(Model)$ are over-plotted on the observational profiles already shown in Fig. 6.2. Fig. 6.4c shows the 8 directions of the cuts on the model jet image of the comet constructed for the R filter.

The difference seen between $I_{O_{j+c}}^n$ and $I_{M_{j+c}}^n$ cuts, especially the sunward direction, is due to the deviation in the coma profile from the assumed $1/\rho$ relation used for normalizing the observed images. The observed profile falls less steeply than $1/\rho$ and this may be attributed to 1) Sun-comet-Earth viewing geometry. Only when $\alpha = 0$, a perfectly spherically symmetric coma can be expected. 2) Grain from the shells dispersing along the anti-sunward direction may also increase the ambient background which will contaminate the coma profile. 3) The coma is compressed due to effect of solar radiation pressure force. All these effects may reduce the radial intensity gradient in the anti-sunward direction.

Since the observed color profiles are not absolute but relative with respect to the coma, the model color profiles were multiplied by a constant factor to match the first peak on the observed color profile cut at 0° to enable a direct comparison. The rest of the model color profiles in other directions, match well with the observations within the error bars using the same multiplication factor.

The cut at -45° falls at the intersection of the two jet shells from latitudes at $+5^\circ$ and $+65^\circ$ (see Fig 4.5). The model color in this direction therefore shows a complex structure which is smoothed out in the observed profile.

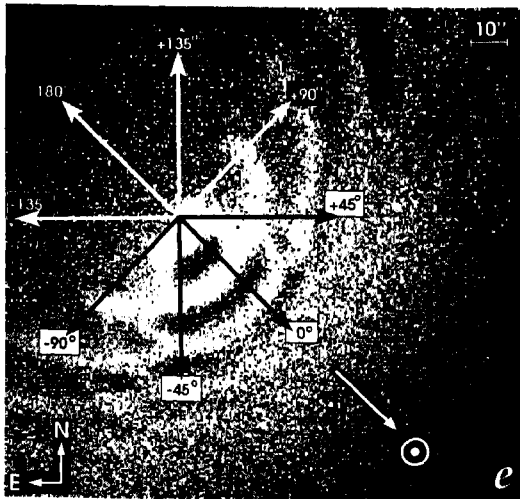
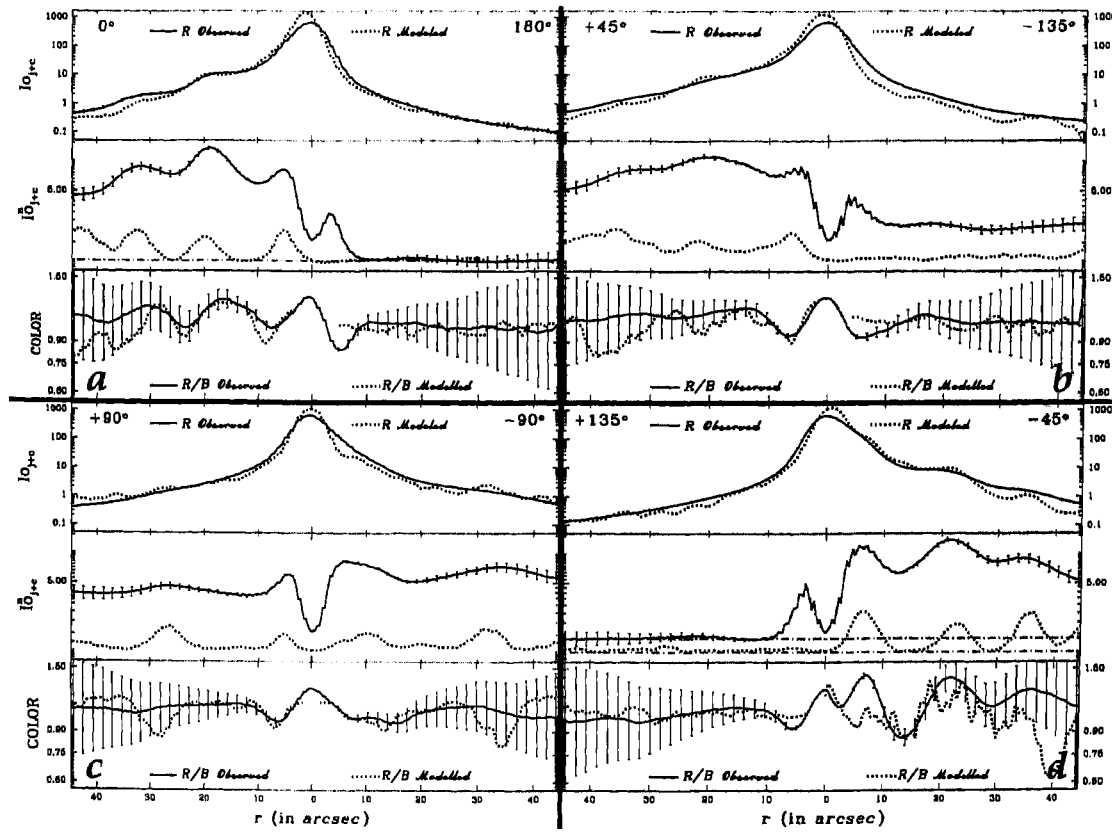


Figure 6.4: The 8 radial cuts of the model profiles (dotted lines) overplotted on the observed profiles (solid lines). The cuts diametrically opposite are plotted together. The sunward and anti-sunward directions are taken as 0° and 180° respectively. Each cut is separated by 45° . The model color profiles fit well the observed profiles within the error bars, except for the cut at -45° which samples two sets of shells.

6.5 Results

The results of the fit indicate that the dust compositions derived through polarimetry in *Chapter 5*, also explain the observed color of the shells. The simulated dust shells using the dust grains selected from fit to spectropolarimetric data, show a morphological structure very close to the observed structure.

Using the normalized observed and the model dust shell images in *R*, *G* and *B*

filters, composite color images of the dust shells of comet Hale-Bopp are created. These two images are displayed in Fig. 6.5.

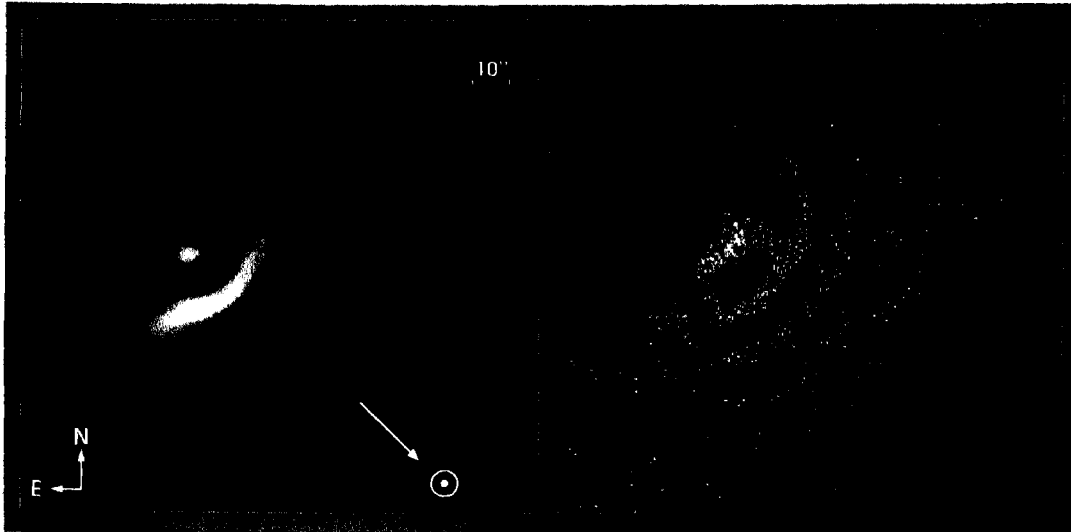


Figure 6.5: Composite color images using R , G and B filters of the dust shells of Comet Hale-Bopp. The left image is the normalized observed image, while the right image is the modeled dust shells. In both images the dust shells appear blue.

In this work, we assume that all the three jets at $+65^\circ$, $+5^\circ$ and -5° of the comet are of the same dust composition. It is however probable that there might be some differences in the overall dust composition in each jet because of their physic locations on the comet. The spectropolarimetric data from aperture Ap_J in Chapter 5 is for the shell from the source at 65° . The dust compositions derived from the model fit to this data was applied to all the three shells. The color fits are well within the observational error for most of the cuts. It would be difficult to investigate the difference in dust composition from each of the three jets using the color technique with this limited dataset.

The present work also assumes that the Ap_J in Fig. 4.3 samples only the shell and the coma background is negligible. A more detailed investigation by changing the aperture size of Ap_J is planned in the future which will help investigating the background coma near this shell.

References

- Farnham, T. L., Schleicher, D. G. and A'Hearn, M. F. 2000. *Icarus* **147**, 180.
- Finson, M. L., and Probst, R. F. 1968. *ApJ* **154**, 327.
- Furusho, Reiko; Suzuki, Bunji; Yamamoto, Naotaka; Kawakita, Hideyo; Sasaki, Toshiyuki; Shimizu, Yasuhiro; and Kurakami, Tomio, 1999, *PASJ* **51** 367.
- Hanner, M. S., 1983. in *Cometary Exploration*, ed. T. I. Gombosi (Debrecen: Hungarian Acad. Sci.), 1.
- Hanner, M. S., Tedesco, E., Tokunaga, A. T., Veeder, G. J., Lester, D. F., Wittborn, F. C., Bregman, J. D., Gradie, J., and Lebofsky, L., 1985. *Icarus* **64**, 11.
- Hayward, T. L., Hanner, M. S., and Sekanina, Z., 2000. *ApJ* **538**, 428.
- Krishna Swamy, K.S. and Shah, G.A., 1987, *Earth, Moon, and Planets*, **38**, 273
- Vasundhara, R. 2001. submitted to *A & A*.

Chapter 7

CONCLUSIONS AND FUTURE WORKS

7.1 Conclusions

In this work dust from selected comets (*viz.* Comet Hale-Bopp and Comet Wild 2) have been studied through dynamics and scattering properties of dust grains. Instrumentation, observations, data reductions, and modeling of cometary jets, formed the ground work of this thesis. In *Chapter 2* and *Chapter 3*, instrumentation, observations, and data reductions are covered. *Chapter 4* deals with modeling of dust jets from comet Hale-Bopp. In *Chapter 5*, a polarimetric investigation was conducted and spectropolarimetric data of comet Hale-Bopp and Wild 2 were modeled. Using the dust jet modeling and spectropolarimetric data modeling results, the relative color of the dust shells in the post-perihelion images of comet Hale-Bopp was investigated in *Chapter 6*.

To study the wavelength dependent polarization of the scattered light from cometary dust, an Optical, Dual-Beam, Automated Medium Resolution SpectroPolarimeter (O-DB.AMRSP) was fabricated, calibrated and characterized for its performance at the VBT. A depolarization technique was developed for obtaining flats. To remotely operate the instrument during observation, a real-time instrument control software was written. A spectropolarimetric data reduction software (SPRS) was developed to

extract the Stokes parameters. Elimination of instrumental polarization, telescope polarization and response corrections are implemented in SPARS. It was found that the polarization introduced by the telescope is $\sim 2\%$ towards the red. This could be successfully modeled by observing standard unpolarized stars. The attainable accuracy of the instrument was found to be dependent on the S/N. With the data set used for calibrating the instrument, accuracies of $\sim \pm 0.5\%$ at 4000\AA and $\sim \pm 0.3\%$ at 7500\AA in polarization measurements, have been attained at a spectral resolution of $\sim 7.2\text{\AA}$.

Jet and shell structures from comet Hale-Bopp during the period September 1996 to October 1997, were modeled using data from the Vainu Bappu Observatory (VBO) and from the observatory of the Naturwissenschaftlicher Verein Osnabrück. The jet and shell structures during the period of observations could be attributed to activity from sources near $+65^\circ$, $+35^\circ$, $+5^\circ$, -5° , -35° , -65° in latitude. The pole positions during the one year period of observations are found to vary between 260° and 290° in right ascension and -50° to -65° in declination indicating a complex state of rotation of the comet. Approximate estimates of the longitude of the sources active between February and May, 1997, at latitudes of $+65^\circ$, $+5^\circ$ and -5° , were made. The positions of these longitude are presented in Fig. 4.3. The average value of dust to gas production ratio between February 1997 - May 1997 was found to be near 5. During April, the source at $+65^\circ$ appears to account for about 29% of the observed total water emission reported by Schleicher *et al.* (1997).

Although the jets from Comet Hale-Bopp could be reasonably matched with the simulations, the present model assuming a single nucleus does not however replicate the exact shapes of the shells from sources at $\pm 5^\circ$ latitudes and the complex observed shell patterns in the February images. Detailed modeling taking into account a possible binary nature of the comet (Sekanina 1997b, 1998b) may be required to explain these intricate shell structures. Recent adaptive optics observations of the innermost coma of comet Hale-Bopp by Marchis *et al.* (1999) indicate a double peak which would be easily understood if two nuclei were involved.

Polarimetric observations of comets contain important information about cometary dust. Proper modeling of polarimetric data can reveal information on the cometary

grain type, its silicate to organic ratio, and the porosity. It is seen that the polarization of the scattered light from a cometary grain is strongly dependent on the phase angle and the wavelength. The parameters P_{min} and P_{max} determined through trigonometric fits, indicate that Hale-Bopp is an extremely high polarization comet, while Wild 2 is a low polarization comet.

To explain the continuum polarization, the scattering properties of the dust grains were investigated. Different grain types with a range of absorptivity, organic content R_m , porosity p and size distribution laws were considered. By fitting the spectropolarimetric data, it was found that regions close to the center within ≈ 7 arcsec, contain a larger fraction of organics compared to the surrounding outer regions within ≈ 13 arcsec. This could be due to breaking up of the porous grains and evaporation of the volatile organic content as inferred by Kolokolova, *et al.* (2001) from their imaging polarimetric data. Partial dispersal of organic refractory will leave behind grains of reducing organic content or increasing the number of grains with $R_m > 8$ in the outer regions. The spectropolarimetric data on the shell (aperture Ap_J) indicate larger polarization and larger color of polarization. Fits to this data set between 4000Å to 6400Å indicate a lower fraction of organics and smaller grains in the ensemble. A steep increase in polarization at longer wavelength in this aperture is puzzling. This could be due to aligned non spherical of grains in the shells. The present model assuming spherical grain is inadequate to model such grains. Hence our result of modeling of shell polarization may not be conclusive.

The model fitting to the spectropolarimetric data of comet Wild 2, indicates that the dust grains in this comet, are rich in organics and less porous compared to that of comet Hale-Bopp. The polarization *vs* wavelength curve for comet Wild 2 is quite flat. For comet Hale-Bopp, the presence of a population of narrow size distribution appear to produce the large polarization color gradient. These could be subunits of large highly porous clusters or individual small grains. For Wild 2, the fits indicate the presence of larger and highly absorptive grains either due to high organic content or poor Mg content. Both these components have high absorption in blue. Selective absorption in blue or a larger grain size will increase the polarization at shorter wavelengths and reduce the polarization gradient as it is noticed for comet

Wild 2.

Comet Wild 2 is now important because of the STARDUST mission, sponsored by NASA. The STARDUST space craft plans to fly by this comet and for the first time ever, bring primitive samples of cometary dust back to Earth. The present study of dust polarization from this comet will hopefully provide some prior knowledge of the dust properties of this comet, before the spacecraft encounters it in 2004.

The residual polarization after subtraction of the model continuum polarization from the spectropolarimetric data of comet Hale-Bopp, indicate the presence of emission polarization from the cometary molecular bands.

From the modeling of cometary jets it is also observed that the nature, grain size and porosity of the grains effect the jet dynamics. Cometary dust characteristics obtained from modeling the polarimetric and spectropolarimetric data was applied for modeling the cometary shells and derive the color of the shells with respect to the coma. These were compared with the color of the observed dust shells in the post-perihelion CCD images of comet Hale-Bopp with respect to the coma. The results of the fit to the color of the shells are in conformity with the polarimetric and spectropolarimetric modeling. This was an independent method to verify the dust compositions in the shell derived through polarimetry and spectropolarimetry. Though information on dust mineralogy can only come from IR observations, the porosity, silicate to organic ratio and size distribution of the dust grains can be studied using dust dynamics and modeling of the polarimetric and spectropolarimetric data. In this thesis, an attempt has been made to investigate dust from these specific comets using our optical observations.

Comets like Hale-Bopp are believed to be pristine comets originating far off in the Oort cloud. They are frozen reservoirs of the most primitive pre-solar dust grains and ices. The nature of the original material of the solar/pre-solar nebula and its relation to the various solar system objects and their inter-relationship is of great interest. Carbon chemistry or organics may be used as a probe for a qualitative discussion of this cosmic connection.

It is therefore hoped that the results of this thesis would help in a small way, our understanding of the primitive pre-solar dust grains.

7.2 Future Works and Further Improvements

7.2.1 Guiding a Comet with a nearby Field Star

Guiding on a nearby field star observed through the main telescope can be observed by providing a velocity to the guiding unit in an opposite direction to compensate for the relative motion between a field star and the comet. This facility could easily be provided to an offset guiding unit through a simple instrumentation. As future improvements for guiding solar system objects using the online offset guiding unit, the following instrumentation is proposed at VBO.

To understand this instrumentation problem, let us investigate what exactly is seen by the offset guiding unit. Fig. 7.1 shows the top view of the offset guiding unit we have seen in Fig. 2.1. The circle with radius R_1 is the limit of the central beam that

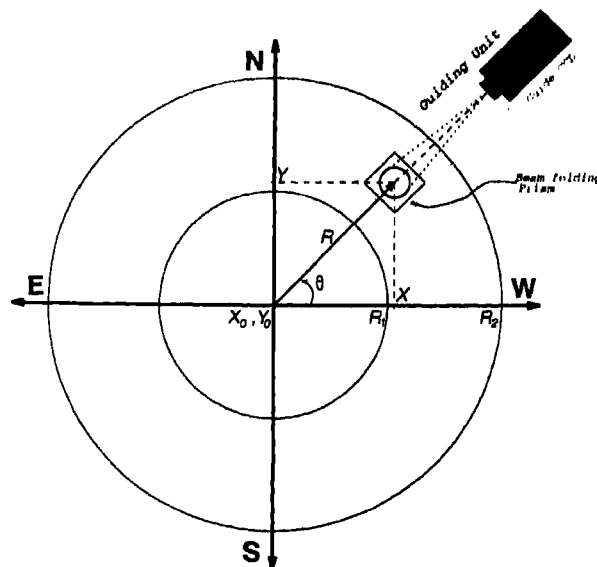


Figure 7.1: Guiding the Telescope with a field star. X increases to the right and α increases to the left as per convention.

goes to the main detector. The guide star for the guiding unit should be located between the circles of radius R_1 and R_2 . The guiding unit is rotated in θ and moved in R within the limits R_1 and R_2 to locate a guide star.

$$R = \sqrt{\Delta X^2 + \Delta Y^2}, \quad \theta = \arctan\left(\frac{\Delta Y}{\Delta X}\right), \quad (7.1)$$

where $\Delta X = X - X_0$ and $\Delta Y = Y - Y_0$. As the plane of Fig. 7.1 is the image plane

of the telescope, ΔX and ΔY can be represented by

$$\Delta X = \Delta\alpha \cos(\delta + \Delta\delta), \quad \Delta Y = \Delta\delta, \quad (7.2)$$

where α and δ are the comet's *RA* and *Dec* coordinates and $\Delta\alpha$ and $\Delta\delta$ are the coordinate separations between the comet and the guide star. From Eq. 7.2 it is easy to compute the velocities $v_R = dR/dt$ and $v_\theta = d\theta/dt$ of the guiding unit corresponding to the velocities $\dot{\alpha}$ and $\dot{\delta}$ provided to the telescope for tracking the comet. Hence, as the telescope tracks the comet, the guiding unit tracks the guide star, keeping it fixed on the guide monitor for online fine guiding.

Such a guiding unit is ideal for observations of solar-system objects. This guiding facility can easily be achieved through computer driven motorization of the radial and angular motion of the guiding unit. Two stepper motors could be used for the purpose. When the ephemerides of the object is provided to the computer, it will be able to identify the potential guide stars from the star catalogue, within the circles R_1 and R_2 (Fig. 7.1). From the ephemerides, the velocities v_R and v_θ can also be computed at every instant and applied to the guiding unit motors.

7.2.2 Estimation of the Coma Profile by Linear Fit to the Image

In *Chapter 2* Section 2.5.2, the coma is considered to be formed of a spherically symmetric outflow. This is an approximation. The coma would appear symmetric if seen from the sun, but to a terrestrial observer, due to finite solar phase angle, this will not be the case. The observer will also be viewing part of the comet on the night side where there are no emissions. Further, the solar radiation pressure compresses the coma in the sun-ward direction. Hence the coma profile cannot be represented as ρ^{-1} in all directions. A rigorous expression for the coma profile $I_{oc}(i, j)$ can be represented as

$$I_{oc}(i, j) = I_{oc}(\rho, \theta) = k\rho^{-a(\theta)}. \quad (7.3)$$

where $a(\theta)$ depends on position angle θ . Substituting $I_{oc}(i, j)$ in Eq. 2.11 rearranging the terms, the intensity of the jets $I_{oj}(i, j)$ is given by

$$I_{oj}(i, j) = I_o(i, j) - k\rho^{-a(\theta)}.$$

A profile $k\rho^{-a(\theta)}$ can be fitted to $I_o(i, j)$ by selecting the pixels between the jet shells where $I_o(i, j) \simeq 0$.

The transformation from the Cartesian (x, y) to (ρ, θ) described in *Chapter 2* Section (2.5.1) is now again made use of:

$$\begin{aligned} I_o^t(i_\rho, j_\theta) &= k i_\rho^{-a(\theta)} \quad \text{or,} \\ I_o^t(i_\rho, j_\theta) &= k i_\rho^{-a(j_\theta)}. \end{aligned} \quad (7.5)$$

Eq. 7.5 is linearized by taking the log;

$$\log [I_o^t(i_\rho, j_\theta)] = k - a(j_\theta) \log [i_\rho], \quad (7.6)$$

to determine $a(j_\theta)$ using linear regression.

It is expected that $a(\theta)$ is close to 1.0 while k should be close to the value of k estimated in *Chapter 2* Section 2.5.2. The parameter $a(\theta)$ should also be periodic with a period 2π ; $a(\theta + 2\pi) = a(\theta)$. We know that a positive deviation from the fit is mostly due to $I_o(i, j)$, while the negative deviation may only occur due to error emerging from the S/N of the data. Thus one can expect a much higher positive deviation to the fit, than a negative one. While performing a linear χ^2 fit to $\log [I_o^t(i_\rho, j_\theta)]$, the positive deviation can be biased by a weight W , so that $\sigma_+ = W\sigma_-$.

The weight W that biases the jets compared to the noise is extremely subjective. Therefore in our analysis of color of dust shell from the images of comet Hale-Bopp (*Chapter 6*) we made use of normalization by a synthesized coma (*Chapter 2*, Section 2.5.2). This estimation of the actual coma profile by linear fit will be attempted in future work.

7.2.3 Measurements of Circular Polarization

The Spectropolarimeter O-DB.AMRSP developed for the VBT can at present only measure linear polarization. The instrument can also be used for measurements of circular polarization by replacing the HWP by a superachromatic Quarter wave plate (QWP). The present design of "Section-1" permits such an alteration even during the observations if required. For extending O-DB.AMRSP for circular polarization a superachromatic QWP needs to be **acquired**.

7.2.4 Improvement in the Reduction Software SPRS

The present version of SPRS cannot be directly applied to a long-slit spectropolarimetric observation. However, the software with a little modification can handle a long-slit data as series of 1d spectropolarimetric data.

Astronomical observations are often photon starved, photon noise is high, leading to a poor S/N . To improve the S/N , many sets of observations are averaged or median smoothed. Fourier smoothing can also be applied to the data before the application of the SPRS. Fligge & Solanki (1997) have developed a method of noise reduction in astronomical spectra using wavelet packets. The wavelet representation of a signal due to the additional wavelength resolution of the decomposed signal, offers great flexibility in de-noising astronomical spectra compared to the classical Fourier smoothing. Fligge and Solanki's code when incorporated as a pre-SPRS module, would significantly improve the accuracy of polarization measurements.

7.2.5 An Imaging and Spectroscopic Polarimeter (I&S-P)

With the experience gathered by the fabrication of the Spectropolarimeter for the VBT, it is now possible to venture into a multipurpose instrument. A future plan for the fabrication of an Imaging and Spectroscopic Polarimeter (I&S-P) instrument is proposed. This instrument could be fabricated for the newly installed 2m telescope at the Indian Astronomical Observatory (IAO). Fig. 7.2 shows a conceptual optical design for the I&S-P.

The instrument is planned as a multi-mode instrument with imaging, Spectroscopic and polarimetric facility on a cassegrain telescope. By moving the Grism or the polarimetric section in or out of the optical path the different modes of observation are achieved (see Fig. 7.2).

We propose to use similar polarimetric optics as used for the Spectropolarimeter at VBT. For measurement of circular polarization the HWP will be replaced with a superachromatic Pancharatnam quarter-wave plate (QWP).

For high dispersion spectropolarimetry or spectroscopy, the CCD can be replaced by a fiber link to an Echelle spectrograph. The I&S-P should then be on the imaging mode (Grism out of the optical path).

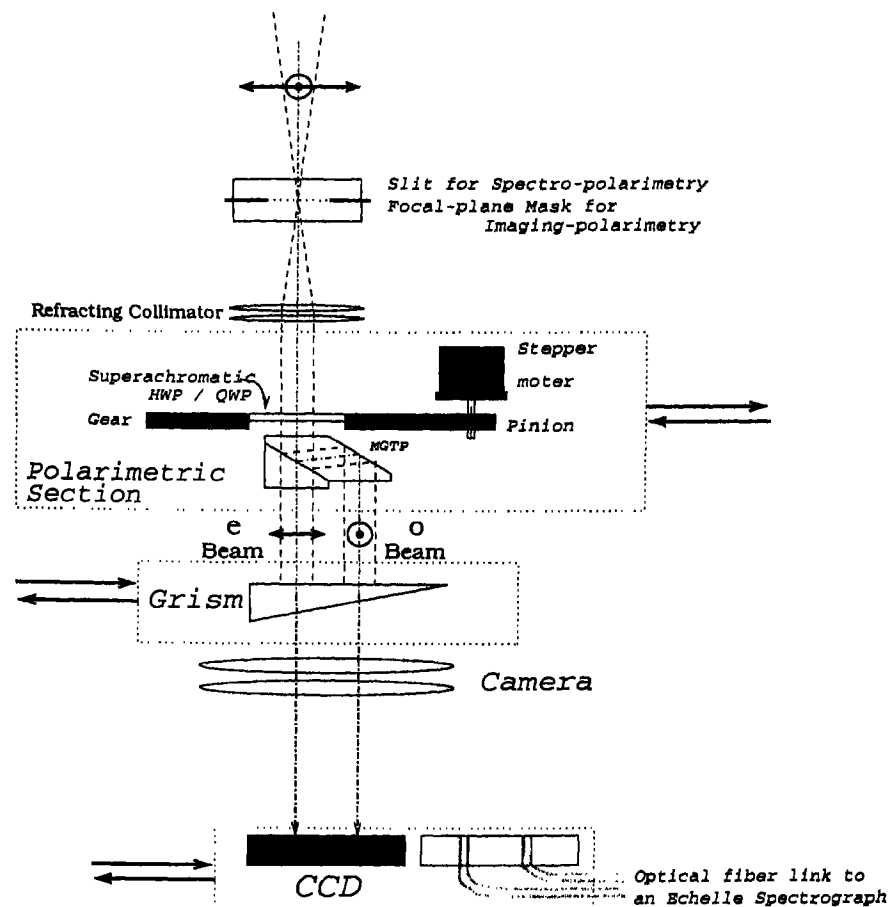


Figure 7.2: A conceptual optical design for the I&S-P (Not to Scale)

The instrument can be totally automated through a two stage automation. The first stage will be linking the instrument to a local instrument control computer (LICC) which would be I/O intensive. The second stage will connect the LICC, through a command line, to a remote computer (may be through satellite network). The two stage automation will minimize the load on the long distance command line. The real advantage with such multi-mode instrument is that the change of instrument could be made electronically. The instrument will have the capability for

- Normal filter imaging,
- Low resolution longslit spectroscopy,
- High resolution spectroscopy through fiber fed Echelle spectrograph,
- Dual beam Imaging polarimetry with filters for linear and circular polarization,
- Dual beam low resolution longslit spectropolarimetry for linear and circular polarization,

- *Dual beam High resolution spectropolarimetry through fiber fed Echelle spectrograph for linear and circular polarization.*

Such an instrument will require precise engineering and a sufficiently large budget.

7.2.6 A Four Beam Imaging Polarimeter (FBImP)

A Four Beam Imaging Polarimeter (FBImP) will be a much simpler instrument to fabricate compared to I&S-P. It is a single mode instrument for imaging polarimetry for measurement of linear polarization on an extended source. For studying polarization from cometary shells, it is essential to obtain polarimetric images at different continuum regions. Conventionally, to obtain a polarimetric image, observations have to be made at four positions (0° , 45° , 90° and 135°) of the incident beam. FBImP makes simultaneous observations at all the four positions, reducing the data acquisition time and the complications of rotating the HWP through four precise angles.

The instrument consists of a focal plane mask, refracting collimator, a four beam polarimetric analyzer, a re-imaging camera and a CCD detector. Fig. 7.3 shows this conceptual optical design. The four beam polarimetric analyzer is made of 2 MGTPs sandwiched together. For one of the MGTP, the Calcite crystal it is cut along the optical axis while for the other MGTP, it is cut at 45° to the optical axis. As a result, the first MGTP splits the incoming beam at 0° and 90° while the second MGTP splits the incoming beam at 45° and 135° . The combination of the two MGTP placed one beside the other provide a simultaneous four beam output at 0° , 45° , 90° and 135° . The focal plane mask is needed to restrict the observable field so that the 4 output images do not overlap.

Since all the four beams are simultaneously imaged, the atmospheric and instrumental transmission T would be the same and can easily be eliminated. The different gain factors of the four images will be normalized by flat-fielding. These flats are to be obtained from a totally depolarized source. Therefore, provision for a depolarization mechanism will be made in this instrument. Apart from depolarization, the instrument will have to be calibrated using a polarizing prism.

The moving parts in the instrument like the filter wheel, the depolarization unit

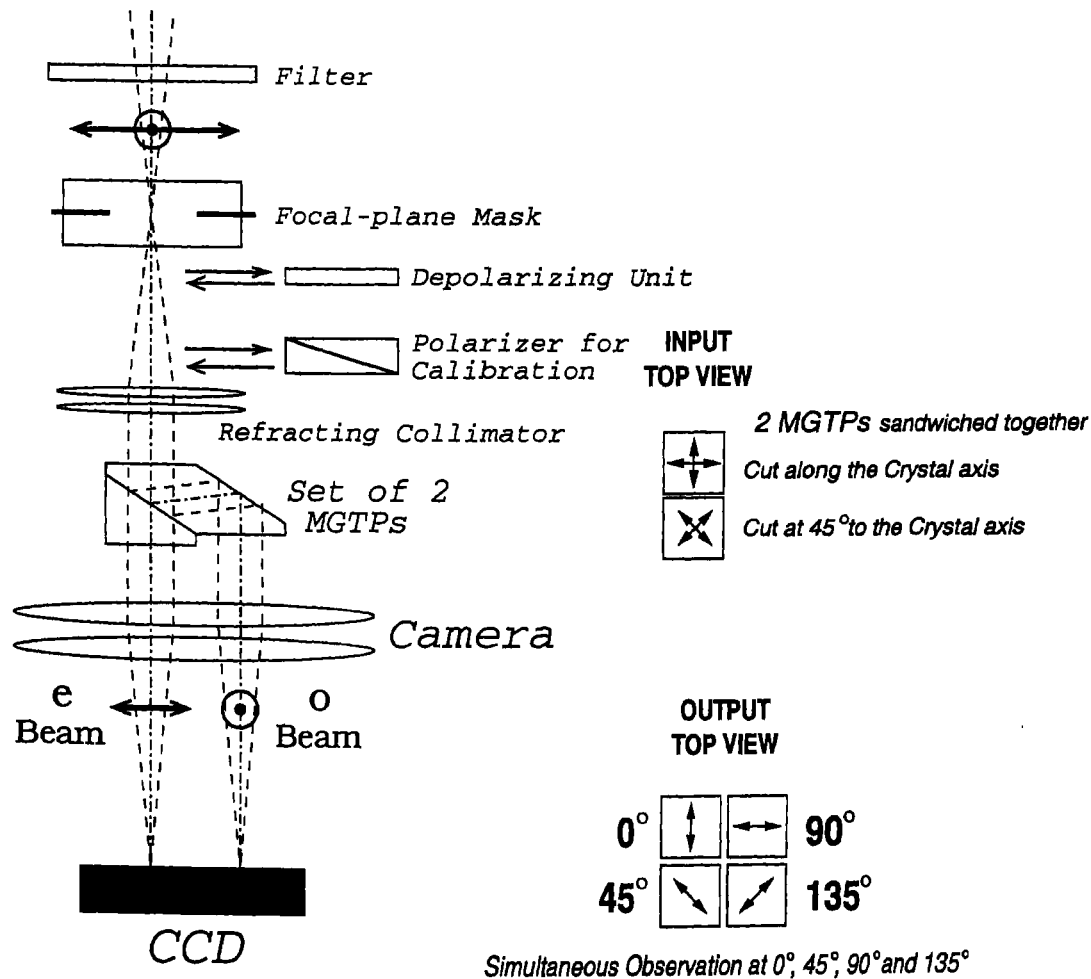


Figure 7.3: A conceptual optical design for the FBImP (Not to Scale)

and the calibration unit require only coarse movements and need not have any anti-backlash arrangements. Although, for measurement of circular polarization an insertion of a QWP in the optical path just in front of the four beam polarimetric analyzer, will be required, it need not have a rotation facility.

7.2.7 Dust scattering Code

The Mie scattering code, published in the appendix of Bohren and Huffman (1983), has been used with EMT in *Chapter 5* and *Chapter 6*.

Instead of computing the effective refractive index using EMT and scattering matrix using Mie theory for porous and composite grains, one can use the powerful technique of Discrete Dipole Approximation (DDA) by Draine (1988) and Draine and Flatau (1994). This technique assumes the scatterer to be made up of a large number

of dipoles. The resultant scattering matrix linking the set of dipoles and incident wave gives exact results if the dipoles have sizes in the Rayleigh region. Grains of any shape can be treated by arranging the dipoles accordingly. Porous grains can be constructed by introducing voids in the matrix. The technique demands large computation time and large RAM as the size of the grain increases beyond 1μ . Since cometary grain size distributions extend beyond this size, this method could not be adopted in the present work with our limited computational facilities. It is aimed to repeat the analysis using DDA if access to a supercomputer becomes possible in future.

7.2.8 Polarization and Dust Modeling

Future bright comets will be observed polarimetrically and spectropolarimetrically for investigating their dust characteristics.

Investigations of emission polarization of molecular bands in comets is a challenging field which is not well explored. An in-depth study of the polarization of molecular bands seen in our data will be taken up in a future work.

Dust shells, at varying distances from the nucleus of the comet, will be fitted with different silicate to organic ratios, porosities and different power-law size distributions. This will provide an insight into the changing properties of the dust grains due to sublimation or fragmentation.

References

- Bohren C. F., and Huffman, D. R., 1983. *Absorption and scattering of light by small Particles*, A Wiley-Interscience Publication, John Wiley & Sons Inc., 1983.
- Draine, B. T., 1988. *ApJ*, **333**, 848.
- Draine, B. T., and Flatau, P. J., 1994. *J. Opt. Soc. Am. A*, **11**, No. 4, 1491.
- Fligge, M. and Solanki, S. K., 1997. *A & A Suppl. Ser.*, **124**, 579.

Marchis, F., Boehnhardt, H., Hainaut, O. R., and Le Mignant D., 1999. *A&A*, **349**, 985.

Kolokolova, L., Jockers, K., Gustafson, B. Å. S., and Lichtenberg, G., 2001. *J. Geophys. Res. in Press*.

Schleicher, D.G., Millis, R.L., Farnham, T. L., Lederer, S. M., 1997. *Bull. Am. Astron. Soc.*, **29**, p.1033.

Sekanina, Z., 1997b. *EM&P*, **77** 155.

Sekanina, Z., 1998b. *ApJ*, **509** L133.

Appendix:A

Polarimetric Optics

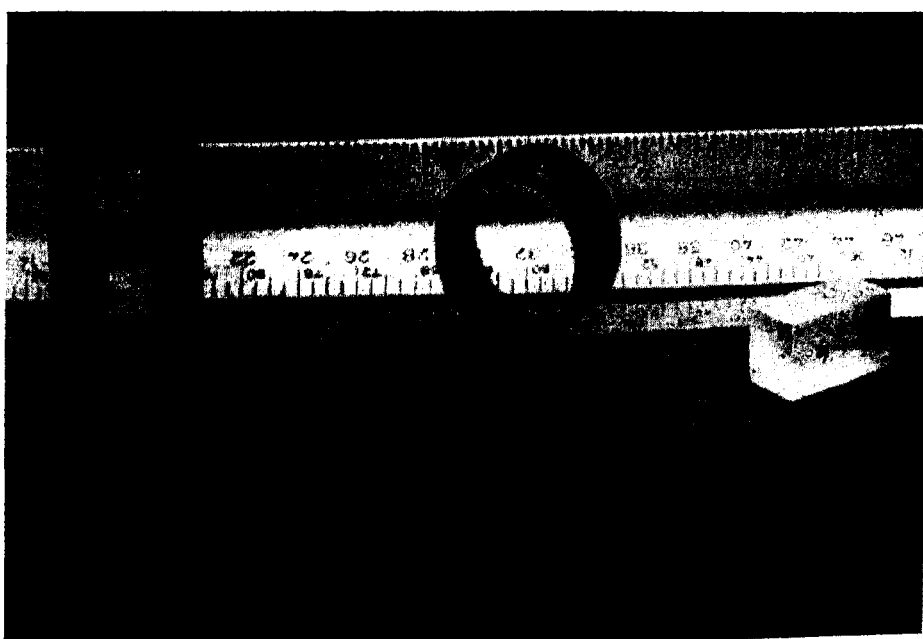


Figure A.1: Polarimetric optics used in the spectropolarimeter: (from Right to Left) The Path Length Compensator (PLC); The superachromatic Half-wave plate (HWP); and the polarizing beam splitter, a Modified Glan-Taylor Prism (MGTP).

The polarimetric optics used in the optical dual-beam, automated medium resolution spectropolarimeter for the the VBT (*Chapter 3*) are the Half-Wave Plate (HWP), the Modified Glan-Taylor Prism (MGTP), and the Path Length Compensator (PLC). Fig. A.1 is a photograph of these polarimetric optics. These optical components were custom built by Karl Lambrecht Corporation, Chicago, U.S.A.

A.1 Half-Wave Plates

HWPs are used for rotation of the incoming wavefront relative to the analyzer. They are generally made of uniaxial (non-linear) crystals. Its crystalline optic axis is often called the “fast” axis, while the axis normal to it, is the “slow” axis. These crystals have directional refractive indices; $\mu_{\perp}(\lambda)$ and $\mu_{\parallel}(\lambda)$ in the perpendicular and parallel directions to the fast axis. Due to this birefringence, an incident light through a crystal of thickness d will undergo a differential retardation and a phase rotation of

$$\delta = \left(\frac{2\pi}{\lambda}\right) (\mu_{\perp}(\lambda) - \mu_{\parallel}(\lambda)) d. \quad (\text{A.1})$$

For a HWP, the phase rotation is half the wave ($\delta = \pi$), hence,

$$(\mu_{\perp}(\lambda) - \mu_{\parallel}(\lambda)) d = \frac{\lambda}{2}. \quad (\text{A.2})$$

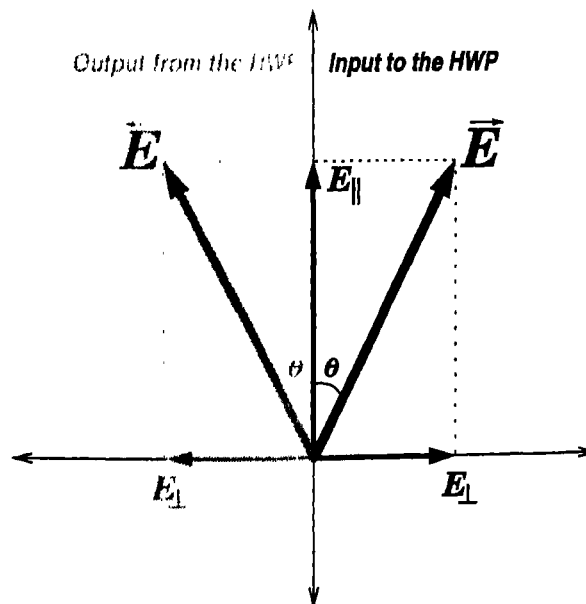


Figure A.2: Input and output wavefronts from a HWP.

Fig. A.2 shows the input and output wavefront from an ideal HWP. For simplicity, a completely linearly polarized input beam is assumed. The electric vector \vec{E} of light at the input, makes an angle θ to the axis of the HWP. The electric vector \vec{E} can be represented by two component vectors \vec{E}_{\perp} and \vec{E}_{\parallel} , perpendicular and parallel to the HWP axis. As the light travels through the HWP, a phase lag of $\delta = \pi$ is introduced.

in \vec{E}_\perp relative to \vec{E}_\parallel . Thus at the output, \vec{E}_\perp is flipped to $-\vec{E}_\perp$ with reference to \vec{E}_\parallel . As a consequence of this effect, the wavefront is rotated by 2θ (Born and Wolf 1999).

From Eqs. A.1 and A.2, one can see that a HWP is wavelength dependent and building an achromatic or superachromatic HWP is challenging. Pancharatnam 1955 demonstrated construction of an achromatic wave plate by stacking three normal HWPs together. In the design by Goodrich 1991, a stack of such achromatic HWPs, made from quartz and single magnesium fluoride (MgF_2) were used in the Pancharatnam configuration to obtain a superachromatic performance.

A.1.1 The Superachromatic HWP.

The design of the superachromatic HWP used in the spectropolarimeter is similar to that of Goodrich. Fig. A.3 shows a schematic layout of the superachromatic HWP design. Each crystal is delicately thinned and polished, so that the entire stack

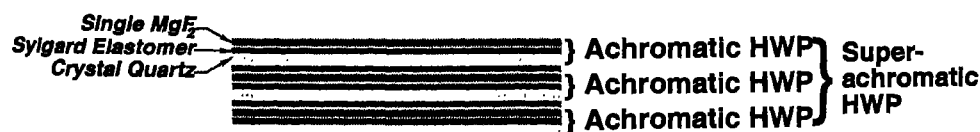


Figure A.3: Schematic layout of the superachromatic HWP design. Six plate Pancharatnam design HWP optimized for 3500\AA to 10000\AA , made of three plates of single magnesium fluoride (MgF_2) and three plates of crystal quartz, cemented with UV transmitting Sylgard Elastomer, without anti-reflection coating. The thickness of the entire stack is ~ 1 mm.

constituting the superachromatic HWP is just ~ 1 mm thick. It is necessary that the HWP be made thin so that the focusing unit of the telescope is least altered from the normal spectroscopic observing mode to that of spectropolarimetric observing mode.

This superachromatic HWP is encased in a 12.7 mm thick black anodized aluminum cell of 28.575 mm outside diameter.

A.1.2 Response Curve of the Superachromatic HWP

The performance of the superachromatic HWP as p Corporation is shown in Fig. A.4. The tests were

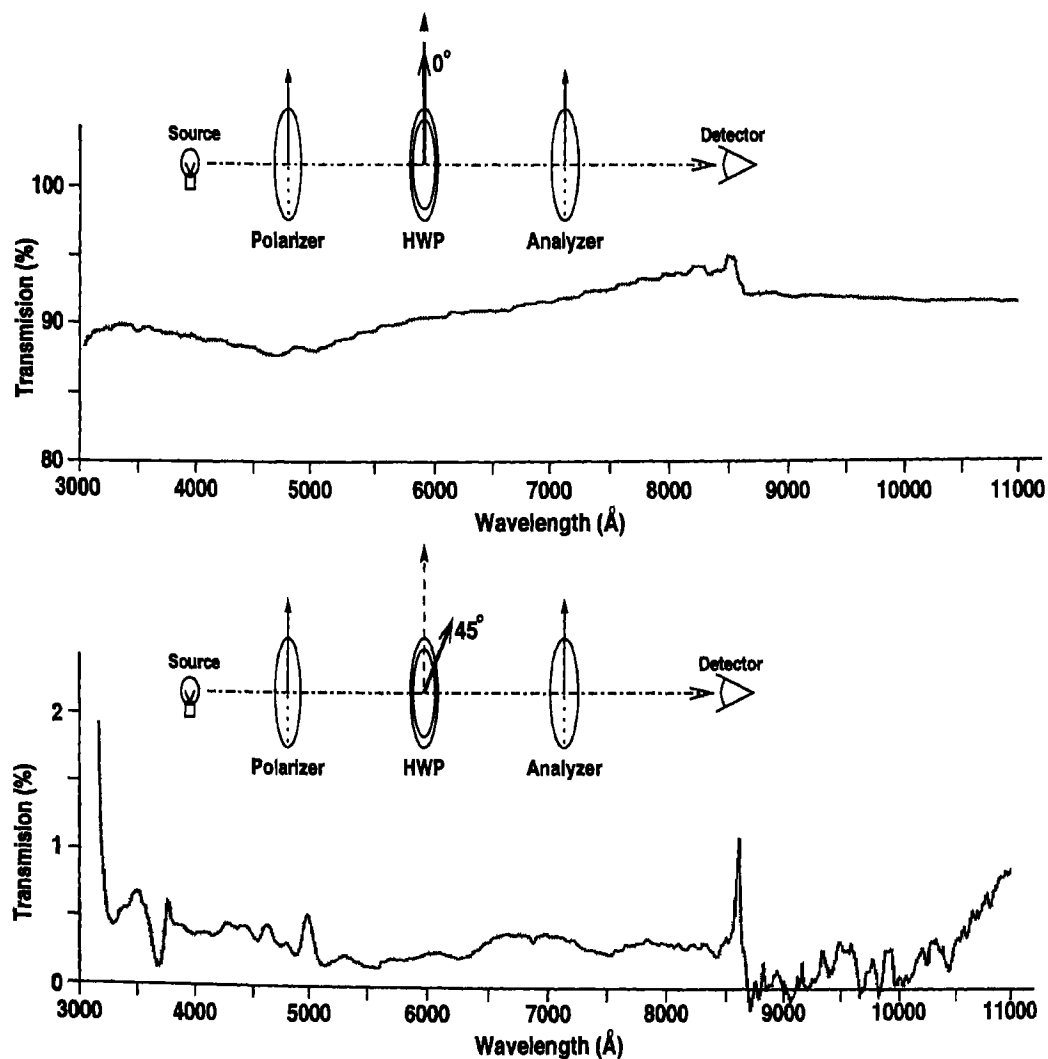


Figure A.4: Response curve of the superachromatic HWP. The spike at $\sim 8500\text{\AA}$, is an artifact of changeover of detectors.

high extinction (60 DB) UV Calcite Glan-Thompson prism polarizers in transmission mode placed in the cavity of a spectrophotometer. The superachromatic HWP was placed between the two polarizers at 0° azimuth. At this position of the HWP, maximum transmission is expected. The top panel of Fig. A.4 shows this transmission as a function of wavelength. The HWP was then turned to 45° azimuth. At this position the HWP should ideally rotate the linear polarized light by 90° for all wavelengths and the analyzer should cut off the light completely. The transmission vs wavelength at this position of the HWP is plotted in the bottom panel Fig. A.4. The spike at $\sim 8500\text{\AA}$ seen in Fig. A.4, is an artifact of changeover of detectors.

A.2 Modified Glan Taylor Prism and the Path Length Compensator

The MGTP shown in Fig. A.5, is made of A-grade Calcite. The extinction of the two beam is $\sim 10^{-4}$ without anti-reflection coating. The input clear aperture is of 10 mm. The nominal beam separation between the e and o beam is 11.86 mm. The

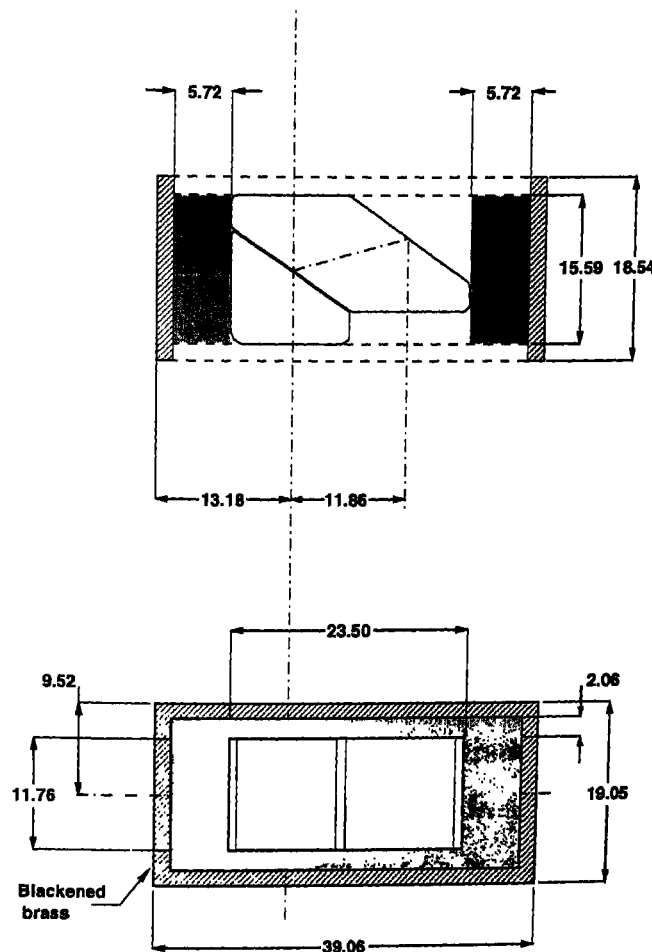


Figure A.5: Drawing of the Modified Glan-Taylor Prism (MGTP) provided by the Karl Lambrecht Corp. (dimensions are in mm).

MGTP is fixed in a blackened brass casing. The small grey inner rectangular box shown in the lower panel of Fig. A.5 represents the area on the input face of the MGTP, which is illuminated by the spectropolarimeter slit.

The PLC is right rectangular prism of Fused quartz with 10 mm clear aperture and 19.845 mm thickness. The entrance and exit surfaces have been polished to a high accuracy.

A.2.1 Lab Test with the MGTP + PLC for the e and o beam response.

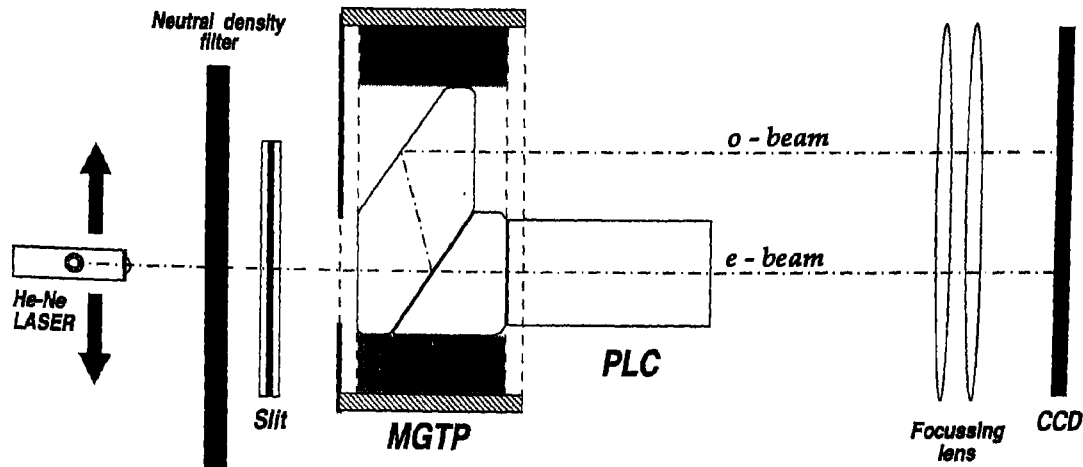


Figure A.6: The laboratory experiment setup with the MGTP + PLC.

A laboratory experiment with the MGTP coupled with the PLC (see *Appendix C.2*) was conducted to check the response and possible distortion of the system on the e and o beam output, as we scan along input surface of the MGTP. The experimental setup is shown in Fig. A.6.

A He-Ne Laser of 50 mW was fixed on a translation device to obtain a fine vertical movement of 0.5 ± 0.01 mm along a slit so that different points of the MGTP could be scanned. Neutral density filters were placed in front of the laser to reduce the intensity of the laser to a safe level for imaging on to a commercial uncooled CCD with an attached camera lens. The CCD output was in a continuous video mode. This output was digitized to an 8-bit data with an IRIS card on a PC. Each data image represents an average of ten frames. Fig. A.7 shows one such image obtained at the center of the MGTP input aperture.

The horizontal fringe pattern seen in Fig. A.7, is the diffraction pattern of the slit. The central peak of the diffraction pattern was selected for analysis. Flux of the vertical columns, within the box indicated with a dashed line in Fig. A.7 were added to from an intensity scan. The top panel of Fig. A.8 shows the intensity scans vertically shifted to show the location of illumination on the slit and the lower panel shows the same intensity scans over plotted for intensity comparison. The side lobes

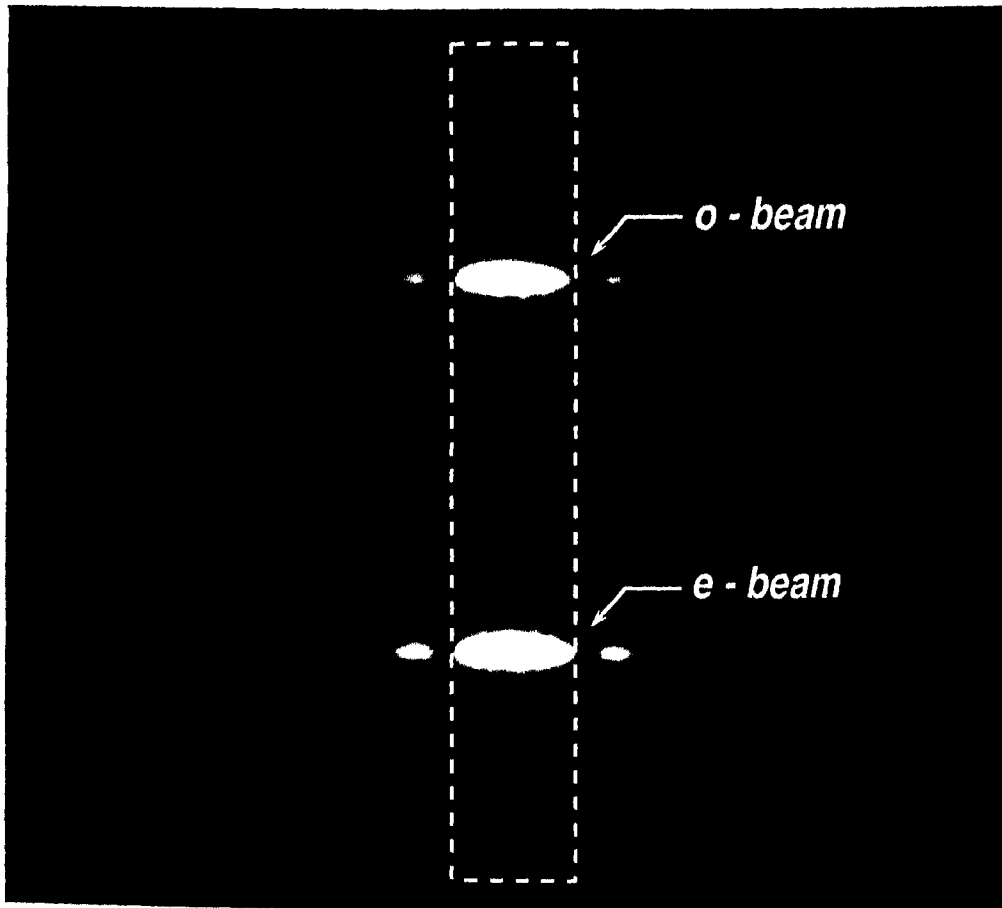


Figure A.7: An output image at the center of the MGTP input aperture.

arise because of the diffraction at the extreme edges of the MGTP.

Fig. A.8 shows that

1. The response of both the e and o beam are similar across the input aperture of the MGTP.
2. The addition of the PLC does not attenuate the e -beam compared to the o -beam.
3. For the total aperture, both the beams are well separated.

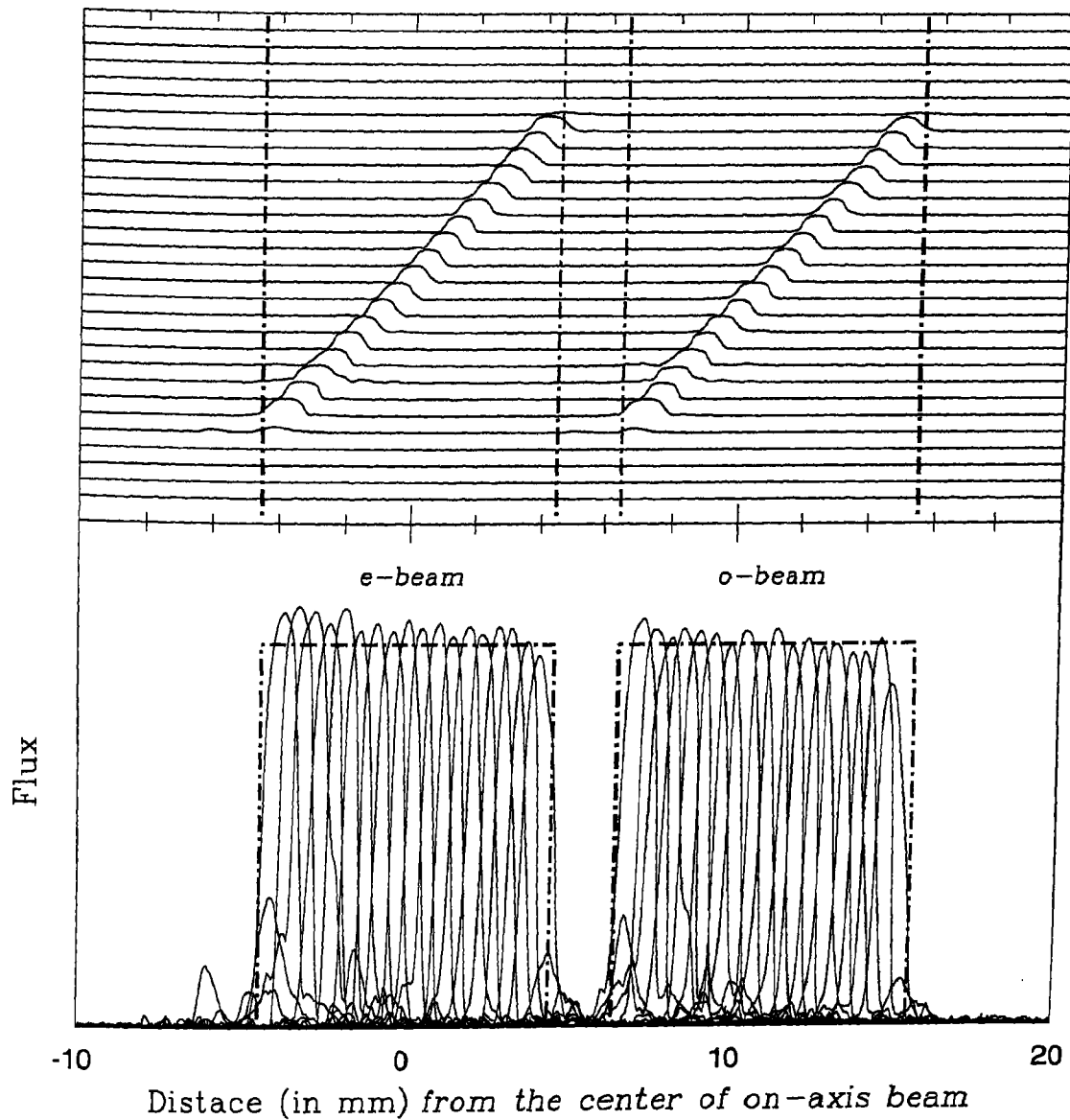


Figure A.8: The scan across the MGTP + PLC. The top panel shows the intensity scans y-shifted to indicate the location of illumination and on the lower panel these are over-plotted for intensity comparison. The vertical dash-dot lines show the limits of the MGTP aperture. The x-axis is centered on the on-axis beam.

References

- Born, M. and Wolf, E. *Principles of Optics*, 1999. 7th Ed. Cambridge University Press.
- Goodrich, R. W. 1991. *PASP* 103, 1314.
- Pancharatnam, S. 1955. *Proc. Indian Acad. Sci.*, Vol. XLI, No. 4, Sec. A, 137.

Appendix:B

Spectrograph & Spectropolarimeter

B.1 Gratings and Diffraction Theory

In a Grating spectrograph, light is dispersed by a combination of diffraction and interference rather than the refractive index variation with wavelength. Light is diffracted and interfered by a regularly spaced ruled surface called the Grating. Joseph Fraunhofer 1823 was probably the first to make and use a diffraction grating. The diffraction pattern from a ruled grating is given by the following equation (Jenkins & White).

$$E = E_0 \operatorname{sinc}^2(\pi w \sin \theta / \lambda) \left[\frac{\sin(n\pi s(\sin \theta - \sin \theta_0) / \lambda)}{\sin(\pi s(\sin \theta - \sin \theta_0) / \lambda)} \right]^2, \quad (\text{B.1})$$

where n is the order number, w the ruling width, s is the ruling spacing, θ is the diffraction angle, θ_0 is the incidence angle, and λ is the wavelength of the light.

B.2 Resolution and Resolving power

From interference law the position of the peaks can be calculated by

$$n\lambda = s(\sin \theta_i - \sin \theta_d), \quad (\text{B.2})$$

where θ_i is the angle of incidence and θ_d is the diffraction direction. Thus the resolution can be found by differentiation

$$d\lambda = \frac{s \cos \theta_d}{n} d\theta_d. \quad (\text{B.3})$$

Better spectral resolution is obtained at higher order n , smaller line spacing s and at angle θ_d approaching 90 deg. A grating has a constant wavelength resolution as a function of angle on the image plane.

The resolving power is given by

$$Q = \frac{\lambda}{d\lambda} = nN \quad (\text{B.4})$$

The resolving power is the order number n times the number of lines N in the grating. However since the efficiency usually decreases with the order number and due to a finite size of the gratings, it is not possible to obtain an extremely high resolving power.

B.3 Dispersion

The linear dispersion in the focal plane of the camera is defined as

$$\frac{\Delta l}{\Delta \lambda} = f \frac{n}{d \cos \theta}. \quad (\text{B.5})$$

Here f is the focal length of the camera and d is the spectrograph slit separation. Eq. B.5 shows that for a given small wavelength difference $\Delta \lambda$, the linear separation Δl is proportional to the order n . Thus the second order spectrum is twice as wide as the first order, etc. Δl is also inversely proportional to the slit separation d .

B.4 Throughput

The throughput can be calculated as the product of the spectrograph slit area and projected area of the grating divided by the square of the focal length of the collimator.

B.5 Blazing Ruling

The efficiency may be increased by making the rulings triangular and using the slope to reflect the light to a particular order. The grating manufacturer will specify the blaze direction and the efficiency of a grating. The rulings are still rectangular in cross section; they are slanted within the groove (Fig.B.2).

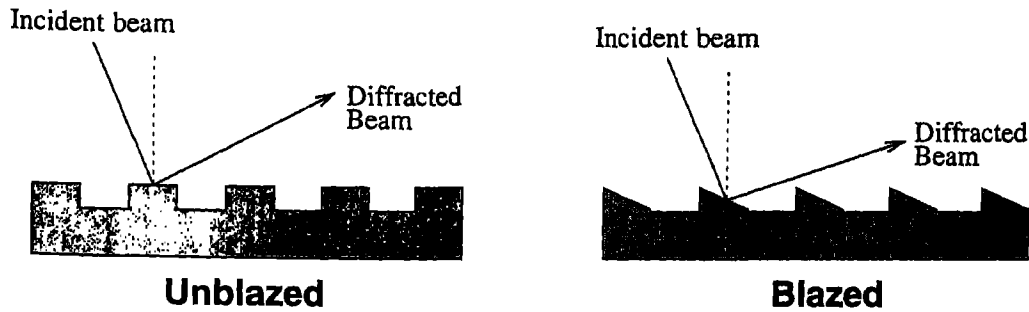


Figure B.1:

B.6 The Boller & Chivens long slit cassegrain spectrograph

The long slit cassegrain spectrograph built by the Boller & Chivens Division of the Perkin-Elmer Corporation, USA for the Anglo-Australian Observatory (AAO), was acquired by Indian Institute of Astrophysics (IIA) in 1985. The Spectrograph After acquisition, the spectrograph camera was replaced with a Carl Zeiss camera of 110mm aperture and 150mm focal distance. The Camera is a semi-solid Schmidt-cassegrain system so that a CCD could be used as a detector. The field is flattened and corrected for an angular field of $\pm 5^\circ$; A TK1024 Photometric liquid N_2 cooled CCD is now used as detector. An Intensified CCD in video-mode is used for remote slit guiding.

The spectropolarimeter, was designed as an add-on equipment to this spectrograph. Fig. ?? shows the optical layout of the spectrograph. The spectrograph grating can be changed. The existing grating for this spectrograph at the observatory are:

150l/mm	Blazed at 5000\AA	$9.90\text{\AA}/\text{pixel}$ for $n = 1$
300l/mm	Blazed at 5000\AA	$4.95\text{\AA}/\text{pixel}$ for $n = 1$
600l/mm	Blazed at 5000\AA	$2.48\text{\AA}/\text{pixel}$ for $n = 1$
850l/mm	Blazed at 5000\AA	$1.75\text{\AA}/\text{pixel}$ for $n = 1$
1200l/mm	Blazed at 5000\AA	$1.24\text{\AA}/\text{pixel}$ for $n = 1$

All these gratings can be used for spectropolarimetry; however in this work only the grating with 300l/mm has been used.

The spectropolarimeter is now remotely operated from a 66MHz 486 Personal Computer in the console room.

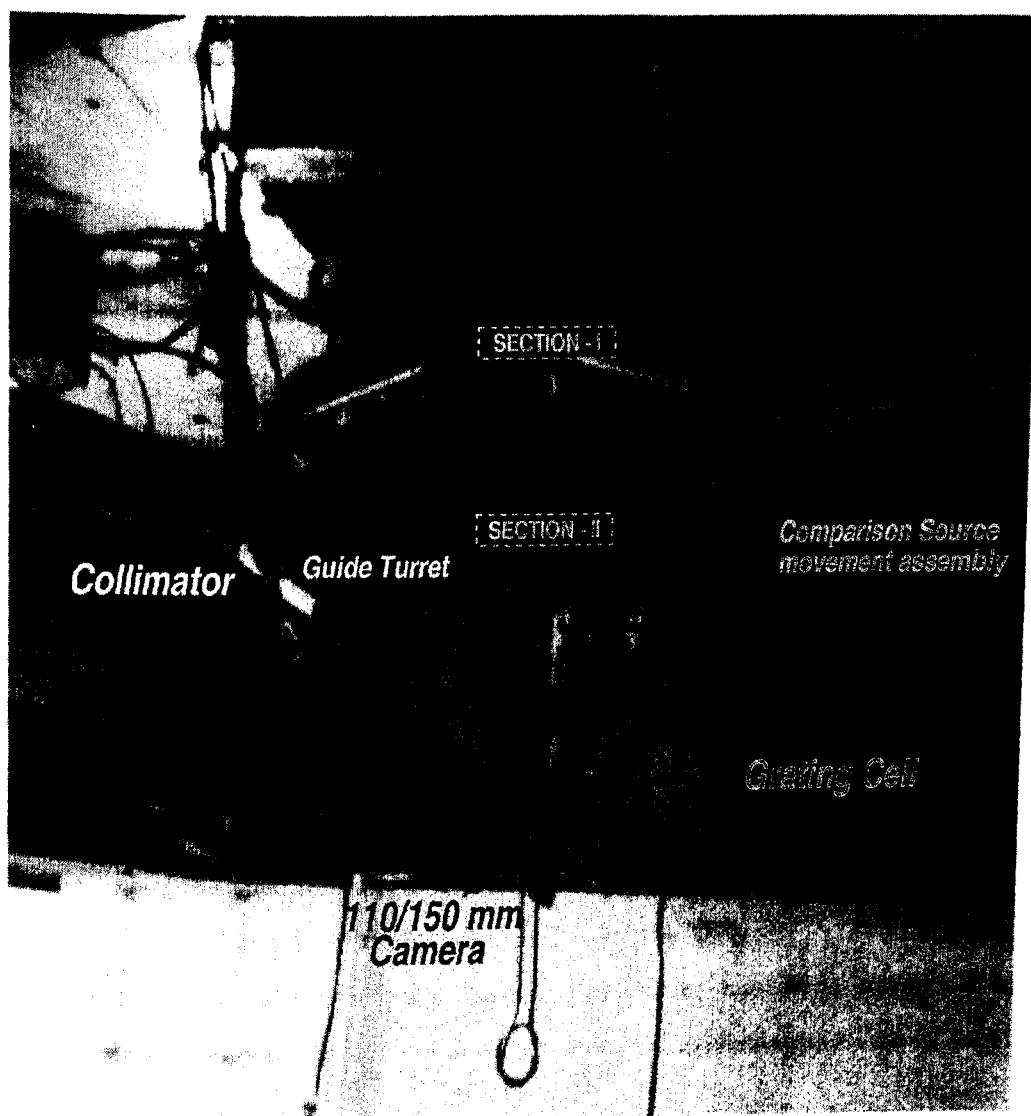


Figure B.2: The Boller & Chivens long slit cassegrain spectrograph now converted into a spectropolarimeter. The major sections of the spectrograph are marked. The locations of the polarimetric attachments "Section-I" and "Section-II" are also indicated. In this picture, the CCD camera is not mounted.

References

Fraunhofer, J. 1823. *Annalen der Physik* 74, 337

Jenkins, F. A. & White, H. E., *Fundamentals of Optics*, McGraw Hill, 1981.

Appendix:C

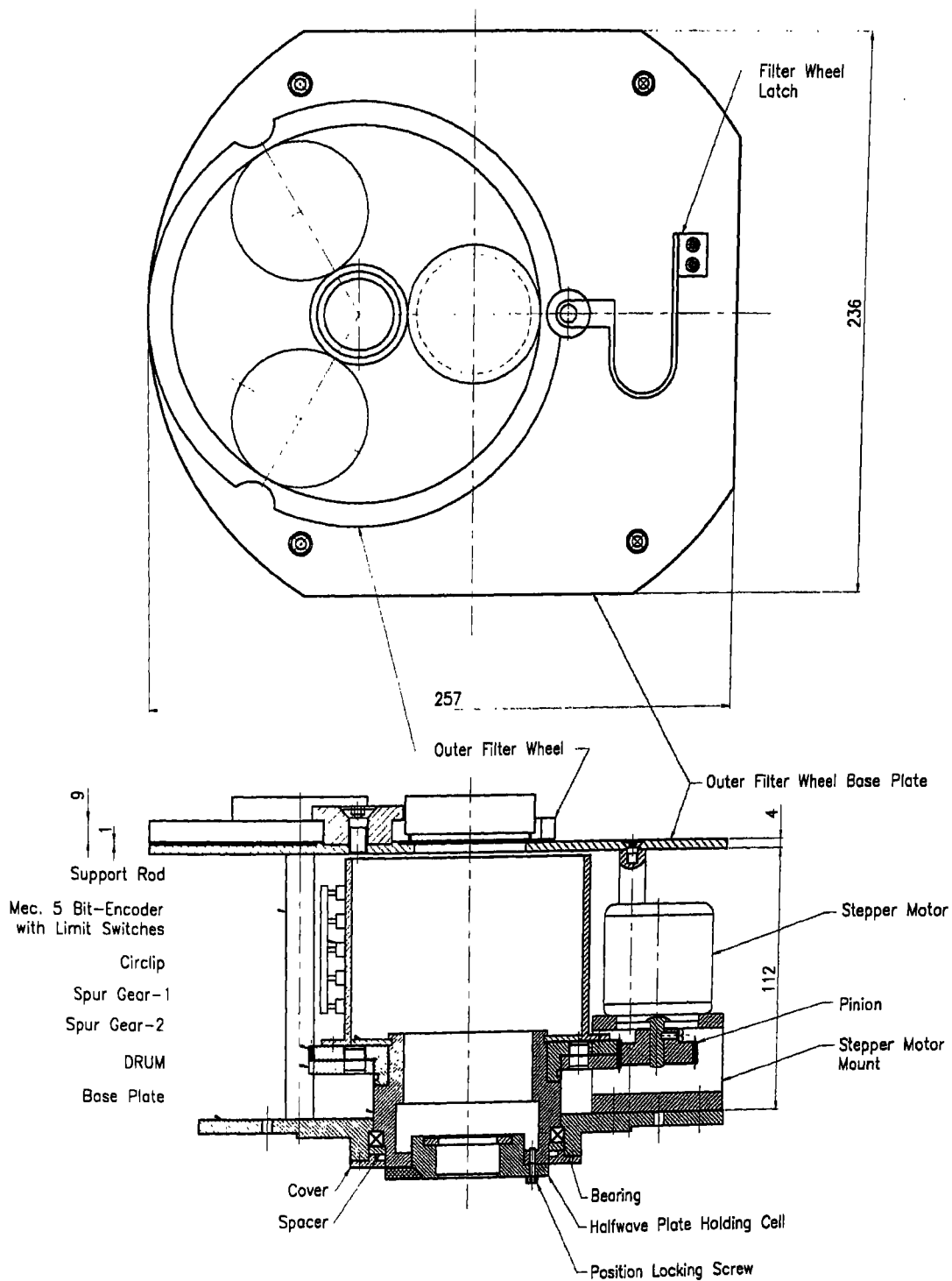
Drawings of the Spectropolarimeter

The spectropolarimeter, was designed as an add-on equipment to the Boller & Chivens long slit cassegrain spectrograph. The details about the spectrograph is provided in *Chapter 3* and *Appendix B.6*. For the instrumentation, calibration and observation of the spectropolarimeter, *Chapter-3* and *Chapter-5* can be referred. The spectropolarimeter is now remotely operated from a 66MHz 486 Personal Computer from the telescope console room.

Fig. 3.2, shows the optical layout of the spectrograph. The polarimetric optics is mounted on to the spectrograph in two separate sections. *Section-1* is attached at the top of the spectrograph flange, going into the central hole of the telescope's instrument mounting flange, while *Section-2* replaces the existing filter wheel of the spectrograph. The location of the two *Sections* are marked by two boxes in Fig. 3.2. In this appendix, we look into the detailed Engineering drawings of these two sections.

C.1 Engineering Drawings to The Section-1

Fig. C.1 is the assembly drawing of the *Section-1* of the spectropolarimeter. This section consists of the HWP rotating unit, provision for an online calibration with a stack of polarizing filters and a facility for filtering the second order spectra.



Section-1 Assembly

Figure C.1: An assembly drawing of the Section-1 of the spectropolarimeter. This section consists of the HWP rotating unit, an online calibration arrangement with a stack of polarizing filters. The unit also has the facility of filtering the second order spectra.

The HWP rotating unit consists of a "HWP holding cell" (Fig C.2, bottom) which holds the Pancharatnam design superachromatic half wave plate (HWP). This cell

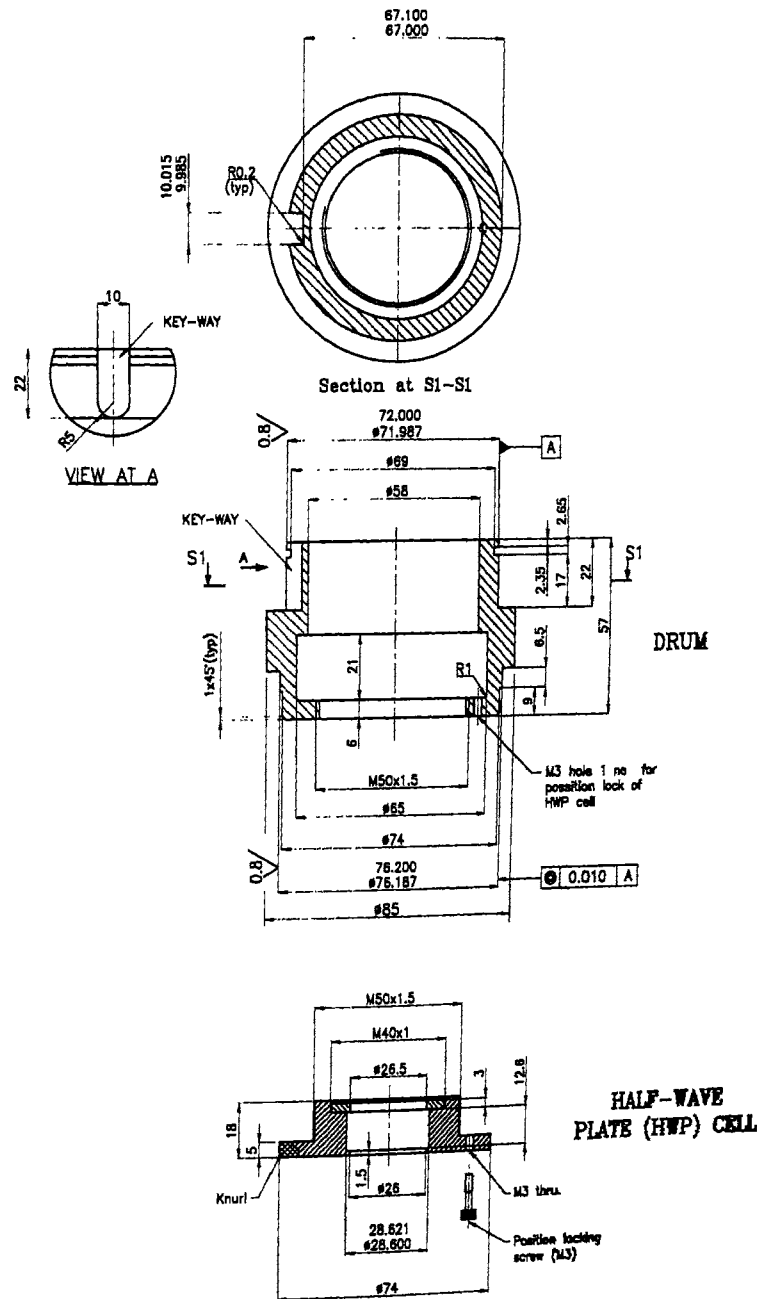


Figure C.2: The HWP holding cell and the drum. The HWP holding cell is threaded on to the drum and position locked with a position locking screw.

is threaded on to the "drum" (Fig C.2 top), which brings the HWP in the cell close to the spectrograph slit. The threaded HWP holding cell's position is locked on to the drum with a position locking screw. The drum is mounted on a KA030XP0 slim bearing supplied by Kaydon Corp. USA. For the rotation of the HWP, the drum

is fixed to a split anti-backlash, on axis spur gear. The split sections of the gear is shown as "Spur Gear 1" and "Spur Gear 2" in the upper section of Fig C.3. The

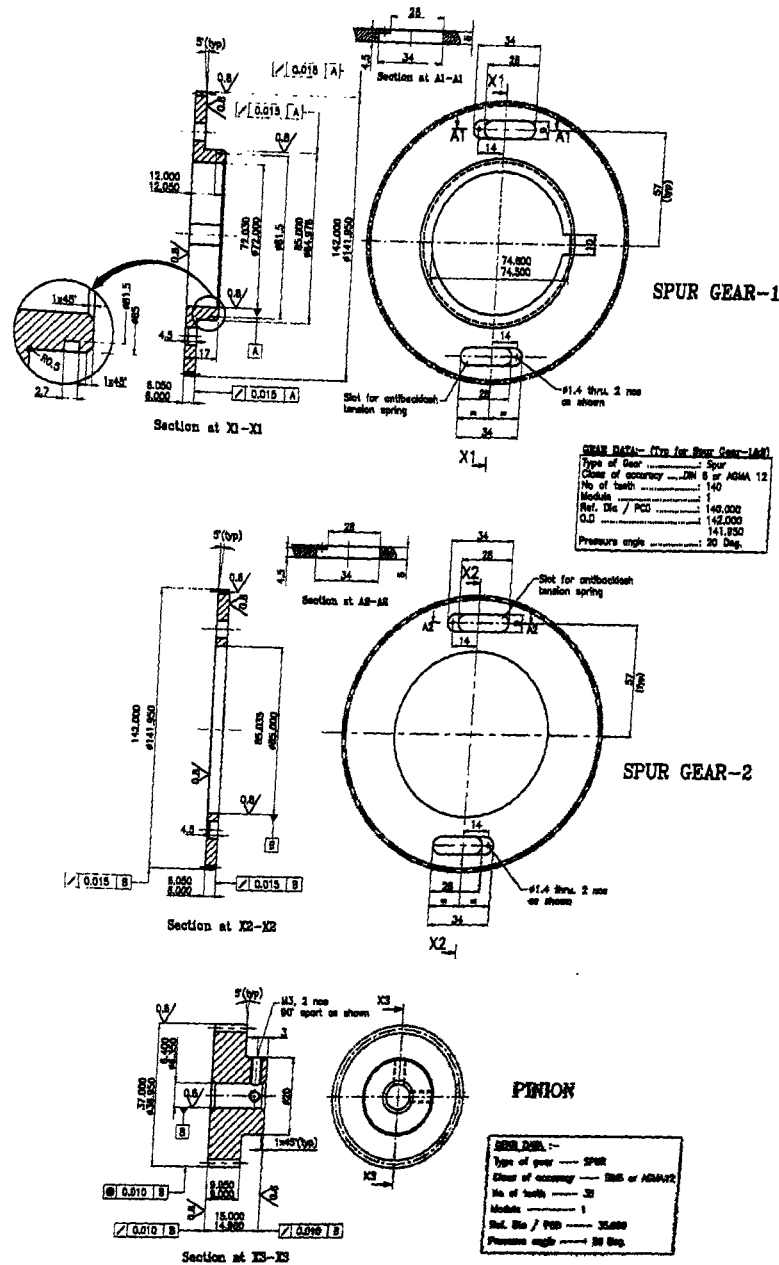


Figure C.3: 1:4 Spur Gear Unit. The "Spur Gear 1" and "Spur Gear 2" are the two sections of the split anti-backlash unit held together on both sides by tension springs. The pinion is thus locked against these split gears.

two slots shown on the top and bottom of each of the split gears, are for the tension springs that holds two sections of the split anti-backlash unit, together. It also locks on to a single pinion (Fig C.3, bottom), that rotates the gears. The gear ratio of the

spur gear unit is 1:4. The pinion is mounted on to a *M061FD08*, "Slo-syn" stepper motor that drives the gear unit in a single direction. The "stepper motor mount" is shown in Fig C.4 top.

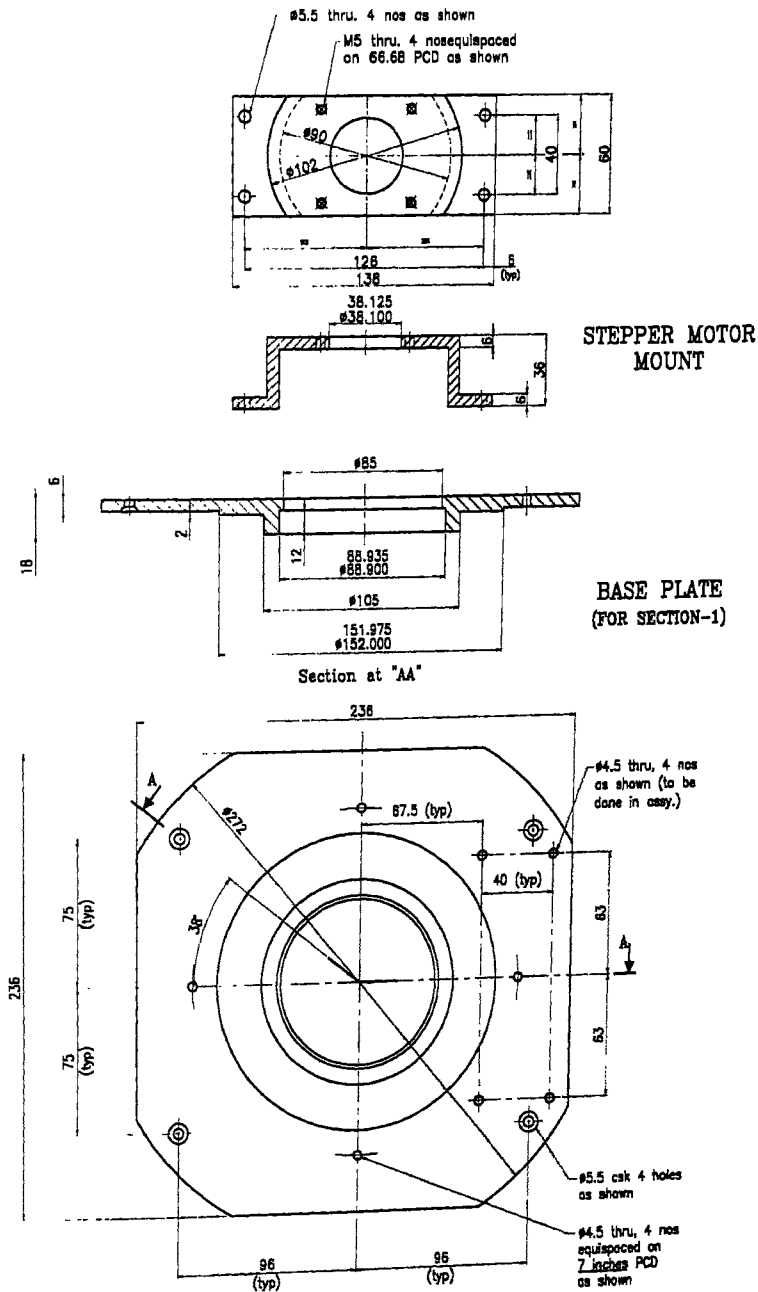


Figure C.4: The stepper motor mount and the base plate for the Section-1

To avoid joints, the stepper motor mount is carved out from a single aluminum piece on a lathe. Fig C.4 also contains the drawing of the "base plate" for the *Section-1* which is snug fitted and screwed on to the spectrograph at four equi-spaced points on a 7 inches PCD (Pitch circle diameter). The entire *Section-1* is assembled on

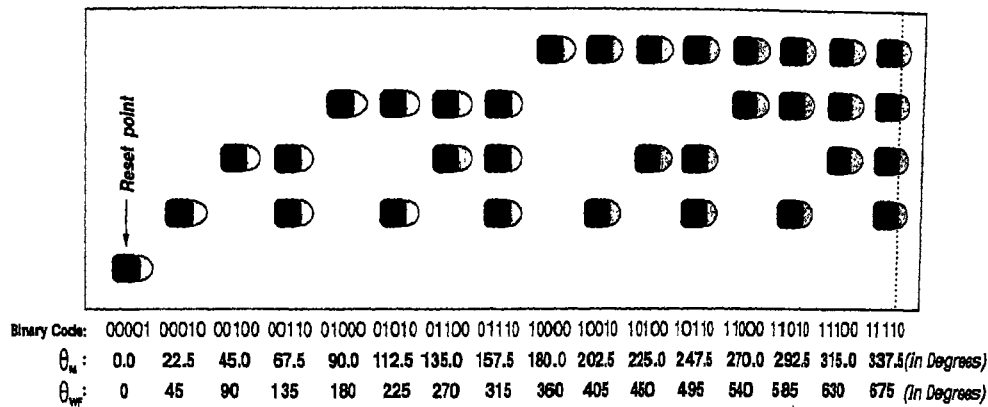


Figure C.5: The outer surface of the mechanical absolute encoder cylinder. The shaded squares are the binary coded grooves. The corresponding binary code along with θ_M and θ_{WF} (in degrees) are written below. The dotted line near $\theta_{WF} = 675^\circ$ is the joining point to the left end as a completion of the cylinder.

this 'base plate'.

On the gears, an on-axis mechanical 5-bit absolute encoder is mounted (Fig C.1). This encoder is a hollow cylinder with binary coded grooves on its outer surface, as shown schematically in Fig C.5. The shaded squares are the binary coded grooves. The cylinder is rigidly fixed on to the gear and rotates with the HWP. The stationary 5 equally spaced limit switches, are in constant contact with the cylinder. As the cylinder rotates along with the HWP, the limit switch heads rolling on its outer surface, are activated and deactivated, as they fall in and out of the grooves. The trailing edges of the grooves are sloped to the surface of the cylinder so that the limit switch heads that fall into the grooves can easily roll out of them. The signal from the 5 limit switches are read as a 5-bit binary code which is then translated by the instrument control computer into the rotation angle θ_M of the encoder gear unit and further translated into the wavefront rotation angle $\theta_{WF} = 2\theta_M$ due to a HWP (Appendix A.1). The binary codes, and corresponding values of θ_M and θ_{WF} are shown along with the groove layout in Fig C.5. The shaded squares in Fig C.5 are the binary coded grooves.

Apart from the rotation mechanism and the absolute encoder, *Section-1* has the online calibration and the second order cutoff filter unit. This unit consist of a filter wheel denoted as the "Outer Filter Wheel" which rests on four aluminum

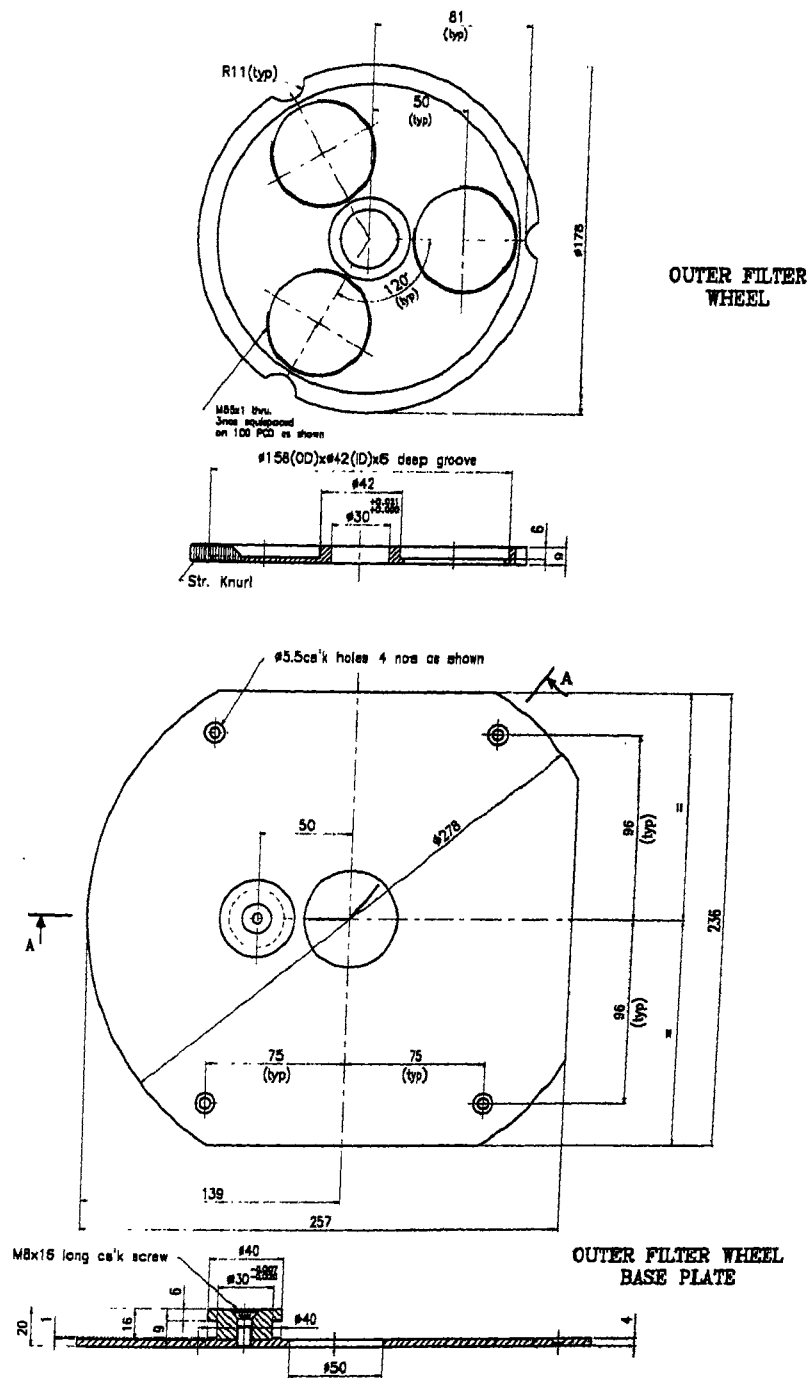


Figure C.6: The online calibration and the second order cutoff filter unit. The "Outer Filter Wheel" and the "Outer Filter Wheel Base Plate".

rods, just above the mechanical absolute encoder cylinder. The top view of the assembled unit can be seen in Fig C.1. The "Outer Filter Wheel" and the "Outer Filter Wheel Base Plate" are separately shown in Fig C.6. The outer filter wheel has three filter slots to hold 55 mm filters and is fixed to its base plate with a

brass bush bearing. A $\phi 158(OD) \times \phi 42(ID) \times 6$ mm deep groove has been provided to facilitate the threading of the filter cells on to the slots. The first slot is kept empty for regular spectropolarimetric observations. On the second slot, a stack of polarizing filters are mounted for an online calibrations. The polarizing filters have a much lower efficiency than a polarizing prism. Since a polarizing prism with 55 mm clear aperture accepting an $f/13$ beam would be extremely costly, it was decided to improve the efficiency of the polarizer by stacking a couple of polarizing filters. The coupled polarizing filters have been well aligned with each other to obtain a maximum efficiency from them. The third slot is fixed with a 2 mm thick *GG-495* glass filter to cut off the second order blue and to enable observations up to 9500\AA . The outer filter wheel is not automated, hence changes between the three modes of operations, have to be made at the instrument. A knurling has been provided on the outer edge of the filter wheel. The filter wheel is reached through a small circular opening just above the telescope flange and can be locked into the desired position with a spring loaded bearing latch.

C.2 Engineering Drawings to The Section-2

Section-2 is the analyzer section of the spectropolarimeter. A Modified Glan-Taylor Polarizing Prism (MGTP) is used as the dual beam analyzer. Fig. A.5 of the Appendix A.2 shows the optical drawing of the MGTP. The MGTP was provided in a blackened brass casing by the Karl Lambrecht Corp. The path length compensator (PLC), is coupled to the on-axis exit (the *e-beam*) of the MGTP. The total assembly of MGTP + PLC is housed just below the spectrograph slit in order to accept the beam without vignetting. Fig. C.8 shows the cell assembly consist-

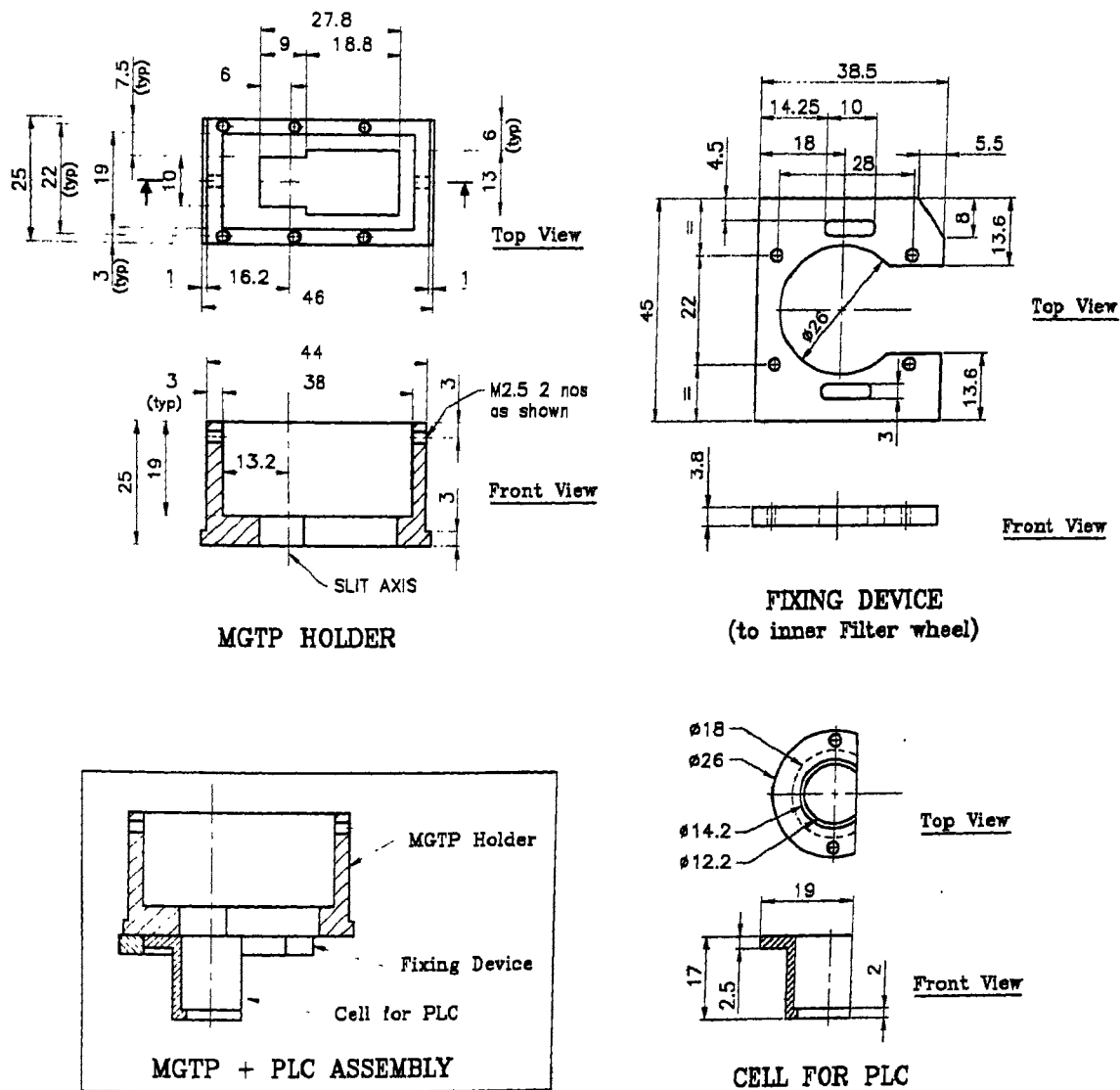


Figure C.7: The analyzer unit: The MGTP + PLC assembly.

ing of the MGTP holder, cell for PLC, and the mounting device that attaches the MGTP + PLC assembly on to the inner filter wheel. A decker mask is placed on the 10 mm entrance aperture of the MGTP, restricting it to ~ 8 mm along the slit length. Masking is necessary to ensure that the diverging $f/13$ beam does not hit the sides of the MGTP or the PLC.

The order separating filter wheel, just below the spectrograph slit, of the B & C Spectrograph was replaced by a redesigned filter wheel shown in Fig. C.7. This filter wheel has three slots, one of them is for the MGTP + PLC assembly. The other two slots are kept for normal spectroscopic observations with or without an order

separating filter.

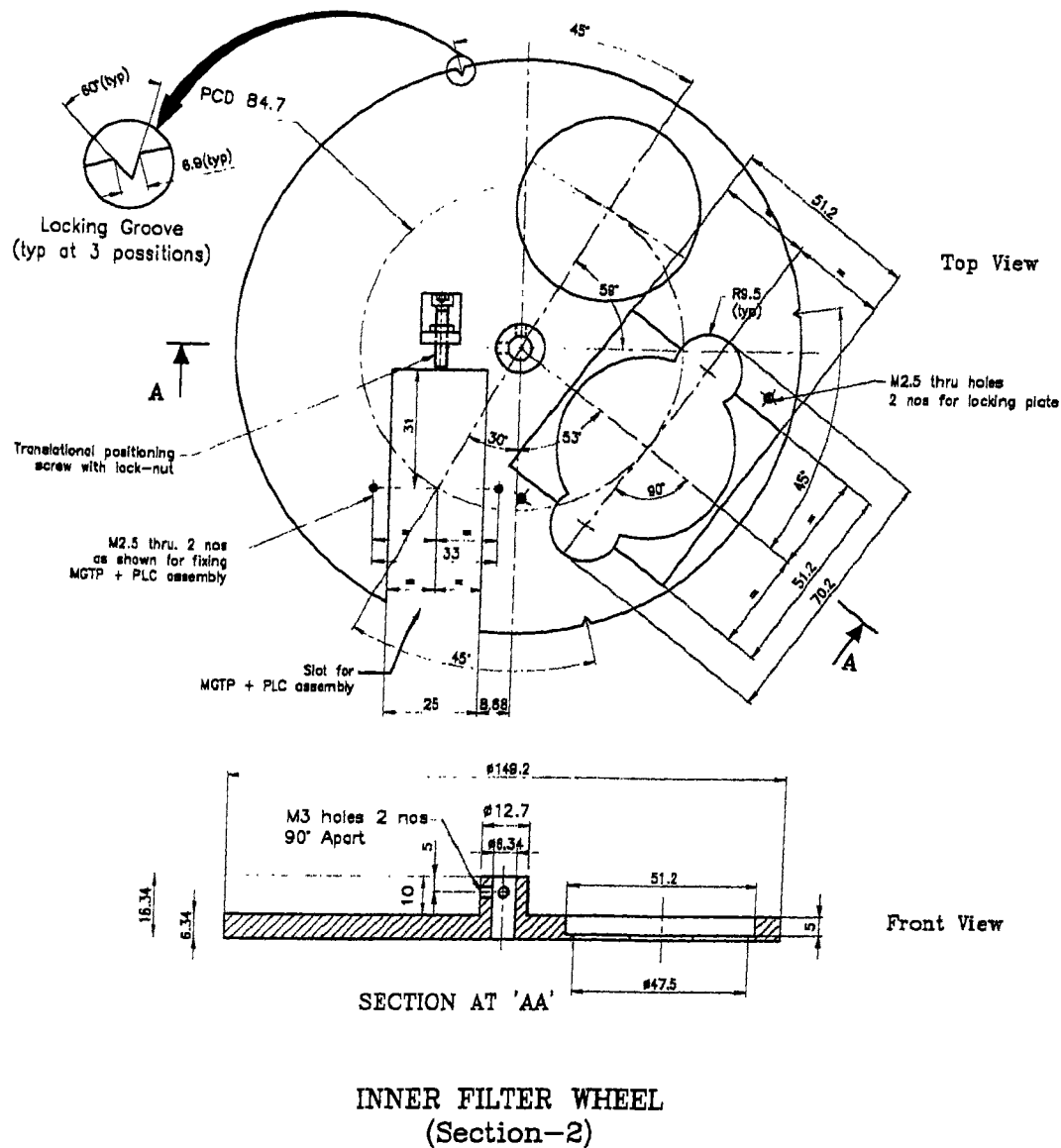


Figure C.8: The "Inner Filter Wheel" that holds the analyzer unit (the MGTP + PLC assembly) close to the spectrograph slit. This filter wheel has three slots, one of them is for the MGTP + PLC assembly and the other two slots are for normal spectroscopic observations.

The MGTP + PLC assembly is fixed at two points with M2.5 screws. The slots on the fixing device of the MGTP + PLC assembly (Fig. C.8) enable the analyzer unit to be moved along the length of the slit. The translational positioning screw with lock-nut aids in the translation along the slit and to lock it at its most optimum position. The filter wheel is locked into position by a spring loaded ball-lock, locking into the locking grooves.

Note, that the three slots of this inner filter wheel are not equi-distant from each other around the PCD of the filter wheel. This is done on purpose to allow the use of all the three slots, without the MGTP + PLC assembly being restrained or hit by the filter wheel holding rod.

C.3 Shutter

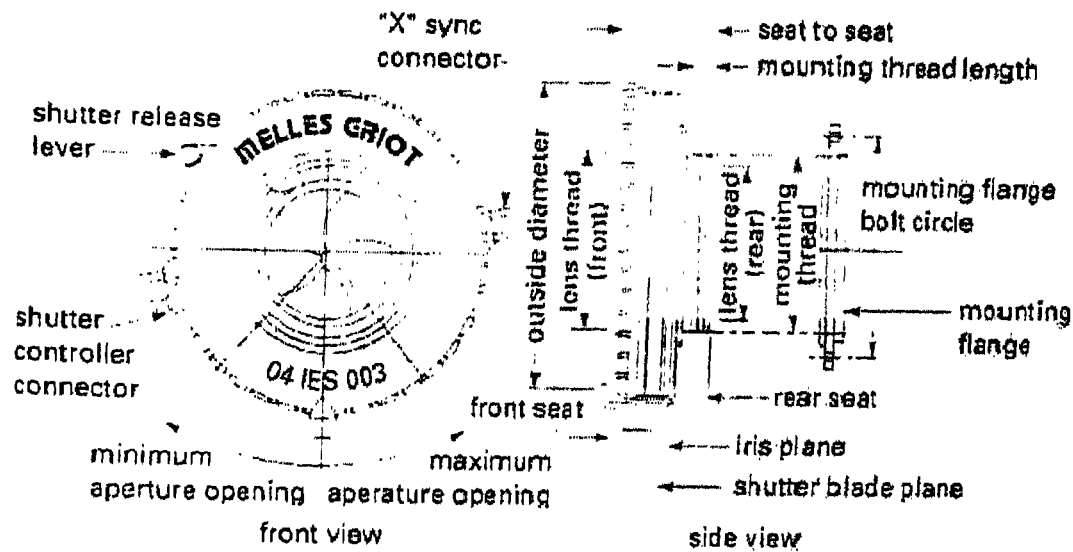


Figure C.9: Shutter for the spectropolarimeter. A 63.5 mm aperture Melles Griot 04 IES 003.

The shutter of the spectrograph was replaced with a larger 63.5 mm aperture Melles Griot 04 IES 003 shutter, to allow both the on-axis *e-beam* and the off-axis *o-beam* without obstructions. Fig. C.9 shows drawing of this shutter. The iris of the shutter is kept fully opened and is not used. The shutter is operated remotely by the data acquisition computer through the CCD controller. The CCD controller connects, through an electronic circuit, to the shutter at the shutter controller connector (see Fig. C.9). Through the "X" sync connector, the status of the shutter is obtained. When the shutter is open, the "X" sync connector pins are shorted and when the shutter is closed the pins are opened. The "X" sync connector is sensed by the instrument control computer. This establishes the cross communication between the data acquisition computer and the instrument control computer. The importance of the cross communication and automation is discussed in *Section 3.4 of Chapter 3*.

Appendix:D

Real Time Instrument Control and Execution of SPRS

D.1 Real Time Instrument Control

A PC based instrument control was developed for the Automated Medium Resolution Spectropolarimeter at the Vainu Bappu Telescope (VBT). The requirements for the instrument controls were:

1. Rotate the HWP to a specified angle α .
2. Continuous rotation of the HWP, required for depolarization.
3. Verification of the rotated angle α of the HWP; an encoder readout.
4. Switch ON and OFF the comparison source ($FeAr$, $FeNe$) of the spectropolarimeter.
5. To open and close the protective shutter for the I-CCD which is being used for spectrograph slit viewing.

The present instrumentation facility at the VBT provides an option of using 6 stepper motors and a digital I/O for encoder readings at prime and cassegrain end. The stepper motors are selected through a multiplexer and each of the stepper motors can be operated one after the other. Only the selected motor is energized while the rest of the motors are de-energized. The selection of the stepper motor port, the direction of rotation of the stepper motor and the clock pulse for rotation of the stepper motor is provided by the 16 bit digital I/O port on the instrument control PC.

The spectropolarimeter uses 3 stepper motors for the requirements 1, 2, 4 and 5, (mentioned above).

D.1.1 Switching of the Comparison Source

Switch ON and OFF the comparison source involves the movement of the *M1 L1 D1* assembly with the comparison source, in and out of the optical path (see Fig. 3.2). A stepper motor driven screw rod moves the assembly onto the optical path. The movement is stopped by a limit switch which also switches on the comparison source bulb. Similarly the assembly is retracted from the optical path by reverse rotation of the stepper motor until the other limit is sensed. The source is also switched off by the retraction of the assembly.

The instrument control PC reads the two limit signals through the digital I/O port to stop the rotation of the stepper motor. The direction of rotation of the stepper motor is selected depending on the command of switching "ON" or "OFF" the comparison source.

D.1.2 Operation of the Protective Shutter for the I-CCD

The protective shutter for the I-CCD is provided just below the eyepiece/CCD guide turret. It is to protect the I-CCD from the intense light of the comparison source and it is also used during observations of very bright sources. Due to space constraints, a conventional shutter was not used. The shutter is a sliding one and operates with a stepper motor in the same principle as the switching of the comparison source.

D.1.3 Rotation of the HWP

The HWP is rotated around the optical axis through a 1:4 anti-backlash spur gear unit. The pinion is coupled to a stepper motor. The locking of the gear unit for holding the HWP fixed, is provided by keeping the stepper motor continuously energized. This required a modification on a stepper motor power driver card which is configured for driving 3 stepper motors with a single clock. The clock pulse for rotation of this stepper motor had to be also isolated from the clock pulse for the other two stepper motors. Two separate clocks were made available, one was

reserved for the rotation of the HWP while the other clock was for switching the comparison source or for operating the I-CCD protective shutter.

For moving the HWP by an angle¹ $\alpha/2$, the exact number of pulses provided to the stepper motor is

$$n_{\alpha} = \text{Integer of } \left(4 \times \frac{\alpha/2}{1.8} \right), \quad (\text{D.1})$$

where 4 is the gear ratio and 1.8 is the step angle of the stepper motor. The rotational accuracy of the HWP, in the worst case when α is not a multiple of 0.9, is 0.45, which is the rounding-off error ($(\sigma_{\alpha})_r \leq 0.45$). Driving the stepper motor by providing exact number of pulses, has been found to be extremely reliable. However, as a further check, the position angle of the HWP, is read by a 4-bit absolute encoder with 4 binary coded limit switches at 16 positions of the HWP. This encoder signals back the position angle of the HWP at the LSB (least significant bit) resolution of 22.5, to the instrument control computer. An extra limit switch is provided on the encoder to reset the HWP to zero position by resetting the gear.

To ensure speedy data acquisition, the data acquisition and the instrument control were done simultaneously. The time gap between each exposure required for reading the CCD data was effectively used for instrument control by sensing the shutter closing of the main CCD detector and initiating the required angle movement. The required observations at different angles were initiated using a Macro command of Data acquisition software.

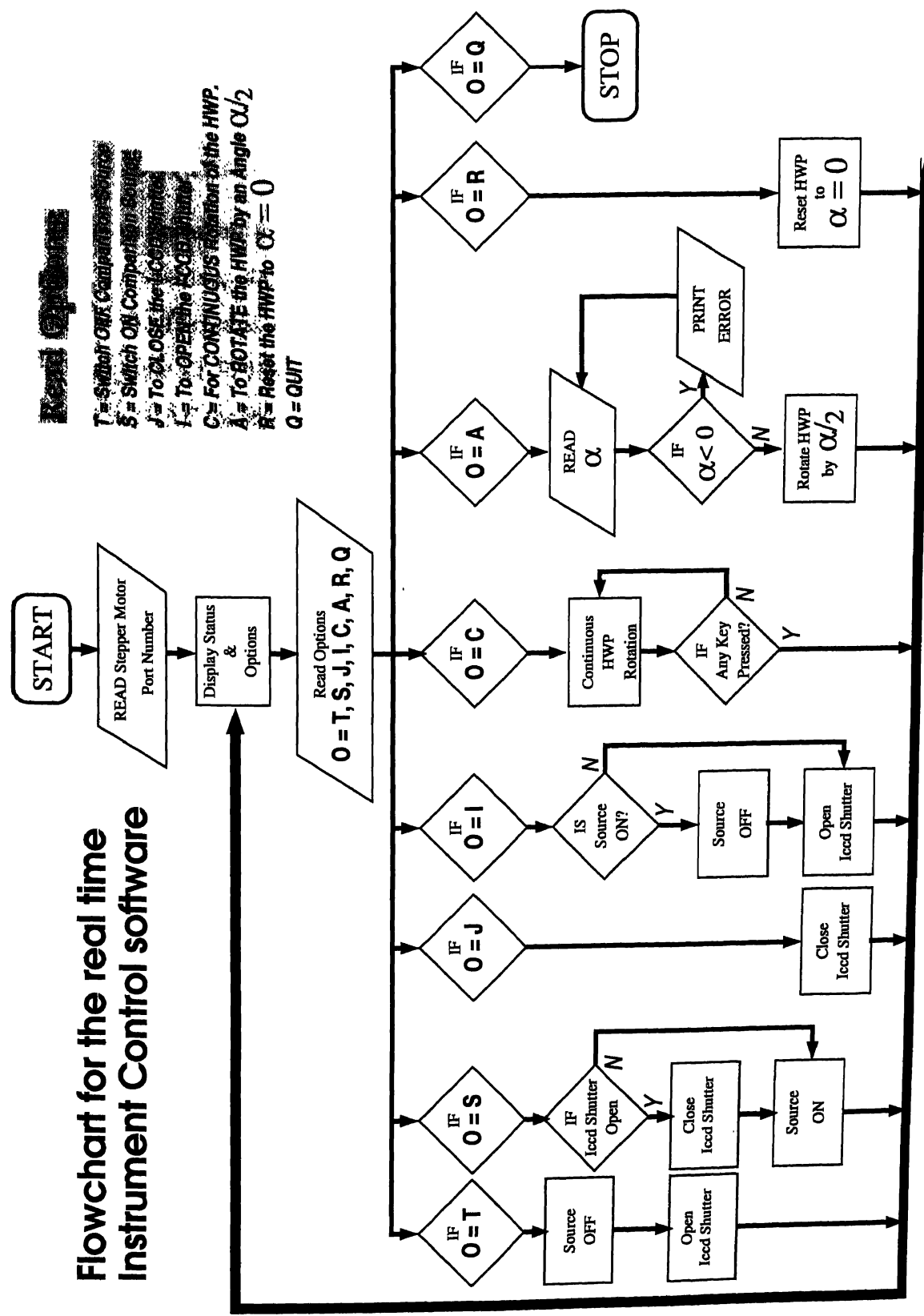
The starting reference position called reset position, taken as angle 0, is sensed by the actuation of the above said reset switch.

D.1.4 Software

The software for the instrument control was written in Borland Pascal version 7.0. The main routines of the code is shown in the following flowchart. The additional features provides movement in equal steps of $\alpha/2$ (e.g. steps of 22.5 for $\alpha = 0^{\circ}, 45^{\circ}, 90^{\circ}$ and 135°).

¹As per the convention, the rotation of the HWP is expressed as $\alpha/2$ because the incoming wavefront through the HWP is rotated by twice this angle.

Flowchart for the real time Instrument Control software



Read Options
 T = Switch OFF Computer
 S = Switch ON Computer
 J = To CLOSE the ICCD Shutter
 I = To OPEN the ICCD Shutter
 C = For CONTINUOUS rotation of the HWP.
 A = To ROTATE the HWP by an Angle $\alpha/2$
 R = Reset the HWP to $\alpha = 0$
 Q = QUIT

Continuous rotation of the HWP for depolarization is also incorporated. The online information about the total angle moved from the zero reference position and the reading of the positional encoding system are all displayed on the computer terminal.

D.2 Execution of SPRS

SPRS is an acronym for SpectroPolarimetric Reduction Software developed for reducing the spectropolarimetric data obtained by the fabricated spectropolarimeter (*Chapter 3*). The capability of SPRS has been described in *Section 3.8 of Chapter 3*. The core code of SPRS is written in fortran using subroutine calls from “imfort” package in IRAF for direct handling of the data in an IRAF image format. The “imfort” subroutine calls used in our fortran code are listed with their short description, in Table D.1. The details on these subroutines can easily be obtained from an IRAF

imsdir	:	Defines the directory of the image pixel file.
imopen	:	Open an existing image.
imgl	:	Get (read) an image line.
imcrea	:	Create a new image.
imhcpy	:	Copy an image header.
impl	:	Put (rewrite) an image line.
imclos	:	Closes an image.
imemsg	:	Convert an imfort error code into an error message.

Table D.1: The “imfort” subroutines used in SPRS

manual or through the IRAF online help. The fortran code is compiled using the “fc” command in IRAF environment, which automatically compiles and links the “imfort” libraries and creates the executable file. This executable fortran code is embedded in a script (spolari.cl). The script is defined as an IRAF “task”.

By executing

```
cl> task spolari = spolari.cl
```

a new task “spolari” is added to the “current package”, i.e., the package that is listed when “?” is entered. Then, like a normal IRAF package, the input and output

parameters to SPRS can be edited through the IRAF command

```
cl > eparm spolari.
```

The command “*eparm spolari*” will open the following parameter table for editing.

```

                                I R A F
                                Image Reduction and Analysis Facility
PACKAGE = clpackage
TASK = spolari

(sp000 =          sp000) e & o Spectra at  0-deg.
(sp045 =          sp045) e & o Spectra at 45-deg.
(sp090 =          sp090) e & o Spectra at 90-deg.
(sp135 =          sp135) e & o Spectra at 135-deg.
(Nape =           1) Aperture for e-Spectrum.
(Napo =           2) Aperture for o-Spectrum.
(Nb =             1) Band for the SPECTRUM.
(Nbe =           4) Band for SIGMA.
(Nmed =          3) Median Smooth (Number of pixel).
(spP5 =          OutputP) Output Spectra (F, Q, U, P & Position Angle).
(bCal =          yes) Perform Instrumental Response Correction?
(bZero =         yes) Perform Telescope Polarization Correction?
(spCal =         InstResp) Instrumental Response Spectra.
(spzero =        TelPol) Telescope polarization (Q0, U0) Spectra.
(CalA =          0.) Offset angle to be subtracted (in deg).
(bqu =           no) Re-compute Q & U from P & Position Angle?
(pixdir =        /home/pavan/tmp/) Directory for the pix-file. .
) _ode =         ql
```

Table D.2: The *eparm spolari* parameter table used for SPRS

The first four parameters “*sp000*”, “*sp045*”, “*sp090*” and “*sp135*” are the filenames of the extracted input spectra. These files contain the four spectra L_0 , L_{45} , L_{90} and L_{135} in “*multispec*” format of IRAF. Each spectrum contains two apertures for *ordinary* and *extraordinary* beams.

The next two parameters in the parameter table, *Nape* and *Napo* are the aperture number for the *e* and *o* spectrum respectively. *Nb* is the band number containing the flux spectrum and *Nbe* is the sigma or the noise of the flux spectrum computed from photon noise while extraction during pre-processing. *Nmed* is the number of pixel used for a running median smoothening of the input spectra *sp000*, *sp045*, *sp090* and *sp135*. Median smoothening is done before any computation is performed on these spectra. *spP5* is the name of output spectra denoted in the above parameter table by the file name “*OutputP*”. The output spectra contains the flux $F(\lambda)$, the normalized Stokes parameters $Q_n(\lambda)$ and $U_n(\lambda)$, the degree of polarization $P(\lambda)$ and the position angle $\Theta(\lambda)$. The layout of the output spectrum is given in Table 3.2.

The next two parameters *bCal* and *bZero* are boolean parameters (yes/no), to perform instrumental response correction and telescope polarization correction respectively. These two boolean parameters have to be set to “no” when SPRS is being used to compute the instrumental response spectra *spCal* and telescope polarization spectra *spzero*. If these boolean parameters are “yes” then the filename of the instrumental response spectra (“*InstResp*”) has to be provided at *spCal* and the filename of the telescope polarization spectra (“*TelPol*”) has to be provided at *spzero*.

CalA is the offset angle that is subtracted to the position angle. This subtraction is required for correction of the instrumental offset.

bqu is a boolean parameter (yes/no). If *bqu* = *yes* then $Q_n(\lambda)$ and $U_n(\lambda)$ are recomputed from $P(\lambda)$ and $\Theta(\lambda)$ (Eq. 3.20). This re-computation will calibrate $Q_n(\lambda)$ and $U_n(\lambda)$ of the instrumental responses; since these correction were performed directly on $P(\lambda)$ and $\Theta(\lambda)$ (Eq. 3.19).

pixdir is the address of the directory containing the pixel files. The string entered at this parameter is the input to the IRAF subroutine call “*imsdir*”.

After all these parameters are properly filled, the command

```
cl> spolari
```

is the only command required to run SPRS. If the parameters in *eparm spolari* are entered as shown in Table D.2, then on the output spectra file (“*OutputP*”) header, the following information will be added:

```
INST_RES= 'Correction Done with InstResp'
TEL_POL = 'Correction Done with TelPol'
AP1_BD1 = 'Flux= I0 + I45 + I90 + I135'
AP2_BD1 = 'Normalized Stoke's Vector (Q/I)'
AP3_BD1 = 'Normalized Stoke's Vector (U/I)'
AP4_BD1 = 'Degree of LINEAR POLARIZATION (1=100%) [Calibrated]'
AP5_BD1 = 'Position ANGLE of POLARIZATION (in Deg) [Calibrated]'
AP1_BD2 = 'SIGMA in Flux = (dI0 + dI45 + dI90 + dI135)'
AP2_BD2 = 'SIGMA in Normalized Stoke's Vector (Q/I)'
AP3_BD2 = 'SIGMA in Normalized Stoke's Vector (U/I)'
AP4_BD2 = 'SIGMA in Degree of LINEAR POLARIZATION (1=100%)'
AP5_BD2 = 'SIGMA in Azimuth ANGLE of POLARIZATION (in Deg)'
```

This will provide the user the required information about the content of each aperture (AP) and the bands (BD) and the calibration files used.

Appendix:E

Phase Dependent Polarization

E.1 Phase Dependent Polarization of Comet Hale-Bopp

The Following Tables were compiled from literature and phase dependent observations obtain through privet communication with different authors. This phase dependent polarization through different filters has been used in Fig. 5.1.

Table E.1: *Phase dependent polarization data for Comet 1995 O1 Hale-Bopp*

Phase Angle	P %	σ_P %	Filter Å	Aperture Arcsec(dia)	Date of Observation	r AU	Δ AU	Ref.
3.1	-1.00	0.05	6840 (90)	22.5	1996 Jul. 7.23	3.87	2.86	M
4.79	-1.19	0.17	7228 (1140)		1996 Jun. 20.95	4.03		K
5.03	-1.20	0.17	7228 (1140)		1996 Jun. 19.94	4.04		K
5.25	-1.33	0.40	6840 (90)		1996 Jun. 18.96	4.05		K
6.16	-0.58	0.16	7228 (1140)		1996 Jul. 18.92	3.73		K
6.45	-1.25	0.12	7228 (1140)		1996 Jul. 19.87	3.72		K
6.9	-0.4	0.4	6700 (1000)	22.5	1996 Jun. 12.2	4.1	3.2	H
6.9	-1.0	0.8	5230 (80)	..	1996 Jun. 12.2	4.1	3.2	H
7.3	-0.3	0.4	6700 (1000)	..	1996 Jun. 10.2	4.1	3.2	H
7.5	-0.5	0.3	5230 (80)	..	1996 Jun. 9.3	4.2	3.3	H
12.78	-1.20	0.10	7228 (1140)		1996 Aug. 9.83	3.48		K
13.04	-1.24	0.09	7228 (1140)		1996 Aug. 10.81	3.47		K
16.3	-0.86	0.10	7600 (80)	8.2	1996 Aug. 25.13	3.31	2.79	M
"	-0.60	0.07	7600 (80)	15.5	"	"	"	M
"	-0.82	0.08	7600 (80)	22.5	"	"	"	M
17.2	-2.01	0.22	6840 (90)	52.4	1996 Nov. 1.00	2.52	3.05	G
"	-1.26	0.27	4845 (65)	"	"	"	"	G
"	-2.69	2.17	3650 (80)	"	"	"	"	G
18.0	-0.34	0.08	7600 (80)	8.2	1996 Sep. 4.92	3.22	2.81	M
"	-0.54	0.06	7600 (80)	15.5	"	"	"	M

Table E.1: Phase dependent polarization: Comet Hale-Bopp (continued)

Phase Angle	P %	σ_P , %	Filter Å	Aperture Arcsec(dia)	Date of Observation	r AU	Δ AU	Ref.
18.8	-3.85	1.16	6840 (90)	52.4	1996 Oct. 16.64	2.70	3.04	G
"	-3.13	0.85	4845 (65)	"	"	"	"	G
"	-3.11	2.40	3650 (80)	"	"	"	"	G
18.9	-0.56	0.11	7600 (80)	8.2	1996 Oct. 16.99	3.04	2.71	M
19.0	-0.51	0.04	7600 (80)	15.5	1996 Oct. 15.98	3.04	2.72	M
"	-0.46	0.04	7600 (80)	22.5	"	"	"	M
19.5	2.1	0.9	6700 (1000)	..	1996 Oct. 3.0	2.8	3.0	H
19.6	1.5	0.6	6700 (1000)	..	1996 Sep. 30.0	2.9	3.0	H
27.7	3.75	0.10	6840 (90)	26.5	1997 May. 4.60	1.08	1.83	G
"	2.73	0.10	4845 (65)	"	"	"	"	G
"	2.30	1.00	3650 (80)	"	"	"	"	G
28.9	3.97	0.09	4260 (65)	15.5	1997 May 3.07	1.07	1.80	M
28.9	2.92	0.08	4845 (65)	8.2	1997 May 3.06	1.07	1.80	M
28.9	4.07	0.14	6840 (90)	8.2	1997 May 3.05	1.07	1.80	M
"	3.89	0.06	6840 (90)	15.5	"	"	"	M
28.9	3.97	0.09	7000 (175)	15.5	1997 May 3.06	1.07	1.80	M
29.3	5.0	2.0	6700 (1000)	..	1997 Feb. 6.9	1.3	1.3	H
30.8	5.05	0.09	6840 (90)	26.5	1997 Apr. 29.60	1.04	1.74	G
"	3.98	0.09	4845 (65)	"	"	"	"	G
"	3.15	0.40	3650 (80)	"	"	"	"	G
30.8	5.22	0.07	4260 (65)	15.5	1997 Apr. 30.07	1.05	1.75	M
30.8	4.05	0.07	4845 (65)	8.2	1997 Apr. 30.06	1.05	1.75	M
30.8	5.41	0.11	6840 (90)	8.2	1997 Apr. 30.05	1.05	1.75	M
30.8	5.22	0.07	7000 (175)	15.5	1997 Apr. 30.06	1.05	1.75	M
"	5.07	0.08	6840 (90)	15.5	"	"	"	M
31.4	5.67	0.07	6840 (90)	26.5	1997 Apr. 28.60	1.03	1.72	G
"	4.50	0.05	4845 (65)	"	"	"	"	G
"	4.50	0.25	3650 (80)	"	"	"	"	G
31.5	5.30	0.06	7600 (80)	5.5	1997 Feb. 11.46	1.25	1.81	M
"	5.00	0.04	7600 (80)	8.2	"	"	"	M
"	5.42	0.06	7600 (80)	10.6	"	"	"	M
"	5.89	0.04	7600 (80)	15.5	"	"	"	M
"	5.80	0.08	7600 (80)	31.1	"	"	"	M
32.6	5.67	0.08	6840 (90)	52.4	1997 Feb. 13.02	1.23	1.77	G
"	4.40	0.07	4845 (65)	"	"	"	"	G
"	3.94	0.25	3650 (80)	"	"	"	"	G
32.7	4.80	0.17	4845 (65)	8.2	1997 Apr. 27.08	1.02	1.70	M
"	5.04	0.09	4845 (65)	22.5	"	"	"	M
"	5.91	0.08	6840 (90)	8.2	1997 Apr. 27.04	1.02	1.70	M
"	5.94	0.07	6840 (90)	15.5	"	"	"	M
"	6.36	0.09	7000 (175)	8.2	1997 Apr. 27.06	1.02	1.70	M
"	5.96	0.06	7000 (175)	15.5	"	"	"	M

Table E.1: Phase dependent polarization: Comet Hale-Bopp (continued)

Phase Angle	P %	σ_P %	Filter Å	Aperture Arcsec(dia)	Date of Observation	r AU	Δ AU	Ref.
34.19	4.66	0.39	3448 (84)		1997 Apr. 24.78	1.01		K
"	5.41	0.10	4450 (67)		1997 Apr. 24.77	1.01		K
34.20	5.90	0.09	5260 (56)		1997 Apr. 24.76	1.01		K
"	7.22	0.10	7128 (58)		1997 Apr. 24.75	1.01		K
34.8	7.40	0.07	6840 (90)	8.2	1997 Feb. 17.40	1.19	1.69	M
"	7.30	0.06	6840 (90)	15.5	"	"	"	M
"	7.28	0.07	6840 (90)	31.1	"	"	"	M
34.8	8.19	0.06	7600 (80)	8.2	1997 Feb. 17.39	1.19	1.69	M
"	8.03	0.09	7600 (80)	15.5	"	"	"	M
"	7.96	0.07	7600 (80)	22.5	"	"	"	M
36.04	5.38	0.15	4060 (70)		1997 Feb. 19.11	1.16		K
"	6.23	0.12	4845 (65)		1997 Feb. 19.10	1.16		K
"	4.78	0.10	5140 (90)		1997 Feb. 19.10	1.16		K
"	7.83	0.02	6840 (90)		1997 Feb. 19.09	1.16		K
36.05	5.70	0.28	3650 (80)		1997 Feb. 19.12	1.16		K
36.62	5.79	0.16	4060 (70)		1997 Feb. 20.12	1.15		K
"	6.67	0.10	4845 (65)		1997 Feb. 20.11	1.15		K
"	5.13	0.11	5140 (90)		1997 Feb. 20.11	1.15		K
"	8.20	0.09	6840 (90)		1997 Feb. 20.10	1.15		K
36.63	6.22	0.37	3650 (80)		1997 Feb. 20.13	1.15		K
37.19	5.24	0.13	5140 (90)		1997 Feb. 21.10	1.14		K
"	8.56	0.14	6840 (90)		1997 Feb. 21.09	1.14		K
37.20	5.90	0.50	3650 (80)		1997 Feb. 21.12	1.14		K
"	6.97	0.13	4845 (65)		1997 Feb. 21.11	1.14		K
40.0	6.71	0.11	4060 (70)	15.5	1997 Apr. 16.10	0.95	1.53	M
"	6.80	0.09	4060 (70)	31.1	"	"	"	M
40.0	10.24	0.05	6840 (90)	8.2	1997 Apr. 16.04	0.95	1.53	M
"	9.91	0.05	6840 (90)	15.5	"	"	"	M
"	10.29	0.05	6840 (90)	31.1	"	"	"	M
40.0	8.29	0.06	4845 (65)	8.2	1997 Apr. 16.06	0.95	1.53	M
40.04	10.46	0.10	6840 (90)		1997 Feb. 26.09	1.09		K
40.05	7.70	0.30	3650 (80)		1997 Feb. 26.11	1.09		K
"	6.03	0.16	4060 (70)		1997 Feb. 26.10	1.09		K
"	8.55	0.09	4845 (65)		1997 Feb. 26.09	1.09		K
40.05	6.46	0.09	5140 (90)		1997 Feb. 26.09	1.09		K
40.06	10.54	0.09	6840 (90)		1997 Feb. 26.11	1.09		K
"	10.25	0.12	6840 (90)		1997 Feb. 26.12	1.09		K
40.5	10.55	0.07	4260 (65)	8.2	1997 Apr. 16.05	0.95	1.51	M
"	10.40	0.06	4260 (65)	15.5	"	"	"	M
"	11.02	0.11	4260 (65)	31.1	"	"	"	M
40.5	10.55	0.07	7000 (175)	8.2	1997 Apr. 16.05	0.95	1.51	M
"	10.40	0.06	7000 (175)	15.5	"	"	"	M

Table E.1: Phase dependent polarization: Comet Hale-Bopp (continued)

Phase Angle	P %	σ_P %	Filter Å	Aperture Arcsec(dia)	Date of Observation	r AU	Δ AU	Ref.
40.5	11.02	0.11	7000 (175)	31.1	1997 Apr. 15.08	0.95	1.51	M
40.6	9.04	0.10	4845 (65)	8.2	1997 Apr. 15.06	"	"	M
"	8.75	0.06	4845 (65)	22.5	"	"	"	M
"	9.00	0.06	4845 (65)	22.5	"	"	"	M
40.6	10.61	0.09	6840 (90)	5.5	1997 Apr. 15.10	0.95	1.51	M
"	10.43	0.07	6840 (90)	8.2	"	"	"	M
"	10.22	0.07	6840 (90)	10.6	"	"	"	M
"	10.32	0.06	6840 (90)	15.5	"	"	"	M
"	10.30	0.06	6840 (90)	22.5	"	"	"	M
"	10.42	0.05	6840 (90)	31.1	"	"	"	M
41.1	12.16	0.04	6840 (90)	26.5	1997 Feb. 28.02	1.08	1.50	G
"	9.33	0.04	4845 (65)	"	"	"	"	G
"	7.87	0.11	3650 (80)	"	"	"	"	G
41.7	11.63	0.05	6840 (90)	26.5	1997 Mar. 1.01	1.07	1.49	G
"	9.43	0.07	4845 (65)	"	"	"	"	G
"	7.83	0.28	3650 (80)	"	"	"	"	G
41.7	11.73	0.07	6840 (90)	52.4	"	"	"	G
"	9.57	0.05	4845 (65)	"	"	"	"	G
"	8.08	0.10	3650 (80)	"	"	"	"	G
42.5	12.16	0.07	4260 (65)	15.5	1997 Apr. 12.12	0.94	1.47	M
42.5	10.35	0.08	4845 (65)	8.2	1997 Apr. 12.11	0.94	1.47	M
42.5	11.66	0.04	6840 (90)	8.2	1997 Apr. 12.03	0.94	1.47	M
"	11.63	0.07	6840 (90)	15.5	"	"	"	M
"	11.99	0.14	6840 (90)	31.1	"	"	"	M
42.5	12.16	0.07	7000 (175)	15.5	1997 Apr. 12.11	0.94	1.47	M
43.1	12.27	0.06	6840 (90)	26.5	1997 Apr. 10.61	0.93	1.44	G
"	10.24	0.04	4845 (65)	"	"	"	"	G
"	8.82	0.13	3650 (80)	"	"	"	"	G
43.1	12.06	0.07	4260 (65)	15.5	1997 Apr. 11.10	0.93	1.46	M
"	12.58	0.11	4260 (65)	31.1	"	"	"	M
43.1	10.81	0.11	4845 (65)	8.2	1997 Apr. 11.08	0.93	1.46	M
"	10.08	0.05	4845 (65)	22.5	"	"	"	M
"	10.18	0.06	4845 (65)	22.5	"	"	"	M
43.1	11.76	0.06	6840 (90)	8.2	1997 Apr. 11.03	0.93	1.46	M
"	12.01	0.07	6840 (90)	15.5	"	"	"	M
"	12.01	0.06	6840 (90)	31.1	"	"	"	M
43.1	12.06	0.07	7000 (175)	8.2	1997 Apr. 11.06	0.93	1.46	M
"	12.36	0.07	7000 (175)	15.5	"	"	"	M
"	12.58	0.11	7000 (175)	31.1	"	"	"	M
43.2	10.9	0.9	5230 (80)	..	1997 Apr. 10.83	0.9	1.44	H
43.21	7.78	0.06	5141 (118)		1997 Apr. 10.76	0.93		K
43.22	8.85	0.38	3448 (84)		1997 Apr. 10.75	0.93		F

Table E.1: Phase dependent polarization: Comet Hale-Bopp (continued)

Phase Angle	P %	σ_P %	Filter Å	Aperture Arcsec(dia)	Date of Observation	r AU	Δ AU	Ref.
43.22	9.91	0.10	4450 (67)		1997 Apr. 10.75	0.93		K
"	10.25	0.07	5260 (56)		1997 Apr. 10.74	0.93		K
"	12.41	0.12	7128 (58)		1997 Apr. 10.74	0.93		K
43.6	13.4	0.5	6500 (1400)	..	1997 Apr. 9.83	0.9	1.43	H
43.6	12.83	0.08	6840 (90)	8.2	1997 Apr. 10.08	0.93	1.44	M
"	12.61	0.05	6840 (90)	15.5	"	"	"	M
"	12.52	0.08	6840 (90)	31.1	"	"	"	M
43.78	8.79	0.51	3448 (84)		1997 Apr. 9.77	0.93		K
"	10.15	0.10	4450 (67)		1997 Apr. 9.75	0.93		K
43.79	11.08	0.11	5260 (56)		1997 Apr. 9.75	0.93		K
"	12.78	0.12	7128 (58)		1997 Apr. 9.74	0.93		K
44.7	13.2	0.9	6500 (1400)	..	1997 Apr. 7.84	0.9	1.41	H
45.2	13.7	0.6	6500 (1400)	..	1997 Apr. 6.83	0.9	1.40	H
45.23	14.07	0.10	6840 (90)		1997 Mar. 8.02	1.01		K
"	14.11	0.11	6840 (90)		1997 Mar. 8.03	1.01		K
"	14.16	0.13	6840 (90)		1997 Mar. 8.04	1.01		K
45.24	10.06	0.12	4060 (70)		1997 Mar. 8.06	1.01		K
"	11.58	0.10	4845 (65)		1997 Mar. 8.05	1.01		K
"	8.98	0.73	5140 (90)		1997 Mar. 8.05	1.01		K
45.25	10.07	0.20	3650 (80)		1997 Mar. 8.07	1.01		K
45.36	9.94	0.22	3448 (84)		1997 Apr. 6.76	0.92		K
"	11.15	0.10	4450 (67)		1997 Apr. 6.74	0.92		K
"	8.74	0.07	5141 (118)		1997 Apr. 6.74	0.92		K
"	12.01	0.10	5260 (56)		1997 Apr. 6.75	0.92		K
"	13.83	0.12	7128 (58)		1997 Apr. 6.75	0.92		K
45.7	14.4	0.5	6500 (1400)	..	1997 Apr. 5.82	0.9	1.39	H
45.7	13.94	0.15	6840 (90)	5.5	1997 Apr. 6.03	0.92	1.40	M
"	13.67	0.10	6840 (90)	8.2	"	"	"	M
"	13.80	0.13	6840 (90)	15.5	"	"	"	M
"	13.85	0.08	6840 (90)	31.5	"	"	"	M
46.6	12.5	0.8	5230 (80)	..	1997 Apr. 3.86	0.9	1.37	H
46.6	14.56	0.10	6840 (90)	26.5	1997 Apr. 3.62	0.92	1.37	G
"	12.22	0.03	4845 (65)	"	"	"	"	G
"	10.84	0.50	3650 (80)	"	"	"	"	G
46.2	14.15	0.06	6840 (90)	26.5	1997 Apr. 4.59	0.92	1.38	G
"	11.86	0.05	4845 (65)	"	"	"	"	G
"	10.38	0.20	3650 (80)	"	"	"	"	G
46.70	11.08	0.68	3448 (84)		1997 Apr. 3.76	0.92		M
"	11.83	0.16	4450 (67)		1997 Apr. 3.76	0.92		M
"	9.45	0.07	5141 (118)		1997 Apr. 3.76	0.92		M
"	12.56	0.12	5260 (56)		1997 Apr. 3.76	0.92		M
"	14.84	0.15	7128 (58)		1997 Apr. 3.76	0.92		M

Table E.1: Phase dependent polarization: Comet Hale-Bopp (continued)

Phase Angle	P %	σ_P %	Filter Å	Aperture Arcsec(dia)	Date of Observation	r AU	Δ AU	Ref.
47.0	14.63	0.04	6840 (90)	26.5	1997 Apr. 2.59	0.91	1.36	G
"	12.20	0.06	4845 (65)	"	"	"	"	G
"	10.82	0.30	3650 (80)	"	"	"	"	G
47.0	15.8	0.9	6500 (1400)	..	1997 Apr. 2.84	0.9	1.36	H
47.0	14.82	0.11	6840 (90)	5.5	1997 Apr. 3.04	0.92	1.37	M
"	14.44	0.07	6840 (90)	8.2	"	"	"	M
"	14.35	0.05	6840 (90)	10.6	"	"	"	M
"	14.55	0.06	6840 (90)	15.5	"	"	"	M
"	14.17	0.06	6840 (90)	22.5	"	"	"	M
"	14.17	0.06	6840 (90)	31.1	"	"	"	M
47.4	15.2	0.5	6500 (1400)	..	1997 Apr. 1.85	0.9	1.35	H
47.4	12.66	0.09	4845 (65)	8.2	1997 Apr. 3.07	0.92	1.37	M
"	12.29	0.08	4845 (65)	22.5	"	"	"	M
"	12.07	0.08	4845 (65)	22.5	"	"	"	M
47.4	14.81	0.14	6840 (90)	8.2	1997 Apr. 2.06	0.91	1.36	M
"	14.63	0.07	6840 (90)	10.6	"	"	"	M
"	14.69	0.07	6840 (90)	15.5	"	"	"	M
"	14.81	0.07	6840 (90)	22.5	"	"	"	M
"	14.75	0.07	6840 (90)	31.1	"	"	"	M
47.4	15.98	0.08	7600 (80)	8.2	1997 Apr. 2.08	0.91	1.36	M
"	15.99	0.08	7600 (80)	22.5	"	"	"	M
47.46	11.73	0.63	3448 (84)		1997 Apr. 1.75	0.91		K
"	12.53	0.16	4450 (67)		1997 Apr. 1.75	0.91		K
"	9.54	0.06	5141 ()		1997 Apr. 1.75	0.91		K
"	13.51	0.60	5260 (56)		1997 Apr. 1.75	0.91		K
"	15.55	0.12	7128 (58)		1997 Apr. 1.75	0.91		K
47.58	12.65	0.08	4845 (65)		1997 Mar. 14.06	0.97		K
"	9.92	0.08	5140 ()		1997 Mar. 14.06	0.97		K
"	15.30	0.11	6840 (90)		1997 Mar. 14.03	0.97		K
"	15.79	0.11	6840 (90)		1997 Mar. 14.04	0.97		K
47.59	10.94	0.31	3650 (80)		1997 Mar. 14.07	0.97		K
48.08	10.76	0.26	3448 (84)		1997 Mar. 30.75	0.91		K
"	12.84	0.13	4450 (67)		1997 Mar. 30.77	0.91		K
48.09	13.77	0.16	5260 (56)		1997 Mar. 30.73	0.91		K
"	15.75	0.24	7128 (58)		1997 Mar. 30.73	0.91		K
48.54	12.75	0.07	4845 (65)		1997 Mar. 17.76	0.95		K
"	9.00	0.09	5140 (90)		1997 Mar. 17.73	0.95		K
"	9.33	0.08	5140 (90)		1997 Mar. 17.73	0.95		K
"	9.87	0.07	5140 (90)		1997 Mar. 17.73	0.95		K
"	7.54	0.08	5140 (90)		1997 Mar. 17.74	0.95		K
"	10.45	0.08	5140 (90)		1997 Mar. 17.74	0.95		K
"	15.14	0.08	6840 (90)		1997 Mar. 17.71	0.95		K

Table E.1: Phase dependent polarization: Comet Hale-Bopp (continued)

Phase Angle	P %	σ_P %	Filter \AA	Aperture Arcsec(dia)	Date of Observation	r AU	Δ AU	Ref.
48.60	11.60	0.27	3650 (80)		1997 Mar. 18.03	0.95		K
"	13.32	0.08	4845 (65)		1997 Mar. 18.02	0.95		K
"	16.01	0.12	6840 (90)		1997 Mar. 18.02	0.95		K
48.75	15.61	0.57	7128 (58)		1997 Mar. 27.73	0.92		K
49.07	13.26	0.08	4845 (65)		1997 Mar. 21.74	0.93		K
"	10.66	0.08	5140 (90)		1997 Mar. 21.77	0.93		K
"	16.00	0.08	6840 (90)		1997 Mar. 21.76	0.93		K

Ref. No G. Ganesh et al 1998

Ref. No H. Hadamcik et al. 1997 and Hadamcik 1999

Ref. No K. Kiselev 1997

Ref. No M. Manset and Bastien 2000

E.2 Phase Dependent Polarization of Comet Wild 2

Table E.2: Phase dependent polarization data for Comet Wild-2

Phase Angle	P %	σ_P %	Filter \AA	Aperture Arcsec(dia)	Date of Observation	r AU	Δ AU	Ref.
9.7	-1.8	0.5	6500 (1000)		1997 Feb. 4.14	1.82	0.86	H'
1.4	-1.6	0.5	6500 (1000)		1997 Feb. 5.00	1.82	0.86	H'
11.0	-0.9	0.5	6500 (1000)		1997 Feb. 6.16	1.82	0.86	H'
35.7	3.9	0.6	6500 (1000)		1997 Apr. 1.96	1.62	0.99	H'
35.9	3.8	0.5	6500 (1000)		1997 Apr. 2.95	1.62	0.99	H'
36.7	4.6	0.6	6500 (1000)		1997 Apr. 6.92	1.61	1.01	H'
36.9	5.0	0.5	6500 (1000)		1997 Apr. 7.92	1.61	1.02	H'
37.2	5.0	0.6	6500 (1000)		1997 Apr. 9.95	1.61	1.03	H'
38.8	6.29	1.311	6500 (1000)		1997 Apr. 23.72	1.59	1.10	P

Ref. No H'. Hadamcik et al. 2000 and Hadamcik 1999

Ref. No P. From this spectropolarimetric work.

References

- Ganesh, S., Joshi, U.C., Baliyan, K.S. and Deshpande, M.R., 1998. *A & A Suppl. Ser.* **129**, 489.
- Hasegawa, H., Ichikawa, T., Abe, S., Hamamura, S., Ohnishi, K., and Watanabe, J., 1997. *Earth, Moon, and Planets*, **78** 353.
- Hadamcik, E., Levasseur-Regourd, A. C., and Renard, J. B., 1997. *Earth, Moon, and Planets*, **78** 365.
- Hadamcik, E., 1999. Ph.D. Thesis, l'Université Paris 6.
- Kiselev, N. N., and Velichko, F. P., 1997. *Earth, Moon, and Planets*, **78** 365.
- Kiselev, N. N., Kiselev, K. N., Lupishko, D. F., and Krugly, Yu. N., 1997. *28th Annual Lunar and Planetary Science Conference*, p. 735.
- Kiselev, N. N., 2000. (*Privet Communication*).
- Manset, N., and Bastien, P., 2000. *Icarus*, **145** 203.
- Furusho, Reiko; Suzuki, Bunji; Yamamoto, Naotaka; Kawakita, Hideyo; Sasaki, Toshiyuki; Shimizu, Yasuhiro; and Kurakami, Tomio, 1999. *PASJ* **51**, 367.

Appendix:F

Acronyms

F.1 Acronyms Used In this Thesis

AAO	: Anglo-Australian Observatory.
ADS	: Astrophysics Data System: http://ads.harvard.edu/
AGB	: asymptotic Giant Branch.
AU	: Astronomical Unit.
B&C	: Boller & Chivens.
BCCA	: Ballistic Cluster-Cluster Aggregation.
CCD	: Charge Couple Device.
DDA	: Discrete Dipole Approximation.
Dec	: Declination.
e-beam	: Extraordinary beam.
EMT	: Effective Median Theory.
FBImp	: Four Beam Imaging Polarimeter.
FITS	: Flexible Image Transport System.
FORS	: FOcal Reducer/low dispersion Spectrograph.
FWHM	: Full Width at Half Maximum.
GMT	: Greenwich mean time.
HST	: Hubble Space Telescope.
HWP	: Half Wave Plate.
I-CCD	: Intensified CCD.
IDP	: Interplanetary Dust Particle.
IAO	: Indian Astronomical Observatory.
IIA	: Indian Institute of Astrophysics.

I/O	: Input / Output
IR	: Infrared.
IRAF	: Image Reduction and Analysis Facility.
I&S-P	: Imaging and Spectroscopic Polarimeter.
ISO	: Infrared Space Observatory.
LAMS	: Large Area Momentum Sensor.
LICC	: Local Instrument Control Computer.
LSB	: Lowest Significant Byte.
MGTP	: Modified Glan-Taylor Prism.
NASA	: National Aeronautics and Space Administration.
O-DB.AMRSP	: Optical, Dual-beam, Automated. Medium Resolution Spectropolarimeter.
o-beam	: Ordinary beam.
PCD	: Pitch Circle Diameter.
PSF	: Point Spread Function.
PLC	: Path Length Compensator.
PVDF	: PolyVinylidene Fluoride (piezoelectric sensors for the measurement of induced stresses).
QWP	: Quarter Wave Plate.
RA	: Right Ascension.
RAM	: Random Access Memory.
SiA	: Astronomical Silicate.
SiX	: <i>Mg</i> rich Silicate.
SMC	: Small Magellanic Cloud.
SPRS	: SpectroPolarimetric Reduction Software.
SWS	: Short Wavelength Spectrometer.
UT	: Universal Time.
UV	: Ultra Violet.
VBO	: Vainu Bappu Observatory.
VBT	: Vainu Bappu Telescope.
VLT	: Very Large Telescope.
WFPC2	: Wide-Field Planetary Camera 2.

List of Publications

List of Publications, Presentations and Posters based on the work reported in this Thesis.

Publications

1. R. Vasundhara & Pavan Chakraborty, 1999. *Modeling of jets from Comet Hale-Bopp - Observations from the Vainu Bappu Observatory ICARUS.*, Vol. **140**, pp. 221-230.
2. Pavan Chakraborty, 1999. in *International Symposium on Astrophysics Research and Science Education* Ed. Chris Impey, *Sponsored and hosted by the Vatican Observatory*, p. 109.
3. R. Vasundhara, Pavan Chakraborty, Andreas Hänel & Erwin Heiser, 1997. *Modeling Dust Jets and shells from Comet Hale-Bopp Earth Moon and Planets*, **78**, 321.

Presentations

1. Pavan Chakraborty 1998. *Spectropolarimeter for the Vainu Bappu Telescope An oral presentation at the International Symposium on Astrophysics Research And Science Education at The Vatican Observatory June 14-21 1998, Castel Gandolfo, Italy. (Proceedings of the Symposium).*

Posters

1. Pavan Chakraborty, R. Vasundhara, 1998. *Spectropolarimetry of Comet Hale-Bopp A poster presentation at the 19th Meeting of the Astronomical Society of India, (February 1st to 4th 1999), hosted by the Raman Research Institute, Bangalore, India.*

2. Pavan Chakraborty, Andreas Hänel, Erwin Heiser and R. Vasundhara, 1998. *Modeling Dust Jets and shells from Comet Hale-Bopp – A Cooperation of an Amateur Observatory and Professionals Astronomische Gesellschaft Meeting, A poster presentation at the Annual Scientific Meeting of the Astronomische Gesellschaft in Heidelberg from September 14th to 19th 1998, Poster No. P3.*
3. R. Vasundhara, Pavan Chakraborty, Andreas Hänel & Erwin Heiser. 1997. *Modeling Dust Jets and shells from Comet Hale-Bopp Poster at The First International Conference on Comet Hale-Bopp, held at Tenerife, Spain.*
4. R. Vasundhara, Pavan Chakraborty and K. Jayakumar, 1996. *Comet Hale-Bopp, Intensity Variation across the inner comma A poster presentation at the ASI meeting at Guwahati, Jan. 1996.*